Physics of quantum fluids in two-dimensional topological systems

Olivier Bleu

UNIVERSITE CLERMONT AUVERGNE - CLERMONT-FERRAND

ECOLE DOCTORALE DES SCIENCES FONDAMENTALES

UFR SCIENCES ET TECHNOLOGIES

THESE DE DOCTORAT

Pour accéder au grade de

Docteur d'université en sciences

de l'université Clermont Auvergne - Clermont-Ferrand

Spécialité : Physique, Milieux denses et Matériaux

Défendue par

Olivier BLEU

Physics of quantum fluids

in two-dimensional topological systems

Préparée à l'Institut Pascal - Clermont-Ferrand,

au sein de l'équipe:

Optoélectronique Quantique et Nanophotonique

Soutenue publiquement le 27/09/2018

Commission d'examen:

Présidente :	Pr. Julia Meyer
Rapporteurs :	Dr. Jean-Noël Fuchs
	Pr. Alexander Poddubny
Examinateurs :	Dr. Martine Mihailovic
	Dr. Anna Minguzzi
	Dr. Frédéric Piéchon
Directeurs de thèse :	Dr. Guillaume Malpuech
	Dr. Dmitry Solnyshkov

Remerciements

De la même façon que dans une équipe sportive, un ensemble musical, ou la 34ème Horde, l'entente et la cohésion au sein d'un groupe de recherche sont fondamentales pour avancer. J'ai eu la chance d'effectuer ma thèse dans une formidable atmosphère de ce point de vue.

Pour cela, j'exprime ma profonde gratitude à mes deux directeurs de thèse Dmitry et Guillaume. Nous avons partagé notre bureau et nos journées pendant plus de trois ans et il m'est impossible de résumer ici tout ce qu'ils ont pu m'apporter. Du point de vue scientifique, c'est une chance énorme pour un doctorant de pouvoir échanger, réfléchir, débattre et progresser chaque jour avec des chercheurs de leur niveau. Si l'on ajoute tous les moments et conversations plus personnels et tout aussi enrichissants, cela donne trois excellentes années, et une barre placée vraiment très haut pour mes futurs collègues.

Je tiens à remercier mes rapporteurs de thèse Jean-Noël Fuchs et Alexander Poddubny pour leurs commentaires et leur temps utilisé pour la relecture de mon manuscrit. Je remercie aussi tous les membres du jury: Julia Meyer, Martine Mihailovic, Anna Minguzzi, et Frédéric Piéchon d'avoir accepté de venir jusqu'à Clermont-Ferrand pour l'évaluation de ma soutenance ainsi que pour leurs questions et les discussions intéressantes que nous avons eu à cette occasion.

Je remercie chaleureusement les différents collègues expérimentateurs avec qui j'ai eu la chance de discuter et de collaborer. En premier lieu, je remercie la co-équipe du C2N et PhLAM dirigée par Jacqueline Bloch et Alberto Amo. Merci à Marijana Milićević, Philippe St-Jean et Nicola Carlon Zambon pour leurs implications dans nos travaux communs qui sont maintenant publiés! Je remercie également l'équipe de Lecce dirigée par Daniele Sanvitto, notamment Antonio Gianfrate pour son intérêt pour notre proposition et sa motivation.

Je voudrais témoigner ma reconnaissance et ma sympathie à l'ensemble de mes collègues au sein de l'Institut Pascal, qu'ils soient chercheurs, doctorants ou de l'équipe administrative. Je remercie particulièrement Sergei qui nous a rejoints dans le bureau et dont la présence pendant ma rédaction a parfois été salvatrice, l'équipe de spectroscopie optique pour tous nos échanges amicaux, ainsi que Françoise et Vanessa pour leur aide lors de mes différentes démarches administratives.

Je remercie aussi mes amis, doctorants ou non (je ne cite pas tout le monde, il y a trop d'affreux!), pour tous ces moments de retrouvailles qui font du bien, que ce soit la musique, les soirées, les séjours parfois rocambolesques ou même le sport! Mention spéciale à tous les colocataires, là encore, il y a de sacrés souvenirs.

Le clou du spectacle reste bien sûr pour la fin, la brique élémentaire sans laquelle personne ne serait remercié ci-dessus, merci à ma famille. Merci à mes parents de m'avoir permis d'en arriver là, de m'avoir poussé par moments quand la motivation me faisait défaut, vous aviez raison ça valait certainement le coup.

Résumé

Cette thèse est consacrée à la description de la physique à une particule ainsi qu'à celle de fluides quantiques bosoniques dans des systèmes topologiques.

Les deux premiers chapitres sont introductifs. Dans le premier, nous introduisons des éléments de théorie des bandes et les quantités géométriques et topologiques associées : tenseur métrique quantique, courbure de Berry, nombre de Chern. Nous discutons différents modèles et réalisations expérimentales donnant lieu à des effets topologiques. Dans le second chapitre, nous introduisons les condensats de Bose-Einstein ainsi que les excitons-polaritons de cavité.

La première partie des résultats originaux discute des phénomènes topologiques à une particule dans des réseaux en nid d'abeilles. Cela permet de comparer deux modèles théoriques qui mènent à l'effet Hall quantique anormal pour les électrons et les photons dû à la présence d'un couplage spin-orbite et d'un champ Zeeman. Nous étudions aussi l'effet Hall quantique de vallée photonique à l'interface entre deux réseaux de cavités avec potentiels alternés opposés.

Dans une seconde partie, nous discutons de nouveaux effets qui émergent due à la présence d'un fluide quantique interagissant décrit par l'équation de Gross-Pitaevskii dans ces systèmes. Premièrement, il est montré que les interactions spin anisotropes donnent lieu à des transitions topologiques gouvernées par la densité de particules pour les excitations élémentaires d'un condensat spineur d'exciton-polaritons. Ensuite, nous montrons que les tourbillons quantifiés d'un condensat scalaire dans un système avec effet Hall quantique de vallée, manifestent une propagation chirale le long de l'interface contrairement aux paquets d'ondes linéaires. La direction de propagation de ces derniers est donnée par leur sens de rotation donnant lieu à un transport de pseudospin de vallée protégé topologiquement, analogue à l'effet Hall quantique de spin.

Enfin, revenant aux effets géométriques linéaires, nous nous sommes concentrés sur l'effet Hall anormal. Dans ce contexte, nous présentons une correction non-adiabatique aux équations semi-classiques décrivant le mouvement d'un paquet d'ondes qui s'exprime en termes du tenseur géométrique quantique. Nous proposons un protocole expérimental pour mesurer cette quantité dans des systèmes photonique radiatifs.

Mots-clés: Isolants topologiques, géométrie de bandes, courbure de Berry, effet Hall anormal, isolant de Chern, couplage spin-orbite, photonique topologique, exciton-polaritons, condensats de Bose-Einstein, excitations de Bogoliubov, vortex quantifiés.

Abstract

This thesis is dedicated to the description of both single-particle and bosonic quantum fluid Physics in topological systems.

After introductory chapters on these subjects, I first discuss single-particle topological phenomena in honeycomb lattices. This allows to compare two theoretical models leading to quantum anomalous Hall effect for electrons and photons and to discuss the photonic quantum valley Hall effect at the interface between opposite staggered cavity lattices.

In a second part, I present some phenomena which emerge due to the interplay of the linear topological effects with the presence of interacting bosonic quantum fluid described by mean-field Gross-Pitaevskii equation. First, I show that the spin-anisotropic interactions lead to density-driven topological transitions for elementary excitations of a condensate loaded in the polariton quantum anomalous Hall model (thermal equilibrium and out-of-equilibrium quasi-resonant excitation configurations).

Then, I show that the vortex excitations of a scalar condensate in a quantum valley Hall system, contrary to linear wavepackets, can exhibit a robust chiral propagation along the interface, with direction given by their winding in real space, leading to an analog of quantum spin Hall effect for these non-linear excitations.

Finally, coming back to linear geometrical effects, I will focus on the anomalous Hall effect exhibited by an accelerated wavepacket in a two-band system. In this context, I present a non-adiabatic correction to the known semiclassical equations of motion which can be expressed in terms of the quantum geometric tensor elements. We also propose a protocol to directly measure the tensor components in radiative photonic systems.

Keywords: Topological insulators, band geometry, Berry curvature, anomalous Hall effect, Chern insulators, spin-orbit coupling, topological photonics, exciton-polaritons, Bose-Einstein condensates, Bogoliubov excitations, quantized vortices.

Contents

Introduction

The classification of solids as metals or insulators is based on the knowledge of their electronic band structure and of the position of their Fermi level. Hence, if the Fermi level lies in a forbidden energy gap the system is insulating whereas the system is conducting if the Fermi level lies in an allowed energy band. The discovery of the quantum Hall effect in the 80's has allowed to understand that such classification is not complete. Indeed, the eigenstates associated with the energy bands can have a non-trivial structure. Locally, a non-trivial change of the eigenstates in reciprocal space is associated with a Berry curvature. In two dimensions, this quantity integrated over the whole Brillouin zone gives a topological invariant known as the Chern number. If the sum of the Chern number over all the bands below a bulk band gap is different from zero it implies the presence of gapless states at the boundaries of the system. A topological insulator is a system insulating in the bulk with such conducting boundaries. Their classification requires the knowledge of the bulk invariant in addition to the bulk band structure and the Fermi level position.
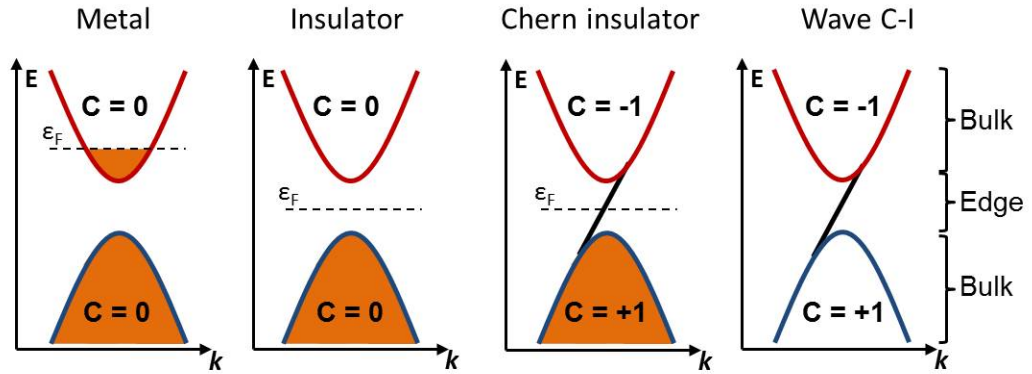
Figure 1: Schematic band structures of metals, insulators, Chern insulators and Chern insulator analogs for arbitrary waves.

Whereas the Fermi level concept is deeply linked with the Pauli exclusion principle and therefore to the fermionic nature of electrons, the existence of a discontinuous band structure is due to interference effects thanks to their wave behaviour. Hence, one can expect the existence of topological invariants and their associated edge states in other wave systems. Actually, the research of new transport phenomena related to the presence of Berry curvature in reciprocal space has been extended to many area of Physics and is nowadays an exponentially growing field.

The use of analog systems provides new experimental facilities allowing an access to quantities beyond the reach in solid state systems. From the fundamental point

of view, novel effects are expected due to the different system specificities. Of particular interest is the interplay of quantum fluid phenomena such as superfluidity with topological effects. The well mastered cold atom or exciton-polariton platforms, where Bose-Einstein condensation and superfluidity have been observed, appear as good candidates to explore such new physics. Moreover, some of these new platforms bring novel application opportunities. For instance, the ability to engineer chiral edge states for light could be used to solve the problem of reciprocal transport, a crucial step to build efficient integrated optical circuits.

The work presented in this manuscript takes place in this context. In the first chapter, we introduce the geometrical objects associated with the band eigenstates that we use along the thesis. We also present several models and/or experimental realizations where topological edge states have been predicted and/or observed. A quick introduction to Bose-Einstein condensates and cavity polaritons specificities is given in chapter 2. Chapters 3, 4 and 5 report different interrelated results that I have obtained during the last three years as a Ph.D student. Chapter 3 is devoted to single particle topological phenomena in honeycomb lattices. First, we give a comparison between electronic and photonic quantum anomalous Hall effects based on a combination of spin-orbit coupling with a Zeeman field. Then, we present the quantum valley Hall effect and discuss it existence and robustness in cavity based honeycomb lattices. In chapter 4, we present some novel phenomena occurring thanks to the interplay between interacting condensates with band topology. We first show that spin anisotropic interactions specific of polariton systems can lead to density driven topological phase transitions for bogolon density waves. We then discuss the possibility to organize robust chiral vortex propagation when a scalar condensate is loaded in a staggered honeycomb lattice. Finally, the chapter 5 focuses on band geometry. We present a protocol to measure the components of the quantum geometric tensors in several photonic systems. The possibility to use the quantum metric to estimate the non-adiabaticity and to correct the semiclassical equations of motion of the anomalous Hall effect in a two band system is discussed in the last section.

Introduction to band geometry and topology

Contents

With the discovery of the quantum Hall effect and its quantized conductivity explained in terms of topological invariants, condensed matter physicists understood that the knowledge of the energy spectra is not sufficient to characterize the electronic properties of metals and insulators. New phases of matter have been discovered like topological superconductors and insulators. To understand their origin and behaviour, physicists had to introduce novel objects in their toolbox not present in standard textbooks of solid-state Physics [1, 2] which characterize geometrical and topological properties of the eigenstates of the system.

In this chapter, we introduce the different geometrical and topological quantities which will be used at different moments throughout this thesis. In the first section 1.1, we give a quick historical introduction of the quantum metric and Berry curvature and the link between the two. In section 1.2, we introduce non-interacting Bloch Hamiltonians and show that both the metric and the Berry curvature can be defined for Bloch state vectors in the quasi-momentum space which are commonly used in condensed matter and in wave physics. We give also a quick introduction to tight-binding approximation which is a useful tool to build minimal models. Section 1.3 is dedicated to the presentation of some important condensed matter models where band geometry and topology play a crucial role. Finally, we discuss the emergence of these concepts in other physical systems where wave phenomena are involved in section 1.4.

Of course, the goal of this chapter is not to give a complete overview of topological Physics which is by itself an enormous research field at the crossover between many areas and could require a whole thesis and even more, but to introduce the concepts which will be useful to read this manuscript. Several reviews and textbooks have been recently published on this subject both in condensed matter [3, 4, 5, 6] and other fields [7, 8, 9].

1.1   Historical viewpoint

1.1.1   Quantum metric tensor

The distance between two quantum states is defined by the Fubini-Study distance:

$$d_{FS} = \arccos(|\langle\psi_1|\psi_2\rangle|) \tag{1.1}$$

Where $|\langle\psi_1|\psi_2\rangle| = F$ is the fidelity which quantify the overlap between the two states. In this form d_{FS} can be interpreted as an angle which runs from 0 to $\pi/2$. If we assume that $|\psi(\boldsymbol{\xi})\rangle$ depends on some parameters, $\boldsymbol{\xi} = (\xi_1, \xi_2, ...)$ one can define the infinitesimal distance between two neighbouring states $|\psi(\boldsymbol{\xi})\rangle, |\psi(\boldsymbol{\xi} + d\boldsymbol{\xi})\rangle$ in the parameter space. Assuming $F \to 1$ it reads:

$$d_{FS}^2 \approx 1 - |\langle\psi(\boldsymbol{\xi})|\psi(\boldsymbol{\xi} + d\boldsymbol{\xi})\rangle|^2 = ds^2 \tag{1.2}$$

This elementary distance ds^2 written in this form is also referred as Fubini-Study distance in the literature and we will use this denomination along the thesis. The

next step is to derive the metric tensor as a function of the parameter coordinates $\boldsymbol{\xi}$. We use the Taylor expansion:

$$|\psi(\boldsymbol{\xi} + d\boldsymbol{\xi})\rangle = |\psi(\boldsymbol{\xi})\rangle + \partial_{\xi_i}|\psi(\boldsymbol{\xi})\rangle d\xi_i + \frac{1}{2}\partial_{\xi_i}\partial_{\xi_j}|\psi(\boldsymbol{\xi})\rangle d\xi_i d\xi_j \qquad (1.3)$$

where we use Einstein summation convention. A key ingredient of the derivation is the normalisation condition of Hermitian quantum mechanics $\langle\psi|\psi\rangle = 1$ which implies:

$$\langle\partial_{\xi_i}\psi|\psi\rangle = -\langle\psi|\partial_{\xi_i}\psi\rangle \quad \Longleftrightarrow \quad \Re[\langle\psi|\partial_{\xi_i}\psi\rangle] = 0 \qquad (1.4)$$

This reality condition allows to deduce another useful property for the second partial derivatives:

$$\Re[\langle\partial_{\xi_i}\psi|\partial_{\xi_j}\psi\rangle] = -\Re[\langle\psi|\partial_{\xi_i}\partial_{\xi_j}\psi\rangle] \qquad (1.5)$$

Using these properties, we can Taylor expand Eq. (1.2) up to the second order:

$$ds^2 = \left(\Re[\langle\partial_{\xi_i}\psi|\partial_{\xi_j}\psi\rangle] - \langle\partial_{\xi_i}\psi|\psi\rangle\langle\psi|\partial_{\xi_j}\psi\rangle\right) d\xi_i d\xi_j = g_{ij}d\xi_i d\xi_j \qquad (1.6)$$

where g_{ij} are the elements of the quantum metric tensor. Importantly, this object is invariant under the $U(1)$ gauge transformations $|\psi(\boldsymbol{\xi})\rangle \to e^{i\alpha(\boldsymbol{\xi})}|\psi(\boldsymbol{\xi})\rangle$. It is not surprising since Eq. (1.1) was already invariant under such transformations, however, it has an important meaning. This metric characterizes distances between "families" of states $|\tilde{\psi}\rangle = \left\{e^{i\alpha}|\psi\rangle, \alpha \in \mathbb{R}\right\}$. The space of $|\tilde{\psi}\rangle$ is known as the projective Hilbert space or the space of rays and ξ_i are nothing else than the coordinates in this space. This notion of projective space had been crucial to extend the work of Berry on geometrical phases beyond the adiabatic limit that we are going to introduce in the next section. It is also important to underline that no specific eigenbasis has been introduced for this definition.

The quantum metric tensor has been introduced in 1980 in the seminal paper of Provost and Vallée [10] in a slightly different manner: starting from the distance $|||\psi_1\rangle - |\psi_2\rangle||^2$ they derive the metric and rearrange the result to recover the gauge invariance. From the fundamental point of view, this quantum metric has been used later to make the link between the integral of the time-energy uncertainty for an arbitrary quantum evolution and the length of the corresponding curve in the projective Hilbert space [11]. In quantum information theory, the quantum distance of pure states (1.1) has been related to the statistical distance [12] and then extended to mixed states described by density matrix [13].

1.1.2 Adiabatic Berry phase, curvature and quantum geometric tensor

In 1984, M. V. Berry [14] who wasn't aware of the work of Provost and Vallée, wrote an important paper on geometrical phases in quantum mechanics in the adiabatic approximation. This work highlights that after a cyclic evolution of the Hamiltonian, the phase acquired by the wavefunction can be separated in two contributions: the dynamical and geometrical ones. The geometrical part appears to be independent of the duration of evolution but only characterized by the geometrical path followed by adiabatic wavefunction or the Hamiltonian in parameter space.

Berry phase.   To re-derive this important result, we start with the time-dependent Schrödinger equation.

$$i\hbar\frac{\partial}{\partial t}\left|\Psi(t)\right\rangle = \hat{H}[\boldsymbol{\lambda}(t)]\left|\Psi(t)\right\rangle \tag{1.7}$$

where the Hamiltonian depends explicitly on the parameter $\boldsymbol{\lambda} = (\lambda_1, \lambda_2, ...)$. Moreover, for all $\boldsymbol{\lambda}$ values there exists an orthonormal basis satisfying the stationary Schrödinger equation:

$$\hat{H}[\boldsymbol{\lambda}]\left|\psi_n(\boldsymbol{\lambda})\right\rangle = E_n(\boldsymbol{\lambda})\left|\psi_n(\boldsymbol{\lambda})\right\rangle \tag{1.8}$$

Note that this basis is not unique, any multiplication of the set of eigenvectors $\left|\psi_n(\boldsymbol{\lambda})\right\rangle$ by a global phase factor $e^{i\alpha}$ ($U(1)$ gauge transformation) is also a basis of $\hat{H}[\boldsymbol{\lambda}]$. Assuming the initial condition $\left|\Psi(t=0)\right\rangle = \left|\psi_n\right\rangle$, the adiabatic approximation implies that at each time t the system remains in the initial eigenstate, meaning that the wavefunction can be written as:

$$\left|\Psi(t)\right\rangle = c_n(t)\left|\psi_n[\boldsymbol{\lambda}(t)]\right\rangle \tag{1.9}$$

where $c_n(t) \in \mathbb{C}$ ($|c_n| = 1$) is the important quantity which encodes the phase that we want to analyse. Inserting (1.9) in (1.7), we obtain

$$i\dot{c}_n(t) = c_n(t)\left(E_n[\boldsymbol{\lambda}(t)] - i\left\langle\psi_n[\boldsymbol{\lambda}(t)]\right|\frac{\partial}{\partial t}\left|\psi_n[\boldsymbol{\lambda}(t)]\right\rangle\right) \tag{1.10}$$

Assuming the cyclic evolution ($\boldsymbol{\lambda}(T) = \boldsymbol{\lambda}(0)$) and integrating over one period T gives: $c_n(T) = c_n(0)e^{i(\gamma_{dyn}+\gamma_B)}$ with the two contributions given by:

$$\gamma_{dyn} = -\frac{1}{\hbar}\int_0^T E_n[\boldsymbol{\lambda}(t)]dt \tag{1.11}$$

$$\gamma_B = i\int_0^T \left\langle\psi_n[\boldsymbol{\lambda}(t)]\right|\frac{\partial}{\partial t}\left|\psi_n[\boldsymbol{\lambda}(t)]\right\rangle dt \tag{1.12}$$

$$= i\int_0^T \left\langle\psi_n[\boldsymbol{\lambda}(t)]\right|\nabla_{\boldsymbol{\lambda}}\left|\psi_n[\boldsymbol{\lambda}(t)]\right\rangle \cdot \dot{\boldsymbol{\lambda}}dt$$

$$= i\oint_C \left\langle\psi_n(\boldsymbol{\lambda})\right|\nabla_{\boldsymbol{\lambda}}\left|\psi_n(\boldsymbol{\lambda})\right\rangle .d\boldsymbol{\lambda} \tag{1.13}$$

γ_B is the adiabatic geometrical phase which is nowadays referred as Berry phase. The integrand in the last expression of γ_B (1.13) is called Berry connection.

$$\boldsymbol{\mathcal{A}}_n(\boldsymbol{\lambda}) = i\left\langle\psi_n(\boldsymbol{\lambda})\right|\nabla_{\boldsymbol{\lambda}}\left|\psi_n(\boldsymbol{\lambda})\right\rangle \tag{1.14}$$

It is a vector whose dimension is given by the parameter space dimensionality. The Berry connection is not invariant under gauge transformations $\left|\psi_n(\boldsymbol{\lambda})\right\rangle \rightarrow e^{i\alpha(\boldsymbol{\lambda})}\left|\psi_n(\boldsymbol{\lambda})\right\rangle$ and transforms as $\boldsymbol{\mathcal{A}}_n(\boldsymbol{\lambda}) \rightarrow \boldsymbol{\mathcal{A}}_n(\boldsymbol{\lambda}) - \nabla_{\boldsymbol{\lambda}}\alpha(\boldsymbol{\lambda})$. However, the single valuedness of $\alpha(\boldsymbol{\lambda})$ at the beginning and the end of the path guaranteed by the closed contour imposes the gauge-invariance of the Berry phase (1.13) modulo 2π. Hence, as anticipated, the Berry phase (1.13) is time independent and appears to be completely defined by the path of the closed contour in the $\boldsymbol{\lambda}$ parameter space.

Note. The single valuedness condition for $\alpha(\boldsymbol{\lambda})$ invoked above is valid only if we deal non-degenerate energy levels E_n. The notion of adiabatic Berry phase can be generalized for degenerate levels. In this case the Berry connexion becomes a matrix and a meaningful integral over a closed loop can be achieved by using path ordered integral. Such extension has been proposed by Wilczek and Zee in ref. [15]. We do not introduce this formalism here because it will not be used in the present manuscript where we will always consider non-degenerate states.

Berry curvature. The closed contour (C) allows to define the boundary of an oriented surface (S) in parameter space. Hence if the Berry connection $\mathcal{A}_n(\boldsymbol{\lambda})$ is a C^1 vector field ($\mathcal{A}_i$ derivable and $\partial_j \mathcal{A}_i$ continuous) one can use Stokes theorem to rewrite Eq. (1.13) as a surface integral. In the general case when the parameter space is D-dimensional it gives [3]:

$$\gamma_B = \int_S \sum_{i,j}^D \frac{1}{2} \Omega_{ij}^{(n)} (d\lambda_i \wedge d\lambda_j) \tag{1.15}$$

Where the exterior products $(d\lambda_i \wedge d\lambda_j) = -(d\lambda_j \wedge d\lambda_i)$ are related to the surface elements. We have introduced the Berry curvature antisymmetric tensor $\Omega_{ij}^{(n)}$:

$$\begin{aligned}
\Omega_{ij}^{(n)}(\boldsymbol{\lambda}) &= \partial_{\lambda_i} \mathcal{A}_n^j - \partial_{\lambda_j} \mathcal{A}_n^i \tag{1.16} \\
&= i \left(\langle \partial_{\lambda_i} \psi_n | \partial_{\lambda_j} \psi_n \rangle - \langle \partial_{\lambda_j} \psi_n | \partial_{\lambda_i} \psi_n \rangle \right) \tag{1.17} \\
&= -2\Im[\langle \partial_{\lambda_i} \psi_n | \partial_{\lambda_j} \psi_n \rangle] \tag{1.18}
\end{aligned}$$

(Where we use the identity: $(i(z - \bar{z}) = -2\Im[z], z \in \mathbb{C})$ for the last line.) This is a general definition which is independent of the dimension D of the parameter space. The $\Omega_{ij}^{(n)}$ elements are invariant under $U(1)$ transformation contrary to the Berry connection. Therefore, the Berry curvature can be important if we look for observable physical consequences.

The important special case of a three dimensional parameter space allows to write the Stokes theorem in a more common form:

$$\gamma_B = \int_S \boldsymbol{\mathcal{B}}_n . d\mathbf{S} \tag{1.19}$$

where we have introduced the Berry curvature in the pseudo-vector form using the curl.

$$\boldsymbol{\mathcal{B}}_n(\boldsymbol{\lambda}) = \nabla_{\boldsymbol{\lambda}} \times \boldsymbol{\mathcal{A}}_n \tag{1.20}$$

In this case the invariance of $\boldsymbol{\mathcal{B}}_n$ under the gauge transformation $\mathcal{A}_n(\boldsymbol{\lambda}) \rightarrow \mathcal{A}_n(\boldsymbol{\lambda}) - \nabla_{\boldsymbol{\lambda}} \alpha(\boldsymbol{\lambda})$ is easily checked using the fact that the curl of a gradient always vanishes. The pseudo-vector and tensor components are related as: $\Omega_{ij}^{(n)} = \varepsilon_{ijk} (\boldsymbol{\mathcal{B}}_n)_k$ or equivalently $\boldsymbol{\mathcal{B}}_n = (\Omega_{23}^{(n)}, \Omega_{31}^{(n)}, \Omega_{12}^{(n)})$. Note that if the parameter space is two dimensional, the Berry curvature admits only one non-zero component $\Omega_{12}^{(n)}$.

Adiabatic quantum geometric tensor.   The antisymmetric Berry curvature tensor is not the only gauge invariant tensor here. The symmetric metric tensor g_{ij} introduced in the previous section can also be defined in terms of the adiabatic states $|\psi_n(\boldsymbol{\lambda})\rangle$ that we are using here. Moreover, these two tensors can be unified in a more general tensor called quantum geometric tensor (QGT) [16].

$$T_{ij}^{(n)} = \langle \partial_{\lambda_i} \psi_n | \partial_{\lambda_j} \psi_n \rangle - \langle \partial_{\lambda_i} \psi_n | \psi_n \rangle \langle \psi_n | \partial_{\lambda_j} \psi_n \rangle = g_{ij}^{(n)} - i \frac{\Omega_{ij}^{(n)}}{2} \qquad (1.21)$$

Whereas the metric $g_{ij}^{(n)}$ characterizing the distance between the adiabatic states is the real part of the quantum geometric tensor, the Berry curvature appears to be closely related to its imaginary part.

$$g_{ij}^{(n)} = \Re[T_{ij}^{(n)}] \quad , \quad \Omega_{ij}^{(n)} = -2\Im[T_{ij}^{(n)}] \qquad (1.22)$$

It is important to stress however that here the tensor is defined in the parameter space which is directly linked with the Hamiltonian dependence on $\boldsymbol{\lambda}$ and to the adiabatic approximation. This space is *different* from the general projective Hilbert space of a time dependent wavefunction without the adiabatic constraint (which means that $|\Psi\rangle$ is not necessarily an instantaneous eigenstate $|\psi_n(\boldsymbol{\lambda})\rangle$) introduced in the last section. Interestingly, the notion of geometrical phase has been extended later to the more general case of non-adiabatic cyclic evolutions [17] and soon after to non-adiabatic and non-cyclic evolutions [18]. Both extensions use the notion of the projective Hilbert space to generalize Berry's result (1.13). The non-cyclic case is achieved by introducing the geodesic trajectories defined by the quantum metric tensor to close the contour in the projective Hilbert space in order to compute the geometric phase without gauge "uncertainty" problem.

Hamiltonian formulation.   The benefit to work in the adiabatic approximation is that the different quantities introduced above are dependent on the parameter of the Hamiltonian. For now, we have written them in terms of the adiabatic eigenstates, therefore they are related to the continuity of the adiabatic basis as a function of $\boldsymbol{\lambda}$. It can be useful to reformulate these expressions in terms of the parametrized Hamiltonian which is assumed to be continuous in $\boldsymbol{\lambda}$. A way to do this is to start from parameter derivative of the stationary Schrödinger equation (1.8):

$$\partial_{\lambda_i}(\hat{H}|\psi_n\rangle) = \partial_{\lambda_i}(E_n|\psi_n\rangle) \qquad (1.23)$$

Multiplying on the left by $\langle \psi_m|$ gives when $m \neq n$:

$$\langle \psi_m| \, \partial_{\lambda_i}\hat{H} \, |\psi_n\rangle = (E_n - E_m) \langle \psi_m | \partial_{\lambda_i} \psi_n \rangle \qquad (1.24)$$

Then using the expansion:

$$\langle \partial_{\lambda_i} \psi_n | \partial_{\lambda_j} \psi_n \rangle = \sum_m \langle \partial_{\lambda_i} \psi_n | \psi_m \rangle \langle \psi_m | \partial_{\lambda_j} \psi_n \rangle \qquad (1.25)$$

We can rewrite the quantum geometric tensor (1.21) in the form:

$$T_{ij}^{(n)} = \sum_{m \neq n} \frac{\langle \psi_n | \partial_{\lambda_i} \hat{H} | \psi_m \rangle \langle \psi_m | \partial_{\lambda_j} \hat{H} | \psi_n \rangle}{(E_n - E_m)^2} \qquad (1.26)$$

which can be decomposed in the real metric part:

$$g_{ij}^{(n)} = \Re[\sum_{m \neq n} \frac{\langle \psi_n | \partial_{\lambda_i} \hat{H} | \psi_m \rangle \langle \psi_m | \partial_{\lambda_j} \hat{H} | \psi_n \rangle}{(E_n - E_m)^2}] \qquad (1.27)$$

and Berry curvature part:

$$
\begin{aligned}
\Omega_{ij}^{(n)} &= -2\Im[T_{ij}^{(n)}] = i(T_{ij}^{(n)} - T_{ji}^{(n)}) \qquad (1.28) \\
&= i \sum_{m \neq n} [\frac{\langle \psi_n | \partial_{\lambda_i} \hat{H} | \psi_m \rangle \langle \psi_m | \partial_{\lambda_j} \hat{H} | \psi_n \rangle - \langle \psi_n | \partial_{\lambda_j} \hat{H} | \psi_m \rangle \langle \psi_m | \partial_{\lambda_i} \hat{H} | \psi_n \rangle}{(E_n - E_m)^2}]
\end{aligned}
$$

In the set of expressions (1.26),(1.27) and (1.28) the derivatives act on the Hamiltonian instead of the eigenstates which from a practical point of view can make the numerical computation easier. Moreover, this allows to see directly the possible divergence when two eigenenergies tend to a crossing point $(E_n - E_m) \to 0$. Note that if such a degeneracy occurs, the adiabatic approximation is not valid anymore. Generally, the geometrical quantities will have their maximal values near the anti-crossing points in the spectrum where the adiabatic condition needs to be more restrictive. The expression (1.28) allows to deduce that for all $\boldsymbol{\lambda}$, the sum of the Berry curvatures for all the eigenstates of the adiabatic basis is necessarily zero.

$$\sum_n \Omega_{ij}^{(n)}(\boldsymbol{\lambda}) = 0, \quad \forall \boldsymbol{\lambda} \qquad (1.29)$$

Note: The concept of geometrical phase is closely related with the Pancharatnam phase introduced earlier for polarized light beams [19, 20]. Experimental signatures of the adiabatic Berry phase have been reported in different systems in the 80's [21, 22, 23]. Beyond these confirmations, the Berry curvature defined in momentum space appears to be a major ingredient toward new transport phenomena as we will see along the thesis. The real part of the adiabatic QGT has been introduced recently to characterize many-body quantum phase transitions where $|\psi_0\rangle$ plays the role of the ground state wavefunction of a parameter-dependent Hamiltonian $\hat{H}(\boldsymbol{\lambda})$ [24, 25].

1.2   Band theory of crystals

1.2.1   Bloch theorem and energy bands

Electronic properties of solid crystals are well described by band theory. In this approach, the electrons are non-interacting and move in a periodic potential created

by the underlying ions supposed to be static. A crystal is a periodic arrangement of an elementary pattern. This periodic arrangement is a Bravais lattice: an infinite array generated by discrete translations $\mathbf{R} = \sum_i^D n_i \mathbf{a}_i$ (where $n_i \in \mathbb{Z}$, $\mathbf{a}_i$ are the primitive vectors and D is the dimension of the lattice). Of course, crystals in nature are of dimension $D \leq 3$, but mathematically it is not forbidden to define lattices in higher dimensions and it appears to be commonly used for tight-binding models with synthetic dimensions. In the following, we will restrict our discussion to $D \leq 3$. The equation to be solved is the Schrödinger one with the following single particle Hamiltonian:

$$\hat{H} = \frac{\hat{p}^2}{2m} + U(\hat{r}) \tag{1.30}$$

with $U(\mathbf{r})$ a periodic function with the periodicity of the Bravais lattice.

$$U(\mathbf{r} + \mathbf{R}) = U(\mathbf{r}) \tag{1.31}$$

This periodicity imposes the commutation of the Hamiltonian with the lattice translation operators $[\hat{H}, \hat{T}_{\mathbf{R}}] = 0$, which implies the existence of a common basis which diagonalizes $\hat{H}$ and the translation operators $\hat{T}_{\mathbf{R}_i}$. Bloch theorem tells us that such basis wavefunctions can be written as the product of a plane wave and a function with the periodicity of the Bravais lattice:

$$\Psi_{n,\mathbf{k}}(\mathbf{r}) = e^{i\mathbf{k}.\mathbf{r}} u_{n,\mathbf{k}}(\mathbf{r}) \tag{1.32}$$

where n is the band index and $\mathbf{k}$ labels the crystal momentum, and $u_{n,\mathbf{k}}$ respects the periodic condition:

$$u_{n,\mathbf{k}}(\mathbf{r} + \mathbf{R}) = u_{n,\mathbf{k}}(\mathbf{r}) \tag{1.33}$$

Inserting the Bloch eigenstates in the stationary Schrödinger equation $\hat{H} \ket{\Psi_{n\mathbf{k}}} = E_{n,k} \ket{\Psi_{n\mathbf{k}}}$, implies that the $\ket{u_{n\mathbf{k}}}$ must satisfy the eigenvalue problem:

$$\hat{H}_{\mathbf{k}} \ket{u_{n\mathbf{k}}} = E_{n,\mathbf{k}} \ket{u_{n\mathbf{k}}} \tag{1.34}$$

where the Bloch Hamiltonian $\hat{H}_{\mathbf{k}} = e^{-i\mathbf{k}.\hat{r}} \hat{H} e^{i\mathbf{k}.\hat{r}}$ is now parametrized by the quasi-momentum $\mathbf{k}$. For each $\mathbf{k}$, there is a set of discrete energies $E_{n,\mathbf{k}}$ which vary continuously with $\mathbf{k}$ and define an energy band in $\mathbf{k}$-space. These bands are periodic in the reciprocal space $E_n(\mathbf{k} + \mathbf{G}) = E_n(\mathbf{k})$ (with $\mathbf{G} = \sum_i n_i \mathbf{b}_i$ a linear combination of elementary reciprocal space vectors $\mathbf{b}_i$ defined by $\mathbf{b}_i.\mathbf{a}_j = 2\pi\delta_{ij}$), which allows to restrict their study to the first Brillouin zone. The set of $E_n(\mathbf{k})$ in the first Brillouin zone is called the *electronic band structure*. In general, the number of bands n is infinite and the study is restricted to a subset of N bands which can be selected using the projection operator $P_{\mathbf{k}} = \sum_n^N \ket{u_{n\mathbf{k}}} \bra{u_{n\mathbf{k}}}$.

Note: Bloch theorem is not restricted to the Schrödinger equation and is in general a very useful tool for any type of wave equation in a periodic media. For example, it is commonly used to compute the eigenmodes of photonic crystals [26] which consist of a periodic array of regions with different refractive index. These artificial

crystals for optical waves have been introduced by Yablonovitch [27] and Sajeev [28] in 1987 as a way to control the spontaneous emission for the former and to study wave localization phenomena analogous to single particle wave localization in the Schrödinger equation for the latter. Nowadays, both from the modelisation and the experimental point of view, the study of photonic crystals has become a research field by itself.

1.2.2 Band geometry and topological Chern number

Using Bloch theorem, we arrived at an eigenvalue problem where the Hamiltonian is parameter dependent. This problem is still very difficult to solve but one of its consequences is particularly important: at each $\mathbf{k}$ point, there exists an eigenbasis $|u_{n,\mathbf{k}}\rangle$. These are the mathematical ingredients which were used by Berry to introduce the geometrical quantities using the adiabatic basis. Therefore, one can re-write them in the momentum space formulation, where now the eigenenergies will correspond to the electronic band structure in a periodic potential. The Berry connection can then be defined as:

$$\boldsymbol{\mathcal{A}}_n(\boldsymbol{k}) = i \langle u_{n,\mathbf{k}} | \nabla_{\mathbf{k}} | u_{n,\mathbf{k}} \rangle \tag{1.35}$$

the Berry curvature tensor:

$$\Omega_{ij}^{(n)}(\mathbf{k}) = i \left(\langle \partial_{k_i} u_n | \partial_{k_j} u_n \rangle - \langle \partial_{k_j} u_n | \partial_{k_i} u_n \rangle \right) \tag{1.36}$$

and the quantum geometric tensor:

$$T_{ij}^{(n)}(\mathbf{k}) = \langle \partial_{k_i} u_n | \partial_{k_j} u_n \rangle - \langle \partial_{k_i} u_n | u_n \rangle \langle u_n | \partial_{k_j} u_n \rangle \tag{1.37}$$

The dimension of the reciprocal space is given by the dimension of the direct lattice in real space. The periodicity of the eigenenergies, the Berry curvature and the QGT in reciprocal space allows to consider the first Brillouin zone as a compact closed manifold (for example, in 1D the BZ can be thought as a circle, in 2D as a torus, etc.) for these quantities. Dealing with the Berry curvature, this allows to define topological invariants such as the Chern numbers. In general, Chern numbers can be defined for any closed surface of even dimension. For the sake of concreteness, we restrict ourself to 2D Chern numbers which will be used throughout this thesis.

2D Chern numbers. In two dimensions, the closed Brillouin zone allows to introduce the first Chern number, a topological invariant defined by the integral of the Berry curvature over the first BZ.

$$C_n = \frac{1}{2\pi} \int_{BZ} d^2k \, \Omega_{xy}^{(n)}(\mathbf{k}) \tag{1.38}$$

Physically, the Chern number corresponds to the flux of the Berry curvature through the closed surface defined by the Brillouin zone.
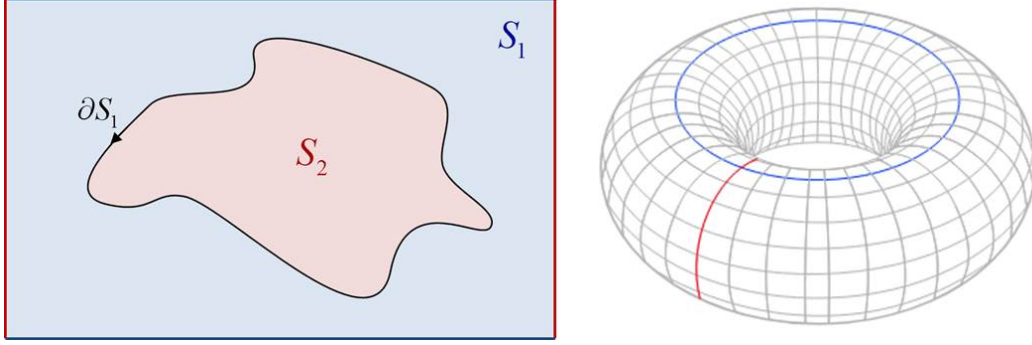
Figure 1.1: Scheme of a 2D Brillouin zone divided in two subspace S_1 and S_2. Due to the periodicity in reciprocal space, colored edges can be identified which gives the torus closed surface shown on the right panel.

The first property of Chern numbers is their integer values. It is linked to the fact that the Berry curvature flux through any 2D closed surface is an integer modulo 2π and can be understood as follows. A closed surface has no boundary by definition, which means that we cannot define a contour. However, we can divide it in two different surfaces S_1 and S_2 separated by the contour $\partial S_1 = -\partial S_2$

$$C_n = \frac{1}{2\pi} \int_{S_1+S_2} d^2k \, \Omega_{xy}^{(n)}(\mathbf{k}) = \frac{1}{2\pi} \oint_{\partial S_1} \boldsymbol{\mathcal{A}}_{n,1}(\mathbf{k}).d\mathbf{k} + \frac{1}{2\pi} \oint_{\partial S_2} \boldsymbol{\mathcal{A}}_{n,2}(\mathbf{k}).d\mathbf{k} \quad (1.39)$$

where $\partial S_1 = -\partial S_2$. Since the Berry connection is gauge dependent, in general $\boldsymbol{\mathcal{A}}_{n,1}$ and $\boldsymbol{\mathcal{A}}_{n,2}$ are different in the two subspaces. Each contour integral corresponds to a Berry phase (1.13) acquired in momentum space, which implies:

$$C_n = \frac{1}{2\pi} \oint_{\partial S_1} (\boldsymbol{\mathcal{A}}_{n,1}(\mathbf{k}) - \boldsymbol{\mathcal{A}}_{n,2}(\mathbf{k})).d\mathbf{k} = \frac{\gamma_1 - \gamma_2}{2\pi} \quad \Longrightarrow \quad C_n \in \mathbb{Z} \qquad (1.40)$$

Hence, the Chern number appears to be proportional to the difference of Berry phases which is necessarily a multiple of 2π since they are computed around the same contour ∂S_1. Interestingly, this reasoning allows to understand that a non zero Chern number is linked with the impossibility to define the Berry connection in the same gauge for $|u_n\rangle$ over the whole Brillouin zone (if $\boldsymbol{\mathcal{A}}_{n,1} = \boldsymbol{\mathcal{A}}_{n,2}, \quad C_n = 0$).

Another useful property which directly stems from (1.29), is that their sum over all the bands is necessary zero:

$$\sum_n C_n = 0 \qquad (1.41)$$

This will be useful to understand how the Chern numbers can be distributed between the bands in models with a finite set of bands. For example, for two-band models, it is sufficient to know the Chern number associated with one band, the second one being the opposite.

Finally, it is important to note that a non-zero Chern number implies the breaking of time-reversal symmetry. Indeed, if the Hamiltonian has time-reversal symmetry one has $|u_{n,\mathbf{k}}\rangle = |u_{n,-\mathbf{k}}\rangle^*$, which implies that $\Omega_{ij}^{(n)}(\mathbf{k}) = -\Omega_{ij}^{(n)}(-\mathbf{k})$ and the integrated Berry curvature over the first BZ vanishes.

Historically, the Chern number has been used in the 80's by Thouless et al. [29] to explain the quantization of the transverse conductivity in the quantum Hall effect observed experimentally by Klitzing et al. [30]. This conductance is given by the formula:

$$\sigma_{xy} = \frac{e^2}{h} \sum_{n_{occ}} C_n \tag{1.42}$$

where the sum is taken over the occupied Landau levels ($C_n = 1$ for each level). Here, time-reversal symmetry is explicitly broken by the large transversal applied magnetic field which leads to the formation of Landau levels. Qualitatively, by increasing the external magnetic field, the number of Landau levels below the Fermi energy increases and the conductivity increases by plateaux of conductance quantum e^2/h.

Actually, the topological nature of C_n has been underlined by Avron et al. in [31] and the link with Berry's work and its mathematical interpretation in term of "fiber bundles" was done in [32]. A major consequence of its topological character is that the Chern number cannot change without the occurrence of a band degeneracy. In the quantum Hall context, this implies that the Hall conductance is insensitive to an external perturbation if this one is small enough so that the bulk bandgap remains open. Another huge consequence of a non zero Chern number is the occurrence of gapless chiral edge modes on the boundaries of the system. The number of such edge modes is directly given by the Chern number characterizing the bulk of the sample thanks to the so-called *Bulk-Boundary correspondence* [33, 34].

All these mathematical definitions work for every Hamiltonian. We stress that whereas even dimensions and time-reversal symmetry breaking are needed to have non-zero topological Chern numbers (1.38), it is not required if we are interested in the *geometrical* Berry curvature (1.36) or the quantum metric (1.37). This means that the geometrical quantities are intrinsic to Bloch Hamiltonians exactly as the periodic band structures are. However, finding the Bloch eigenenergies and eigenstates is in general a difficult task and approximate methods are needed especially if we want to keep analytical computation suitable. A particularly useful one to introduce minimal models with non trivial band topology is the tight-binding approximation introduced below.

1.2.3 Tight-binding approximation

Tight-binding approximation is the lowest approximation which allows to keep track of the geometry of the underlying lattice. The approach consists to assume that

electrons are tightly bound to the discrete atomic sites. The Hamiltonian is then considered to be the sum of on-site atomic Hamiltonians with a small correction $\Delta U(\mathbf{r}, \mathbf{p})$:

$$\hat{H} = \sum_i^{N_c} \hat{H}_{at}^{\mathbf{R}_i} + \Delta U \tag{1.43}$$

First, we assume that one orbital is sufficient to describe the problem $\hat{H}_{at}^{\mathbf{R}_i} |w_{\mathbf{R}_i}\rangle = \varepsilon |w_{\mathbf{R}_i}\rangle$. Therefore, we can express the single particle wavefunction as a combination of on-site s-orbitals

$$|\Psi_{n,\mathbf{k}}\rangle = \frac{1}{\sqrt{N_c}} \sum_i e^{-i\mathbf{k}\cdot\mathbf{R}_i} |w_{\mathbf{R}_i}\rangle \tag{1.44}$$

where the sum is taken on the total number of unit cells N_c. The important parameters of such models are the overlap integrals which encode the tunnelling between two separated sites.

$$t_{ij} = \langle w_{\mathbf{R}_i}| \Delta U |w_{\mathbf{R}_j}\rangle = \int d\mathbf{r}\, w(\mathbf{r} - \mathbf{R}_i)^* \Delta U(\mathbf{r}) w(\mathbf{r} - \mathbf{R}_j) \tag{1.45}$$

Using the t_{ij} as parameters the T-B Hamiltonian can then be written as:

$$\hat{H} = \sum_i^{N_c} \varepsilon |w_{\mathbf{R}_i}\rangle \langle w_{\mathbf{R}_i}| - \sum_{i,j} t_{ij} |w_{\mathbf{R}_i}\rangle \langle w_{\mathbf{R}_j}| \tag{1.46}$$

and the eigenenergy is given by:

$$E(\mathbf{k}) = \langle \Psi_{n,\mathbf{k}}| \hat{H} |\Psi_{n,\mathbf{k}}\rangle \tag{1.47}$$

$$= \varepsilon - \frac{1}{N_c} \sum_{i,j} t_{ij} e^{i\mathbf{k}\cdot(\mathbf{R}_i - \mathbf{R}_j)} \tag{1.48}$$

A commonly used approximation is to keep only the nearest neighbour coefficient different from zero.

$$t_{ij} = \begin{cases} t, & \text{if} \quad |\mathbf{R}_i - \mathbf{R}_j| = a \\ 0, & \text{otherwise} \end{cases} \tag{1.49}$$

where a is the lattice constant. This gives $E(\mathbf{k}) = \varepsilon - \sum_j t' e^{i\mathbf{k}\cdot\mathbf{d}_j}$, where $\mathbf{d}_j$ ($|\mathbf{d}_j| = a$) are the nearest neighbour vectors and the prefactor $1/N_c$ has been included in t'.

The restriction to one orbital per unit cell means that we end up with only one energy band $E(\mathbf{k})$. Therefore, we can drop the band index of the Bloch state $|\psi_{\mathbf{k}}\rangle$. Interestingly, this implies that the $|u_{\mathbf{k}}\rangle$ states are independent of $\mathbf{k}$. This can be seen by looking at the explicit form of $|u_{\mathbf{k}}\rangle$ after the introduction of the discrete position operator:

$$\hat{\mathbf{r}} = \sum_i r_i |w_{\mathbf{r}_i}\rangle \langle w_{\mathbf{r}_i}| \tag{1.50}$$

which allows to deduce:

$$|u_{\mathbf{k}}\rangle = e^{i\mathbf{k}\cdot\hat{\mathbf{r}}} |\psi_{\mathbf{k}}\rangle = \frac{1}{\sqrt{N_c}} \sum_i |w_{\mathbf{r}_i}\rangle = |u\rangle \tag{1.51}$$
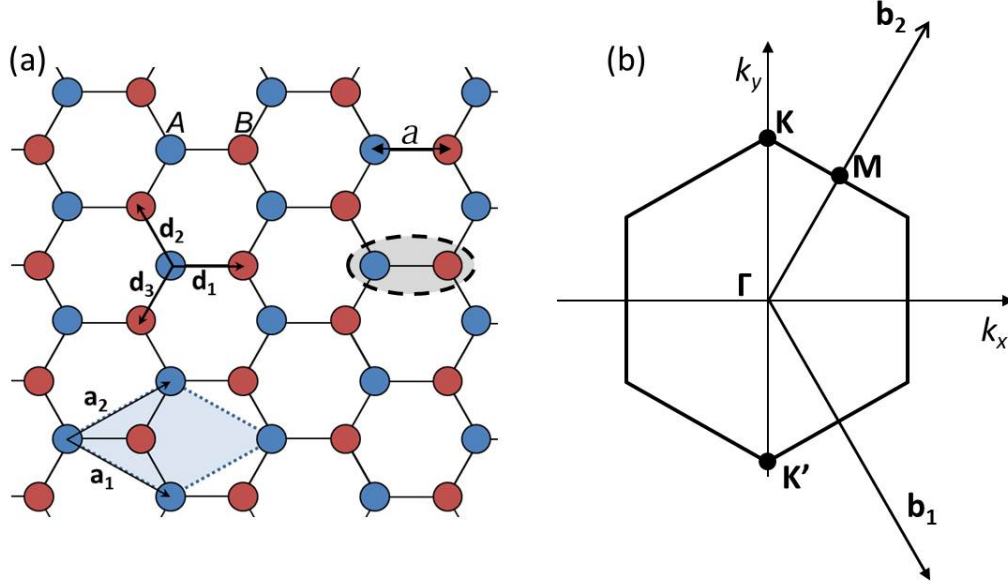
Figure 1.2: a) Honeycomb lattice with Bravais lattice basis vectors $\mathbf{a}_1, \mathbf{a}_2$ and nearest neighbour vectors $\mathbf{d}_i$. The unit cell is highlighted in grey color. b) The corresponding Brillouin zone in reciprocal space with the high symmetry points.

From their definition in quasi-momentum parameter space (1.35),(1.36),(1.36), we can understand that the geometrical quantities in quasi-momentum space cannot be defined in such one band models. Multi-band models are required. Such multi-band models can be achieved in T-B approximation when some internal degrees of freedom are taken into account (eg: spin or other on-site orbitals) or if the lattice in consideration contains several atoms in a unit cell (such as honeycomb or Lieb lattices in 2D). In the following, we introduce the latter with the honeycomb lattice.

Two atoms per unit cell. We consider the honeycomb lattice case here but the reasoning is applicable to any system with several atoms per unit cell. In the honeycomb lattice there are two inequivalent lattice sites A and B in a Bravais lattice unit cell (see Fig. 1.2). A Bloch eigenstate can be written as a linear combination of their respective orbital states.

$$|\Psi_{n,\mathbf{k}}\rangle = \frac{1}{\sqrt{N_c}} \sum_i e^{-i\mathbf{k}\cdot\mathbf{R}_i} \left(c_A(\mathbf{k}) |w_{A,\mathbf{R}_i}\rangle + e^{i\phi} c_B(\mathbf{k}) |w_{B,\mathbf{R}_i+\mathbf{d}_1}\rangle \right) \qquad (1.52)$$

where we choose the Bravais vectors $\mathbf{R}_i = n_1\mathbf{a_1}+n_2\mathbf{a_2} = \mathbf{R}_{A,i}$ defined by the position of A sites by convention (see the unit cell in Fig. 1.2) with $\mathbf{a}_{1,2} = (a3/2, \pm a\sqrt{3}/2)^T$. The position of B sites is given by $\mathbf{R}_{B,i} = \mathbf{R}_i + \mathbf{d}_1$ with $\mathbf{d}_1 = (a,0)^T$. ϕ encodes the relative phase between the sublattices. Whereas different choices are possible [35],

we choose the quite natural one used by Wallace [36] where the phase encodes the relative position between A/B atoms in a unit cell: in our convention (Fig. 1.2), we have therefore $\phi = \mathbf{k}.\mathbf{d}_1$. (Besides being widely used [37, 38], this basis where the sublattice relative position is kept appears to be the good choice to define the Berry curvature without ambiguity for gapped graphene [39, 40].) In this basis, the $|u_{n,\mathbf{k}}\rangle$ are given by:

$$|u_{n,\mathbf{k}}\rangle = \frac{1}{\sqrt{N_c}} \sum_i \left(c_A(\mathbf{k}) |w_{A,\mathbf{R}_i}\rangle + c_B(\mathbf{k}) |w_{B,\mathbf{R}_i+\mathbf{d}_1}\rangle\right) \qquad (1.53)$$

On can project it on a unit cell using the projector $\hat{P}_j = |w_{A,\mathbf{R}_j}\rangle \langle w_{A,\mathbf{R}_j}| + |w_{B,\mathbf{R}_j+\mathbf{d}_1}\rangle \langle w_{B,\mathbf{R}_j+\mathbf{d}_1}|$ which gives a two component vector:

$$|\tilde{u}_{n,\mathbf{k}}\rangle = \begin{pmatrix} c_A(\mathbf{k}) \\ c_B(\mathbf{k}) \end{pmatrix} \qquad (1.54)$$

(In the following, we remove the upper $\sim$ symbol for commodity.) The nearest neighbour T-B Hamiltonian can be written as:

$$\hat{H} = \sum_{i,\alpha} \varepsilon_\alpha |w_{\alpha\mathbf{R}_{\alpha,i}}\rangle \langle w_{\alpha,\mathbf{R}_{\alpha,i}}| - \sum_{i,l} t \left(|w_{A,\mathbf{R}_i}\rangle \langle w_{B,\mathbf{R}_i+\mathbf{d}_l}| + |w_{B,\mathbf{R}_i+\mathbf{d}_l}\rangle \langle w_{A,\mathbf{R}_i}|\right)$$
$$(1.55)$$

where we use $\alpha = A/B$ index and $1 \leq l \leq 3$ the nearest neighbour vectors index. We can introduce the sublattice basis states:

$$|\psi_{A,\mathbf{k}}\rangle = \frac{1}{\sqrt{N_c}} \sum_i e^{-i\mathbf{k}.\mathbf{R}_i} |w_{A,\mathbf{R}_i}\rangle, \quad |\psi_{B,\mathbf{k}}\rangle = \frac{1}{\sqrt{N_c}} e^{-i\mathbf{k}.\mathbf{d}_1} \sum_i e^{-i\mathbf{k}.\mathbf{R}_i} |w_{B,\mathbf{R}_i+\mathbf{d}_1}\rangle$$

$$|w_{A,\mathbf{R}_i}\rangle = \int d\mathbf{k} e^{i\mathbf{k}.\mathbf{R}_i} |\psi_{A,\mathbf{k}}\rangle, \quad |w_{B,\mathbf{R}_i+\mathbf{d}_1}\rangle = \int d\mathbf{k} e^{i\mathbf{k}.\mathbf{R}_i} e^{i\mathbf{k}.\mathbf{d}_1} |\psi_{B,\mathbf{k}}\rangle \qquad (1.56)$$

which allows to rewrite the Hamiltonian (1.55) in the form:

$$\hat{H} = \int d\mathbf{k} \left(|\psi_{A,\mathbf{k}}\rangle, |\psi_{B,\mathbf{k}}\rangle\right) H_{\mathbf{k}} \left(\langle\psi_{A,\mathbf{k}}|, \langle\psi_{B,\mathbf{k}}|\right)^T \qquad (1.57)$$

where $H_{\mathbf{k}}$ is a two-by-two matrix which after diagonalization gives the eigenenergies $E_n(\mathbf{k})$ and the eigenvectors $|u_{n,\mathbf{k}}\rangle$. For the honeycomb lattice, $H_{\mathbf{k}}$ is given by:

$$H_{\mathbf{k}} = \begin{pmatrix} \varepsilon_A & -tf_{\mathbf{k}} \\ -tf_{\mathbf{k}}^* & \varepsilon_B \end{pmatrix} \qquad (1.58)$$

with the off-diagonal coefficients $f_{\mathbf{k}}$:

$$f_{\mathbf{k}} = e^{-i\mathbf{k}.\mathbf{d}_1} + e^{-i\mathbf{k}.\mathbf{d}_2} + e^{-i\mathbf{k}.\mathbf{d}_3} \qquad (1.59)$$

Considering $\varepsilon_A = -\varepsilon_B = \Delta$, the eigenenergies are given by:

$$E_{\pm,\mathbf{k}} = \pm\sqrt{(\Delta^2 + t^2|f_{\mathbf{k}}|^2)} \qquad (1.60)$$

and using $f_{\mathbf{k}} = |f_{\mathbf{k}}|e^{-i\phi_{\mathbf{k}}}$ the spinor eigenstates read

$$|u_{\pm,\mathbf{k}}\rangle = \frac{1}{\sqrt{t^2|f_{\mathbf{k}}|^2 + |\Delta + E_{\pm,\mathbf{k}}|^2}} \begin{pmatrix} \pm e^{-i\phi_{\mathbf{k}}}(\Delta + E_{\pm,\mathbf{k}}) \\ t|f_{\mathbf{k}}| \end{pmatrix} \qquad (1.61)$$

which reduce to $|u_{\pm,\mathbf{k}}\rangle = \frac{1}{\sqrt{2}}(\pm e^{-i\phi_{\mathbf{k}}}, 1)^T$ when $\Delta = 0$. One can remark that in this basis, the coefficients $f_{\mathbf{k}}$ are expressed in terms of the nearest neighbour vectors, consequently they don't have the periodicity of the BZ: $f_{\mathbf{k}+\mathbf{G}} \neq f_{\mathbf{k}}$. Hence, whereas $|f_{\mathbf{k}}|$ and the eigenenergies remain $\mathbf{G}$-periodic, this is not the case for the matrix $H_{\mathbf{k}}$ and its associated eigenstates $|u_{\pm,\mathbf{k}}\rangle$. This fact is quite generic for T-B models with several atoms per unit cell with such choice of basis.

The two-by-two matrix form of the Hamiltonian (1.58) allows to express it as an effective magnetic field acting on the sublattice pseudospin using the Pauli matrices σ_i: $H_k = -\mathbf{h}(k).\hat{\boldsymbol{\sigma}}$.

$$H_{\mathbf{k}} = -t\Re[f_{\mathbf{k}}]\sigma_x + t\Im[f_{\mathbf{k}}]\sigma_y + \Delta\sigma_z \qquad (1.62)$$

Hence, the eigenstates $|u_{n,\mathbf{k}}\rangle$ correspond to states aligned or anti-aligned with the field. The resulting in-plane effective field $(h_x, h_y)^T$ texture in momentum space is shown in figure 1.3 (b). This allows to visualize the tripling of periodicity of $H_{\mathbf{k}}$ and the opposite winding of the in-plane field around the K and K' points at the corner of the BZ. The tripled periodicity and its signatures in a Stückelberg interferometry experiment is discussed in ref. [41]. A plot of the typical band structure when $\Delta = 0$ is shown in figure 1.3 (a). One can see the occurrence of Dirac cones at the corner of the Brillouin zone K and K' where the coupling between the sublattices encoded by the in-plane effective field vanishes.

Second quantized notation. Whereas the expression in terms of the single particle orbital states is convenient to understand the structure of the Bloch states in the T-B approximation, the braket notation can make the equations quite long. Therefore, for the rest of the thesis we will use second quantization formalism to write such Hamiltonians. This approach consists in writing the Hamiltonians in term of the on-site ladder operators:

$$\hat{\mathcal{H}} = \sum_i^N \varepsilon_i \hat{a}_{\mathbf{R}_i}^\dagger \hat{a}_{\mathbf{R}_i} - \sum_{ij}(t_{ij}\hat{a}_{\mathbf{R}_i}^\dagger \hat{a}_{\mathbf{R}_j} + h.c.) \qquad (1.63)$$

Where the operators $\hat{a}_{\mathbf{R}_i}^\dagger, (\hat{a}_{\mathbf{R}_i})$ create (destroy) an excitation located on site $\mathbf{R}_i$: $\hat{a}_i^\dagger |vac\rangle = |w_{\alpha,\mathbf{R}_i}\rangle$. It will work in the same way for multi-orbital systems. The fermionic or bosonic nature of these operators is not important as far as we are dealing with single particle problems. The matrix Hamiltonian $H_{\mathbf{k}}$ to diagonalize is achieved as before by introducing the Fourier transformed operators:

$$\hat{a}_{\mathbf{R}_i} = \int d\mathbf{k}\, e^{i\mathbf{k}.\mathbf{R}_i}\hat{a}_{\mathbf{k}}, \quad \hat{a}_{\mathbf{R}_i}^\dagger = \int d\mathbf{k}\, e^{-i\mathbf{k}.\mathbf{R}_i}\hat{a}_{\mathbf{k}}^\dagger \qquad (1.64)$$

In general, the number of orbitals considered per unit cell gives the dimension of the resulting $H_{\mathbf{k}}$.
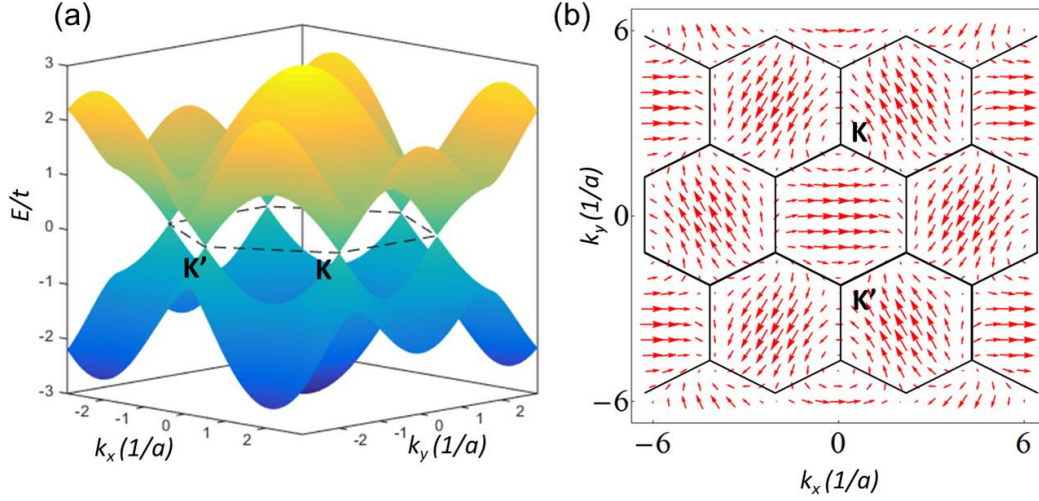
Figure 1.3: (a) Honeycomb nearest neighbour T-B dispersion. (b) In-plane effective field texture showing the tripled periodicity of the phase and the opposing winding around K and K' points.

1.3   Topological systems in condensed matter: examples

Now that we have the T-B tool in our hands, the goal of this section is to quickly introduce some important historical models where band topology allows to explain phenomena in the modern language. We begin with a 1D SSH model [42] which allows to introduce the Zak phase. Then, we present the seminal Haldane model of quantum anomalous Hall effect [43]. Having the Haldane model at hand will allow us to we present the Kane-Mele model of quantum spin Hall effect [44].

1.3.1   Su-Schrieffer-Heeger model

This model has been introduced by Su, Schrieffer and Heeger (SSH) in 1980 [45, 42] to describe the occurrence of solitons in polyacetylene polymer chains. This is also one of the simpler systems which exhibits non-trivial topology with the possibility to label the band with a Berry phase (often called Zak phase in this case)[46] which allows to predict the presence of localized states corresponding to the SSH solitons. The system consists of a 1D dimer chain: two atoms A and B in a unit cell are coupled with the strength t' whereas the inter-cell coupling strength is t (Fig. 1.4. (a)). The tight-binding Hamiltonian reads [47]:

$$\hat{H} = \sum_m t' \hat{b}_m^\dagger \hat{a}_m + t \hat{a}_{m+1}^\dagger \hat{b}_m + H.c. \tag{1.65}$$

where $\hat{a}, \hat{b}$ are the annihilation operators on the corresponding atoms (A and B, Fig. 1.4) in the unit cell m. After Fourier transformation, the momentum space
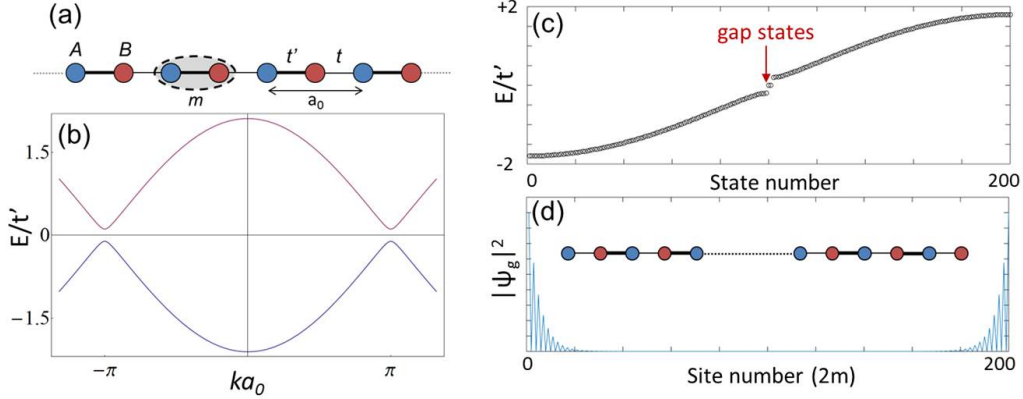
Figure 1.4: (a) 1D dimer chain scheme with $t' > t$ and $A - B$ unit cell highlighted in grey. (b) T-B band structure with $t' = 0.9t$. (c) Finite chain T-B eigenenergies showing two degenerated gap-states at $E = 0$, (d) Corresponding in-gap eigenstate absolute value profile showing the strong localization on the edges. (number of unit-cells $m = 100$, $t' = 0.8t$)

Hamiltonian reads:

$$H_k = - \begin{pmatrix} 0 & t' + te^{-ika_0} \\ t' + te^{ika_0} & 0 \end{pmatrix} \tag{1.66}$$

where a_0 is the distance between each unit cell. The two-by-two matrix form of the Hamiltonian (1.66) allows to express it as an effective magnetic field acting on the sublattice pseudospin using the Pauli matrices σ_i: $H_k = -\mathbf{h}(k).\hat{\boldsymbol{\sigma}}$, where $\mathbf{h}(k)$ components are given by:

$$h_x = t' + t\cos\left(ka_0\right), \quad h_y = t\sin\left(ka_0\right), \quad h_z = 0 \tag{1.67}$$

The eigenvalue equation $H_\mathbf{k} \left| u_{n,k} \right\rangle = E_{n,k} \left| u_{n,k} \right\rangle$ allows to find the energies and eigenvectors in $(u_A, u_B)^T$ basis:

$$E_{\pm}(k) = \pm |\mathbf{h}| = \pm\sqrt{t^2 + t'^2 + 2tt'\cos\left(ka_0\right)} \tag{1.68}$$

$h_z = 0$ implies the identity $(h_x + ih_y) = |h|e^{i\phi_k}$ which allows to write the states in a convenient form:

$$\left| u_{\pm,k} \right\rangle = \frac{1}{\sqrt{2}} \begin{pmatrix} \pm e^{-i\phi_k} \\ 1 \end{pmatrix} \tag{1.69}$$

Hence, the eigenstates lie on the equator of the Bloch sphere in the sublattice pseudospin representation. If $t \neq t'$, a gap opens in the dispersion as shown in Fig. 1.4.(b) and we can define a Zak phase for each band as the integral of Berry connection over the 1D Brillouin zone:

$$\gamma_{Z\pm} = i \int_{-\pi/a_0}^{\pi/a_0} dk \left\langle u_\pm \right| \frac{\partial}{\partial k} \left| u_\pm \right\rangle = \int_{-\pi/a_0}^{\pi/a_0} dk \frac{\partial \phi_k}{\partial k} \tag{1.70}$$

One can then deduce the winding number $\mathcal{W} = \frac{1}{2\pi}\gamma_Z$ which encodes the number of times the phase ϕ_k changes by an amount of 2π when k is varied in the BZ. This integer number is a topological invariant because if we keep $h_z = 0$ it cannot change without bandgap closing at some k. For the SSH model studied here, there are only two possibilities:

$$\mathcal{W} = \begin{cases} 1, & \text{if} \quad t' > t \\ 0, & \text{if} \quad t' < t \end{cases} \tag{1.71}$$

However, it is important to note that contrary to the Chern number (1.38), $\mathcal{W}$ is not a gauge invariant quantity since it is linked to the Berry connection and it can change if we add a **k**-dependent global phase to $|u_{n,k}\rangle$. Moreover, for an infinite system, it is dependent on the choice of unit cell which is arbitrary (one could choose the reverse unit cell label $B - A$ in Fig. 1.4. (a) which will reverse the resulting winding numbers (1.71)).

For a finite system however, if we choose to begin and finish the chain with the unit cell $A - B$: the case with $\mathcal{W} = 1$ will correspond to a finite chain which begins and finishes with weakly bound atoms, and $\mathcal{W} = 0$ to the case of tightly bound atoms on the edges. In the first case this leads to occurrence of localized edge states whose energy is lying in the gap. An example of eigenenergies computed for a finite size chain (100 unit-cells) is shown in figure 1.4 (c), where we can see two states lying in the gap at $E = 0$. The profile of these gap states is shown in Fig. 1.4 (d) and allows to observe their strong localization on the edges. The physical meaning of the winding number is also recovered if we consider the difference of winding between two domains with $t > t'$ and $t' > t$ computed using the same basis unit cell. This difference will not be affected by the choice of the common unit cell. Actually, such interface state between domains corresponds exactly to what Su-Schrieffer-Heeger studied in polyacelylene.

The profile of these zero energy-states can also be understood by linearizing the Hamiltonian near the band edges at $k = \pi/a_0$:

$$H = \begin{pmatrix} 0 & m + iaqt \\ m - iaqt & 0 \end{pmatrix} \tag{1.72}$$

where $q = k - \pi/a_0$ and $m = t' - t$. Taking the continuous limit allows to replace q by $-i\partial_x$. One can then model a domain wall by a varying mass parameter $m(x)$ with the two limits $m(x \to \infty) = m_+$ and $m(x \to -\infty) = m_-$. The wavefunction can then be found by solving the zero energy equation:

$$\begin{pmatrix} 0 & m(x) + at\partial_x \\ m(x) - at\partial_x & 0 \end{pmatrix} \begin{pmatrix} \psi_A \\ \psi_B \end{pmatrix} = 0 \tag{1.73}$$

which leads to a solution of the form:

$$\psi(x) = \begin{pmatrix} 1 \\ 0 \end{pmatrix} e^{-\frac{1}{ta}\int_0^x m(x')dx'} \tag{1.74}$$

This model has been initially studied by Jackiw-Rebbi in the particle physics context [48] and the SSH model can be seen as its condensed realization [49]. Theoretically,

these localized solitons have been associated to charge fractionalization in electronic systems without spin degree of freedom [48, 50]. This approach toward charge fractionalization for localized bound states has even been extended to 2D graphene-like lattices recently [51, 52, 53]. However, to out knowledge, no experimental signature of this type of fractionalization has been reported yet.

The SSH chain model has also been studied for bosons. In photonics, such localized states have been evidenced in the microwave domain in a lattice of resonators [54]. In optics, lasing occurring in the edge states using an active medium first discussed theoretically in ref. [55] in the polariton framework has been observed recently in different platforms [56, 57, 58]. Moreover, the careful study of mean field Gross-Pitaevskii equation in an SSH chain [59] has allowed to shed a new light on the chiral behaviour of non-linear gap solitons observed in experiments previously [60].

1.3.2   Haldane model

As explained previously, the occurrence of the Chern numbers in Physics is closely related to the discovery of the quantum Hall effect. Actually, the explanation of the quantized plateaux has really been a challenge at that time and many theoretical efforts have been done to understand this effect [61]. Most of the studies were carried to understand deeper the electron behaviour under strong magnetic fields. Physicists considered the influence of disorder on free electron Landau levels or Harper-Hofstadter like Hamiltonians where the application of a strong magnetic field leads to a fractionalization of the zero-field Bloch bands, each subband being characterized by Chern numbers [62, 63]. (Even if this kind of "quantum Hall like" models, due to the interplay between lattice potential and external magnetic field, exhibits really nice Physics with the appearance of self-similar energy spectrum, we will not introduce them here because this type of magnetic response will not be considered in the present thesis.)

In his seminal paper, Haldane presented a "toy" model where quantized conductance occurs without the need of a strong magnetic field. This was really a pioneer work toward the extension of topological number classification to any band theory and he won the Nobel prize in 2016 partly for this discovery. His model is based on a honeycomb lattice with complex second-neighbour tunnelling coefficients which could result from a transversal periodic inhomogeneous magnetic field with zero flux per hexagonal unit cell (which means no Hofstadter butterfly). The T-B Hamiltonian reads:

$$\hat{H} = -t_1 \sum_{i,\alpha} a_{\mathbf{R}_i}^\dagger b_{\mathbf{R}_i + \mathbf{d}_\alpha} - t_2 \sum_{i,\beta} \left(a_{\mathbf{R}_i}^\dagger a_{\mathbf{R}_i + \mathbf{a}_\beta} e^{i\nu_\beta \phi} + b_{\mathbf{R}_i + d_1}^\dagger b_{\mathbf{R}_i + \mathbf{d}_1 + \mathbf{a}_\beta} e^{-i\nu_\beta \phi} \right) + h.c.$$

$$(1.75)$$

where $1 \leq \alpha \leq 3$ and $1 \leq \beta \leq 3$ are the first and next-nearest-neighbour (NNN) indices. $\mathbf{d}_\alpha$ and $\mathbf{a}_\beta$ are first and NNN vectors as defined in figure 1.2 (a). $\nu_\beta = (-1)^\beta$ gives the sign of the acquired phase depending on the tunnelling direction as shown in figure 1.5.(a). If we add the staggering potential $\sum_i \Delta(a_i^\dagger a_i - b_i^\dagger b_i)$ [64], the

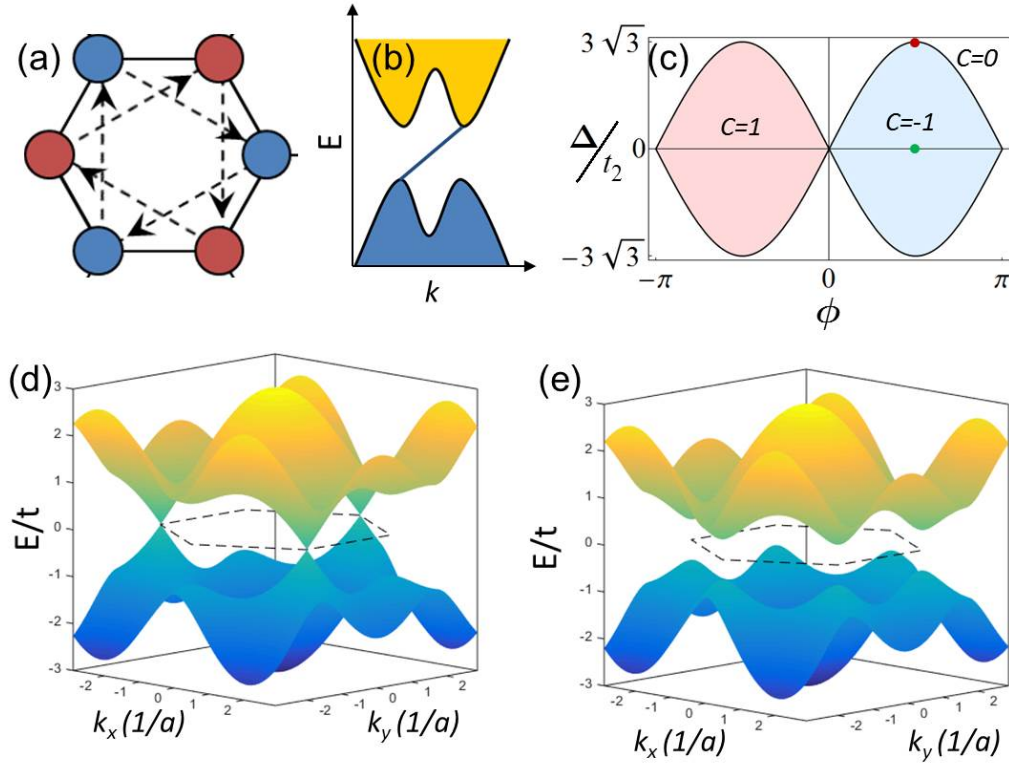Figure 1.5: (a) Scheme of the phase pattern inside a unit cell (arrows correspond to direction with $e^{i\phi}$ associated phase). (b) Chern insulator projected band structure scheme with the chiral edge mode crossing the bulk gap. (c) Topological phase diagram of the Haldane model. (d)-(f) Bulk T-B band structures corresponding to red (green) dot in the phase diagram (c) ($t_2 = t_1/12$, $\phi = \pi/2$).

Hamiltonian in momentum space obtained after Fourier transformation reads:

$$H_{\mathbf{k}} = \begin{pmatrix} \Delta - 2t_2 f_{A,\mathbf{k}} & -tf_{\mathbf{k}} \\ -tf_{\mathbf{k}}^* & -\Delta - 2t_2 f_{B,\mathbf{k}} \end{pmatrix} \tag{1.76}$$

with the coefficients:

$$f_{\mathbf{k}} = e^{-i\mathbf{k}.\mathbf{d_1}} + e^{-i\mathbf{k}.\mathbf{d_2}} + e^{-i\mathbf{k}.\mathbf{d_3}} \tag{1.77}$$

$$f_{A/B,\mathbf{k}} = \cos\left(\mathbf{k}.\mathbf{a}_1 \pm \phi\right) + \cos\left(\mathbf{k}.\mathbf{a}_2 \mp \phi\right) + \cos\left(\mathbf{k}.\mathbf{a}_3 \pm \phi\right) \tag{1.78}$$

One can decompose the matrix as $H_{\mathbf{k}} = h_0 + \mathbf{h}.\hat{\boldsymbol{\sigma}}$ using Pauli matrices with the following matrix components:

$$\begin{aligned} h_0 &= -2t_2 \cos\phi \left(\cos(\mathbf{k}.\mathbf{a}_1) + \cos(\mathbf{k}.\mathbf{a}_2) + \cos(\mathbf{k}.\mathbf{a}_3)\right) & (1.79) \\ h_x &= -t_1 \left(\cos(\mathbf{k}.\mathbf{d}_1) + \cos(\mathbf{k}.\mathbf{d}_2) + \cos(\mathbf{k}.\mathbf{d}_3)\right) & (1.80) \\ h_y &= -t_1 \left(\sin(\mathbf{k}.\mathbf{d}_1) + \sin(\mathbf{k}.\mathbf{d}_2) + \sin(\mathbf{k}.\mathbf{d}_3)\right) & (1.81) \\ h_z &= \Delta - 2t_2 \sin\phi \left(\sin(\mathbf{k}.\mathbf{a}_1) - \sin(\mathbf{k}.\mathbf{a}_2) + \sin(\mathbf{k}.\mathbf{a}_3)\right) & (1.82) \end{aligned}$$

and the eigenenergies can then be written in the simple form: $E_\pm(\mathbf{k}) = h_0 \pm \sqrt{|\mathbf{h}|}$. Both the staggering potential Δ and a non-zero NNN tunnelling t_2 lead to a gap opening at K and K' points. The staggering potential breaks the spatial inversion symmetry (think about the inversion center on a $A-B$ link for example) keeping the T-R symmetry, $t_2 \neq 0$ breaks time-reversal symmetry and keeps inversion symmetry. As we have seen in section 1.2.2, the Chern number cannot be different from zero in T-R symmetric systems, therefore $\Delta \neq 0$ alone opens a trivial gap. On the contrary, the action of a non-zero NNN hopping alone opens a topological gap. Hence, there should be a topological phase transition depending on the interplay between these parameters. It turns out that the gap is topological with an associated Chern number $C = \pm 1$ if $|\Delta/t_2| < 3\sqrt{3}\sin\phi$ and becomes trivial when $|\Delta/t_2| > 3\sqrt{3}\sin\phi$. At the boundary, between the two topological phases the bandgap has to close somewhere in reciprocal space. The phase diagram of this model is presented in Fig. 1.5 (c) with the corresponding Chern numbers. In Figures 1.5 (d)-(e), we plot the bulk dispersions for $\phi = \pi/2$ which correspond to the colored dot in (c).

To have more insight on the model, and understand the crucial ingredients leading to a topological gap, let us consider $\phi = \pi/2$ and linearize (1.76) around K and K' points:

$$H_{\tau_z} = (\Delta + \tau_z 3\sqrt{3}t_2)\sigma_z + v(\tau_z q_y \sigma_x - q_x \sigma_y) \tag{1.83}$$

where τ_z is the valley index ($\tau_z = \pm 1$ for K/K' valleys), $v = \frac{3}{2}at_1$ and $\mathbf{q} = (\mathbf{k} \mp \mathbf{K})$. The Z-component of the Berry curvature can then be computed analytically:

$$\mathcal{B}_{\tau_z}(\mathbf{q}) = \frac{v^2 \tau_z (\Delta + \tau_z 3\sqrt{3}t_2)}{2\left(v^2(q_x^2 + q_y^2) + |\Delta + \tau_z 3\sqrt{3}t_2|^2\right)^{3/2}} \tag{1.84}$$

For the two extreme cases with only staggering potential or NNN tunnelling, one can therefore directly deduces the following properties:

$$\mathcal{B}_K(\mathbf{q}) = \begin{cases} -\mathcal{B}_{K'}(\mathbf{q}), & \text{if} \quad t_2 = 0, \Delta \neq 0 \\ \mathcal{B}_{K'}(\mathbf{q}), & \text{if} \quad t_2 \neq 0, \Delta = 0 \end{cases} \tag{1.85}$$

Hence, the staggering potential Δ opens a gap with opposite Berry curvature at K and K' points where the windings of the in-plane field are opposite (See (1.84) and also Fig. 1.3. (b)). The Chern number after integration over the full BZ is therefore zero and the gap is trivial. In the opposite limit, the sign of the Z-component of the effective field $(\tau_z 3\sqrt{3}t_2)$ changes between the two valleys, and leads to same-sign Berry curvatures and therefore a non-zero topological invariant. This last term is sometimes called *Haldane mass* in the literature [65]. The resulting Chern number is given by:

$$C = \frac{1}{2}\left(\text{sgn}(3\sqrt{3}t_2 + \Delta) + \text{sgn}(3\sqrt{3}t_2 - \Delta)\right) \tag{1.86}$$

which can be equal to ± 1 or 0. Hence, bulk-boundary correspondence tells us that there exists one chiral edge mode in the former configuration as schematized in figure 1.5. (b).

The Haldane model is the first example of a class of topological insulators with non-zero Chern numbers which are called *Chern insulators* nowadays. We will use this denomination and also *quantum anomalous Hall phase* (QAH) to design this type of topological phase in the following. Despite its fundamental interest from the theoretical point of view, which has led many other works from the birth of Chern insulators to the Kane-Mele model discussed in the next section, this design is quite unrealistic from the experimental point of view for real graphene as recognized by the author himself in the original paper. However, these last years, there have been big efforts to engineer artificial systems with topological bands and in this context, the Haldane model has been realized recently using ultracold atoms in optical lattices in [66]. Even if the Haldane model has not been realized in solid-state systems, other proposals exist toward the realization of the quantum anomalous Hall effect [67, 68, 69]. Experimental signatures of electronic QAH phases have been reported recently in magnetic topological insulators under external magnetic fields by several groups [70, 71, 72].

1.3.3 Quantum spin Hall effect

In 2005, Kane and Mele introduced a new kind of 2D insulator [44, 73], nowadays called $\mathbb{Z}_2$ topological insulator. Their work is based on the Haldane model where they include the spin degree of freedom. Importantly, they consider that each spin component $\pm$ is subjected to opposite phase through NNN tunnelling. Therefore, this model recovers time-reversal symmetry since it consists of two opposite copies

of the Haldane model. The tight-binding Hamiltonian in real space reads:

$$\hat{H} = -t_1 \sum_{i,\alpha,\sigma} a^{\sigma\dagger}_{\mathbf{R}_i} b^{\sigma}_{\mathbf{R}_i+\mathbf{d}_\alpha} - t_2 \sum_{i,\beta,\sigma} \left(a^{\sigma\dagger}_{\mathbf{R}_i} a^{\sigma}_{\mathbf{R}_i+\mathbf{a}_\beta} e^{i\nu_\beta\sigma\phi} + b^{\sigma\dagger}_{\mathbf{R}_i+d_1} b^{\sigma}_{\mathbf{R}_i+\mathbf{d}_1+\mathbf{a}_\beta} e^{-i\nu_\beta\sigma\phi} \right) + h.c.$$

(1.87)

where we use the same notation convention as for the Haldane model and $\sigma = \pm$ encodes the spin (up/down) index. The matrix Hamiltonian in momentum space is expressed as a four-by-four matrix in the basis $(\psi^+_A, \psi^+_B, \psi^-_A, \psi^-_B)$

$$H_{\mathbf{k}} = \begin{pmatrix} H^+ & 0 \\ 0 & H^- \end{pmatrix}$$

(1.88)

The spectrum consists of four energy bands degenerated by pairs corresponding to the eigenvalues of the two-by-two diagonal blocks H^+ and H^-. These blocks correspond to the Haldane matrix Hamiltonian (1.76) with ϕ for H^+ and $-\phi$ for H^-. Since these blocks are not coupled, one can also compute the Chern numbers for each spin sub-space separately. If we add the staggering potential Δ, the phase diagram in (Δ, ϕ) space for one spin component is therefore exactly the same as the one of the Haldane model (Fig. 1.5) and the opposite for the opposite spin. Hence, if we consider the full system, the sum of the Chern numbers below the bandgap vanishes: $C = C_+ + C_- = 0$ as it should be for any T-R symmetric Hamiltonian. Does this mean that the gap is trivial and that there are no propagating edges states at the boundaries of such system? Of course, as in the Haldane model there are edge states but now there are two of them: one for each spin component and each of these have opposite group velocities. These edge states are called *helical* edge states.

However, the gap Chern number is zero and this invariant cannot be used to see the difference with a conventional insulating phase. Actually, in a second paper [73], Kane and Mele introduced a new type of invariant for spin 1/2 fermionic particles in 2D T-R symmetric systems called the $\mathbb{Z}_2$ index. When there is no coupling between the spin species as in (1.88), this index is related to the difference between the independent Chern numbers $C^\pm$ [4]:

$$\nu = \frac{(C^+ - C^-)}{2} \mathrm{mod}2$$

(1.89)

where $\nu = 0$ corresponds to a conventional insulator and $\nu = 1$ to a *quantum spin Hall insulator* or $\mathbb{Z}_2$ *topological insulator*. In the original paper, they considered the case of $\phi = \pi/2$, a scheme of the corresponding projected dispersion is shown in figure 1.6 where colored lines correspond to spin-up spin-down edge states respectively.

In this spinful model the spin dependent NNN-hopping is known as the intrinsic spin orbit coupling and should be present in graphene. In this second paper [73], they considered the robustness of this effect against TR-preserving perturbation such as the Rashba SOC by adding the corresponding nearest-neighbour tunnelling
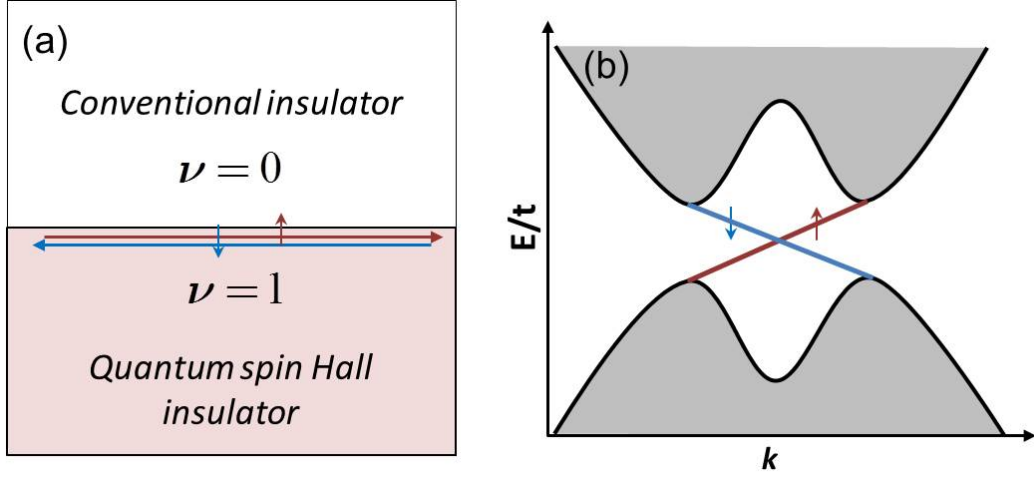
Figure 1.6: Quantum spin Hall effect. (a) Interface between a quantum spin Hall insulator and a conventional insulator. (b) Scheme of the projected band structure of the Kane-Mele model, with opposite group velocities for up-down spins.

term in the Hamiltonian:

$$H_R = i\lambda_R \sum_{i,\alpha} \left(a_{\mathbf{R}_i}^{+\dagger}, a_{\mathbf{R}_i}^{-\dagger} \right) \left(\boldsymbol{\sigma} \times \frac{\mathbf{d}_\alpha}{|\mathbf{d}|} \right) \begin{pmatrix} b_{\mathbf{R}_i+\mathbf{d}_\alpha}^+ \\ b_{\mathbf{R}_i+\mathbf{d}_\alpha}^- \end{pmatrix} - \left(b_{\mathbf{R}_i+\mathbf{d}_\alpha}^{+\dagger}, b_{\mathbf{R}_i+\mathbf{d}_\alpha}^{-\dagger} \right) \left(\boldsymbol{\sigma} \times \frac{\mathbf{d}_\alpha}{|\mathbf{d}|} \right) \begin{pmatrix} a_{\mathbf{R}_i}^+ \\ a_{\mathbf{R}_i}^- \end{pmatrix}$$
$$(1.90)$$

Taking into account this term implies the presence of off-diagonal blocks in (1.88) which means that the S_z spin component is not conserved anymore. They found that the helical edge states are still present if the Rashba SOC and staggering perturbation are sufficiently small. This is because the Rashba SOC respects fermionic T-R symmetry. Indeed, the $\mathbb{Z}_2$ index can be generalized to the case where S_z is not conserved and is deeply linked with the existence of the Kramers pairs in T-R symmetric system with half-integer spins [4]. It is important to keep in mind that such pairs are well defined only in fermionic systems. To our knowledge this model is one of the first proposals of *symmetry-protected* topological phases and has really inspired many other works in this direction toward a recent symmetry classification of topological phases for fermionic systems [74, 75, 76].

Despite the fundamental interest of this work which clearly participated to launch a research field, the QSH phase in graphene has never been observed. It seems that the intrinsic SOC and the linked topological gap are really to small to be observed in graphene [77, 78, 79].

However, another important proposal for quantum spin Hall effect has been done at that time [80, 5] based on an effective **k.p** Hamiltonian in HgTe quantum wells which can be written in the form of (1.88). Qualitatively, they found that this system can be in the QSH phase or in the trivial phase depending on the

width of the quantum wells. Soon after the proposal, the experimental evidence of gapless interface conducting states has been claimed in such system [81, 82]. To our knowledge, spin-resolved measurements have not been performed yet.

Note. The Kramers theorem, valid for spin $\frac{1}{2}$ particles, implies that in a time-reversal symmetric system the two orthogonal spin states are degenerate in energy. In fact, this theorem does not directly relate on the statistics (fermionic or bosonic) of the corresponding particles but on their behaviour under time-reversal operation ($T^2 = -1$). Hence, it should be applicable for arbitrary pseudospin $\frac{1}{2}$ particles with the same behaviour. However, the existence of such (quasi)-particles with an *internal* pseudospin degree of freedom following this law is not clear. For example, it is not the case of the polarization pseudospin of photons.

1.4 Extension to analog systems

As we have said in a previous remark, Bloch's theorem is not restricted to electronic systems but can be used to describe any waves moving in a periodic structure. Since the introduction of band geometry is related to the existence of several bands in the energy spectrum and their associated eigenstates and not to the statistics of the underlying particles, it seems quite natural to expect that similar objects can be defined in any wave system. It seems simple, but actually it has not been so easy. The first proposal of such analogy is due to Haldane and Raghu in 2005 [83](almost 30 years after the proposal of the former for quantum anomalous Hall effect!) and it took them three years for make their paper accepted.

This pioneer work has been a starting point of renewal in topological physics toward many proposals and experimental realizations of systems where band topology plays a role. From the experimental point of view, this extension to many different research fields implies a strong increase of the possible observables given by the peculiarity of each system. This allows an experimental access to some features inaccessible in condensed matter physics and is of strong interest to increase the general comprehension of topological band phenomena.

The goal of this section is to give to the reader an idea of the recent development in this direction in different fields and is not at all an exhaustive review of this rapidly growing field. For this we encourage the interested reader to look at the different reviews cited below.

1.4.1 Photonics

The field of topological photonics has grown exponentially these last years dealing with many proposals and realizations in various systems of various dimensions. For the sake of concreteness, in this section, we mainly introduce the original Haldane-Raghu proposal of quantum anomalous Hall effect analog for light in two dimensional photonic crystals and present the first experimental observation of the corresponding chiral edges states. Indeed, these original works belong to the same family of
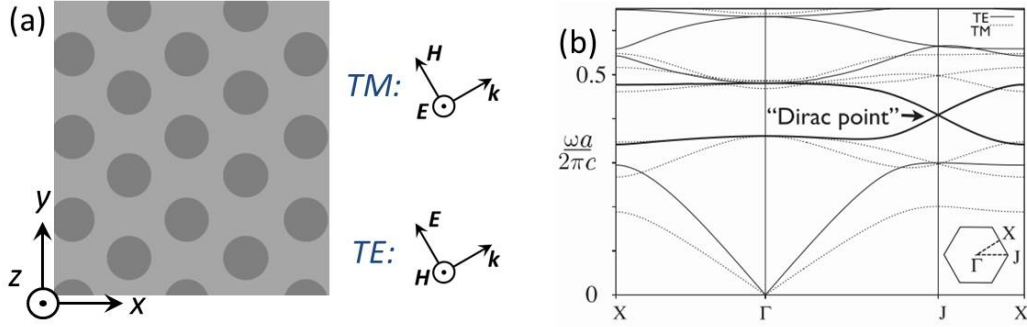
Figure 1.7: (a) Scheme of a two-dimensional triangular photonic crystal with the corresponding TE and TM modes representation. (b) Photonic band structure of a triangular photonic crystal for TE and TM modes respectively (from ref. [83]). There is a linear TE band crossing occurring in a TM bandgap.

photonic Chern insulators as the proposal in polariton system which will be discussed in chapter 3. For some recent overviews of the field of topological photonics we encourage the reader to consult the following review papers [7, 8] and references therein.

Gyrotropic photonic crystals.   In 2005, Haldane-Raghu proposed to use the Faraday effect to open a topological bandgap in a two-dimensional gyrotropic photonic crystal thanks to an external magnetic field [83, 84]. Soon after, this effect has been studied and realized in square lattice with gyromagnetic materials under external magnetic field [85, 86]. The tool to describe theoretically light propagation in photonic crystals are Maxwell equations. In a source and loss free media they read:

$$\nabla \times \mathbf{E} = -\bar{\bar{\mu}}(\mathbf{r})\frac{\partial \mathbf{H}}{\partial t}, \quad \nabla.(\bar{\bar{\varepsilon}}(\mathbf{r})\mathbf{E}) = 0 \tag{1.91}$$

$$\nabla \times \mathbf{H} = \bar{\bar{\varepsilon}}(\mathbf{r})\frac{\partial \mathbf{E}}{\partial t}, \quad \nabla.(\bar{\bar{\mu}}(\mathbf{r})\mathbf{H}) = 0 \tag{1.92}$$

where $\bar{\bar{\mu}}(\mathbf{r})$ and $\bar{\bar{\varepsilon}}(\mathbf{r})$ are the local permeability and permittivity hermitian tensors of the medium. For an oscillating electromagnetic field $\mathbf{E}(\mathbf{r}, t) = \mathbf{E}(\mathbf{r})e^{i\omega t}$ with frequency ω these equations leads to the following eigenvalue problem:

$$\nabla \times \left[\bar{\bar{\mu}}(\mathbf{r})^{-1}\nabla \times \mathbf{E}\right] = \omega^2 \bar{\bar{\varepsilon}}(\mathbf{r})\mathbf{E} \tag{1.93}$$

(An analogous equation can be achieved for the magnetic field $\mathbf{H}$). In typical photonic crystals [26] the permittivity and permeability tensors are taken real diagonal and the periodicity is given by the permittivity tensor $\varepsilon(\mathbf{r} + \mathbf{R}) = \varepsilon(\mathbf{r})$, the permeability being taken equal to the vacuum constant μ_0. These assumptions are not

valid anymore if we consider *gyrotropic* materials which break time reversal symmetry. In this case $\bar{\bar{\varepsilon}}$ and(or) $\bar{\bar{\mu}}$ are anisotropic and hermitian. For example, in their original proposal Haldane and Raghu [83] proposed to use a *gyroelectric* material with permittivity tensor of the form:

$$\bar{\bar{\varepsilon}} = \begin{pmatrix} \varepsilon_x & i\eta & 0 \\ -i\eta & \varepsilon_y & 0 \\ 0 & 0 & \varepsilon_z \end{pmatrix} \tag{1.94}$$

Similarly, for the first experimental observation of topological edge states for light, Wang et al. [85, 86] used a *gyromagnetic* material which is modelized in Maxwell equations by the following permeability tensor:

$$\bar{\bar{\mu}} = \begin{pmatrix} \mu_x & i\kappa & 0 \\ -i\kappa & \mu_y & 0 \\ 0 & 0 & \mu_z \end{pmatrix} \tag{1.95}$$

(In both cases we consider the magnetization direction to be along z axis.) In general, both $\bar{\bar{\varepsilon}}$ and $\bar{\bar{\mu}}$ components will be periodic functions with the periodicity of the photonic crystal. The Bloch theorem applies as for the Schrödinger equation and the Bloch function is given by the electric field vector which can be written in the form:

$$\mathbf{E}_{n\mathbf{k}}(\mathbf{r}) = e^{i\mathbf{k}.\mathbf{r}}\mathbf{u}_{n,\mathbf{k}}(\mathbf{r}) \tag{1.96}$$

Note that the periodic part $\mathbf{u}_n$ is now a three dimensional vector. As a consequence, we have $\mathbf{k}$ dependent bands and associated eigenstates, which is one ingredient needed to define the geometric quantities in quasi-momentum space. However, another important property is present in the Berry phase definition which is the Hermitian nature of the time independent Schrödinger eigenvalue problem. Strictly speaking, this property is not valid for the Maxwell equations (1.93) due to the presence of the $\bar{\bar{\varepsilon}}$ tensor on the right part. It actually corresponds to a *generalized* Hermitian eigenvalue problem. In this context the Berry connection can be defined as [85]:

$$\boldsymbol{\mathcal{A}}_n(\mathbf{k}) = \frac{\int d\mathbf{r}\mathbf{u}_{n,k}^\dagger(\mathbf{r}).\bar{\bar{\varepsilon}}\nabla_{\mathbf{k}}\mathbf{u}_{n,k}(\mathbf{r})}{\int d\mathbf{r}\mathbf{u}_{n,k}^\dagger(\mathbf{r}).\bar{\bar{\varepsilon}}\mathbf{u}_{n,k}(\mathbf{r})} \tag{1.97}$$

The associated Berry curvature and 2D Chern numbers are then achieved from the standard formula $\boldsymbol{\mathcal{B}}_n = \nabla_{\mathbf{k}} \times \boldsymbol{\mathcal{A}}_n$.

In two dimensional photonic crystals with periodicity in x-y plane, the z independence implies that equation (1.93) can be decomposed into two decoupled equations for the so called Transverse-Electric (TE) and Transverse-Magnetic (TM) polarized modes corresponding to in-plane $\mathbf{E}_{TE} = (E_x, E_y, 0)^T$ or out of plane $\mathbf{E}_{TM} = (0, 0, E_z)^T$ electric fields respectively (see the scheme in Fig. 1.7 (a)). This peculiarity is actually the key element in the original Haldane-Raghu paper which proposed to lift a TE band degeneracy inside a TM bandgap. The corresponding bulk photonic band structure before the degeneracy lifting is shown in figure 1.7 (b).
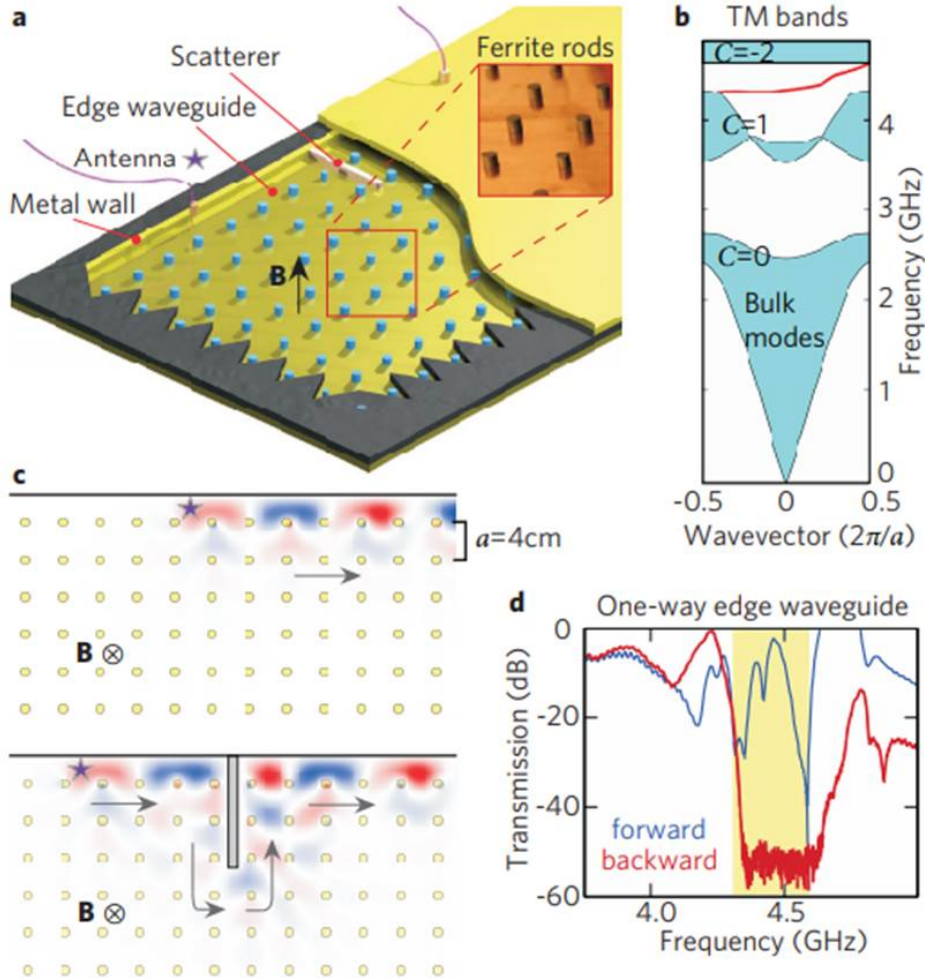
Figure 1.8: **First experimental observation of photonic topologically protected edge states in microwaves domain.** a) Picture of the structure constituted of a square lattice of ferrite rods embedded between two copper plates with metallic boundaries. b) Projected computed TM energy bands showing the bulk dispersion in blue and the chiral edge state in red. c) Real space image of the chiral edge state E_z electric field calculated with COMSOL software. The star represents the antenna and the arrow the direction of propagation. The top panel shows the electric field profile without scatterer whereas the lower one represents the situation when a metallic obstacle is present on the edge. d) Measured transmission spectra upon inclusion of the scatterer and the antenna as shown in (a) showing the high contrast between forward and backward signals for frequencies lying in the second gap of (b). (Pictures taken from [7, 86])

This degeneracy lifting is achieved thanks to the antisymmetric off-diagonal terms in the permittivity tensor (1.94).

The same approach has been realized experimentally for TM bands in the ref. [86] whose results are shown in figure 1.8. The system used in this work is a square array of vanadium-doped calcium-iron-garnet (ferrite) rods embedded between two copper plates with metallic boundaries (see scheme in Fig. 1.8. (a)). They managed to achieve a photonic band-gap for TM modes in the crystal slab by applying a transverse magnetic field which leads to a permeability of the form (1.95) in the microwave domain. The computed projected TM band structure is shown in figure 1.8(b) showing several bulk bands together with their associated Chern numbers. The sum of the Chern numbers below the second bandgap is equal to 1 ($\sum_{n=1}^{2} C_n = 1$), which implies the presence of one chiral edge mode crossing this gap shown in red. The panel c) represents the corresponding E_z field profile in real space during its propagation without and with an additional metallic defect on its path. The experimentally measured transmission is plotted on panel d) showing the very high contrast between forward and backward transmission in the frequency range corresponding to the second bandgap. However, it is interesting to note that the TE-modes are not shown contrary to the Haldane-Raghu work where both polarization bulk dispersions are shown (Fig. 1.7 (b)). Indeed, whereas the metallic defect used in their experiment does not couple TE and TM modes, a non-metallic one will be able to scatter light in the bulk region if no full bandgap is present.

From the experimental point of view gyrotropic effects are strongly dependent on the frequency and a permeability of the above form is typically restricted to the microwave domain. Recently, similar one way photonic edge modes have been observed using electron cyclotron resonance effect in semiconductor (providing a permittivity of the form (1.94)) at the terahertz frequency range [87]. Despite the very small photonic bandgap achieved, this platform has allowed the first observation of a 2D topological laser [88] and is of huge interest for applications.

On the theoretical side, the analogy with quantum mechanics can be pushed further by writing Maxwell's equations in the Schrödinger form.

$$i\frac{\partial}{\partial t}\boldsymbol{\Psi} = M\boldsymbol{\Psi} \tag{1.98}$$

with $\boldsymbol{\Psi} = (\mathbf{E}, \mathbf{H})^T$ and the matrix M defined by:

$$M = \begin{pmatrix} \bar{\bar{\varepsilon}}^{-1} & 0 \\ 0 & \bar{\bar{\mu}}^{-1} \end{pmatrix} \begin{pmatrix} 0 & i\nabla\times \\ -i\nabla\times & 0 \end{pmatrix} \tag{1.99}$$

Recently, such matrix formulation has been used to make a rigorous symmetry classification of photonic crystals [89, 90] by analogy with the classification developed for fermionic systems based on the Cartan-Altland-Zirnbauer symmetry classification [76]. Interestingly, this approach allows to confirm the absence of $\mathbb{Z}_2$ topological class starting from Maxwell equations. Moreover, in this approach, the Berry connection should be defined as:

$$\boldsymbol{\mathcal{A}}_n(\mathbf{k}) = \frac{\int d\mathbf{r} \mathbf{u}_{n,k}^\dagger(\mathbf{r}).M^{-1}\nabla_\mathbf{k}\mathbf{u}_{n,k}(\mathbf{r})}{\int d\mathbf{r} \mathbf{u}_{n,k}^\dagger(\mathbf{r}).M^{-1}\mathbf{u}_{n,k}(\mathbf{r})} \tag{1.100}$$

with the 6 component vectors $\mathbf{u}_{n,k}$ written in the form $\mathbf{u}_{n,k} = (\mathbf{u}^{\mathbf{E}}_{n,k}, \mathbf{u}^{\mathbf{H}}_{n,k})^T$. This formulation was actually already used in the Haldane-Raghu paper. This implies that we have several definitions for the Berry curvature. The form (1.97) allows to define "electric" and "magnetic" Chern numbers whereas the second form (1.100) defines one general Chern number. Whereas the different definitions are used by physicists depending on the system of interest, it is interesting to note that the link between the three is still not well understood from the mathematical point of view [90]. Actually, this peculiarity is a reminiscence of Maxwell equations, in the rest of the thesis, the results presented will always be linked with the Schrödinger equation where this problem is absent.

Other approaches toward 2D photonic edge states. After the observation in the microwave domain, different directions have been followed in order to extend such one way states to the optical domain. One important realization is based on a 2D array of coupled 1D waveguides. This type of system is well described in the paraxial limit by a Schrödinger equation where the time derivative is replaced by the derivation along the direction of the 1D waveguides. A periodic modulation in the z direction can be used to emulate a Floquet type of topological insulator. One way chiral edge states in such structure have been reported in ref. [91]. Nowadays, this approach has been extended to higher dimensions and is an active subject of research [8].

A second approach to the problem was to find a way to generate artificial magnetic field for photons. A model of this kind which can be mapped to a Harper-like T-B Hamiltonian has been proposed [92] and realized [93]. Qualitatively, this system does not break time-reversal symmetry and the synthetic magnetic field is acting oppositely for two pseudospins components. This leads to counter-propagating edge states for the two pseudospin components. As a consequence, this system is an analog of quantum spin Hall effect for photons. However, time-reversal symmetry protection which is crucial in the electronic quantum spin Hall effect is not valid in this photonic system where the pseudospin degree of freedom rely on the lattice (site) structure. Hence, these photonic helical edge states can always be backscattered by any disorder (not only magnetic disorder) present on the edges. Experimental signature of lasing in this type of helical edge modes using a gain medium has been reported recently [94, 95].

1.4.2 Cold-atoms systems

The study of band topology has also emerged in cold atom Physics. Indeed, nowadays, bosonic or fermionic atomic gases are routinely loaded in optical lattice potentials [96]. In the past years, the high-tunability of such systems concerning both

the interaction between particles and the depth of the periodic potentials has made of this area of physics a very interesting platform to probe many-body phenomena [97, 98].

The possibility to use such systems in the non-interacting regime to study topological properties associated with the periodic band structures has been exploited more recently. Indeed, the high control of artificial optical lattices has allowed to emulate several type of non-interacting Hamiltonians with non trivial topologies such as the Harper-Hofstadter Hamiltonian in a square lattice [99] or the 1988 Haldane model [66]. The experimental observation of the edge states being quite challenging in real optical lattices, different approaches have been developed to probe the Bloch states topology from bulk properties. One of them uses the possibility to create and manipulate atomic wavepackets adiabatically in a given band. Hence, experimental measurement of the Zak phase (1.70) in one dimensional SSH system has been reported in [100]. In 2D, the anomalous drift of an accelerated wavepacket in a given band induced by the local Berry curvature has been used to extract the corresponding Chern numbers [101, 66]. A different approach based on the ability to switch off the optical lattice potentials has been proposed [102] and realized [103] to map out the local Berry curvature in 2D two-band systems thanks to time of flight measurements.

Despite the fact that the above measurements appear quite indirect compared to what is done in photonics where edge states are directly probed, the cold atom platform is still very promising for future studies. Indeed, the high tunability achievable can be used to emulate higher dimensional lattices using internal degrees of freedom as additional synthetic dimensions. Another fascinating direction is to combine topological band effects with interactions where particle statistics will become important. A recent review of this growing field has been submitted online for the interested reader [9].

1.4.3   Other wave systems

Band topology concepts have also been introduced for other waves such as mechanical or sonic waves in various systems. For example, Chern insulator models have been predicted theoretically for phonons in 2D lattice of proteins [104] in Biophysics, at the nanoscale in optomechanical crystals [105] and for acoustic waves in a phononic crystal where time reversal symmetry is broken by the addition of a moving fluid [106]. Also, topological bound modes have been studied in coupled oscillators lattices [107, 108] where Newton coupled equations can be recast in the Schrödinger form similar to tight-binding models in condensed matter systems [109].

Even more astonishing and beautiful for us is the recent use of this tool at larger scales to explain the chiral behaviour of equatorial geophysical waves [111]. This type of geophysical waves are well described by shallow water equations used to describe quasi-two dimensional fluid mechanics (the height of the fluid is small
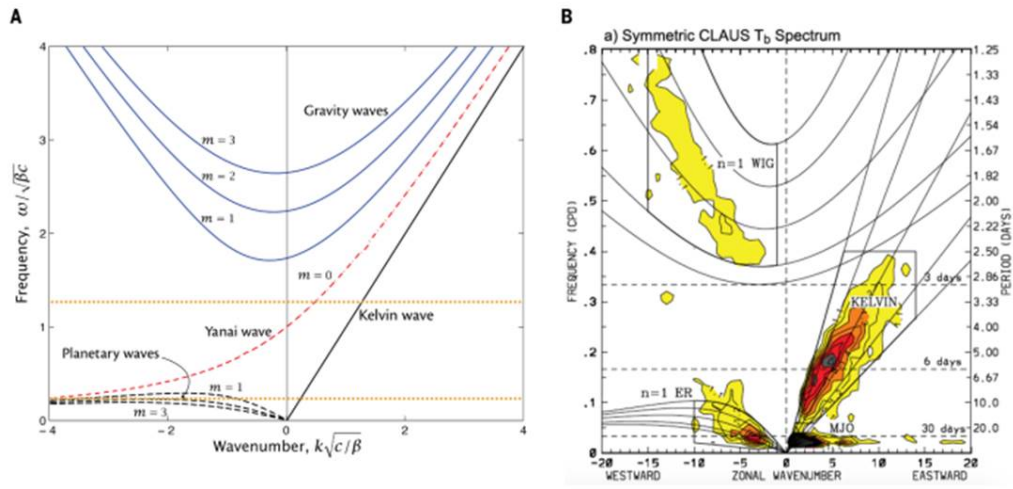
Figure 1.9: **Chiral equatorial waves.** (a) Calculated dispersions based on shallow water equations on equatorial tangent plane ("β-plane approximation") with a linearly varying Coriolis parameter $f = \beta y$ showing the two gapless Yanai and Kelvin waves (propagation in the x direction), (b) Observational evidence of the gapless Kelvin mode (Original data and a similar spectra showing the evidence of Yanai mode can be found in the paper [110]). (Pictures reprinted from ref. [111])

compared to the size of the bath) written as [112]:

$$\frac{\partial}{\partial t}h + \nabla.(h\mathbf{v}) = 0 \tag{1.101}$$

$$\frac{\partial}{\partial t}\mathbf{v} + (\mathbf{v}.\nabla)\mathbf{v} = -g\nabla h - f\mathbf{n} \times \mathbf{v} \tag{1.102}$$

where h is height of the fluid, $\mathbf{v}$ is the velocity, $\mathbf{n}$ is the normal to the sphere, $f = 2\mathbf{\Omega}.\mathbf{n}$ is the Coriolis parameter being positive (negative) in north (south) hemisphere ($\mathbf{\Omega}$ is the earth angular rotation vector). After linearization near the stationary solution $h = H$ and $\mathbf{v} = \mathbf{0}$, these equations can be recast in the Schrödinger form with eigenmodes of the form $\Psi e^{i(\omega t - k_x x - k_y y)}$ which lead to the eigenvalue equation:

$$\omega \begin{pmatrix} \psi_1 \\ \psi_2 \\ \psi_3 \end{pmatrix} = \begin{pmatrix} 0 & k_x & k_y \\ k_x & 0 & -i\tilde{f} \\ k_y & i\tilde{f} & 0 \end{pmatrix} \begin{pmatrix} \psi_1 \\ \psi_2 \\ \psi_3 \end{pmatrix} \tag{1.103}$$

The diagonalization gives three energy bands which are gapped when $f \neq 0$. The Berry curvature associated to the bands is found to be opposite between the two hemispheres ($f > 0$ or $f < 0$). Since we are dealing with continuous dispersion without Brillouin zone, some care is needed to define a real topological invariant [111], but qualitatively, the opposite BC in the two hemispheres implies the presence of two chiral gapless modes at the equator where $f = 0$. These waves were originally predicted theoretically in the 60's using shallow water equations with some specific boundary conditions [113] leading to a spectra of the form shown in Fig. 1.9(a) and are known as Yanai and Kelvin waves. An example of their observational evidence is shown in figure 1.9(b) [110].

1.5   Conclusion

In this chapter we have introduced the Berry curvature and a metric associated with normalized eigenstates of parameter dependent hermitian eigenvalue equations. Then, we have shown that these objects can be used in momentum space. The periodicity of crystals imposes the presence of several bands with associated geometrical quantities. Importantly, in two dimensions considering the Brillouin zone as a closed surface allows to introduce the Chern number: a topological invariant at the heart of topological insulators physics. We then gave some historical tight-binding model where band topology arises before the last section where we attempted to show different directions toward extensions of these concepts in other areas both in quantum and classical Physics.

While in our examples the concepts of Berry curvature and Chern number have been widely used, the metric consequences have not been discussed. This is due to the fact that this metric is far less known and used in modern Physics. This is understandable because the robustness of topological effects against external perturbations makes them a very attractive subject due to their universality. Nevertheless, the metric and possible associated effects have been studied recently. In condensed

matter, it appears to play a role in different contexts, ranging from contribution to the orbital susceptibility [114, 115] and corrections to the anomalous Hall effect [116, 117], to the exciton Lamb shift in TMDs [118] and superfluidity in flat bands [119, 120]. In chapter 5, we present our results related to this object.

Another subject that we did not discuss at all is the effect of interactions. In electronic systems, this field dates back to the discovery of the fractional quantum Hall effect (FQHE) [121] soon after the integer one. FQHE is still under ongoing research nowadays as one of the most striking examples of strongly correlated states of matter giving rise to interesting Physics such as the occurrence of excitations with fractional statistics and fractional charges [122, 123, 124]. In a similar way, strongly correlated bosonic systems are studied theoretically.

The new avenue which is opened with the analog systems can bring some insight in this direction too. Chapter 4 is dedicated to the presentation of new effects linked with the mean-field interactions of Bose-Einstein condensates loaded in periodic potentials.

Introduction to Bose-Einstein condensates and cavity polariton Physics

Contents

In the first section 2.1, we introduce a type of macroscopic bosonic quantum fluid namely the Bose-Einstein condensates. We introduce the Bose-Einstein distribution allowing bosonic particles to be in the same quantum state which can then be described by the same single particle wavefunction or order parameter. Then, we present the Gross-Pitaevskii equation which describes the evolution of this macroscopic wavefunction in presence of mean field interactions. Two types of excitations are discussed: the Bogoliubov excitations corresponding to density waves of small amplitude on the top of a condensate and vortices which are topological excitations of the full non-linear equation. The section 2.2 is devoted to a quick introduction to cavity polaritons quasi-particles and their possible description in terms of Gross-Pitaevskii equations when high densities are involved.

2.1   Bose-Einstein condensates

2.1.1   Bose-Einstein statistics

Statistical Physics is a useful tool to describe macroscopic thermodynamic properties of gases in term of microscopic principles. When approaching low temperatures, the quantum nature of the underlying particles becomes relevant. The story of Bose-Einstein condensation started with the work of Einstein [125] on the statistics of a gas of identical bosons based on the previous rederivation of Planck's law by Bose [126]. From these pioneer works we know that an ideal non-interacting boson gas confined in a R^d volume obeys the so-called Bose-Einstein distribution:

$$f_B(\mathbf{k}, T, \mu) = \frac{1}{e^{\beta(\varepsilon(\mathbf{k}) - \mu)} - 1} \tag{2.1}$$

where $\beta = (k_b T)^{-1}$ with k_b the Boltzmann constant and T the temperature. μ is the chemical potential. $\mathbf{k}$ is the d dimensional wavevector. It gives the expected particle occupation number in a single particle state of energy $\varepsilon(\mathbf{k})$. A fundamental state of energy $\varepsilon(0) = 0$ implies a negative chemical potential. The total number of particles is then given by:

$$N(T, \mu) = \sum_{\mathbf{k}} f_B(\mathbf{k}, T, \mu) \tag{2.2}$$

where we can separate the ground state contribution from the other states:

$$N(T, \mu) = \frac{1}{e^{\beta(-\mu)} - 1} + \sum_{\mathbf{k} \neq 0} f_B(\mathbf{k}, T, \mu) \tag{2.3}$$

In the thermodynamic limit, one can replace the sum by an integral in reciprocal space and obtain the density:

$$n(T, \mu) = \lim_{R \to \infty, N \to \infty} \frac{N(T, \mu)}{R^d} = n_0 + \frac{1}{(2\pi)^d} \int_0^\infty f_B(\mathbf{k}, T, \mu) d\mathbf{k} \tag{2.4}$$
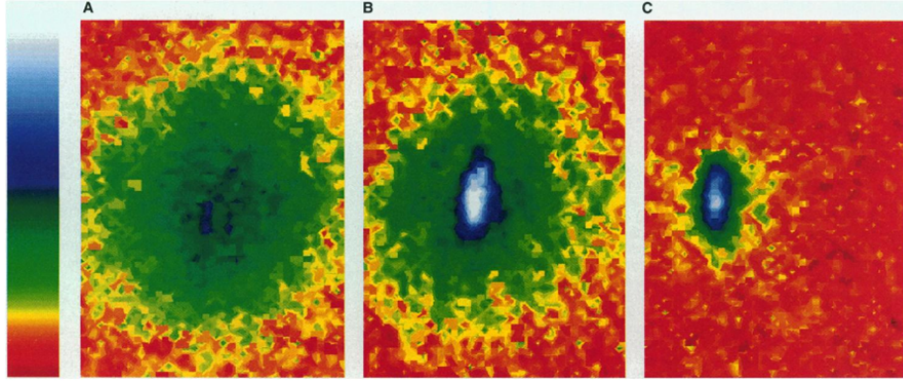
Figure 2.1: **Experimental observation of Bose-Einstein condensation in an atomic vapor**. Velocity distributions (a) just before the transition, (b) after the transition: the elliptic blue area corresponds to the condensate fraction, (c) after evaporation allowing to achieve a nearly pure condensate. The color represent the number of atom at each velocity, with white being the most and red the fewest. (From ref. [127])

where:

$$n_0 = \lim_{R \to \infty} \frac{1}{R^d} \frac{1}{e^{-\beta(\mu)} - 1} \tag{2.5}$$

The ground state density n_0 vanishes for non-zero μ. On the contrary, the integral over reciprocal space increases when μ increases. It means that the increase of the particle number N in the system is associated to the increase of the chemical potential μ. However, μ is bound from above to zero for the positive definiteness of N. The maximum density achievable by the integral part is then given by:

$$n_c(T) = \lim_{\mu \to 0} \frac{1}{(2\pi)^d} \int_0^\infty f_B(\mathbf{k}, T, \mu) d\mathbf{k} \tag{2.6}$$

This function can be computed analytically in the case of massive particles with parabolic dispersion. It converges for $d > 2$ and diverges when $d \leq 2$. Therefore, when $d > 2$, n_c is a critical density above which it seems that no more particles can be added. In fact, above this density, the additional particles collapse into the ground state, whose density can be defined by:

$$n_0(T) = n(T) - n_c(T) \tag{2.7}$$

This is a phase transition above which a macroscopic number of bosons can accumulate ("condense") in the same quantum state. It is interesting to note that no interactions are needed to achieve the Bose-Einstein condensation in this original formulation. Two ways can be used to cross this transition: increase the density at a fixed (low) temperature, or decrease the density at a fixed (high) density or a

combination of the two. For massive bosons in 3D, the critical values are:

$$n_c(T) = \zeta(3/2) \left(\frac{mk_bT}{2\pi\hbar^2} \right)^{3/2}, \quad \text{or} \quad T_c(n) = \left(\frac{n}{\zeta(3/2)} \right)^{2/3} \frac{2\pi\hbar^2}{mk_b} \qquad (2.8)$$

Qualitatively, the lighter are the particles, the easier it is for them to condense. When $d \leq 2$ the divergence implies the absence of such phase transition for a non-interacting boson gas. However, in realistic finite 1D and 2D systems the resulting integral (2.6) converges and quasi-condensation can be achieved.

In the 30's, soon after the discovery of superfluid helium, the analogy with Bose-Einstein condensation has been proposed [128] but in this liquid phase the interactions are not negligible and the ideal gas approximation is too crude. In fact, the first clear experimental evidences of BEC were reported in 1995 in systems of dilute atomic gas cooled at ultracold temperatures ($T \approx 10^{-7}K$) by three different groups [127, 129, 130]. Figure 2.1 shows the results from the paper of Anderson et al. displaying the velocity distributions of the atomic cloud before the condensate appearance (a), just after its appearance (b) and after some further evaporation leading to a nearly pure condensate (blue and white region). These discoveries allowed by the preceding important development of cooling and trapping techniques of atomic gases, participated to the growth of the field of cold atom Physics [131].

A few years after these observations in cold atom systems, BEC observation has been claimed in different systems with bosonic quasi-particles such as excitons, magnons [133] and exciton-polaritons [132, 134]. Despite the fact that the particle number is not strictly conserved in this system (photon leakage out of the cavity), a thermalization of the polariton gas can be achieved if the relaxation time to the ground state is smaller than the polariton lifetime in the cavity. In such regime, one can consider the particle number approximately conserved and the occupancy of the ground state obeys the Bose-Einstein statistics with an effective temperature of the gas. The cavity polariton platform allows to study this thermal regime and also the kinetic regime where the ground state is macroscopically occupied but does not obey the Bose-Einstein distribution [135]. The interplay between these two regimes is controlled experimentally by the detuning between the cavity and excitonic modes (See 2.2.1.1).

Figure 2.2 shows the results from the first cavity polariton condensation observation performed in a CdTe/CdMgTe microcavity at $T = 5K$. Panel (a) represents the angular distribution of the spectrally integrated emission measured at different excitation powers. Below threshold (left) the emission exhibits a smooth distribution centred at zero degrees corresponding to the in plane wavevector $\mathbf{k} = \mathbf{0}$. When the excitation intensity is increased (which qualitatively increases polariton density), the emission from $\mathbf{k} = \mathbf{0}$ becomes predominant at threshold (center) and forms a sharp peak above (right). Panel (b) shows the corresponding energy and angle resolved emission intensities. Above threshold the emission mainly comes from the lowest energy state corresponding to a macroscopically occupied state.
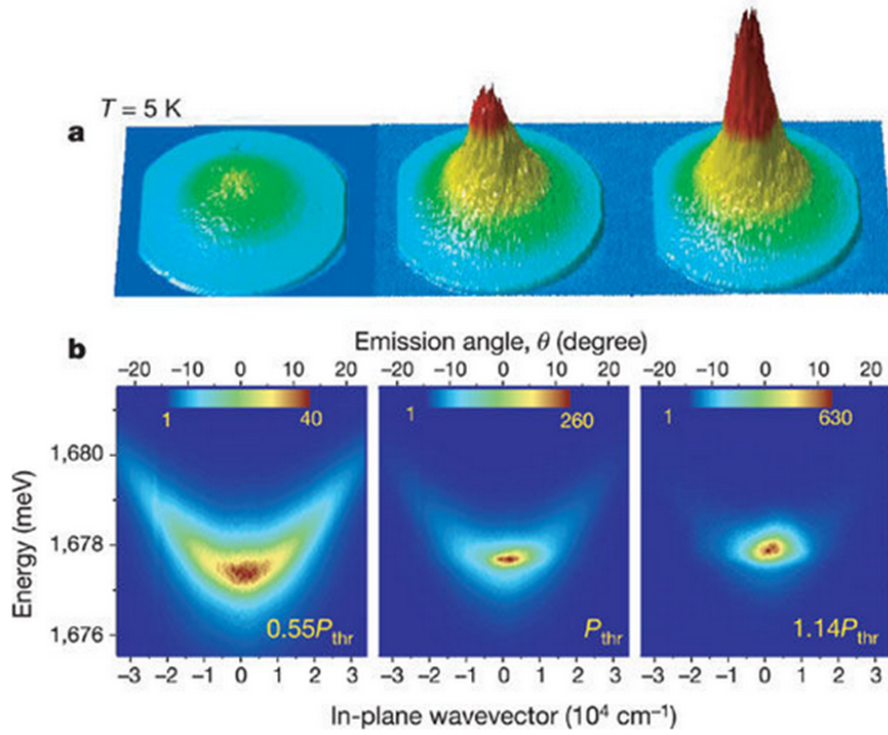
Figure 2.2: **Condensation of cavity polaritons..** (a) Far field images of real-space intensity emission below threshold at threshold and above threshold. (b) Corresponding angular and energy resolved emission showing the high population of the ground state above threshold. (From ref. [132])

2.1.2 Gross-Pitaevskii equation

The problem of a homogeneous weakly interacting boson gas has been initially studied by Bogoliubov as a way to explain superfluidity of liquid Helium [136]. The non-homogeneous case is described by the Gross-Pitaevskii equation that we introduce below following ref. [137]. This equation can be derived starting from the Hamiltonian for many binary interacting bosons:

$$\hat{H} = \int \left[\frac{\hbar^2}{2m} |\nabla \hat{\Psi}(\mathbf{r})|^2 + \hat{\Psi}(\mathbf{r})^\dagger V_{ext} \hat{\Psi}(\mathbf{r}) \right] d\mathbf{r} + \frac{1}{2} \int \hat{\Psi}(\mathbf{r})^\dagger \hat{\Psi}(\mathbf{r}')^\dagger V(\mathbf{r}-\mathbf{r}') \hat{\Psi}(\mathbf{r}) \hat{\Psi}(\mathbf{r}') d\mathbf{r} d\mathbf{r}' \tag{2.9}$$

where $V_{ext}(\mathbf{r},t)$ is the external potential (for example a trap to confine the particles) and $V(\mathbf{r} - \mathbf{r}')$ is the interaction potential between two particles. The field operators obey the standard bosonic commutation rules:

$$[\hat{\Psi}(\mathbf{r}'), \hat{\Psi}(\mathbf{r})^\dagger] = \delta(\mathbf{r} - \mathbf{r}'), \quad [\hat{\Psi}(\mathbf{r}'), \hat{\Psi}(\mathbf{r})] = 0, \quad [\hat{\Psi}(\mathbf{r}')^\dagger, \hat{\Psi}(\mathbf{r})^\dagger] = 0 \tag{2.10}$$

One obtains the exact equation for the field operator evolution by using Heisenberg equation $i\hbar \frac{\partial}{\partial t} \hat{\Psi}(\mathbf{r},t) = [\hat{\Psi}(\mathbf{r},t), \hat{H}]$ which gives:

$$i\hbar \frac{\partial \hat{\Psi}(\mathbf{r},t)}{\partial t} = \left(-\frac{\hbar^2 \nabla^2}{2m} + V_{ext} + \frac{1}{2} \int \hat{\Psi}(\mathbf{r}')^\dagger V(\mathbf{r} - \mathbf{r}') \hat{\Psi}(\mathbf{r}') d\mathbf{r}' \right) \hat{\Psi}(\mathbf{r}) \tag{2.11}$$

Then, two approximations are used to achieve the GPE. First, the boson gas is considered sufficiently dilute such that the interaction potential can be replaced by contact interaction $V(\mathbf{r} - \mathbf{r}') = \alpha \delta(\mathbf{r} - \mathbf{r}')$. Second, assuming $T = 0$ and all the particles in the single particle ground state forming the condensate, one can replace the field operator $\hat{\Psi}(\mathbf{r},t)$ by the classical field $\Psi(\mathbf{r},t) = \left\langle \hat{\Psi}(\mathbf{r},t) \right\rangle$ (mean field approximation). One finally obtains:

$$i\hbar \frac{\partial \Psi(\mathbf{r},t)}{\partial t} = \left(-\frac{\hbar^2 \nabla^2}{2m} + V_{ext}(\mathbf{r},t) + \alpha |\Psi(\mathbf{r},t)|^2 \right) \Psi(\mathbf{r},t) \tag{2.12}$$

We end with a classical non-linear wave equation also known as the non-linear Schrödinger equation. Its formulation for nonuniform coherent Bose gases is due to independent works by Gross and Pitaevskii in the 60's [138, 139, 140] and is nowadays the main theoretical tool for investigating such systems. The mean field approximation means that we neglect the thermal or quantum depletion of the condensate, and leads to the normalisation $N = \int |\Psi(\mathbf{r})|^2 d\mathbf{r}$. Ψ can be seen as a macroscopic wavefunction of the condensate also referred to the condensate order parameter. It encodes its density n and its phase θ: $\Psi(\mathbf{r},t) = \sqrt{n(\mathbf{r},t)} e^{i\theta(\mathbf{r},t)}$.

The important change compared to the standard Schrödinger equation describing an ideal gas is the non-linear density dependent term $\alpha |\Psi(\mathbf{r},t)|^2$. In what follows, we will consider the case $\alpha > 0$ which corresponds to repulsive interaction between particles. Stationary solutions are found by writing $\Psi(\mathbf{r},t) = \psi(\mathbf{r}) e^{-i\mu t}$ where μ is the chemical potential leading to the stationary GPE:

$$\mu\psi = \left(-\frac{\hbar^2\nabla^2}{2m} + V_{ext} + \alpha|\psi|^2\right)\psi \tag{2.13}$$

Remark. In the following and in general along the thesis we will always consider the two-dimensional GPE. Moreover, each time we will speak about interacting bosonic quantum fluid the above mean field approximation will be assumed.

2.1.3 Elementary excitations

Now, that we have an efficient equation to describe the condensate, we introduce its elementary excitations, known as *Bogoliubov excitations* or *bogolons*. We are looking for small oscillations of the order parameter around equilibrium, we can start from the order parameter of the form:

$$\Psi(\mathbf{r}, t) = (\psi(\mathbf{r}) + \delta\psi(\mathbf{r}, t))e^{-i\mu t/\hbar} \tag{2.14}$$

where $\psi(\mathbf{r})$ is the condensate wavefunction and $\delta\psi$ is a small quantity of the form:

$$\delta\psi(\mathbf{r}, t) = \sum_i [u_i(\mathbf{r})e^{-i\omega_i t} + v_i^*(\mathbf{r})e^{i\omega_i t}] \tag{2.15}$$

The peculiar form of $\delta\psi$ as a linear combination of complex coefficients results from the coupling of $e^{i\omega_i t}$ and $e^{-i\omega_i t}$ terms by the nonlinearity when inserted in the GPE. Considering weak density perturbations propagating on top of a *homogeneous* condensate, the above perturbed wavefunction can be written as:

$$\Psi(\mathbf{r}, t) = (\sqrt{n} + ue^{i(\mathbf{k}\cdot\mathbf{r}-\omega t)} + v^*e^{-i(\mathbf{k}\cdot\mathbf{r}-\omega t)})e^{-i\mu t/\hbar} \tag{2.16}$$

where the stationary part is $\psi(\mathbf{r}) = \sqrt{n}$, and u and v^* are small amplitudes of the counter-propagating modes with frequency ω. Inserting, this ansatz in the GPE equation (2.12) keeping only first order in u and v^* yields the following system:

$$\hbar\omega u = \frac{\hbar^2 k^2}{2m}u + \alpha n(u+v) \tag{2.17}$$

$$-\hbar\omega v = \frac{\hbar^2 k^2}{2m}v + \alpha n(u+v) \tag{2.18}$$

The bogolon dispersion is achieved using determinant method:

$$\hbar\omega_\pm(k) = \pm\sqrt{\left(\frac{\hbar^2 k^2}{2m}\right)^2 + \frac{\hbar^2 k^2}{m}\alpha n} \tag{2.19}$$

(Equivalent result can be achieved following the original Bogoliubov development [136]). In the limit of small wave vectors, the dispersion becomes linear $\hbar\omega(k) \approx \hbar c_s k$ and one can define the speed of sound $c_s = \sqrt{\alpha n/m}$. This linear phonon dispersion is the hallmark of the superfluid behaviour of interacting BEC. At large k the bogolon dispersion recovers the particle-like parabolic shape shifted by the interaction energy: $\hbar\omega(k) \approx \frac{\hbar^2 k^2}{2m} + \alpha n$ (See Fig. 2.3).
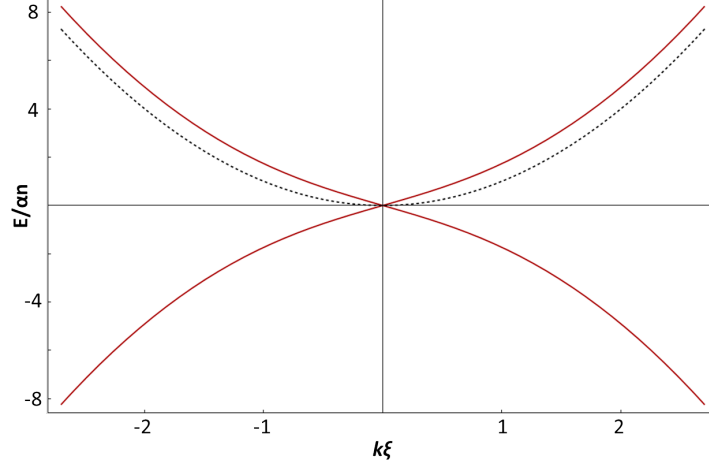
Figure 2.3: **Elementary excitations.** Red lines show Bogoliubov dispersions (2.19) and dashed black line represents the free particle dispersion.

The transition between phonon and particle-like dispersion takes place around $\frac{\hbar^2 k_\xi^2}{2m} = \alpha n = mc_s^2$ which allows to define a characteristic length of the condensate:

$$\xi = \frac{1}{k_\xi} = \frac{\hbar}{\sqrt{2\alpha nm}} \tag{2.20}$$

This is the so-called *healing length* of the condensate. Physically, it defines the scale of the density variation when the condensate is submitted to a sharp potential. For example, in a semi-infinite system with an infinite wall, the density of the condensate in the ground state will be constant everywhere except near the wall where it has to decrease to zero, the size of this region is given by ξ.

A part of the thesis has been dedicated to the study of such excitations and their associated topology for a spinor condensate loaded in honeycomb potential. The corresponding results are presented in Chapter 4.

2.1.4   Vortex excitations

An important characteristic of BECs and superfluids compared to classical fluid that we have not touched yet is their irrotationality. Indeed, starting from the general the form of order parameter:

$$\psi(\mathbf{r}) = \sqrt{n(\mathbf{r})}e^{i\theta(\mathbf{r})} \tag{2.21}$$

the use of the probability current formula,

$$\mathbf{j} = n(\mathbf{r})\mathbf{v} = \frac{\hbar}{2mi}\left(\psi^*\nabla\psi - \psi\nabla\psi^*\right) \tag{2.22}$$

leads to a superfluid velocity proportional to the phase gradient:

$$\mathbf{v} = \frac{\hbar}{m}\nabla\theta \qquad (2.23)$$

Therefore, the existence of ψ imposes the irrotationality of this bosonic quantum fluid: $\nabla \times \mathbf{v} = 0$ everywhere except at zero density points which can be related to phase singularities. The single-valueness of ψ imposes a quantized circulation in unit of h/m:

$$\oint \mathbf{v}.d\mathbf{l} = \frac{h}{m}p \qquad (2.24)$$

where $p \in \mathbb{Z}$. This quantization rule of the circulation in superfluids was originally introduced by Onsager [141] and Feynman [142] in the context of liquid helium. If $p \neq 0$, there is necessary a phase singularity inside the contour corresponding to a zero density point. These excitations are called *quantized vortices*. These are topological excitations [143] whose topological charge is given by p encoding the number of times the phase winds around the core. This charge cannot change without removing completely the singularity from the system. Due to this topological nature, vortices are really robust against disorder or density fluctuations in the system.

In the cylindrically symmetric case the stationary vortex solution can be written in polar coordinates (r, ϕ) in the form:

$$\psi_v(r, \phi) = f_p(r)e^{ip\phi} \qquad (2.25)$$

and the corresponding velocity is:

$$\mathbf{v} = \frac{\hbar p}{mr} \qquad (2.26)$$

One can see that contrary to radial velocity of rotating rigid bodies, this velocity increases when r decreases and diverges at the core of the vortex when $r \to 0$.

The radial profile $\psi_v(r, \phi)$ can be found by solving the stationary GPE numerically. In absence of external potential $V_{ext} = 0$, inserting (2.25) into the stationary GPE (2.13) allows to find the asymptotic behaviour [144, 137]:

$$f_p(r) \propto \begin{cases} r^{|p|}, & \text{when} \quad r \to 0 \\ \sqrt{n_\infty}, & \text{when} \quad r \to \infty \end{cases} \qquad (2.27)$$

where n_∞ is the unperturbed density at infinity. For $p = 1$, a good approximation of $f_1(r)$ can be written as [145]:

$$f_1(r) = \sqrt{n_\infty}\frac{r/\xi}{\sqrt{(r/\xi)^2 + 2}} \qquad (2.28)$$

On can see that the size of the core is determined by the healing length $\xi = \hbar/\sqrt{2\alpha m n_\infty}$. The radial density profile $|\psi_v|^2$ obtained using this formula is shown in panel (a) of figure 2.4 and the corresponding phase pattern is plotted in panel (b).
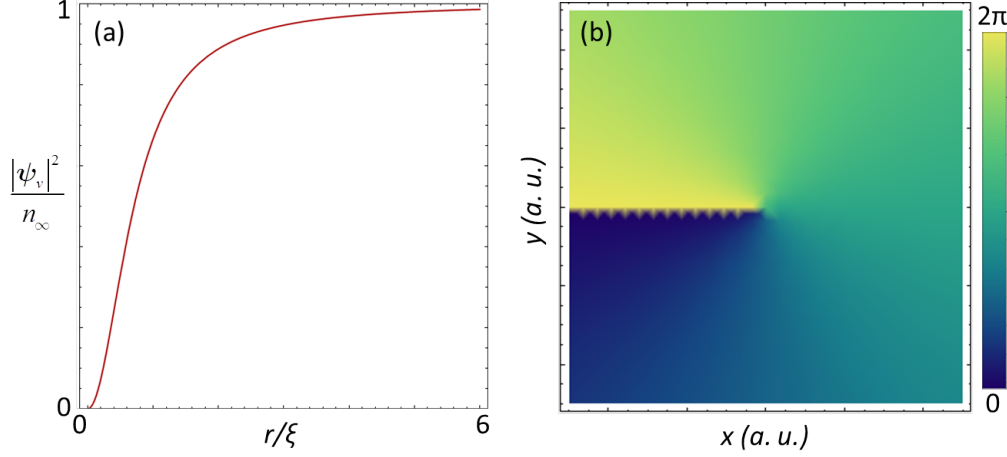
Figure 2.4: **Vortex.** (a) Density profile computed using (2.28). (b) Phase pattern of the wavefunction (2.25) with $p = 1$. The singularity is located at the origin where the density vanishes.

The energy associated with one vortex can be estimated by subtracting the energy functional integral associated with the homogeneous solution of constant density n_∞ to the one with one vortex which yields:

$$E_v = \int \left(\frac{\hbar^2}{2m} |\nabla \psi_v|^2 + \frac{\alpha}{2} \left(|\psi_v|^2 - n_\infty \right)^2 \right) \mathbf{dR} \tag{2.29}$$

One can separate this integral into two regions, the core of size ξ and the region far from the core where the density profile tends to be constant $|\psi_v|^2 \approx n_\infty$. For a large system, the second part dominates and the main contribution to E_v comes from the kinetic energy [144, 140]:

$$E_v^{r>\xi} = p^2 \pi n_\infty \hbar^2 \ln \left(C_p R_0 / \xi \right) / m \tag{2.30}$$

where R_0 is the radial system size and C_p is a numerical constant which depends on the winding ($C_1 \approx 1.56$). Obviously, the quantized vortex with $p = 1$ is the lowest vortex state. In this large system limit, the quadratic dependence of this energy on p means that high energy vortex states ($p = 2, 3, ...$) are less stable than several $(2, 3, ...)$ vortices with $p = 1$. Hence, in general, high order vortices will relax to several vortices of $p = 1$ to minimise their energy.

The existence of quantized vortices is the hallmark of the fact that all the particles share the same wavefunction. In section 4.3, we present a study of vortex excitations when a condensate is loaded in a staggered honeycomb lattice. We show that this can lead to an analog of quantum spin Hall effect for vortices whose robustness against disorder is due to the topological nature of vortices.

2.2 Cavity polaritons

Exciton-polaritons are quasiparticles that appear in solids in the strong coupling regime between light and matter. The bulk excitations have been introduced by Hopfield [146] and Agranovich [147] independently in the 50's. The coupling strength depends on the overlap between electric field and exciton wavefunction which can be improved and controlled by engineering confinement. The first observation of strong coupling in a 2D microcavity [148] has been followed by numerous works based on this geometry nowadays referred to cavity polaritons [149].

Even if the thesis is not strictly dedicated to cavity polariton Physics, it took place in a team specialized on this topic. Hence, when thinking about experiments this system arises naturally and several results presented in the following chapters are related with the specific properties of these quasiparticles. The goal of this section is to introduce some useful properties for the thesis self-consistency and not to formally present this growing field. Several good review papers and textbooks can be consulted for complete overview of the field [149, 150, 151, 152, 153].

2.2.1 Linear regime

2.2.1.1 Exciton-photon coupling

A typical microcavity design is shown on the scheme Fig. 2.5(a). It is constituted of Fabry-Perot cavity made of two Bragg mirrors allowing the confinement of the light. Generally, excitons are themselves confined in 2D quantum wells embedded in the cavity. A simple and efficient way to describe the coupling between an excitonic resonance and a photonic cavity mode is to use the two coupled oscillator model whose Hamiltonian reads:

$$\hat{H} = \sum_{\mathbf{k}} E_X(\mathbf{k}) b_{\mathbf{k}}^{\dagger} b_{\mathbf{k}} + \sum_{\mathbf{k}} E_C(\mathbf{k}) a_{\mathbf{k}}^{\dagger} a_{\mathbf{k}} + \hbar\Omega_R \sum_{\mathbf{k}} (b_{\mathbf{k}}^{\dagger} a_{\mathbf{k}} + a_{\mathbf{k}}^{\dagger} b_{\mathbf{k}}) \qquad (2.31)$$

where $a_{\mathbf{k}}^{\dagger}, a_{\mathbf{k}}, b_{\mathbf{k}}^{\dagger}, b_{\mathbf{k}}$ are bosonic creation and annihilation operators for photons and excitons respectively acting at a given in-plane momentum $\mathbf{k} = (k_x, k_y)^T$. Ω_R is the Rabi frequency which encodes the strength of the exciton-photon coupling. The in-plane exciton dispersion relation is:

$$E_X(k) = E_X(0) + \frac{\hbar^2 k^2}{2m_X}, \qquad (2.32)$$

with $k = \sqrt{k_x^2 + k_y^2}$ and the cavity mode dispersion reads:

$$E_C(k) = \sqrt{E_C(0)^2 + \frac{\hbar^2 c^2 k^2}{n_C^2}} \qquad (2.33)$$

with n_C the refractive index inside the cavity. $E_C(0) = \hbar c k_z / n_C$. Assuming perfect mirrors implies the quantization of $k_z = m\pi/n_C L$ ($m \in \mathbb{N}$). At small wavevectors,
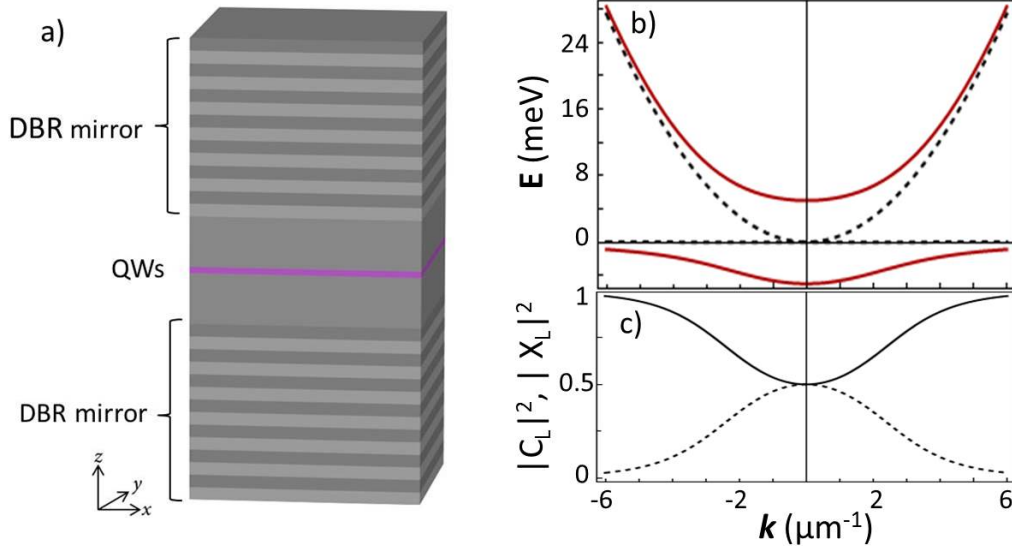
Figure 2.5: **Cavity polaritons.** (a) Scheme of a typical semiconductor plannar microcavity. The Fabry-Perot cavity is consituted by two parrallel distributed Bragg reflectors (DBR). Quantum wells (QWs) embedded in the cavity allow the 2D confinement of excitons. (b) Example of polariton dispersion (red lines), uncoupled exciton and cavity mode (black dashed lines). (c) Corresponding photonic (excitonic) fractions of the lower polariton branch $|C_L|^2, (|X_L|^2)$. ($\hbar\Omega_R = 5$meV, $\delta = 0$meV, $m_X = 0.4m_0$, $m_C = 5.10^{-5}m_0$).

this gives a parabolic dispersion for photons:

$$E_C(k) \approx E_C(0) + \frac{\hbar^2 k^2}{2m_C}, \quad \text{with} \quad m_C = \frac{\hbar\pi n_C}{cL} \tag{2.34}$$

As we can see, the dimension reduction due to the quantification in the z direction implies that cavity photons behave like 2D massive particles. As a consequence, they now have a ground state, a crucial property to achieve quasi-equilibrium Bose-Einstein condensation. The new eigen-energies are achieved by diagonalizing the matrix:

$$M = \begin{pmatrix} E_X & \hbar\Omega_R \\ \hbar\Omega_R & E_C \end{pmatrix} \tag{2.35}$$

which gives two hybrid dispersion branches:

$$E_{U/L} = \frac{1}{2}\left(E_X + E_C \pm \sqrt{(E_C - E_X)^2 + 4\hbar^2\Omega_R^2}\right) \tag{2.36}$$

These are the upper and lower *exciton-polariton* modes. The corresponding normalized eigenvectors give the excitonic $X_{L,U}$ and photonic $C_{L,U}$ fractions of the two

branches. One can introduce new polariton ladder operators as a combination of exciton ans photon operators:

$$p_{L\mathbf{k}} = X_L(\mathbf{k})b_\mathbf{k} + C_L(\mathbf{k})a_\mathbf{k} \tag{2.37}$$

$$p_{U\mathbf{k}} = X_U(\mathbf{k})b_\mathbf{k} + C_U(\mathbf{k})a_\mathbf{k} \tag{2.38}$$

which allow to re-write the Hamiltonian (2.31) in the diagonal form:

$$\hat{H} = \sum_\mathbf{k} E_L(\mathbf{k})p_{L\mathbf{k}}^\dagger p_{L\mathbf{k}} + \sum_\mathbf{k} E_U(\mathbf{k})p_{U,\mathbf{k}}^\dagger p_{U,\mathbf{k}} \tag{2.39}$$

The exciton-polariton appears therefore as a new mixed light-matter quasi-particle. An example of the dispersions is shown in figure 2.5 (b), together with the excitonic and photonic fractions (panel (c)) at zero detuning: $E_C(0) - E_X(0) = \delta = 0$. The shape of the dispersion as well as the excitonic/photonic fractions are detuning dependent. The detuning is experimentally controlled by varying the width of the cavity. The experimental observation of such anti-crossed branches, meaning that the coupling strength $\hbar\Omega_R$ is larger than the linewidths induced by the losses, is typically considered as a signature of the strong light-matter coupling regime.

In what follows, we are interested by the lower polariton branch which is parabolic at small wavevectors mimicking the massive particle one with a mass between m_C and m_X (the exact ratio being detuning-dependent). From the modelization side, this means that we can use a Schrödinger equation to study linear polariton dynamics in the cavity plane.

2.2.1.2 TE-TM splitting: a photonic spin-orbit coupling

In the above picture we have neglected a fundamental property of light, the polarization. At non-zero in-plane wavevector, TE and TM photonic modes can be defined. Importantly, the resulting polariton modes are splitted in energy by the so-called TE-TM splitting which has different origins:

- The 2D confined bare exciton exhibits a $\mathbf{k}$-dependent *longitudinal-transverse* (L-T) splitting due to long-range electron-hole exchange mechanism [154, 155]. This splitting becomes high at large wavevector outside the light-cone.

- In the radiative region, the quantum well exciton-photon coupling strength with TE and TM photonic modes depends on the incidence angle and therefore on the in-plane wavevector. This results in an energy splitting of the corresponding polariton modes. This effect is actually linked with exciton L-T energy splitting which becomes imaginary inside the light-cone [155].

- On the pure photon side, in a cavity based on dielectric mirrors, the difference of reflection coefficients for TE and TM polarizations leads to a different field penetration in the mirrors [156]. Qualitatively, at low wavevectors, one can define polarization dependent effective masses from the different effective cavity widths seen by the two polarizations $m_C^{TE/TM}(L^{TE/TM})$ (see (2.34)).

Considering the lower part of the lower polariton branch in the parabolic approximation, the combined effect of these splittings can be modelized by different effective mass for TE and TM polariton modes. This allows to write the following effective Hamiltonian in the linear polarization basis $(\psi^{TE}, \psi^{TM})^T$

$$H_{lin} = \begin{pmatrix} \frac{\hbar^2 k^2}{2m^{TE}} & 0 \\ 0 & \frac{\hbar^2 k^2}{2m^{TM}} \end{pmatrix} \tag{2.40}$$

One can rewrite this Hamiltonian in the circular polarization basis $(\psi^+, \psi^-)^T$ (which also corresponds to the bright exciton spin projections $S_z^X = \pm 1$) using:

$$\begin{pmatrix} \psi^{TE} \\ \psi^{TM} \end{pmatrix} = \frac{1}{\sqrt{2}} \begin{pmatrix} e^{i\phi} & e^{-i\phi} \\ ie^{i\phi} & -ie^{-i\phi} \end{pmatrix} \begin{pmatrix} \psi^+ \\ \psi^- \end{pmatrix} \tag{2.41}$$

which yields:

$$H_{circ} = \begin{pmatrix} \frac{\hbar^2 k^2}{2m^*} & \beta k^2 e^{-2i\phi} \\ \beta k^2 e^{2i\phi} & \frac{\hbar^2 k^2}{2m^*} \end{pmatrix} \tag{2.42}$$

where $\phi = \arctan(k_y/k_x)$ is the in-plane polar angle and we have introduced the effective mass m^* and the TE-TM coupling term β:

$$\frac{1}{m^*} = \frac{1}{2}\left(\frac{1}{m^{TE}} + \frac{1}{m^{TM}}\right), \quad \beta = \frac{\hbar^2}{4}\left(\frac{1}{m^{TE}} - \frac{1}{m^{TM}}\right) \tag{2.43}$$

The Hamiltonian (2.42) can be decomposed as $H_{circ} = h_0 + \mathbf{h}(\mathbf{k}).\hat{\boldsymbol{\sigma}}$ with the effective magnetic field given by: $\mathbf{h}_{LT} = \beta k^2 (\cos 2\phi, \sin 2\phi)^T = \beta(k_x^2 - k_y^2, 2k_x k_y)^T$. Therefore, the TE-TM splitting appears as an effective $\mathbf{k}$-dependent magnetic field acting on the polarization pseudospin which is nothing else than the definition of spin-orbit coupling (SOC). The analogy can be pushed further by comparing this Hamiltonian with the ones of Dresselhaus or Rashba SOC in 2D electronic systems [157, 158, 159]:

$$H_D = \frac{\hbar^2 k^2}{2m}\mathbb{I} + \alpha_D\left(k_x \sigma_x - k_y \sigma_y\right), \quad H_R = \frac{\hbar^2 k^2}{2m}\mathbb{I} + \alpha_R\left(-k_y \sigma_x + k_x \sigma_y\right) \tag{2.44}$$

The eigenenergies of the Hamiltonians (2.42) and (2.44) are plotted in figures 2.6 (a,b) respectively. Due to the k dependence of Rashba or Dresselhaus SOC, the corresponding dispersion exhibits a linear behaviour around $\mathbf{k} = \mathbf{0}$ and a minimum on a circle of radius $|\mathbf{k}| = k^*$ contrary to the TE-TM one which still has a local minimum at $\mathbf{k} = \mathbf{0}$. The corresponding in-plane field $\mathbf{h}(\mathbf{k})$ textures on an isoenergy circle are shown in Figs (2.6) (c, d, e). The crucial difference between photonic and electronic SOCs is the double winding of the former. Due to this winding, the effective field orientations at $\mathbf{k}$ and $-\mathbf{k}$ are the same whereas they are opposite for electronic SOCs. This fact is a reminiscence of the bosonic and fermionic nature of the underlying particles whose eigenstates behaves differently under time-reversal symmetry operation.

Therefore, taking into account the polarization degree of freedom can lead to non trivial polariton pseudospin dynamics. For example, it has led to the theoretical
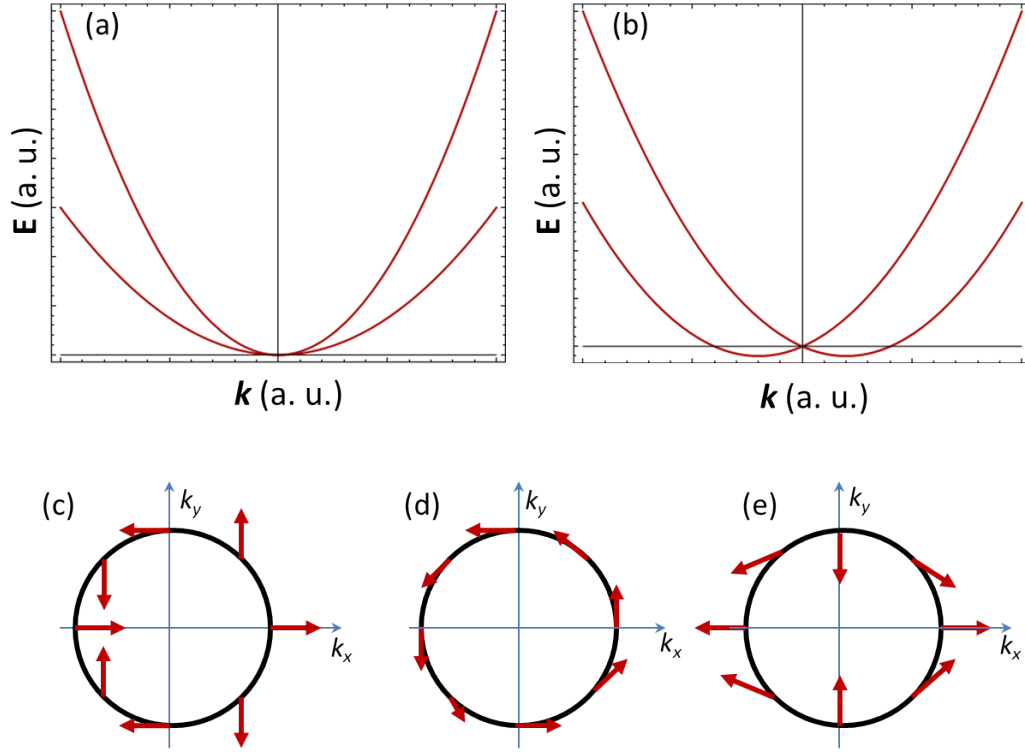
Figure 2.6: **2D spin-orbit couplings.** (a) Dispersion of cavity photons (polaritons), (b) Electronic dispersion with Rashba or Dresselhaus SOC. (c, d, e) Isoenergy effective in plane field textures: TE-TM (c), Rashba (d), Dresselhaus (f).

prediction [160] and experimental observation [161] of the optical spin Hall effect, a photonic analog of the extrinsic spin Hall effect in electronic systems predicted by Dyakonov and Perel in the 70's [162].

Remarks. Due to its different origins, TE-TM splitting exists for mixed exciton-polaritons as well as bare QW excitons or cavity photons. It is interesting to compare the photonic TE-TM splitting in a cavity geometry with the one in waveguides or photonic crystal slabs. Whereas their fundamental origin is the same: light reflection at non-zero incidence angle on any dielectric interface, the splitting between TE and TM modes for high in-plane wavevectors light in waveguides can be arbitrary big (See Fig. 1.7 for an example.) with respect to the one introduced above of cavity photons. The smallness of the latter allows to interpret it as a photonic SOC.

Even if it is always present, the strength of TE-TM splitting depends on specific design of experimental setups. It is sometimes weak compared to the linewidth, and can be neglected.

The advantage of the mixed cavity polaritons on bare photons is their response to an *external* magnetic field thanks to exciton Zeeman splitting ($\Delta\sigma_z$) [163, 164] achievable at optical frequency. Actually, the combination of TE-TM and Zeeman field in a honeycomb cavity lattice can lead to an optical wavelength counterpart of the Haldane-Raghu proposal of quantum anomalous Hall effect for light presented in the previous chapter. This model is discussed in section 3.1.

It is interesting to note that quadratic band crossings occur in other contexts. For example, it has been studied in lattice systems where it is also associated with a double winding of an effective field in the two-band approximation [165, 166]. In these cases, lifting the degeneracy leads to a band gap opening between the the bulk bands and can give rise to non-zero Chern numbers and their associated gap-less chiral states on the boundary of the system. However, this will not happen in the cavity system discussed here because the two parabola have the same curvature sign [Fig. 2.6.(a)] and no real gap can be opened. Another difference is that in lattice models the pseudospin relates on the lattice structure whereas the polarization pseudospin introduced here is an internal degree of freedom.

2.2.2 Non-linear regime

Due to their excitonic part, cavity polaritons interact with each other contrary to bare cavity photons at optical frequencies. Whereas for weak polariton densities these interactions can be neglected, it is not possible anymore when the density is increased. In the strong-coupling regime, signatures of polariton-polariton interactions have been first reported in quasi-resonant pumping experiments with the observation of optical parametric oscillations [167] and bistability [168, 169]. Moreover, when dealing with these composite bosons in the parabolic part of the LPB, these intrinsic non-linearities appear to be a good platform to study quantum fluid physics and many works have been done in this direction toward the observation of Bose-Einstein condensation, superfluid behaviour and quantized vortices

[170, 171, 172, 173].

From the experimental point of view, two main ways are used to create polaritons. The off-resonant excitation, which consist to create a large number of excitons at high energy which then relax to the lower polariton state at $\mathbf{k} = \mathbf{0}$ forming a quasi-equilibrium condensate or a polariton laser. The second approach is to directly inject a macroscopic number of polaritons by using a quasi-resonant optical excitation.

Both of them are widely used and different theoretical approaches have been developed to describe the different features which can be seen in the experiments. An approximation to describe a quasi-equilibrium condensate after its formation is to assume thermal equilibrium and an infinite polariton lifetime which allows to use a particle conserving Gross-Pitaevskii equation. While it is of course not exact due to the finite polariton lifetime (we have to remember that the same thing happens in realistic atomic condensate where atoms evaporate from their traps), it already allows to describe a variety of phenomena. The resonant pump configuration can be described by a driven dissipative GP equation.

2.2.2.1 Origin of interactions

At low wavevectors compared to the Bohr radius ($ka_B \ll 1$) co-polarized exciton-exciton (triplet configuration) interactions are dominated by exchange interaction [174, 175] which can be described by an effective boson interaction term at low density:

$$\hat{H}_{XX} = \frac{1}{2} \sum_{\mathbf{k},\mathbf{k'},\mathbf{q}} V_{\mathbf{q}}^{XX} b_{\mathbf{k+q}}^{\sigma\dagger} b_{\mathbf{k'-q}}^{\sigma\dagger} b_{\mathbf{k}}^{\sigma} b_{\mathbf{k'}}^{\sigma} \tag{2.45}$$

where the matrix element $V_{\mathbf{q}}$ can be approximated by a contact potential V_0 which can has been estimated $V_0 = 6 E_b a_B^2 / A$ with E_b the exciton binding energy, a_B the exciton Bohr radius, A the 2D area occupied by the excitons [175]. Whereas the exciton-photon basis can be useful to study polariton dynamics at large wavevectors, we will always restrict ourself to small wavectors near the bottom of the LPB. Hence, using $X_U = -C_L$, $C_U = X_L$, one can rewrite the above interaction Hamiltonian in the polariton basis. Neglecting the upper branch polaritons yields the effective polariton-polariton interactions [176]:

$$\hat{H}_{PP} = \frac{1}{2} \sum_{\mathbf{k},\mathbf{k'},\mathbf{q}} V_{0,\mathbf{k},\mathbf{k'}}^{PP} p_{L\mathbf{k+q}}^{\sigma\dagger} p_{L\mathbf{k'-q}}^{\sigma\dagger} p_{L\mathbf{k}}^{\sigma} p_{L\mathbf{k'}}^{\sigma} \tag{2.46}$$

with $V_{q,\mathbf{k},\mathbf{k'}}^{PP} = X_L(\mathbf{k+q}) X_L(\mathbf{k'-q}) X_L(\mathbf{k}) X_L(\mathbf{k'}) V_0 \approx X_L^4 V_0$. The last approximation is valid near $\mathbf{k} = \mathbf{0}$. As it could be intuitively understood, the excitonic fraction increases the interaction strength.

Interaction between excitons with opposite spin projections (singlet configuration) is a second order effect implying scattering to dark [177] or biexciton [178] intermediate states. In the strong coupling regime, when we deal with LPB polaritons, the scattering through these intermediate states is strongly reduced because due to the Rabi splitting the LPB energy is far from their respective resonances.

In the mean field description of the condensate, this leads to different interaction constants for triplet (α_1) and singlet configurations (α_2) [151]:

$$\alpha_1 = V_0^{pp} A \neq \alpha_2 \tag{2.47}$$

The exact α_2/α_1 ratio is strongly dependent on the detuning between the cavity mode and the excitonic resonance [179] and can lead to an analog of Feshbach resonance for positive detuning when the two interacting polaritons energy comes in resonance with the biexciton bound state energy [180, 181]. In the following, we will consider the conventional case where the interaction constants are strongly imbalanced $|\alpha_2| \ll \alpha_1$ [174, 182, 151].

2.2.2.2 Quasi-equilibrium spinor condensate

Dealing with the polarization degree of freedom introduced above implies to use a spinor order parameter $\boldsymbol{\Psi}$ to describe polariton condensates [151, 183]. Several basis choices are possible, here we choose the circular polarization basis which corresponds to the true spin projection basis $\boldsymbol{\Psi} = (\psi^+, \psi^-)^T$. In this basis, the kinetic term H_0 is achieved by re-writing (2.42) in term of real space operators $k_{x,y} \rightarrow -i\partial_{x,y}$ [184]:

$$H_0 = \begin{pmatrix} \frac{-\hbar^2}{2m}\nabla^2 & \beta(\partial_y + i\partial_y)^2 \\ \beta(\partial_y - i\partial_x)^2 & -\frac{\hbar^2}{2m}\nabla^2 \end{pmatrix} \tag{2.48}$$

The resulting coupled GPE equations describing the condensate at $T = 0$ read:

$$i\hbar\frac{\partial\psi^+}{\partial t} = -\frac{\hbar^2}{2m}\nabla^2\psi^+ + \beta(\partial_y + i\partial_x)^2\psi^- + \alpha_1|\psi^+|^2\psi^+ + \alpha_2|\psi^-|^2\psi^+ \tag{2.49}$$

$$i\hbar\frac{\partial\psi^-}{\partial t} = -\frac{\hbar^2}{2m}\nabla^2\psi^- + \beta(\partial_y - i\partial_x)^2\psi^+ + \alpha_1|\psi^-|^2\psi^- + \alpha_2|\psi^+|^2\psi^- \tag{2.50}$$

The above equations are similar to the ones used to study binary mixtures of condensates in cold atom systems [185, 186, 187] but with an additional linear coupling due to TE-TM SOC. α_1 and α_2 are the interaction constants between particles with the same and opposite spin projections. As discussed above, for exciton-polariton the interaction constants are strongly anisotropic:

$$\alpha_1 >> |\alpha_2| \tag{2.51}$$

which means that we are dealing with miscible condensates. These equations have been widely used to study topological excitations in polariton condensates such as half-vortices [188, 184] and half-solitons [189, 190] whose existence have been reported in different experiments [191, 192, 193].

When looking for stationary solutions we consider conservation of the total particle number (both spin states). Therefore stationary equation are found by introducing $\boldsymbol{\Psi}(\mathbf{r}, t) = (\psi^+, \psi^-)^T e^{-i\mu t}$ with a unique chemical potential μ.

$$\mu\psi^+ = -\frac{\hbar^2}{2m}\nabla^2\psi^+ + \beta(\partial_y + i\partial_x)^2\psi^- + \alpha_1|\psi^+|^2\psi^+ + \alpha_2|\psi^-|^2\psi^+$$

$$\mu\psi^- = -\frac{\hbar^2}{2m}\nabla^2\psi^- + \beta(\partial_y - i\partial_x)^2\psi^+ + \alpha_1|\psi^-|^2\psi^- + \alpha_2|\psi^+|^2\psi^- \tag{2.52}$$

It is interesting to have a look on the solution of the above system for a homogeneous condensate:

$$\mu = (\alpha_1 + \alpha_2)n/2, \quad \psi = \sqrt{\frac{n}{2}} \begin{pmatrix} 1 \\ 1 \end{pmatrix} \tag{2.53}$$

Hence, at $T = 0$ the ground state of the spinor condensate is linearly polarized.

2.2.2.3   The Spin-Meissner effect

It is certainly useful to remind the equilibrium behaviour of a 2D homogeneous polariton condensate in the presence of a magnetic field. As shown in ref. [194], at low magnetic field an equilibrium condensate in its ground state is elliptically polarized. It generates a self-induced Zeeman field which compensates the Zeeman splitting induced by the applied magnetic field. This is called the spin-Meissner effect, because of the analogy with the Meissner effect in superconductors, where an external magnetic field cannot penetrate into the superconducting region. This effect can be understood as follows. At $T = 0$, the condensate is in its ground state. Assuming that the particle number is conserved, the energy functional is given by the interaction energy:

$$E = \frac{1}{2} \int d\mathbf{r} \left[\alpha_1 |\psi^+|^4 + \alpha_1 |\psi^-|^4 + 2\alpha_2 |\psi^+|^2 |\psi^-|^2 - \mu n \right] \tag{2.54}$$

Introducing the density $n = |\psi^+|^2 + |\psi^-|^2$, and the circular polarization degree

$$\rho_c = \frac{|\psi^+|^2 - |\psi^-|^2}{|\psi^+|^2 + |\psi^-|^2} = \frac{s_z}{n}, \quad -1 \le \rho_c \le 1 \tag{2.55}$$

allows to rewrite the energy as:

$$E = \frac{1}{2} \int d\mathbf{r} \left[\frac{1}{2}(\alpha_1 + \alpha_2)n^2 + \frac{1}{2}(\alpha_1 - \alpha_2)\rho_c^2 n^2 - \mu n \right] \tag{2.56}$$

If an external magnetic field is applied in the direction orthogonal to the cavity plane a Zeeman energy contribution $-\Delta s_z = -\Delta \rho_c n$ to the energy should be added:

$$E = \frac{1}{2} \int d\mathbf{r} \left[\frac{1}{2}(\alpha_1 + \alpha_2)n^2 + \frac{1}{2}(\alpha_1 - \alpha_2)\rho_c^2 n^2 - 2\Delta \rho_c n - \mu n \right] \tag{2.57}$$

where $\Delta = g_X |X|^2 \mu_B B_z / 2$ with g_X the exciton Landé g-factor, μ_B the Bohr magneton, X the excitonic fraction and B_z the amplitude of the applied magnetic field. The stationary solutions of the functional $E = \int d\mathbf{r} I(n, \rho_c)$ are given by the following Euler-Lagrange equations:

$$\frac{\partial I}{\partial \rho_c} = 0 \iff \rho_c(\alpha_1 - \alpha_2)n^2 - 2\Delta n = 0 \tag{2.58}$$

$$\frac{\partial I}{\partial n} = 0 \iff (\alpha_1 + \alpha_2)n + (\alpha_1 - \alpha_2)\rho_c n - \Delta \rho_c - \mu = 0 \tag{2.59}$$

Therefore, we can then distinguish three different regimes:

1. If there is no external field, $\Delta = 0$, (2.58) gives $\rho_c = 0$, the condensate is completely *linearly* polarized and the chemical potential is $\mu = (\alpha_1 + \alpha_2)n/2$. (this development is equivalent to the previous one where we start from GP equation).

2. If a weak field is applied, (2.58) gives $\rho_c = 2\Delta/(\alpha_1 - \alpha_2)n$, the condensate is *elliptically polarized*. The chemical potential given by (2.59) is still $\mu = (\alpha_1 + \alpha_2)n/2$. Whereas the polarization of the condensate has changed, its ground state energy does not.

3. At the critical field $\Delta_C = (\alpha_1 - \alpha_2)n/2$, $\rho_c = 1$, the condensate becomes *circularly polarized*. Above this critical field, replacing $\rho_c = 1$ in (2.59) allows to find the new chemical potential $\mu = \alpha_1 n - \Delta$ which is now linearly dependent on the external Zeeman field.

This peculiar response to an external magnetic field is directly linked with the spin anisotropic character of polariton-polariton interactions. If $\alpha_1 = \alpha_2$ the intermediate region where the external Zeeman field is compensated by the one induced by the interactions is not present. The presence of these three regimes corresponding to different condensate polarizations has to be kept in mind for the study of thermal equilibrium Bogoliubov excitations when an external field is applied [194]. Such study of elementary excitations in polariton graphene will be presented in section 4.1.

2.2.2.4   Quasi-resonant injection

A second important way to create polaritons is the quasi-resonant injection. Using this technique, one can directly create macroscopically occupied and coherent states at any energy, momentum, density and with the pseudospin state controlled by the polarization of the pump. In the mean-field approximation, quasi-resonant excitation can be described by a driven dissipative Gross-Pitaevskii equation which in the spinless case reads:

$$i\hbar\frac{\partial\psi}{\partial t} = \left[-\frac{\hbar^2}{2m}\nabla^2 - i\frac{\hbar}{2\tau} + \alpha_1|\psi|^2\right]\psi + P \tag{2.60}$$

where $P = F_p e^{i(\mathbf{k}_p.\mathbf{r}-\omega_p t)}$ represents the external pump drive with $F_p(\mathbf{r},t)$ the pump profile, and $i\hbar/2\tau$ encodes the losses due to the finite polariton lifetime τ. The energy and wavevector of the created macroocupied state are given by the pump term $\mathbf{k}_p$ and ω_p. Contrary to the Gross-Pitaevskii equation the above equation describes a system out of thermal equilibrium and there is no well-defined chemical potential μ. The spectrum of elementary excitations on top of a homogeneous condensate can be found in a similar manner by injecting in Eq. (2.60) the ansatz:

$$\psi(\mathbf{r},t) = e^{i(\mathbf{k}_p.\mathbf{r}-\omega_p t)}\left(\psi_s + ue^{i(\mathbf{k}.\mathbf{r}-\omega t)} + v^* e^{-i(\mathbf{k}.\mathbf{r}-\omega^* t)}\right) \tag{2.61}$$
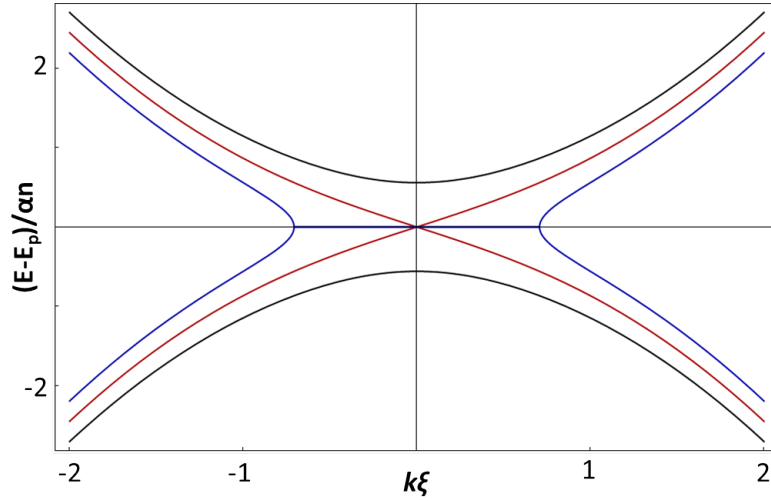
Figure 2.7: **Elementary excitations of a driven mode for $\mathbf{k}_p = 0$.** Red lines $\delta = 0$, blue lines $\delta = 0.5\alpha n$ ($\hbar\omega_p = 1.5\alpha n$), Black lines $\delta = -0.5\alpha n$ ($\hbar\omega_p = 0.5\alpha n$).

where ψ_s is the stationary part of the wavefunction which is given by:

$$\left[\frac{\hbar^2 \mathbf{k}_p^2}{2m} - i\frac{\hbar}{2\tau} - \hbar\omega_p + \alpha_1|\psi_s|^2 \right] \psi_s + F_p = 0 \tag{2.62}$$

The form of the above nonlinear stationary equation equation leads to a possible bistable behaviour of the stationary solution [168, 195]. (In some parameter range, two stationary solutions corresponding to two different populations are available for a given pump term F_p.) The excitation dispersions are found after the same linearization procedure than in 2.1.3 and gives for a homogeneous vertical pump ($\mathbf{k}_p = \mathbf{0}$):

$$\hbar\omega_{1,2} = \hbar\omega_p - i\frac{\hbar}{\tau} \pm \sqrt{(E(\mathbf{k}) - \hbar\omega_p)^2 + \alpha|\psi_s|^2 \left[4(E(\mathbf{k}) - \hbar\omega_p) + 3\alpha|\psi_s|^2\right]} \tag{2.63}$$

with $E(\mathbf{k}) = \frac{\hbar^2 k^2}{2m}$, $|\psi_s|^2 = n$. Some example of spectra are represented on figure 2.7 for different pump energies. Different configurations are achievable depending on the detuning between the pump mode and the renormalized LPB branch: $\delta = \hbar\omega_p - (E(0) + \alpha|\psi_s|^2)$. When $\delta > 0$ the dispersion exhibits a flat part near $\mathbf{k} = \mathbf{0}$ associated with non-zero imaginary part of the square root which can lead to instabilities if the imaginary part of the dispersions becomes positive. If $\delta < 0$ a gap is opened between the two Bogoliubov branches (black lines). When $\delta = 0$, that is, when the detuning compensates exactly the interaction energy αn one recovers the linear Bogoliubov dispersion as in the thermal equilibrium case (see Fig. 2.3). The above approach with a non-zero $\mathbf{k}_p$ has been used in ref. [171] to theoretically study polariton superfluidity in terms of the Landau criterion.
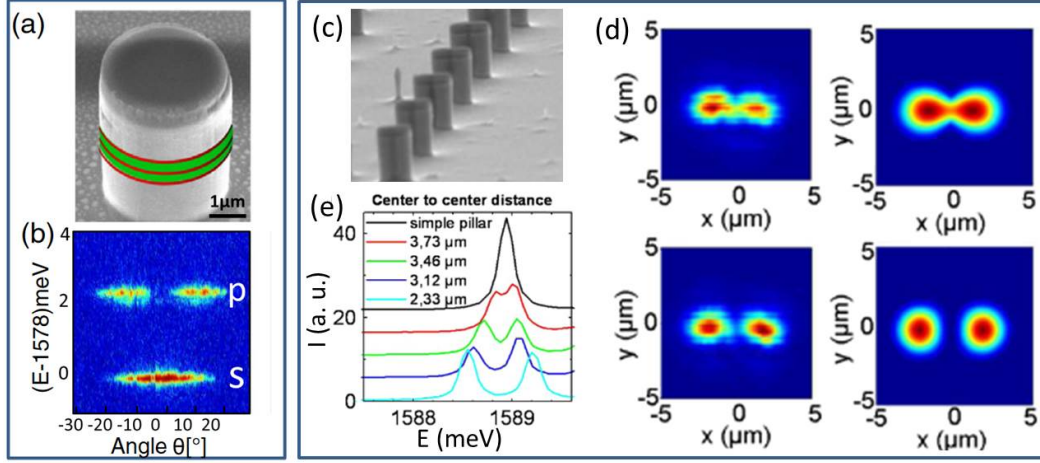
Figure 2.8: **Micropillars and polariton molecules.** (a) Single micropillar scanning electron microscope image, red lines sketch the quantum well positions in the cavity (green). (b) Corresponding angle-resolved photoluminescence spectrum showing the ground state (s) and the first excited (p) 0D confined modes. (c) SEM images of polariton molecules. (c) Photoluminescence spectra showing the hybridisation of s-states as a function of the distance between the centers of the two micropillars. (d) Measured (calculated) emission pattern for the bonding anti-bonding s modes. (panels (a,b) adapted from ref. [198] and (c,d,e) from ref. [199])

The driven-dissipative GP equation can be generalized to the spinor case which yields:

$$i\hbar\frac{\partial\psi^+}{\partial t} = \left[-\frac{\hbar^2}{2m}\nabla^2 - \frac{i\hbar}{2\tau^+} + \alpha_1|\psi^+|^2 + \alpha_2|\psi^-|^2\right]\psi^+ + \beta(\partial_x - i\partial_y)^2\psi^- + P^+ \quad (2.64)$$

$$i\hbar\frac{\partial\psi^-}{\partial t} = \left[-\frac{\hbar^2}{2m}\nabla^2 - \frac{i\hbar}{2\tau^-} + \alpha_1|\psi^-|^2 + \alpha_2|\psi^+|^2\right]\psi^- + \beta(\partial_x + i\partial_y)^2\psi^+ + P^- \quad (2.65)$$

where in general $\tau^+ = \tau^- = \tau$ and the pump polarization is controlled experimentally $(P^+, P^-)^T$. The inclusion of polarization degree of freedom implies a more complex but also interesting behaviour. For example, it has led to the prediction of polarization multistability of the stationary solutions [196]. A detailed theoretical study of stability of the driven mode as well as of the elementary excitation spectra neglecting TE-TM splitting ($\beta = 0$) for different pump polarization configurations can be found in ref. [197].

2.2.3   Potential engineering

With the development of nanotechnology and crystal growth techniques, the control of semiconductor microcavity environment has increased significantly the last
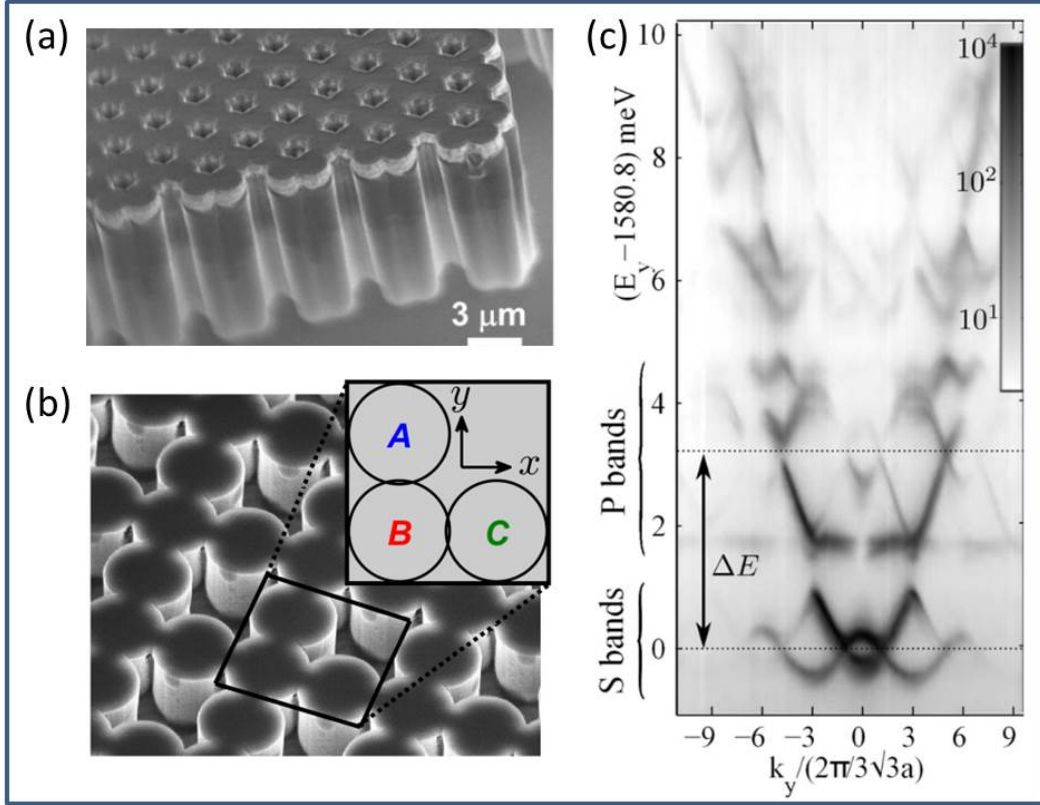
Figure 2.9: **Cavity lattices.** (a)-(b) SEM images of a honeycomb and Lieb cavity lattices respectively. (c) Energy resolved photoluminescence spectrum in the honeycomb lattice. s-bands and p-bands emerging from coupling between single pillar ground state and first excited state are highlighted. (a)-(c) adapted from ref. [200], (b) from ref. [201]

decades. Nowadays, different techniques are commonly used in experiments to create potential landscapes for polaritons such as metal deposition on the top of the sample, microcavity etching, application of surface acoustic waves, and optically induced traps thanks to the excitonic reservoirs [202].

The deep etching technique is particularly interesting because it allows to achieve a very high confinement of light and/or polaritons in arbitrary shape potential (at least in GaAs samples where this approach is well controlled). For example, one can achieve a 0D confinement in a micropillar structure with discrete photonic states as shown in figure 2.8(a,b). Then, several micropillars can be coupled to build photonic molecules, the coupling strength being controlled by the distance between pillar centers [Fig. 2.8(c,d,e)]. This process can be generalized toward lattice engineering as shown in figure 2.9. An interesting aspect of using lattices of coupled photonic micropillars is that the tight-binding description is a very good approxi-

mation [200, 203, 198, 201]. This is well understandable by comparing the energy scales of figures 2.8(b) and 2.9(c) demonstrating the s and p-bands emergence due to the hybridisation of the corresponding quantized states in a single pillar.

In fact, this ability of experimentalists to build high quality artificial lattices (also well developed in cold atom systems [204]) is one of the main motivations of the work presented in this thesis.

Single particle topological effects in honeycomb lattices

Contents

3.1   Photonic versus electronic quantum anomalous Hall effect

As we have seen in the first chapter, the discovery of the quantum Hall effect [30] and its explanation in terms of topology [29, 32] have refreshed the interest to the band theory in condensed matter physics leading to the definition of a new class of insulators [4, 5]. They include quantum anomalous Hall (QAH) phase with broken time reversal (TR) symmetry [43, 67, 68] and quantum spin Hall topological insulators with conserved TR symmetry [44, 80, 81]. The QSH effect was initially predicted to occur in honeycomb lattices because of the intrinsic Spin-Orbit Coupling (SOC) of the atoms forming the lattice, whereas the extrinsic Rashba SOC is detrimental for QSH [44, 77, 78].

On the other hand, the classical anomalous Hall effect is now known to arise from a combination of extrinsic Rashba SOC and of an effective Zeeman field [205]. In a 2D lattice with Dirac cones it leads to the formation of a QAH phase [68, 206], for which the intrinsic SOC is detrimental [207, 208, 209]. In the large Rashba SOC limit, this description was found to converge towards an extended 1988 Haldane model [207].

In photonics, a Rashba-type SOC cannot be implemented for symmetry reasons, but another effective in-plane SOC is induced by the energy splitting between the TE and TM modes. In planar cavities, the related effective magnetic field has a winding number 2 (instead of 1 for Rashba [See Sec. 2.2.1.2]). It is at the origin of a very large variety of spin-related effects, such as the optical spin Hall effect [160, 161], Berry phase for photons [210], and the generation of topologically protected spin currents in polaritonic molecules [211]. The combination of a TE-TM SOC and a Zeeman field in a honeycomb lattice has indeed been found to yield a QAH phase [212, 213, 214, 215, 216, 217], and the corresponding model is related to the seminal Haldane-Raghu proposal [83] of photonic Chern insulator [See also Sec. 1.4.1], which it recovers in the limit of large TE-TM SOC.

In this section, we discuss two models toward the quantum anomalous Hall effect in honeycomb lattices based on the combination of Zeeman splitting and spin-orbit coupling. This recipe has been used independently to predict the occurrence of QAHE in electronic graphene [68] and in its photonic analog [212]. We show the role played by the winding number of the SOC on the QAH phases. We establish the complete phase diagram for both the photonic and electronic graphene. In addition to opposite C_n in the low-field limit, we find the photonic case to be more complex, showing a topological phase transition absent in the electronic system.

3.1.1   Models

First, let us write the spinfull tight-binding Hamiltonian for these models. Typically, it can be decomposed in three parts:

$$\hat{H} = \hat{H}_0 + \hat{H}_{Zeeman} + \hat{H}_{SOC} \tag{3.1}$$

where $\hat{H}_0$ is the nearest-neighbour honeycomb T-B Hamiltonian, $\hat{H}_{Zeeman}$ encodes the on-site Zeeman field, and $\hat{H}_{SOC}$ stands for the spin-orbit coupling which can be written respectively:

$$\hat{H}_0 = -J \sum_{i,j,\sigma} \left(a_{\mathbf{R}_i}^{\sigma\dagger} b_{\mathbf{R}_i+\mathbf{d}_j}^{\sigma} + b_{\mathbf{R}_i+\mathbf{d}_j}^{\sigma\dagger} a_{\mathbf{R}_i}^{\sigma} \right) \tag{3.2}$$

$$\hat{H}_{Zeeman} = \sum_{i,\sigma} \sigma\Delta \left(a_{\mathbf{R}_i}^{\sigma\dagger} a_{\mathbf{R}_i}^{\sigma} + b_{\mathbf{R}_i+\mathbf{d}_j}^{\sigma,\dagger} b_{\mathbf{R}_i+\mathbf{d}_j}^{\sigma} \right) \tag{3.3}$$

with J is the tunnelling coefficient between nearest neighbour micropillars (atoms) and Δ is the Zeeman splitting. $\sigma = \pm$ is the spin index. The SOC part can be written:

$$\hat{H}_{Rashba} = -\lambda_e \sum_{i,j} \left(e^{i\phi_j} a_{\mathbf{R}_i}^{+\dagger} b_{\mathbf{R}_i+\mathbf{d}_j}^{-} - e^{-i\phi_j} a_{\mathbf{R}_i}^{-\dagger} b_{\mathbf{R}_i+\mathbf{d}_j}^{+} \right.$$
$$\left. -e^{-i\phi_j} b_{\mathbf{R}_i+\mathbf{d}_j}^{+\dagger} a_{\mathbf{R}_i}^{-} + e^{-i\phi_j} b_{\mathbf{R}_i+\mathbf{d}_j}^{-\dagger} a_{\mathbf{R}_i}^{+} \right) \tag{3.4}$$

$$\hat{H}_{TE-TM} = -\lambda_p \sum_{i,j} \left(e^{i2\phi_j} a_{\mathbf{R}_i}^{+\dagger} b_{\mathbf{R}_i+\mathbf{d}_j}^{-} + e^{-i2\phi_j} a_{\mathbf{R}_i}^{-\dagger} b_{\mathbf{R}_i+\mathbf{d}_j}^{+} \right.$$
$$\left. +e^{-i2\phi_j} b_{\mathbf{R}_i+\mathbf{d}_j}^{+\dagger} a_{\mathbf{R}_i}^{-} + e^{i2\phi_j} b_{\mathbf{R}_i+\mathbf{d}_j}^{-\dagger} a_{\mathbf{R}_i}^{+} \right) \tag{3.5}$$

where $\mathbf{d}_j$ are the links between nearest-neighbours and $\phi_j = 2\pi(j-1)/3$ their angle with respect to the horizontal axis ($1 \le j \le 3$, as defined in Fig. 1.2). λ_e and λ_p are the magnitudes for the Rashba (electronic) and TE-TM (photonic) induced SOC respectively. Note that λ_p is defined by the difference of tunnelling between longitudinal and traverse polarized photons $\lambda_p = (J_L - J_T)/2 = \delta J$ (both notations λ_p and δJ will be used in the following sections).

This representation (equivalent to formula (1.90) up to a sign for Rashba SOC) allows to directly see that non-zero SOC implies some complex tunnelling, similarly to what happens with an external magnetic field in Harper-like models or in the 1988 Haldane model. Here, the SOC acts as an effective in-plane magnetic field on the spin degree of freedom and an additional on-site Zeeman term is required to open a bandgap.

The resulting momentum space Hamiltonian for electronic [218] and photonic SOC [219] is a 4 by 4 matrix written on the basis $(\Psi_A^+, \Psi_A^-, \Psi_B^+, \Psi_B^-)$, where A and B labels stand for the lattice atom type and $\pm$ for the particle spin:

$$H_{\mathbf{k},i} = \begin{pmatrix} \Delta\sigma_z & F_{\mathbf{k},i} \\ F_{\mathbf{k},i}^{\dagger} & \Delta\sigma_z \end{pmatrix}, \quad F_{\mathbf{k},i} = -\begin{pmatrix} f_k J & f_{k,i}^+ \lambda_i \\ f_{k,i}^- \lambda_i & f_k J \end{pmatrix} \tag{3.6}$$

The complex coefficients f_k and $f_{k,i}^{\pm}$ are defined by:

$$f_k = \sum_{j=1}^{3} e^{(-i\mathbf{k}\mathbf{d}_j)}, \; f_{k,e}^{\pm} = \pm \sum_{j=1}^{3} e^{(-i[\mathbf{k}\mathbf{d}_j \mp \phi_j])} \tag{3.7}$$

$$f_{k,p}^{\pm} = \sum_{j=1}^{3} e^{(-i[\mathbf{k}\mathbf{d}_j \mp 2\phi_j])}$$
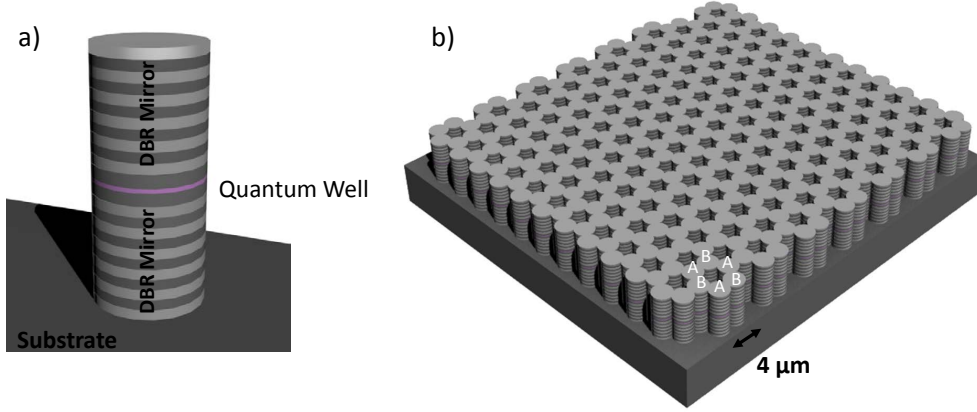
Figure 3.1: (a) Polaritonic micropillar scheme, (b) polaritonic graphene scheme.

Qualitatively, the crucial different ϕ dependences of the tunneling $f_{k,i}^{\pm}$ are due to the different winding numbers of the Rashba and TE-TM effective fields in the bare 2D systems [see eg. Fig. 2.6].

3.1.2   Phase diagram of the photonic and electronic QAH

Without Zeeman field ($\Delta = 0$), the diagonalization of these two Hamiltonians gives four branches of dispersion. Near K and K' points, two branches split, and two others intersect, giving rise to a so-called trigonal warping effect, namely the appearance of three extra Dirac crossing points [see Fig. 3.3(c,d) and Fig. 3.5(a)]. A 3D zoom of the energy fine structure near the K point is presented in figure 3.2. This effect known to occur in monolayer graphene due to the presence of Rashba [220] or TE-TM [219] SOCs is similar to what happens in spinless Bernal stacked bilayer graphene [221, 222, 223] and its trigonal shape is due to the conserved three-fold rotational symmetry of the honeycomb lattice. (The denomination of "trigonal warping" is also used in spinless graphene to designate the triangular shape of the dispersion when getting away from K point. Along this thesis this denomination will always refer to the occurrence of 3 additional Dirac cones.)

The differences between the two Hamitonians in the whole Brillouin zone are clearly visible on the figures 3.3(a-d) which show a 2D view of the 2nd branch spin polarizations (a,b) and energies (c,d). On the panels (a,b), we see the difference of the in-plane winding number around Γ ($w_{\Gamma,e} = 1$ for Rashba and $w_{\Gamma,p} = 2$ for TE-TM SOC). Around K points, the TE-TM SOC texture becomes Dresselhaus-like with a winding $w_{K,p} = -1$ whereas Rashba remains Rashba with $w_{K,e} = 1$. In both cases the winding numbers around the K and K' points have the same sign which implies that the associated Berry curvatures in the two valley will add to each others and give non-zero Chern numbers in both models when TR will be broken. On the panels (c,d), one can clearly observe the formation of small triangles near the Dirac points, the vertices of these triangles corresponding to the crossing points
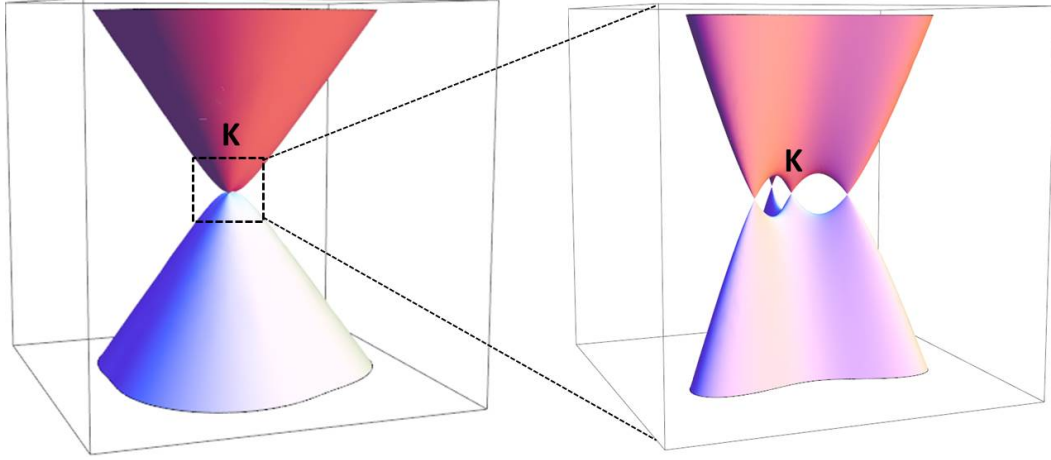
Figure 3.2: **Trigonal warping.** 3D Zoom of the fine energy structure near K point showing the emergence of three additional Dirac cones.

with the third energy band [See Fig. 3.2]. We can observe that the vertices are oriented along the $K - K'$ direction for TE-TM SOC and rotated by $60°$ ($K - \Gamma$ direction) for the Rashba SOC case, a small detail, which has crucial consequences for the topological phase diagram.

The topological character of these Hamiltonians with the appearance of the QAH effect, associated with $C_n = \pm 2$ due to the additivity of the K and K' contributions to the Berry curvature, has already been suggested and discussed by deriving an effective Hamiltonian close to the K point in different limits for both the electronic [68, 207] and photonic cases [213, 212]. However, the presence of other topological phase transitions due to additional degeneracies appearing in other points of the first Brillouin zone was not checked.

The figure 3.4 shows the diagram of topological phases of both models versus the SOC and Zeeman field strength. The different phases are characterized by the band Chern numbers C_n that we calculate using the standard gauge-independent and stable technique of [224]. We remind that change of C_n is necessarily accompanied by gap closing. Obviously, these phase diagrams are symmetric with respect to $\Delta = 0$ (with inverted signs of C_n for the negative part). At low Δ, both models are characterized by $C_n = \pm 2$, as already established. However, we point here that their C_n signs are opposite due to the opposite winding of their SOC around K points.

Figure 3.5(b) shows the corresponding band structure for the photonic case, where the double peak structure around K and K', arising from the trigonal warping effect and responsible for the C_n value, is clearly visible. Increasing either the SOC or the Zeeman field shifts these band extrema. In the photonic case, the band extrema finally meet at the M point, which makes the gap close, as shown on the
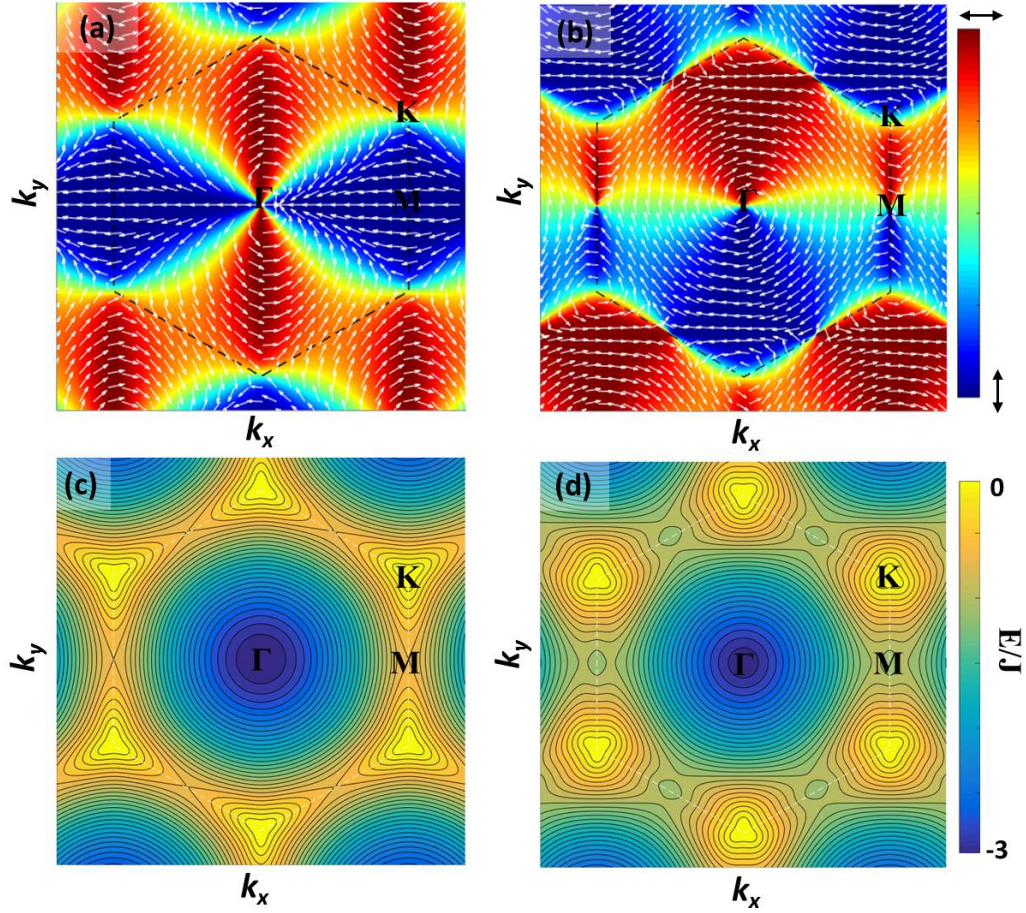
Figure 3.3:   (a) and (b) Spin polarization textures in the presence of TE-TM and Rashba SOC, respectively (second branch). White arrows: The in-plane spin projection. (c) and (d) Dispersions for TE-TM and Rashba SOC. The trigonal warping appears in different directions. ($\Delta = 0$, $\lambda_e = \lambda_p = 0.2J$).
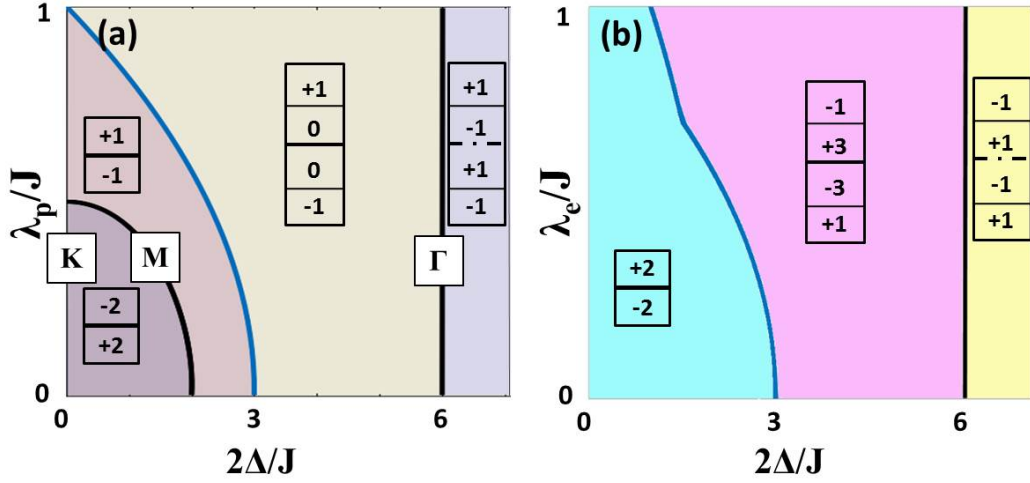
Figure 3.4: **Topological phase diagrams.** (a) for the TE-TM SOC and (b) for the Rashba SOC with an applied field Δ. Each phase is marked by the C_n of the bands.

figure 3.5(c). The critical Zeeman field value at which this transition takes place can be found analytically: $\Delta_1 = \sqrt{J^2 - 4\lambda_p^2}$. Increasing the fields further leads to an immediate re-opening of the gap with the C_n passing from +2 to -1 for the valence band. This case is shown on the figure 3.5(d), where one can clearly see that the number of band extrema is twice smaller than on 3.5(b). This phase transition is entirely absent in the electronic case because of the different orientations of the trigonal warping.

Increasing the field even further leads to a second topological transition this time present in both models and associated with the opening of two additional gaps between the two lower and two upper branches (in the middle of the "conduction" band and of the "valence" band, correspondingly), as shown on the figure 3.5(d). This transition arises, when the minimum energy of the second branch at the Γ point is equal to the maximal energy of the lowest band at the K point, and thus the system of 2 bands (each containing 2 branches) is split into 4 bands (each containing a single branch). The corresponding transition in the photonic case occurs when the Zeeman splitting is: $\Delta_2 = \frac{3(J^2 - \lambda_p^2)}{2J}$.

The last topological phase transition occurs when the middle gap closes at the Γ point for $\Delta_3 = 3J$ and then reopens as a trivial gap, whereas the two other bandgaps are still topological.
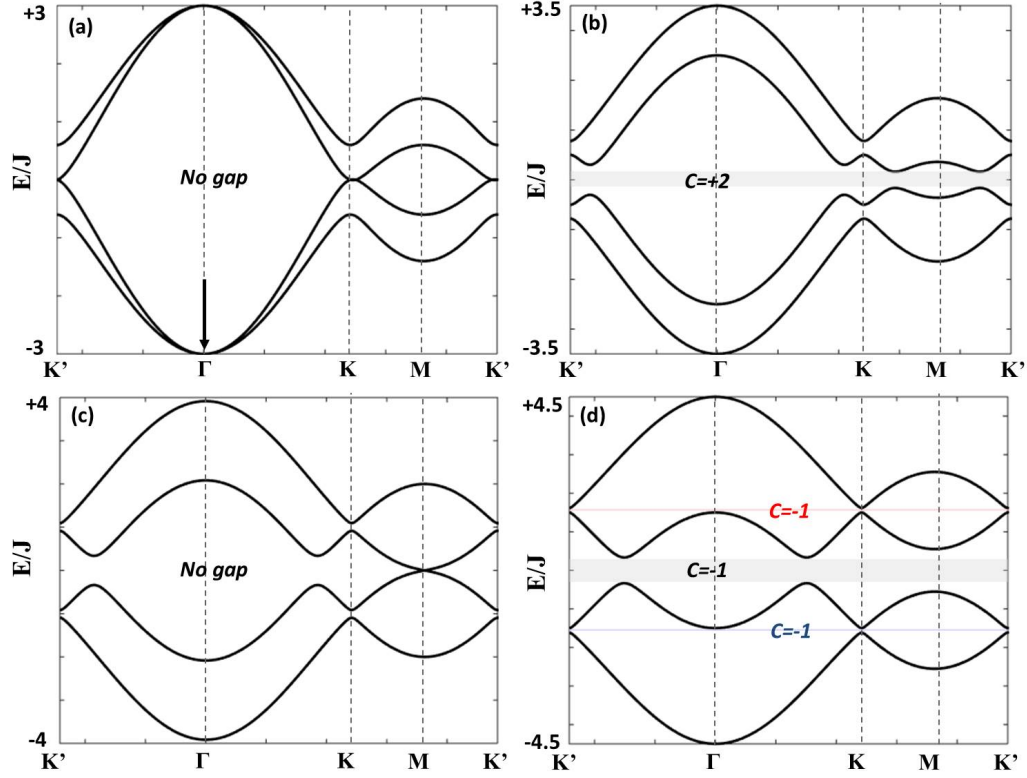
Figure 3.5: **Dispersion of photonic graphene for different Zeeman fields.** (a) $\Delta = 0$, (b) $\Delta = 0.5J$, (c) $\Delta = \Delta_1 = \sqrt{J^2 - 4\lambda_p^2}$, (d) $\Delta = 1.5J$. ($\lambda_p = 0.2J$). The different gaps are shown in grey with the values of the associated gap Chern numbers (also known as Hall numbers, namely the sum of the Chern numbers associated with the bands below the band gap: $C = \sum C_n$, associated with the quantized conductance (1.42) in electronic systems).

3.1.3 Conclusions and other lattices

The above study has allowed to make a bridge between the quantum anomalous Hall effect for light and for electrons. Indeed, the tight-binding approach allows to consider TE-TM splitting as a photonic SOC and to directly compare it to the Rashba SOC in electronic systems. Whereas the addition of a Zeeman term leads to the opening of a topological gap in both systems, we have highlighted their different topological phase diagrams and interpreted it as a consequence of the different windings of the two SOCs.

This type of QAH based on the combination of in-plane SOC and Zeeman field can be extended to other lattice geometries in 2D. For example, Kagome lattice has been considered theoretically both for electrons [208] and photons [217]. Similar phase diagrams could be determined in these systems too.

It is interesting to note however, that the above ingredients do not lead to QAH phase for Lieb lattices. This can be understood as follows: due to the square symmetry, the resulting $f_k^{\pm}$ coefficients are real. As a consequence, there is no in-plane winding of the spin eigenstates in momentum space contrary to the honeycomb case [Fig. 3.3 (a,b)] which is crucial to achieve non-zero Chern numbers when a Zeeman field is added. Different ways can be used to avoid this problem. In the electronic case it has been shown that adding the intrinsic SOC (which appears as a second-neighbour hopping term) in the model can lead to bandgap opening with non-zero Chern numbers [225], whereas a dislocated Lieb lattice has been considered in the photonic case [226].

Finally, the experimental observation of the polariton Chern insulator in a honeycomb lattice has been claimed very recently [227] (after the thesis defence).

3.2 Quantum valley Hall effect

The presence of two valleys around K and K' point in graphene allows to define a valley pseudo-spin. In a staggered honeycomb lattice, A and B sites have an energy difference [64, 37] $2\Delta_{AB}$. In such a case, a gap opens in the dispersion and the system becomes insulating. The presence of this gap combined with the opposite winding of the in-plane field around K and K' points leads to the occurrence of opposite Berry curvature in the two valleys.

This peculiar Hamiltonian is realized in nature by several crystalline structures, such as the transitional metal dichalcogenide (TMD) and boron nitride monolayers [228, 229]. A large part of the unique properties of this class of 2D materials is due to the local Berry curvature of their bands near the K and K' points and to the related orbital moment. For instance, it imposes specific optical selection rules. Only circularly-polarized σ^+ light can be absorbed by the K valley transition, while only σ^- light is absorbed by the K' valley transition [230, 231]. The valley dependent Berry curvature is also at the origin of the valley Hall effect [232, 228, 233] recently observed experimentally in MoS_2 [234] where electrons, accelerated by an electric field, experience a valley-dependent Berry curvature provoking a valley-dependent
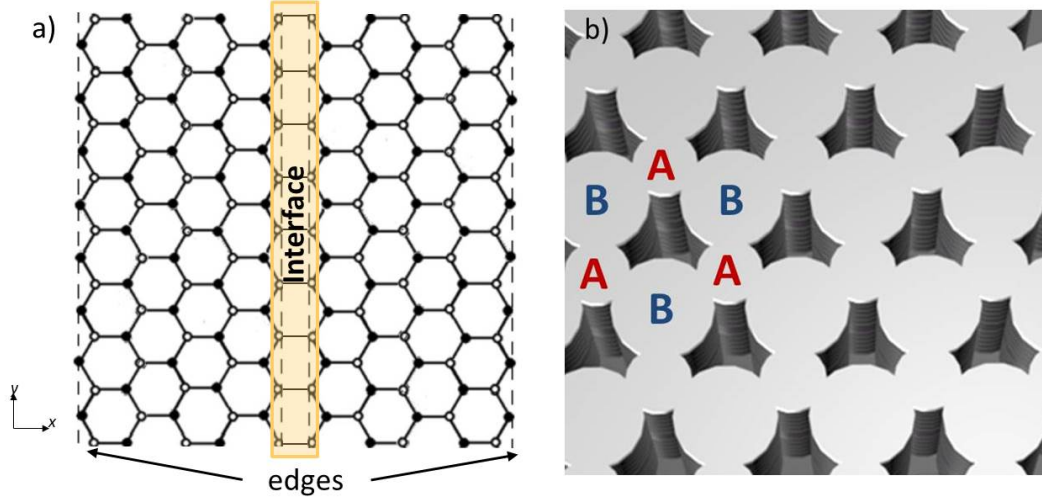
Figure 3.6: (a) Zigzag interface between two TMD lattices with opposite staggering potentials giving rise to zero lines modes and quantum valley Hall effect with a proper choice of parameters. (b) Staggered honeycomb lattices can be made out of etched planar microcavities. The panel shows a top view of such lattice. Each sublattice (A/B) is composed of 0D cavities (micropillars) with different radius.

drift perpendicular to the acceleration direction, which leads to spatial separation of valley electrons.

In this section, we introduce the quantum valley Hall effect occurring at the interface between two opposite staggered honeycomb lattices. We use the tight-binding approach having in mind the possible realization in a photonic system made of coupled micropillars [200]. Indeed, in this system the energy difference between A and B sites (linked with the gap size) should be easily controlled by tuning the pillar diameters. In the second part, taking advantage of this artificial system we emphasize that a sharp interface can be replaced by a wide one without affecting the presence of the chiral valley polarized interface modes.

Even if not very original, this section is a starting point for the next section where we include the TE-TM photonic SOC and to the next chapter where we present a study of vortex excitations in this system.

3.2.1   Valleys topological charges

The spinless tight-binding Bloch Hamiltonian describing a staggered honeycomb lattice reads:

$$H_k = \begin{pmatrix} \Delta_{AB} & -Jf_k \\ -Jf_k^* & -\Delta_{AB} \end{pmatrix}, \quad f_k = \sum_{j=1}^{3} \exp\left(-i\mathbf{k}\mathbf{d}_{\phi_j}\right) \tag{3.8}$$

where $2\Delta_{AB}$ is the energy difference between the ground states of A and B pillars and J is the nearest neighbours tunnelling coefficient. The linearisation of (3.8) around K and K' points yields:

$$H_{K,K'} = \hbar v_f (\tau_z q_x \sigma_x + q_y \sigma_y) + \Delta_{AB} \sigma_z \qquad (3.9)$$

where τ_z is the valley index ($\tau_z = \pm 1$ at K and K' respectively) and $v_f = \frac{3aJ}{2\hbar}$ is the Fermi velocity defined in term of the tight-binding parameters. A non-zero Δ_{AB} leads to the opening of a band gap and induces opposite Berry curvatures around K and K' points, which for the valence band reads:

$$\mathcal{B}_z(q) = \tau_z \frac{9a^2 J^2 \Delta_{AB}}{(4\Delta_{AB}^2 + 9a^2 J^2 q^2)^{3/2}} \qquad (3.10)$$

(See also Eq. (37) of ref. [39] for a formula defined on the whole BZ). If Δ_{AB} is small, the Berry curvature is strongly concentrated around K and K', which allows to introduce a valley Chern number [37, 235] $C_{K,K'} = \frac{1}{2\pi} \int \mathcal{B}_z(q) d\mathbf{q}$ by analogy with the spin Chern number, which is linked to the $\mathbb{Z}_2$ topological invariant characterizing the quantum spin Hall effect (QSHE) [73]. Here this gives $C_{K,K'} = \pm\frac{1}{2}$. The total Chern number of the band $C = C_K + C_{K'}$ is therefore zero and this system is a *trivial* insulator.

The flexibility of artificial systems allows to realize staggered graphene lattices with any sign of Δ_{AB}. The scheme proposed here is therefore to build an interface between two TMD analogs with opposite energy band gaps ($\Delta_{AB} < 0$ for $x < 0$ and $\Delta_{AB} > 0$ for $x > 0$) as first proposed theoretically in [236]. In this situation, one can predict the presence $\mathcal{N}$ of gapless modes in each valley on the interface by computing the difference of the valley Chern numbers across it:

$$\mathcal{N}_{K,K'} = C_{K,K'}(l) - C_{K,K'}(r) = \pm 1 \qquad (3.11)$$

where l and r stand for the left and right domains [237, 238]. In the continuous limit used here, $\mathcal{N}$ is a topological charge used to characterize zero-line modes between two 2D Dirac vacua with inverted mass gaps [239]. In honeycomb lattices, there are two inequivalent valleys with Dirac dispersions, leading to two gapless modes (one for each valley) at the interface.

Note: It is important to keep in mind that the definition of the valley Chern numbers C_K is deeply linked with the continuous limit. Mathematically, this object is different from the real Chern number introduced in the first chapter (Eq. (1.38)) which is obtained by integration of the Berry curvature over a *closed* surface (the whole Brillouin zone). In this sense, the valley Chern number is not a true topological invariant. However, this limit is particularly useful here because it allows to use the domain wall topological charge to predict the valley gapless modes. Of course, this approach is only valid for systems with well defined valleys.
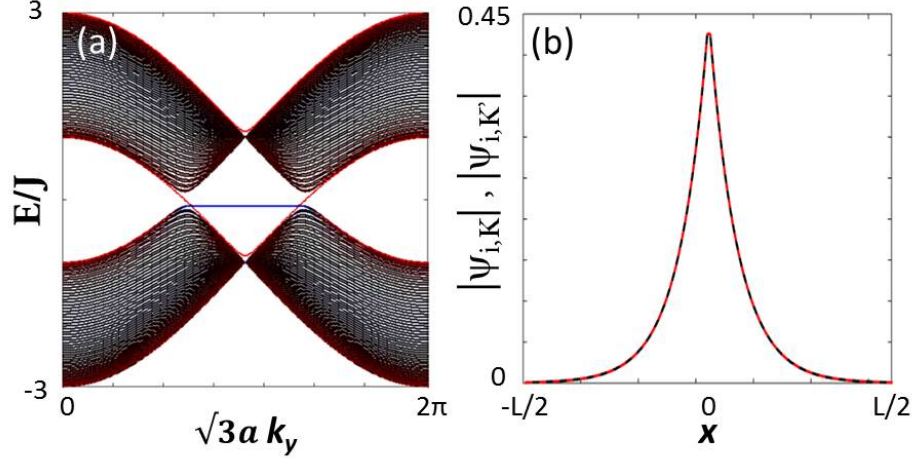
Figure 3.7: (a) Ribbon dispersion (Colors represent localization on the interface (red) and on the edges of the structure (blue)). (b) Corresponding in-gap interface wavefunction absolute values projection on the transverse (x) direction for K (solid-black) and K' (dashed-red) valleys. (Staggered potential: $\Delta_{AB}(r) = -\Delta_{AB}(l) = 0.1J$)

3.2.2   Ribbon of coupled zig-zag chains

To check the above prediction we compute the dispersion of a ribbon with such interface (which can be considered as a domain wall) along the zigzag direction (see scheme Fig. 3.6(a)) using the tight-binding approach.

To compute the interface or edge states spectra in the T-B approximation, we consider a ribbon of N coupled zig-zag chains. In this configuration, the Bloch Hamiltonian in the basis of Bloch waves $\psi_{A/B,m}(k_y)$ (where the index m numerates the chains) can be written as a $(d \times N) \times (d \times N)$ square matrix to diagonalize (Note: the same method has been used to evidence interface states including spin degree of freedom and to compute the Bogoliubov edge states in the next chapter):

$$
H_{k_y} = \begin{pmatrix}
D_{k_y} & S_{k_y} & 0 & . & . & . & 0 & 0 & 0 \\
S_{k_y}^\dagger & D_{k_y} & S_{k_y} & . & . & . & 0 & 0 & 0 \\
0 & S_{k_y}^\dagger & D_{k_y} & . & . & . & 0 & 0 & 0 \\
. & . & . & . & . & . & . & . & . \\
. & . & . & . & . & . & . & . & . \\
. & . & . & . & . & . & . & . & . \\
0 & 0 & 0 & . & . & . & D_{k_y} & S_{k_y} & 0 \\
0 & 0 & 0 & . & . & . & S_{k_y}^\dagger & D_{k_y} & S_{k_y} \\
0 & 0 & 0 & . & . & . & 0 & S_{k_y}^\dagger & D_{k_y}
\end{pmatrix}
\tag{3.12}
$$

where the dimension d and the form of the blocks D_{k_y} and S_{k_y} depend on the system under consideration. The diagonal blocks D_{k_y} describe nearest-neighbour coupling

within one infinite zig-zag chain and the subdiagonal and superdiagonal blocks $S_{k_y}^\dagger$ and S_{k_y} encode the coupling between different chains. For graphene without spin degree of freedom these blocks will be of dimension $d = 2$ ($d = 4$ if the spin is taken into account as in the next section, and $d = 8$ for the Bogoliubov matrices with spin degree of freedom that we study in the next chapter). For the staggered graphene case, one has

$$D_{k_y} = \begin{pmatrix} \Delta_{AB} & -Jf_{k_y} \\ -Jf_{k_y}^* & \Delta_{AB} \end{pmatrix}, \quad S_{k_y} = - \begin{pmatrix} 0 & 0 \\ J & 0 \end{pmatrix} \tag{3.13}$$

where $f_{k_y} = \sum_j^2 e^{-i\mathbf{k}.\mathbf{d}_j}$. Here, the summation is only on the two nearest neighbour inside a zig-zag chain, the third neighbour tunnelling being included in the coupling block S_{k_y}.

We consider a ribbon of size L constructed with $N = 128$ coupled zigzag infinite chains, the interface is located in the middle of the ribbon ($\Delta_{AB} < 0$ when $m \le N/2$ and $\Delta_{AB} > 0$ when $m > N/2$). The dispersion of the full ribbon is plotted in Fig. 3.7(a), where the interface states are shown with red and the real boundary modes are shown with blue (both for left and right edges, which are degenerate). The latter are non-dispersive, connecting the extrema at the top of the valence band. On the other hand, the interface modes (red) are dispersive. They connect the valence and the conduction band in each valley, with group velocities opposite in the two valleys. Hence, these gapless modes are associated with a QVH current on the interface [236, 237, 240].

The overlap of the wavefunctions of the interface states (corresponding to the wavevectors K and K') in real space in the direction perpendicular to the interface is perfect, as shown in Fig. 3.7(b). This implies that these states are not topologically protected against scattering on a defect between the K and K' valleys. In electronic systems, the practical argument which is put forward is that in sufficiently clean systems this kind of backscattering tends to be negligible because of the relatively large distance between the two valleys in momentum space. Nonetheless, the presence of strong defects such as atom vacancies will lead to the formation of localized states [241] and break the propagation.

This arguments fails in photonics, since the valleys are, on the opposite, relatively close in reciprocal space. Only some specific defect shapes, suppressing the scattering in particular directions and thus suppressing the coupling between the valleys, would keep the valley current unperturbed. On the other hand, a random disorder, such as the variation of the pillar diameter in micropillar lattices, or the variation of the hole size in photonic crystal slabs certainly induces an important scattering between the valleys. In the subsection 3.3.3, we demonstrate the absence of topological protection for the valley current in the QVHE by simulating the scattering on a localized defect.
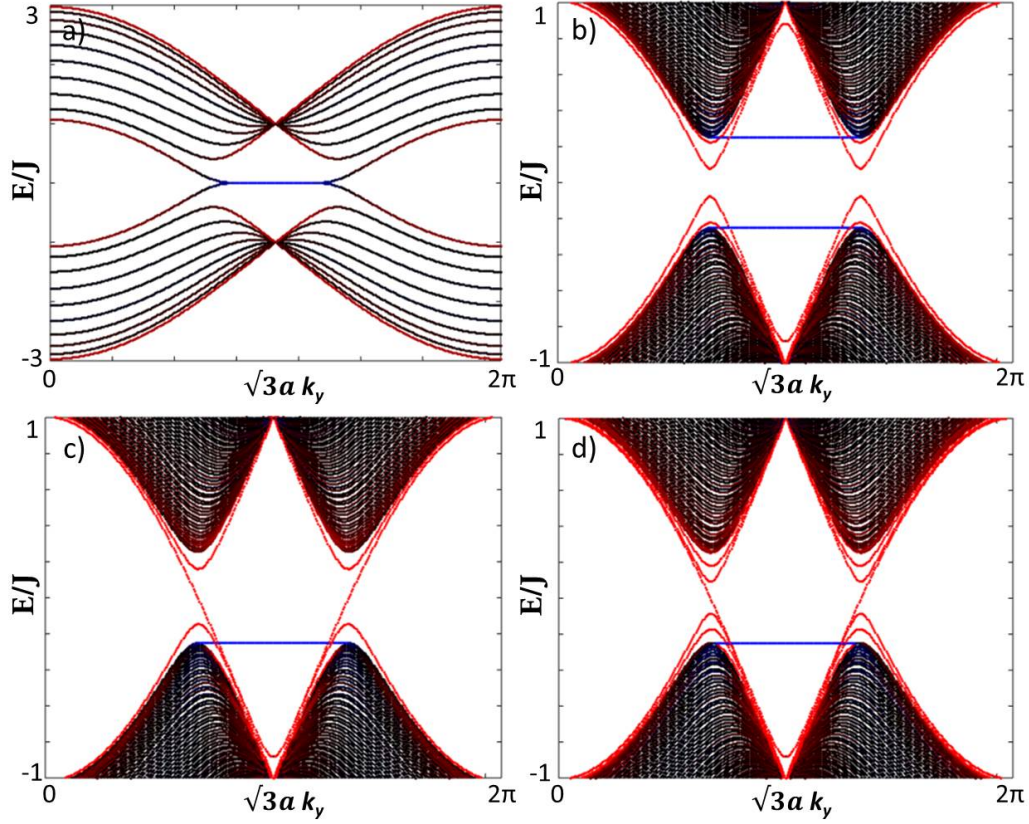
Figure 3.8:   Tight-binding dispersions of zigzag ribbons. (a) 10 zigzag chains of regular honeycomb, (b) wide interface (10 unstaggered chains) between two staggered honeycomb with same staggering potential, (c)-(d) Interface between two staggered honeycomb with opposite staggering potential constituted of 10 and 20 unstaggered chains respectively ($\Delta_{AB} = \pm 0.25J$)

3.2.3   Interface width impact

In artificial systems, one could replace the sharp interface by an extended by adding regular zigzag chains ($\Delta_{AB} = 0$) between the two domains ($\Delta_{AB} > 0$ and $\Delta_{AB} < 0$). In such a case, do we still have the gapless valley modes? To elucidate this question, we consider ribbons of coupled infinite zigzag chains in the tight-binding approximation for several configurations.

   The calculated projected dispersions are plotted in Fig. 3.8. Colors correspond to localization at the edge (blue) or at the center (red) of the ribbon. In panel (a), we plot the dispersion of 10 coupled regular zigzag chains ($\Delta_{AB} = 0$) surrounded by vacuum. This is not an interface, but just a plain graphene ribbon. As expected, the dispersion is gapless, with flat edge states connecting the two valleys. For other panels, this ribbon is inserted between two staggered honeycomb lattices. For this,

we consider a ribbon of a total number of coupled zigzag chains $N = 128$ with different domains inside. In panels (b)-(c), the interface contains 10 zigzag chains with $\Delta_{AB} = 0$, whereas the domains on both side are staggered ($\Delta_{AB} = \pm 0.25J$) with the same (b) or opposite (c) staggering potential . In the case where the staggering is the same on both sides, the system is fully isolating, even in the central regular honeycomb region (red curves), where a gap is opened due to the coupling of the graphene stripe to the two staggered domains. In the case where we have opposite staggering on each side of the interface (panel (c)) the chiral modes crossing the gap are still present. This means that the domain wall topological invariant $\mathcal{N}_{K,K'} = \pm 1$ defined in the previous subsection and the corresponding reasoning predicting the existence of the interface states are still valid when the interface width is increased. If we increase the interface region further, the energy bandgap in this central region remains open (except the single interface mode crossing it) and there is still a single mode crossing the gap in each valley, as predicted by the topological arguments. Finally, another example for an interface of 20 zigzag chains is plotted in panel (d).

3.2.4 Discussion

While it is possible to invert a real TMD lattice simply by turning the 2D sheet upside down, the interfaces between two inverted lattices cannot be formed, because they would correspond to metal-metal or chalcogenide-chalcogenide chemical bonds. It seems therefore very difficult to obtain and study chiral states at such interfaces. Several theoretical works have proposed to use bilayer graphene systems, where a tunable gap can be opened by applying a bias voltage [221, 242] to organize these interface states [237, 243, 235]. Chiral valley-polarized edge states are also predicted in these systems due to the coupling between the two layers with a potential difference [244]. The signature of the existence of the interface modes has been reported experimentally in the bilayer system [245] and the study of valley polarized edge states or QVHE is nowadays a research field in several condensed matter systems [246, 247, 209, 248].

TMD analogs can also be realized using cold atoms in optical lattices, or by coupling optical resonators. In the latter case, Berry curvature can be probed by resonant excitation of the Dirac point in momentum space and measurement of a drift of the wave packet, which, however, is predicted to be relatively small [249]. Recently, photonic quantum valley Hall effect in photonic crystal slabs [250, 251, 252, 253] has been theoretically described. Observation of such photonic interface states have been reported recently in different platforms [254, 255, 256, 257].

In some of these works, the authors have chosen to use the label quantum spin Hall effect or photonic topological insulator. We want to stress that the effective Hamiltonian related to these systems is similar with the one shown in the previous paragraph, which allows to organize interface states and not surface states and relates to the zero line modes due to domain wall between two opposite quantum valley Hall phase rather than to the quantum spin Hall effect. Similarly with the

case we present, the interface current are subject to disorder induced inter-valley scattering.

3.3   Photonic quantum valley Hall effect and perfect valley filter

In subsection 3.3.1, we consider the impact of the splitting between TE and TM optical modes, which is inherent to cavity-based photonic systems which was not considered before. We show that the magnitude of the splitting allows to tune the direction of propagation and number of interface modes. In subsection 3.3.2, we propose a scheme to build a perfect valley filter by using a domain wall between QAH and QVH phases using mixed light-matter exciton-polariton quasi-particles. Finally, some numerical simulations beyond T-B approximation are presented in 3.3.3 to illustrate and confirm the previous paragraphs.

3.3.1   QVH with TE-TM photonic SOC

We now include the light polarization degree of freedom and the so-called TE-TM spin-orbit coupling [213] in our model. The Hamiltonian becomes a 4×4 matrix [219] written here in the $\left(\Psi_A^+, \Psi_A^-, \Psi_B^+, \Psi_B^-\right)$ basis.

$$H_{qvh} = \begin{pmatrix} \Delta_{AB}\mathbb{I} & F_k \\ F_k^\dagger & -\Delta_{AB}\mathbb{I} \end{pmatrix}, \quad F_k = -\begin{pmatrix} f_k J & f_k^+ \delta J \\ f_k^- \delta J & f_k J \end{pmatrix} \tag{3.14}$$

where δJ is the spin orbit coupling ($\delta J = \lambda_p$) strength and $f_k^\pm$ coefficients are defined by: $f_k^\pm = \sum_{j=1}^3 \exp\left(-i[\mathbf{k}\mathbf{d}_{\phi_j} \mp 2\phi_j]\right)$. The definition of valley Chern number when spin-orbit coupling is present is not strict because the SOC brings an additional contribution to the Berry curvature of each band. However, if the valleys are still energetically defined (which means that they are clearly visible in the dispersion), and the two staggering potentials on each side of the interface are exactly inverted, the difference between valley Chern numbers $\mathcal{N}_{K,K'}$ is always a well defined integer.

3.3.1.1   Valley topological charges: analytical results

To demonstrate that the difference between the valley Chern numbers remains integer, we compute analytically the topological charges of the valleys in a staggered honeycomb lattice with TE-TM SOC. For this purpose we derive an effective low-energy Hamiltonian to describe the low energy bands (closest to the central gap) in a given valley. Indeed, a 2×2 Hamiltonian with particle-hole symmetry can be written as a superposition of Pauli matrices: $H_{eff} = \mathbf{h}.\hat{\boldsymbol{\sigma}}$ where $\mathbf{h}$ is an effective magnetic field. Using this notation, the Berry curvature can be computed using:

$$\Omega_{xy} = \mathcal{B}_z = \frac{1}{2|\mathbf{h}|^3}\mathbf{h}.(\partial_{q_x}\mathbf{h} \times \partial_{q_y}\mathbf{h}) \tag{3.15}$$

whose integral $\frac{1}{2\pi}\int\mathcal{B}_z\mathrm{d}\mathbf{q}$ correspond to the winding number of the pseudospin on the Bloch sphere which is equivalent to the Chern topological invariant for 2×2 Hamiltonians.

In order to use the above picture, we need to reduce the number of states in the basis of our system. First, we linearize the 4×4 Hamiltonian defined above around the K point $(0,\frac{4\pi}{3\sqrt{3}a})$. Using the new coordinate $\mathbf{q}=(\mathbf{k}-\mathbf{K})$, we rewrite it in the basis $\left(\Psi_A^+,\Psi_B^-,\Psi_A^-,\Psi_B^+\right)$ where A/B and $\pm$ are the sublattice and spin indices respectively.

$$H_{qvh,K}=\begin{pmatrix}\Delta_{AB} & -\frac{3a\delta J}{2}(q_y-iq_x) & 0 & \frac{3aJ}{2}(q_y+iq_x)\\ -\frac{3a\delta J}{2}(q_y+iq_x) & -\Delta_{AB} & \frac{3aJ}{2}(q_y-iq_x) & 0\\ 0 & \frac{3aJ}{2}(q_y+iq_x) & \Delta_{AB} & -3\delta J\\ \frac{3aJ}{2}(q_y-iq_x) & 0 & -3\delta J & -\Delta_{AB}\end{pmatrix}\quad(3.16)$$

The fact that some spin-orbit coupling term appears linear in $\mathbf{q}$ and the others are constant in the above linearized Hamiltonian (3.16) is a reminiscence of the threefold rotational symmetry of the honeycomb lattice. If $\Delta_{AB}=0$, the constant coefficients $-3\delta J$ define the splitting between the inner and the outer branches at $\mathbf{q}=\mathbf{0}$ whereas the coefficients linear in $\mathbf{q}$ are associated with the occurrence of three additional Dirac crossing between the inner branches (trigonal warping: see Fig. 3.2). H_{qvh} can be written in the block form:

$$H_{qvh,K}=\begin{pmatrix}H_1 & T\\ T & H_2\end{pmatrix}\quad(3.17)$$

where H_1,H_2,T are 2×2 matrices. We are interested in the two branches closest to the gap (the inner branches of the dispersion). The perturbation theory is applicable if the high energy branches are sufficiently far away, which means $\delta J\gg\Delta_{AB}$. Using the perturbation theory, one can derive an effective 2×2 Hamiltonian: $H_{eff}=H_1-TH_2^{-1}T$. In the following, we are interested in two different limits: when $\delta J\ll J$ and when $\delta J\sim J$. In the first limit, one can neglect the term $\sim\delta Jq$ (corresponding to neglect the trigonal warping [219]). The effective Hamiltonian can then be written as:

$$H_{K,eff}^{(1)}=\begin{pmatrix}\Delta_{AB} & 0\\ 0 & -\Delta_{AB}\end{pmatrix}+\frac{1}{\Delta_{AB}^2+9\delta J^2}\begin{pmatrix}\frac{9a^2J^2\Delta_{AB}}{4}q^2 & \frac{27a^2J^2\delta J}{4}(q_y+iq_x)^2\\ \frac{27a^2J^2\delta J}{4}(q_y-iq_x)^2 & -\frac{9a^2J^2\Delta_{AB}}{4}q^2\end{pmatrix}$$
$$(3.18)$$

Due to the absence of the terms $\sim\delta Jq$, when $\Delta_{AB}=0$ the energies are two inverted parabola degenerate at $\mathbf{q}=0$. A similar development around K' $(0,-\frac{4\pi}{3\sqrt{3}a})$ allows to obtain $H_{K',eff}$. Using Eq. (3.15), we compute the Berry curvature in this limit:

$$\mathcal{B}_z^{(1)}=\frac{\tau_z 144a^4\Delta_{AB}J^4\delta J^4 q^2}{(9a^4\delta J^2 J^4 q^4+\Delta_{AB}^2(4\delta J^2+a^2J^2q^2)^2)^{3/2}}\quad(3.19)$$

where $\tau_z=\pm 1$ for K/K' valleys. The corresponding valley Chern number is:

$$C_{K,K'}^{(1)}=\frac{1}{2\pi}\int\mathcal{B}_z\mathrm{d}\mathbf{q}=\tau_z\mathrm{sign}(\Delta_{AB})(1-\frac{\Delta_{AB}}{\sqrt{\Delta_{AB}^2+9\delta J^2}})\quad(3.20)$$

The valley Chern numbers tend to $C^{(1)}_{K,K'} = \tau_z \text{sign}(\Delta_{AB})$ if the high energy bands are far away from the low energy ones ($\Delta_{AB} \ll \delta J$). As a consequence, the topological invariant characterizing the domain wall between two inverted TMD is:

$$\mathcal{N}^{(1)}_{K,K'} = C_{K,K'}(l) - C_{K,K'}(r) = \pm 2\text{sign}(\Delta_{AB}) \tag{3.21}$$

which means that there are two co-propagating interface states in a given valley. One can see from Eq. (3.20), that if the high energy bands are too close, the valley Chern number of a given low energy band is not an integer. This means that the topological charge is shared between the high and low energy bands. In this case, perturbation theory becomes inapplicable and one needs to compute the valley Chern numbers numerically.

In the second limit, where $\delta J \sim J$, the linear terms ($\delta J q$) have to be conserved and we can neglect the quadratic terms q^2. The resulting effective 2×2 Hamiltonian around K and K' can be written in the (Ψ^+_A, Ψ^-_B) and (Ψ^-_A, Ψ^+_B) basis:

$$H^{(2)}_{K,eff} = \begin{pmatrix} \Delta_{AB} & \frac{3a\delta J}{2}(q_y - iq_x) \\ \frac{3a\delta J}{2}(q_y + iq_x) & -\Delta_{AB} \end{pmatrix} \tag{3.22}$$

$$H^{(2)}_{K',eff} = \begin{pmatrix} \Delta_{AB} & -\frac{3a\delta J}{2}(q_y + iq_x) \\ -\frac{3a\delta J}{2}(q_y - iq_x) & -\Delta_{AB} \end{pmatrix} \tag{3.23}$$

By looking on these two effective Hamiltonians, we can directly see that the signs of the diagonal elements are the same, whereas the windings of the effective in-plane fields are opposite, exactly as in staggered honeycomb lattices without SOC. Hence, the Berry curvatures are opposite in each valleys. They can be calculated as:

$$\mathcal{B}^{(2)}_z = -\frac{\tau_z 9a^2 \Delta_{AB} \delta J^2}{(4\Delta^2_{AB} + 9a^2 \delta J^2 q^2)^{3/2}} \tag{3.24}$$

where $\tau_z = \pm 1$ for K/K' valleys. The corresponding valley Chern numbers are $C^{(2)}_{K,K'} = -\frac{\tau_z}{2}\text{sign}(\Delta_{AB})$. The domain wall invariant between two inverted QVH phases is then $\mathcal{N}^{(2)}_{K,K'} = \mp\text{sign}(\Delta_{AB})$ which implies the presence of one interface mode in each valley. The group velocities of these modes in the two valleys are of course opposite.

This low energy study has allowed us to determine analytically the valley topological charge in these two limits and hence to compute the number of valley-polarized interface states. One should note that the topological charge of a given valley changes sign between the two limits. The group velocities of the interface states are inverted as well. In the appendix A, we show the effective Hamiltonian derived in the general case between the two limits considered here.

3.3.1.2   Spectrum and discussion

In the previous subsection, we have derived an effective low energy two-band Hamiltonian in order to compute analytically the valley topological charges. We have shown that it is possible to distinguish between two configurations. In the weak

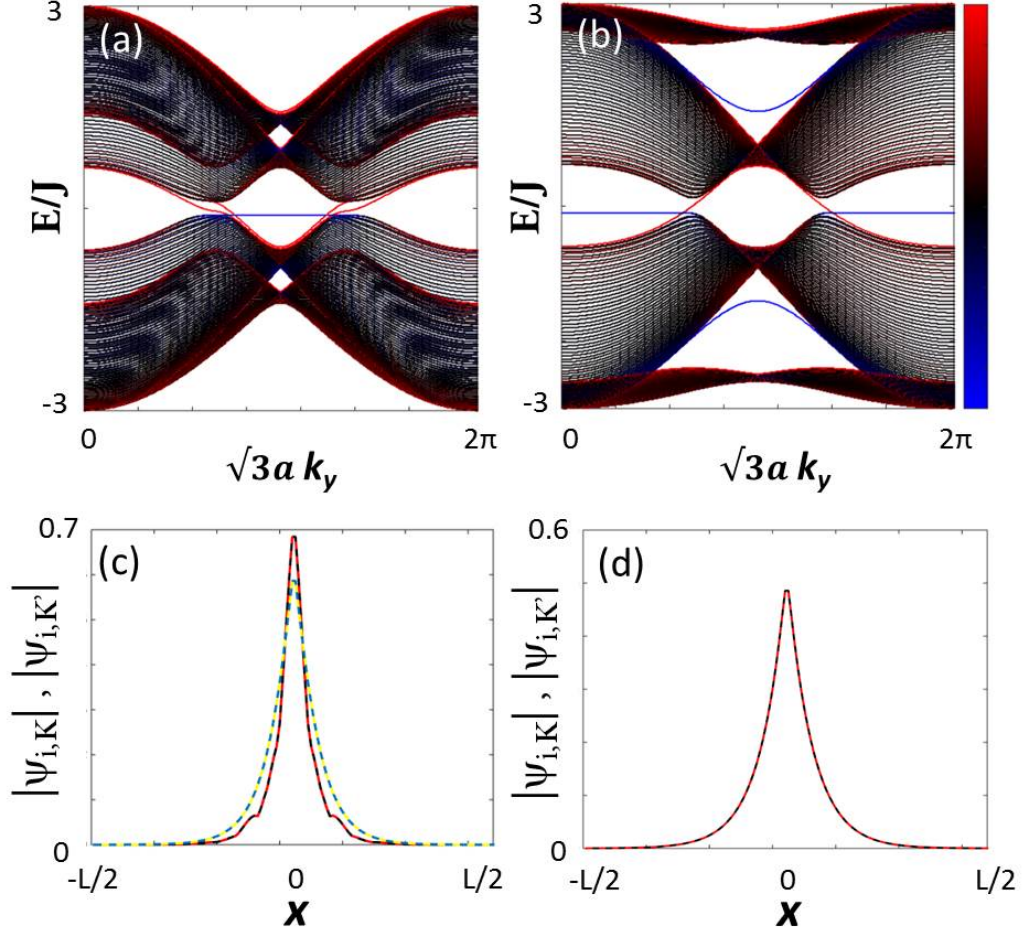Figure 3.9: (a,b) Ribbon dispersions with TE-TM SOC: (a) $\delta J = 0.2J$ and (b) $\delta J = 0.8J$. Colors represent localization on the interface (red) and on the edges of the structure (blue). (c,d) Corresponding absolute values of the interface wavefunctions in K (solid-black and solid-blue) and K' (dashed-red and dashed-yellow) valleys. (Staggered potential: $\Delta_{AB}(r) = -\Delta_{AB}(l) = 0.1J$)

SOC limit, $\mathcal{N}_{K,K'} = \pm 2\mathrm{sign}(\Delta_{AB})$, whereas when $\delta J \sim J$, $\mathcal{N}_{K,K'} = \mp\mathrm{sign}(\Delta_{AB})$. Here, we use the approach presented in the subsection 3.2.2 to compute the corresponding tight-binding dispersions in a ribbon geometry. The results are shown in Fig. 3.9(a) and (b) respectively. In Fig. 3.9(a), there are two interface states in each valley, that are visible within the bandgap. The ribbon dispersion in the second limit is shown in Fig. 3.9(b), this time there is only one interface state in each valley, as predicted from the domain wall topological invariant $\mathcal{N}$. The corresponding spatial overlap of the interface wavefunctions in K and $-K$ valleys is shown in Fig. 3.9(c,d). In Fig. 3.9(c), we plot the two wavefunctions present in each valleys for zero-energy states. We can see a slight difference in their localization profiles whereas they show a perfect overlap with their counter-part in the opposite valley. As in the case without SOC, the backscattering from one valley to the other is not forbidden. However, it should be noted that the presence of TE-TM SOC induces a polarization mismatch between the two valleys (not visible on these figures, showing only the absolute value of the wavefunction), which reduces the exact overlap of the two wavefunctions.

3.3.2   Perfect optical valley filter

Exciton-polaritons, mixed exciton-photon quasi-particles appearing in microcavities in the strong coupling regime, are sensitive to an external magnetic field due to their excitonic part. Optical quantum anomalous Hall (QAH) effect has been predicted to occur in honeycomb lattice of polariton micropillars with TE-TM SOC under a Zeeman field [212, 258] [See also previous section 3.1]. Here, we propose to organize an interface between this QAH phase and the QVH phase presented above, in order to obtain a perfect valley filter as sketched in Fig. 3.10(a), where the colored arrows represent the propagating edge states on the boundaries of the QAH phase. A similar scheme has been recently theoretically proposed for electrons in graphene with Rashba SOC [259]. However, we stress that the QAH effect has not been observed yet in graphene and that the creation of such interface in electronic systems seems quite challenging experimentally.

3.3.2.1   QAH phase: analytical results

The tight-binding Hamiltonian describing the photonic QAH phase is the following [212]:

$$H_{qah} = \begin{pmatrix} \Delta_z \sigma_z & F_k \\ F_k^\dagger & \Delta_z \sigma_z \end{pmatrix} \tag{3.25}$$

where Δ_z is the Zeeman splitting. We propose to create a topological domain wall between QAH and QVH phases. In this subsection we derive an effective low energy theory for the QAH phase. The Hamiltonian around the K point can be written in

the $\left(\Psi_A^+, \Psi_B^-, \Psi_A^-, \Psi_B^+\right)$ basis:

$$H_{qah,K} = \begin{pmatrix} \Delta_z & -\frac{3a\delta J}{2}(q_y - iq_x) & 0 & \frac{3aJ}{2}(q_y + iq_x) \\ -\frac{3a\delta J}{2}(q_y + iq_x) & -\Delta_z & \frac{3aJ}{2}(q_y - iq_x) & 0 \\ 0 & \frac{3aJ}{2}(q_y + iq_x) & -\Delta_z & -3\delta J \\ \frac{3aJ}{2}(q_y - iq_x) & 0 & -3\delta J & \Delta_z \end{pmatrix} \quad (3.26)$$

The difference between this linearized Hamiltonian and the one of QVH phase (3.16) is that the signs of the diagonal elements of H_2 are inverted. In the configuration, where a two-band effective theory can be applied ($\delta J \gg \Delta_z$), we study the same limits as in the previous section: $\delta J \ll J$ and $\delta J \sim J$. In the first limit, one has:

$$H_{eff}^{(1)} = \begin{pmatrix} \Delta_z & 0 \\ 0 & -\Delta_z \end{pmatrix} + \frac{1}{\Delta_z^2 + 9\delta J^2} \begin{pmatrix} -\frac{9a^2 J^2 \Delta_z}{4}q^2 & \frac{27a^2 J^2 \delta J}{4}(q_y + iq_x)^2 \\ \frac{27a^2 J^2 \delta J}{4}(q_y - iq_x)^2 & \frac{9a^2 J^2 \Delta_z}{4}q^2 \end{pmatrix} \quad (3.27)$$

which implies the following Berry curvature when $\delta J \gg \Delta_z$:

$$\mathcal{B}_z^{(1)} = \frac{144 a^4 \Delta_z J^4 \delta J^4 q^2}{(9a^4 \delta J^2 J^4 q^4 + \Delta_z^2 (a^2 J^2 q^2 - 4\delta J^2)^2)^{3/2}} \quad (3.28)$$

A similar development at K' point giving the same result, one can deduce the two valley Chern numbers:

$$C_{K,K'}^{(1)} = \text{sign}(\Delta_z)(1 + \frac{\Delta_z}{\sqrt{\Delta_z^2 + 9\delta J^2}}) \approx \text{sign}(\Delta_z) \quad (3.29)$$

When $\delta J \sim J$, the low energy 2×2 Hamiltonians around K and K' can be written in (Ψ_A^+, Ψ_B^-) and (Ψ_B^+, Ψ_A^-) effective basis respectively as:

$$H_{K,eff}^{(2)} = \begin{pmatrix} \Delta_z & \frac{3a\delta J}{2}(q_y - iq_x) \\ \frac{3a\delta J}{2}(q_y + iq_x) & -\Delta_z \end{pmatrix} \quad (3.30)$$

$$H_{K',eff}^{(2)} = \begin{pmatrix} \Delta_z & -\frac{3a\delta J}{2}(q_y - iq_x) \\ -\frac{3a\delta J}{2}(q_y + iq_x) & -\Delta_z \end{pmatrix} \quad (3.31)$$

We can see that both the Zeeman field and the winding of the in-plane field have the same sign which results in equal Berry curvatures:

$$\mathcal{B}_z^{(2)} = -\frac{9a^2 \Delta_z \delta J^2}{(4\Delta_z^2 + 9a^2 \delta J^2 q^2)^{3/2}} \quad (3.32)$$

leading to valley topological charges $C_{K,K'}^{(2)} = -\frac{1}{2}\text{sign}(\Delta_z)$. These analytical results are useful to understand the behavior of the topologically protected edge states of a quantum anomalous Hall phase at the interface with a QVH phase, where the two valleys are not equivalent. Using the domain wall topological invariant $\mathcal{N}_{K,K'}$ allows to predict the number of *topologically protected* interface states in a given valley. Of course, this topological argument is valid only when the valleys are energetically well defined.

3.3.2.2   Spectrum and discussion

As above, we use a tight-binding approach in order to find the edge states. The two domains are described by H_{qah} and H_{qvh}, respectively. We consider a realistic configuration for a lattice of micropillars where the TE-TM SOC is relatively weak ($\delta J < J/2$).

In the left phase, the total Chern number is equal to $C(l) = 2 \times \text{sign}(\Delta_z)$ whereas in the right one $C(r) = 0$, as explained above. From the bulk-boundary correspondence, the interface supports two modes propagating in the same direction, given by the sign of Δ_z. When the valleys are energetically well defined, one can compute the valley Chern numbers in each side analytically (previous subsection) or numerically. In the weak δJ limit, $C_K(l) = C_{K'}(l) = \text{sign}(\Delta_z)$ in the left domain, whereas $C_K(r) = -C_{K'}(r) = \text{sign}(\Delta_{AB})$ in the right domain. The resulting domain wall invariants for each valley are:

$$\mathcal{N}_{K,K'} = \text{sign}(\Delta_z) \mp \text{sign}(\Delta_{AB}) \tag{3.33}$$

We stress here that even if the valley Chern numbers are not well defined integers for all range of parameters, their difference $\mathcal{N}_{K,K'}$ defined above is always an integer. Therefore, the domain wall invariant always cancels for one valley, and is non-zero for the other valley. The two one-way modes are therefore always valley polarized.

To confirm this analysis based on topological argument, we compute the dispersion of a semi-infinite ribbon as we did in the previous sections. The results are shown in Fig. 3.10. In panel (b), we can see that the interface states (red) are localized in one of the two valleys in momentum space. The non-dispersive edge states of the QVH phase are shown in green. The one-way dispersive edge states of the QAH phase (blue) cross the gap and connect the two valleys. Contrary to the interface between two QVH phases, there is no interface state crossing the gap in the second valley. This means that the valley polarized interface states are really topologically protected against backscattering in the presence of defects. As sketched in Fig. 3.10(a), the topologically protected edge states are purely valley polarized due to the domain wall topological invariant N. To clarify the difference between this scheme and the interface between two QVH phases described in the previous section, we plot in Fig. 4(c,d) the *edge* and *interface* state wavefunction (absolute values) projections in the x direction. We can see that the blue state is clearly localized on the left edge of the structure and only the red ones are localized on the interface. This visual argument allows to understand the topological protection due to the absence of spatial overlap between the two wavefunctions contrary to the cases presented in the previous sections (Fig. 3.9(c,d)).

3.3.3   Numerical simulations

In this part, we present the full numerical simulations using the Schrödinger equation that we have performed in order to confirm the different results obtained in the tight-binding approach. We describe the evolution of polaritons in the honeycomb lattice

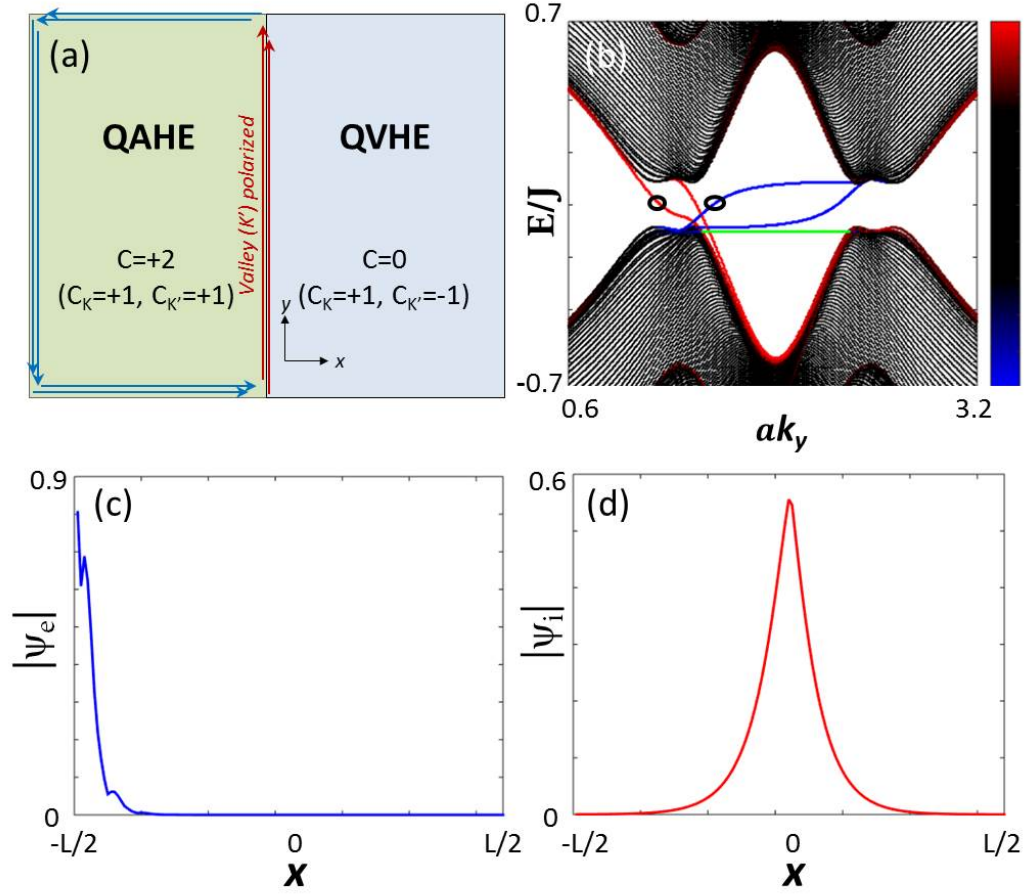Figure 3.10: **Perfect valley filter.** (a) Scheme of the structure, (b) Ribbon dispersion (Colors represent localization on the interface (red) and on the left edge of the structure (blue)). (c,d) Wavefunction projections on the transverse (x) direction for the states highlighted by the circles in (b): (c) edge (d) interface. (Parameters: $\Delta_z(l) = \Delta_{AB}(r) = 0.1J$, $\delta J = 0.2J$, $\Delta_z(r) = \Delta_{AB}(l) = 0$)

potential by solving the spinor Schrödinger equation for polaritons (in the parabolic approximation close to the bottom of the LPB).

$$i\hbar\frac{\partial\psi_\pm}{\partial t} = -\frac{\hbar^2}{2m}\Delta\psi_\pm - \frac{i\hbar}{2\tau}\psi_\pm \pm \Delta_z\psi_\pm + \beta\left(\frac{\partial}{\partial x} \mp i\frac{\partial}{\partial y}\right)^2\psi_\mp + U\psi_\pm + \hat{P} \quad (3.34)$$

where $\psi_+(\mathbf{r},t), \psi_-(\mathbf{r},t)$ are the two circular components, $m = 5 \times 10^{-5}m_{el}$ is the polariton mass, $\tau = 30$ ps the lifetime, β is the TE-TM coupling constant (corresponding to a 5% difference in the longitudinal and transverse masses). Δ_z is the magnetic field (applied only in the QAH region), U is the lattice potential (radius of the pillars $r = 1.5\mu m$, lattice parameter $a = 2.5\mu m$), which for some simulations includes an additional defect potential (a Gaussian potential of 1 meV and $\sigma_{def} = 1$ μm) centered on a certain pillar at the interface, and $\hat{P}$ is the pump operator. We have generated 2 lattice potentials: one for staggered honeycomb lattice and one for unperturbed honeycomb lattice. In the staggered lattice, the deviation of the pillar radius from the average value was chosen to be 15%.

Depending on the configuration (QVH/QVH phases or QVH/QAH phases), we either excite a large spot with a well-defined superposition of wavevectors corresponding to a single valley of the TMD lattice (QVH phase), or a single pillar of the Chern insulator (QAH phase), but always with the frequency within the bulk gap.

3.3.3.1   Bulk and interface dispersions

Figure 3.11(a) shows the dispersion of the bulk TMD analog lattice when TE-TM splitting is neglected. The dispersion is obtained by solving the Schrödinger equation (3.34) (the scalar one because we neglect polarization for clarity here) over time, which gives the time-dependent wavefunction $\psi(\mathbf{r},t)$, which is then Fourier-transformed to give the intensity as a function of energy and wavevector $n(\mathbf{k},E) = |\psi(\mathbf{k},E)|^2$, plotted in Fig. 3.11. In experiments, such dispersion is usually obtained under non-resonant pumping, which can be described by choosing the pump operator $\hat{P}$ as a random uncorrelated Gaussian noise. In numerical experiments, on can also consider a short narrow Gaussian pulse $\hat{P} = A_0 e^{-(\mathbf{r}-\mathbf{r}_0)^2/\sigma^2 - (t-t_0)^2/\tau_0^2}$, where A_0 is the amplitude, r_0 is the position of the center of the pump, $\sigma = 0.7$ μm is its spatial extension, and $\tau_0 = 1$ ps is its duration. This allows highlighting only a part of the whole dispersion (for example, only the interface states). The image in Fig. 3.11 is a cut of a 2D dispersion in the KMK' direction. Such representation allows to better visualize the edge of the Brillouin zone and the gap (shown by dashed white line). Panel (b) shows the dispersion of the states localized on the interface between two mutually inverted TMD analog lattices. To obtain it, the pump was centered on one of the interface pillars. The main intensity comes from the valley-polarized gap states (in the middle). However, the junction of two large pillars at the interface represents a potential trap even without taking into account the staggering inversion, and the localized states of this trap are also visible in panel (b) below the bulk band of panel (a). These states are not valley-polarized, because they are centered at the Γ point. Most interesting are the states in the central
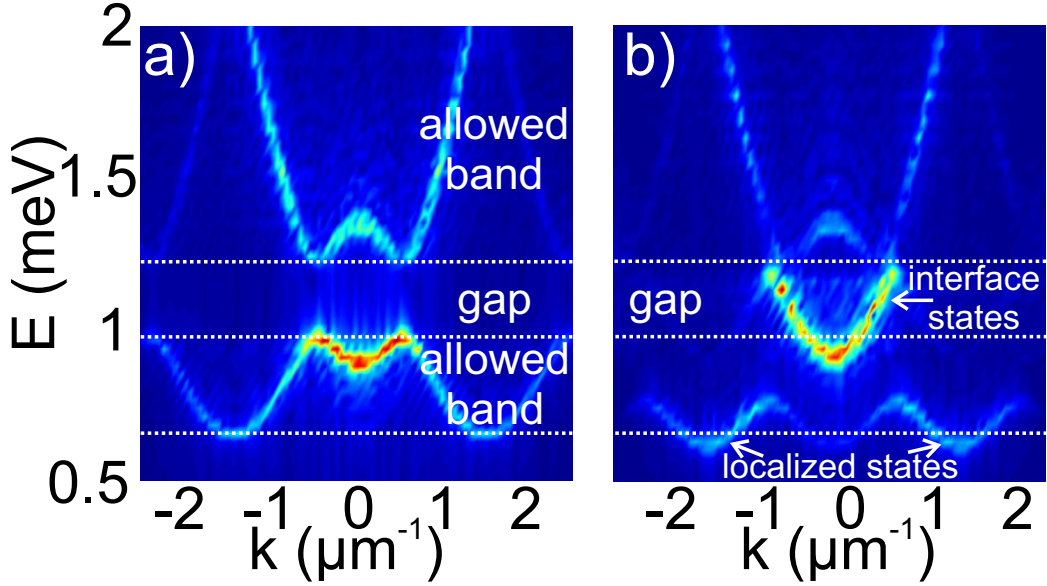
Figure 3.11: Dispersion of the a) bulk QVH and b) the QVH/QVH interface states in its gap. The gap is marked by a dashed white line.

gap, which clearly exhibit opposite group velocities for the K and K' valleys. To excite these interface states, the laser spot was localized at the interface. This also suppresses the excitation of the bulk, whose dispersion therefore does not appear on panel (b).

The above dispersions have been calculated to obtain images close to what can be measured in experiments with realistic parameters. Still, such dispersions can be compared with the tight-binding one in the spinless case [Fig. 3.7]. The elongation of the second band in Fig. 3.11 can be emulated in the TB model by adding second nearest neighbour hopping parameter. However, the tight-binding computation does not take into account the presence of higher energy bands ($p, d...$ bands) which are observable both in experiments [200] and in the above simulation (not shown). One can also note that the TB dispersion shown in Fig. 3.7 correspond to a projection in a ribbon geometry whereas Fig. 3.11 is a cut of a 2D dispersion.

3.3.3.2   Propagation on the interface: numerical experiments

While the TE-TM splitting was neglected for the calculation of the dispersion in Fig. 3.11 in order to obtain a clear image with a higher resolution, we have then included the TE-TM splitting in all numerical calculations presented below, both for QVH/QVH and QVH/QAH interfaces. All spatial images shown below are snapshots taken from the corresponding video files available as a supplemental material for the ref. [260]. These spatial images show the total intensity of emission, given by

Figure 3.12: Behavior at the 120° corners of polygonal interface a) QVH/QVH b) QVH/QAH. Red arrows show the propagation direction.

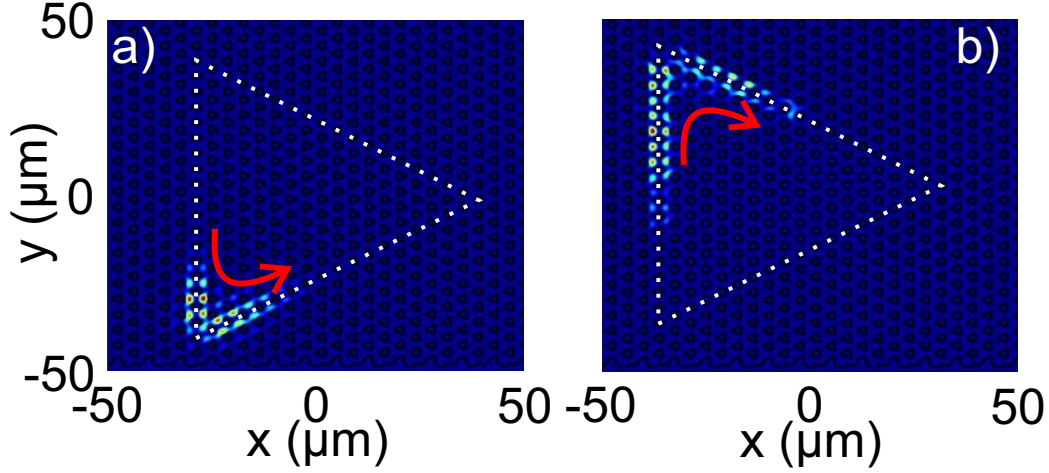$|\psi_+|^2 + |\psi_-|^2$, as a function of spatial coordinates x and y. The colormap is renormalized for each frame, so the overall decay is not visible. Since the duration of the simulations is several hundred picoseconds, observation of the propagation over the whole structure could be experimentally possible only in the most recent highest-quality microcavities, where the polariton lifetime reaches 270 ps [261]. However, propagation around one corner or through a single defect should be well observable in the structures of previous generation with $\tau = 30$ ps. In these simulations, the pulse duration has to be much longer than for the calculation of the dispersion: the energy width of the pulse has to be smaller than the gap. We have used a value of $\tau_0 = 36$ ps, as in previous similar works [212]. The spatial configuration of the pump operator is different for the QVH and QAH cases. For QVH, the choice of the valley is determined by the shape of the pump, which is therefore a large Gaussian spot $\sigma = 15$ μm, centered on a given valley in the reciprocal space by introducing spatial modulation $\exp(i\mathbf{Kr})$, which in experiments is obtained by the incidence angle of the pumping laser. For QAH, only one propagation direction is available and the shape of the spot does not play any role; we therefore excite a single pillar using $\sigma = 1$ μm.

120° corners.   Figure 3.12(a) demonstrates the behavior of interface states at the 120° corners (meaning that the propagation direction changes by 120°) of a polygonal interface between two mutually inverted TMD analog lattices. Such angle allows to have two interfaces of the same type (A-A and A-A or B-B and B-B). As can be seen from the figure and from the associated movie (see supplemental material of ref. [260], video file 1), there is no backscattering on such interface and the wavepacket, initially created at the interface states, continues its propagation
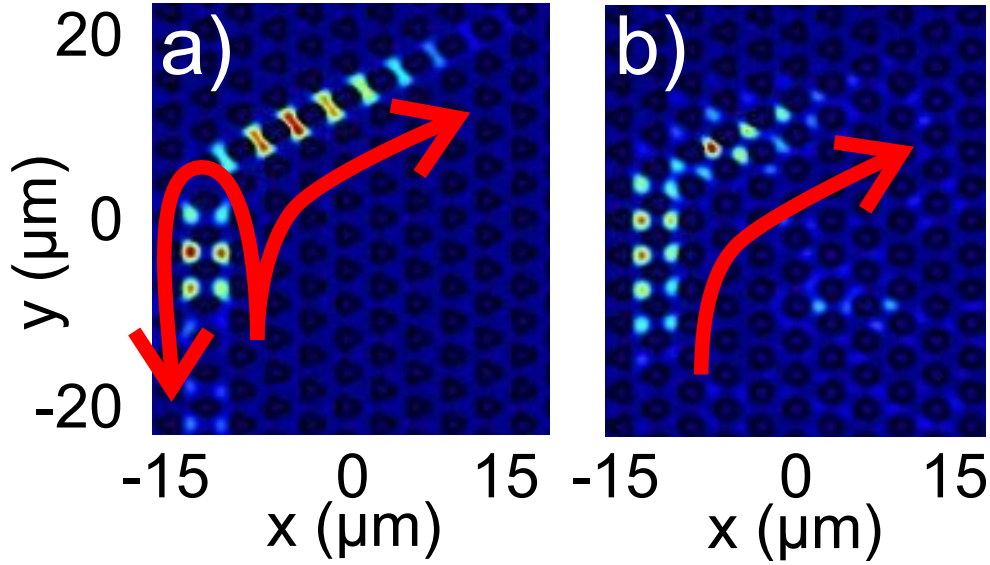
Figure 3.13: Conversion of the interface states at the 60° corners of polygonal interface a) QVH/QVH b) QVH/QAH. Red arrows show the propagation direction.

without being perturbed by such corner. Qualitatively, such corner acts like a mirror (formed by the periodic lattice), which redirects the wavepacket from the input interface state into the output interface state. Both propagation directions along the triangle are available by the choice of the initial valley excitation. Panel (b) shows the same configuration, but for an interface between the QVH/QAH phases. Here, no backscattering is possible for any type of corner, as we shall see below, because of the topological protection. The propagation direction is not defined by the excitation conditions (a single pillar of the interface is excited), but by the sign of the Zeeman splitting. However, a large gap is more difficult to obtain in the QAH phase [258], and therefore one can expect to have a larger excitation of the bulk in this case. As can be seen from the movie (see ref. [260], video file 3), it is impossible to distinguish the topologically protected QVH/QAH phase from the QVH/QVH interface which does not provide any topological protection. The absence of backscattering in one particular experiment does not mean that the system is protected completely, as we shall see below.

60° corners. Figure 3.13 shows a zoomed image of a more interesting configuration, corresponding to a 60° turn of the interface. Panel (a) shows the interface between the two QVH phases. For such angle, the interface changes type (from A-A to B-B or vice versa), which leads to several visible effects. First of all, the change of the interface type, similar to the change of dimerization order in the Su-Schrieffer-
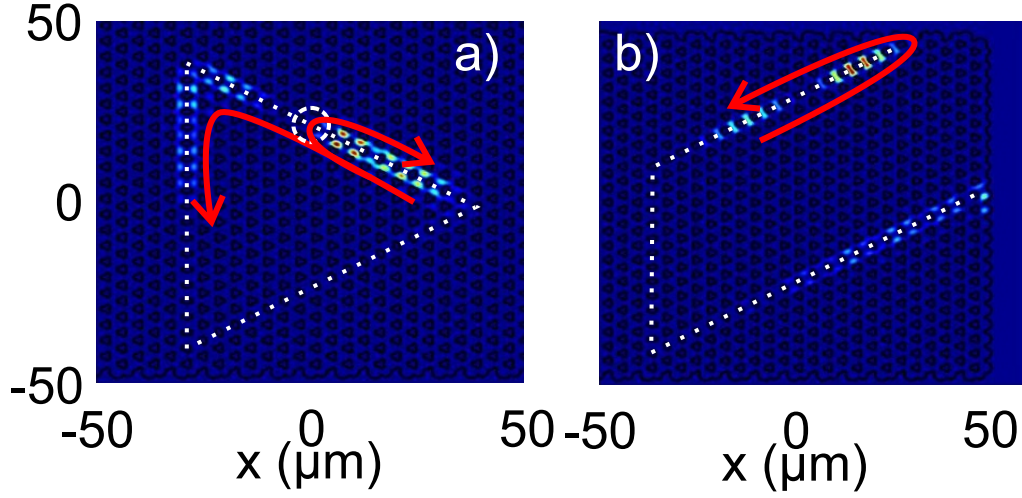
Figure 3.14: Sensitivity of the QVH interface states to the perturbations: backscattering a) on a localized defect b) at the boundary with the "vacuum". Red arrows show the propagation direction.

Heeger model [42], leads to the creation of a defect state (domain wall) between the two regions. This domain wall creates a strong backscattering for the wavepacket on the interface states, contrary to the 120° turn, where the backscattering was completely absent. Moreover, since the interface changes type, the nature of the state changes as well: from the "anti-bonding" state of the first interface (made of two pillars with a larger radius and therefore a lower energy), the state changes into the "bonding" state of the second interface (where there are two smaller pillars). The two red arrows mark the propagation direction for the backscattered part and the main part of the wavepacket. The propagation direction for both of them is clearly visible in the movie (see [260], video file 2).

In the QVH/QAH interface case, shown in Fig. 3.13(b), no backscattering is possible because of the topological protection, provided by the QAH phase, but the interface state also changes its nature at the 60° turn. However, because of the complicated mutual action of the TE-TM SOC and of the Zeeman splitting, it is more difficult to analyze from the spatial pattern of the total intensity. The study of such interface junctions in the perfect valley filter may be a subject for future works. While it is not so clear from the snapshot, the associated movie (see [260], video file 4) clearly shows the absence of backscattering at the junction.

QVH backscattering induced by a localised defect or the lattice boundary.
Finally, we have designed a special numerical experiment to show that the QVH states indeed do not provide topological protection from backscattering. Figure 3.14 shows two distinct situations. Panel (a) demonstrates that a localized defect (created

on a single pillar on the interface) leads to the backscattering of an important fraction of the wavepacket (red arrows), while at the same experiment the corners have shown no backscattering, and one might have concluded that the states are protected (see [260], video file 1). Panel (b) (which corresponds to the calculation of Fig. 3.13 at later times, see [260], video file 2) shows that the interface states can only exist on the interface between two inverted TMD analog lattices, and they cannot propagate at the boundary between the TMD analog and the "vacuum" (absence of pillars). Such boundary leads to complete reflection of the propagating wavepacket.

Topological effects for BECs in honeycomb lattices

Contents

As we have seen in the previous chapters, band topology has became these last years an important research field in various fermionic and bosonic systems. Another field of research, extremely fruitful, is the one dealing with collective effects.

In fermionic systems, the combination of non-trivial topology and many body effects led to the fractional quantum Hall effect [122], and more recently to the description of topological superfluids and superconductors [262, 263, 4, 264]. In the latter, the excitations are split off by the superconducting gap, which is topologically non-trivial for specific pairing, creating topological edge states. A vortex necessarily contains such edge states, which can be Majorana fermion bound states [265] protected by the particle-hole symmetry. The hypothetical non-Abelian statistics of these quasi-particles and the ability to braid them by manipulating vortex pairs renders topological superconductors very attractive for topological quantum computing [266].

In bosonic systems, the most well-known collective effect is the Bose-Einstein condensation [125, 137], leading to fascinating dynamical behaviour such as superfluidity [267], more generally, to the physics of bosonic quantum fluids [239, 268, 152]. Whereas stationary solutions of the non-linear Gross-Pitaevskii equation in periodic potentials have been studied theoretically in terms of Bloch waves [269, 270] previously, the physics of interacting BEC in topological systems is a new field of research which emerges thanks to the extension of topological concepts beyond condensed matter systems. So far, the concept of Chern number and chiral behaviour have been extended to Bogoliubov excitations in various configurations dealing with atomic, magnonic or non-linear photonic systems [271, 272, 273, 274, 275, 276, 277, 278].

Another interesting but less explored direction is the study of non-linear excitations, typical in BECs, in systems with non-trivial single particle band topology. For example several works appeared on the description of solitons in 1D [55, 59] or 2D systems with non trivial band topology. Propagative edge solitons [279, 280] and bistable behaviour [281] have been studied recently in polariton Chern insulator model. One should notice that non-linear edge solitons have also been studied in Floquet photonic topological insulator [91] in ref. [282].

In this chapter we consider the effect of band geometry or topology on the excitations of a BEC loaded in honeycomb lattice in different configurations. In the section 4.1 we consider a thermal equilibrium polariton condensate in the polariton Chern insulator introduced in the previous chapter. We study the interplay between spin-anisotropic interactions and the applied Zeeman field on the Bogoliubov excitations of the condensate. Then, in section 4.2 we present a similar study in the more experimentally realistic quasi-resonant excitation scheme which can lead to a full optical control of topological phase transitions without the need of an external Zeeman field. In the last section 4.3, we study quantized vortex excitations of a scalar condensate loaded in a staggered honeycomb potential. Interestingly, these non-linear excitations exhibit a winding-valley coupling in the bulk of the system allowing a robust chiral propagation along the interface between opposite staggered lattices.

4.1 Thermal equilibrium Bogoliubov excitations in polariton Chern insulator

Cavity polaritons have been well studied in different semiconductor materials and despite their finite and relatively short lifetime, their Bose-Einstein condensation close to thermal equilibrium has been observed in several works [132, 283, 284, 285] dealing with 2D cavities. One should notice, however, that in lattices the formation of gap solitons is much more favoured than the formation of a homogeneous condensate in the ground state [200, 286] because of the higher overlap of the negative-mass states with the excitonic reservoir and a longer lifetime of states with antisymmetric wave functions [287]. Similarly, the slow spin relaxation in the excitonic reservoir makes it difficult to achieve equilibrium between the two spin sub-systems, and prevents the observation of the predicted spin-Meissner effect [288]. These two aspects of real systems make the situation that we consider, namely a quasi-thermal equilibrium for spinor polaritons in a periodic lattice, quite unrealistic at the present stage of technology, but of a theoretical interest. However, similar conclusions can be achieved for quasi-resonant pumping, which will be the subject of the next section, corresponding to the optimal configuration for the experimental verification of our predictions.

We therefore consider that the polariton graphene is filled by a finite density of interacting polaritons at thermal equilibrium at $T = 0$K. The polaritons form a Bose-Einstein condensate which can be described within the mean field approximation by the spinor Gross-Pitaevskii equation. In the T-B approach GP equation can be written in the condensed form:

$$i\frac{\partial \Psi_i(\mathbf{r},t)}{\partial t} = \int \sum_j H_{ij}(\mathbf{k}')\widetilde{\Psi}_j(\mathbf{k}')e^{i\mathbf{k}'.\mathbf{r}}d\mathbf{k}' + \left(\alpha_1|\Psi_i|^2 + \alpha_2|\Psi_{i+(-1)^{(i+1)\mathrm{mod}2}}|^2 - \mu\right)\Psi_i(\mathbf{r},t)$$
(4.1)

where the kinetic term is written in $\mathbf{k}$ space. i index encodes the wavefunction component, H_{ij} are the matrix elements of the polariton graphene Bloch Hamiltonian defined in previous chapters. α_1 and α_2 are the interaction constants between particles with same spins and with opposite spins, respectively. These interaction constants in polaritonic systems are in general different [179], which means that the interactions are spin-anisotropic. The reason is that the exchange in the singlet configuration passes through dark excitonic states.

We are going to look for the solution of this equation including the condensate and its weak excitations which can be written as a 4-component spinor, taking into account sublattice and spin degrees of freedom:

$$\begin{aligned}\mathbf{\Psi}(\mathbf{r},t) &= (\Psi_A^+, \Psi_A^-, \Psi_B^+, \Psi_B^-)^T \\ &= \mathbf{\Psi}_0 + \mathbf{u}e^{i(\mathbf{k}.\mathbf{r}-\omega t)} + \mathbf{v}^*e^{-i(\mathbf{k}.\mathbf{r}-\omega t)}\end{aligned}$$
(4.2)

The first term $\mathbf{\Psi}_0 = (\Psi_{0,A}^+, \Psi_{0,A}^-, \Psi_{0,B}^+, \Psi_{0,B}^-)^T$ is the stationary part of the function. It holds the information about condensate's polarization for the two sublattices

(A/B) and obeys the normalization condition $|\mathbf{\Psi}_0|^2 = n$. For generality, the Bogoliubov coefficients $\mathbf{u}, \mathbf{v}$ are also bispinors of the form $(u_A^+, u_A^-, u_B^+, u_B^-)^T$. Here, the sublattice indexes are defined by A and B, while $\pm$ defines the polariton spin.

For the kinetic term, it is useful to write the above wavefunction in reciprocal space:

$$\widetilde{\mathbf{\Psi}}(\mathbf{k}', t) = \mathbf{\Psi}_0 \delta(\mathbf{k}') + \mathbf{u}\delta(\mathbf{k}' + \mathbf{k})e^{-i\omega t} + \mathbf{v}^*\delta(\mathbf{k}' - \mathbf{k})e^{i\omega t} \tag{4.3}$$

Inserting the stationary part of (4.2) and (4.3) in the GP equation (4.1) allows to find the chemical potential.

$$[H_{\mathbf{k}=\mathbf{0}} + H_{int}]\,\mathbf{\Psi}_0 = \mu\mathbb{1}_4\mathbf{\Psi}_0 \tag{4.4}$$

where $H_{\mathbf{k}=\mathbf{0}}$ is the momentum space Bloch Hamiltonian evaluated at $\mathbf{k} = 0$ and H_{int} is defined by:

$$H_{int} = \begin{pmatrix} \alpha_1|\Psi_{0,A}^+|^2 + \alpha_2|\Psi_{0,A}^-|^2 & 0 & 0 & 0 \\ 0 & \alpha_1|\Psi_{0,A}^-|^2 + \alpha_2|\Psi_{0,A}^+|^2 & 0 & 0 \\ 0 & 0 & \alpha_1|\Psi_{0,B}^+|^2 + \alpha_2|\Psi_{0,B}^-|^2 & 0 \\ 0 & 0 & 0 & \alpha_1|\Psi_{0,B}^-|^2 + \alpha_2|\Psi_{0,B}^+|^2 \end{pmatrix} \tag{4.5}$$

Due to the spin Meissner effect, the groundstate bispinor $\mathbf{\Psi}_0$ will take different forms depending on the strength of the Zeeman field. Then, introducing the whole expressions (4.2) and (4.3) and keeping only linear terms in $\mathbf{u}$ and $\mathbf{v}$ (Bogoliubov approximation as in subsection 2.1.3) leads to an eigenvalues problem for the dispersion and the eigenstates of the elementary low-amplitude excitations of the condensate which can be solved numerically:

$$M\begin{pmatrix} \mathbf{u} \\ \mathbf{v} \end{pmatrix} = \hbar\omega\begin{pmatrix} \mathbf{u} \\ \mathbf{v} \end{pmatrix} \tag{4.6}$$

where M is a 8×8 matrix of the block form:

$$M = \begin{pmatrix} H_{\mathbf{k}} + D - \mu\mathbb{1}_4 & A \\ -A^\dagger & -(H_{-\mathbf{k}}^T + D - \mu\mathbb{1}_4) \end{pmatrix} \tag{4.7}$$

(where $T, \dagger$ symbols denote the transpose and conjugate-transpose transformation respectively). The matrices D and A come from the non-linear terms and are defined as follows.

$$D = \begin{pmatrix} 2\alpha_1|\Psi_{0,A}^+|^2 + \alpha_2|\Psi_{0,A}^-|^2 & 0 & 0 & 0 \\ 0 & 2\alpha_1|\Psi_{0,A}^-|^2 + \alpha_2|\Psi_{0,A}^+|^2 & 0 & 0 \\ 0 & 0 & 2\alpha_1|\Psi_{0,B}^+|^2 + \alpha_2|\Psi_{0,B}^-|^2 & 0 \\ 0 & 0 & 0 & 2\alpha_1|\Psi_{0,B}^-|^2 + \alpha_2|\Psi_{0,B}^+|^2 \end{pmatrix} \tag{4.8}$$

$$A = \begin{pmatrix} \alpha_1\Psi_{0,A}^{+2} & \alpha_2\Psi_{0,A}^-\Psi_{0,A}^+ & 0 & 0 \\ \alpha_2\Psi_{0,A}^-\Psi_{0,A}^+ & \alpha_1\Psi_{0,A}^{-2} & 0 & 0 \\ 0 & 0 & \alpha_1\Psi_{0,B}^{+2} & \alpha_2\Psi_{0,B}^-\Psi_{0,B}^+ \\ 0 & 0 & \alpha_2\Psi_{0,B}^-\Psi_{0,B}^+ & \alpha_1\Psi_{0,B}^{-2} \end{pmatrix} \tag{4.9}$$

One can notice that the block A couples two Bloch Hamiltonians defined at $\mathbf{k}$ and $-\mathbf{k}$, Bogoliubov eigenstates will therefore be a mixture of the opposite linear Bloch states. One defines the Bogoliubov eigenstates $|\Phi_{n,\mathbf{k}}\rangle$ as:

$$|\Phi_{n,\mathbf{k}}\rangle = \begin{pmatrix} \mathbf{u} \\ \mathbf{v} \end{pmatrix} = (u_a^+, u_a^-, u_b^+, u_b^-, v_a^+, v_a^-, v_b^+, v_b^-)^T \tag{4.10}$$

Moreover, the normalisation condition, required for the Bogoliubov transformation to be canonical (namely to keep bogolons as bosons), reads [289, 137]:

$$\sum_{1 \leq i \leq 4} |u_i|^2 - |v_i|^2 = 1 \tag{4.11}$$

where i index labels the different $u_i(v_i)$ components of an eigenstate. This condition physically signifies that the creation of one bogolon corresponds to the creation of a quanta of energy ω.

In the following subsections, we calculate and analyze the dispersions and the corresponding eigenstates in different cases: first without a magnetic field, and then under weak and strong fields. Under a magnetic field when a gap will be opened in the dispersion we compute the Chern numbers. For this task, the peculiar form of M and its eigenstates has to be taken into account to compute the Berry connection. It is typically done by introducing a matrix $\tau_z = \sigma_z \otimes \mathbb{1}_4$ directly in the definition of the Berry connection as first noticed in ref. [271] and commonly used [274, 272, 273, 290]. This gives

$$\boldsymbol{\mathcal{A}}_n(\boldsymbol{k}) = i \langle \Phi_{n,\mathbf{k}}| \nabla_{\mathbf{k}} \tau_z |\Phi_{n,\mathbf{k}}\rangle \tag{4.12}$$

The Chern numbers can then be computed as usual using $C_n = \frac{1}{2\pi} \int_{BZ} \nabla_{\mathbf{k}} \times \boldsymbol{\mathcal{A}}_n(\boldsymbol{k}) d\mathbf{k}$. We use the same approach (from ref. [224]) as the one used in the linear regime to compute them numerically.

Moreover, the Bogoliubov approach typically gives rise to symmetric positive and negative energy branches and their associated Chern numbers are opposite ($C_n = -C_{-n}$) [271, 291]. Therefore, in what follows, we will concentrate on the positive part of the spectrum and analyze its associated topological invariants. For this task, we define two Chern invariants. Each of them is the sum of the Chern numbers of the two branches forming "valence" and "conduction" bands (below and above the gap):

$$C_V = C_1 + C_2, \quad C_C = C_3 + C_4 \tag{4.13}$$

4.1.1 Zero magnetic field

Because of the spin-anisotropic interactions the minimal energy configuration of a polariton condensate corresponds to a linearly polarized state [183] [See subsection 2.2.2]. For the sake of definiteness, we choose at $k = 0$: $\boldsymbol{\Psi}_0 = \sqrt{n/4}(1, 1, 1, 1)^T$ which gives a well defined (horizontal) orientation of the in-plane polarization. In this configuration, the chemical potential is given by:

$$\mu = (\alpha_1 n + \alpha_2 n)/2 - 3J \tag{4.14}$$

where n is the density, J is the TB tunneling coefficient. Using the Bogoliubov formalism, we compute the bogolon dispersion and the corresponding eigenstates. The results for the zero magnetic field case are shown in Fig. 4.1(a),(b),(e),(f).

First, we analyze the simpler case of $\alpha_2 = 0$, which is still spin-anisotropic since $\alpha_1 \neq \alpha_2$. Panel (a) of Fig. 4.1 shows the bogolon dispersion, and panel (e) – the polarization texture: white arrows indicate the in-plane pseudospin direction and color shows the linear (H/V) polarization degree. Close to Γ, the two bogolon dispersions are TE and TM polarized. In other words, the TE-TM symmetry of the system is not broken by the presence of a condensate polarized along a well-defined spatial direction. The reason for this is that α_2 is zero, as we shall see below.

Due to interactions, close to $k = 0$ these two dispersions depend linearly on the wave vector, with a speed of sound given by $c_{te,tm} = \sqrt{\alpha_1 n / m_{te,tm}}$, and the energy splitting (the magnitude of the TE-TM effective field) is also linear in k. At larger momenta, depending on the parameters, one may recover a parabolic dispersion with a parabolic splitting. Close to the K point, the preserved TE-TM symmetry of the system makes the dispersion and polarization structure similar to the ones obtained for polariton graphene with TE-TM splitting in the linear regime (see Fig. 3.3(a)): there is a linear intersection in K point, and 3 additional linear intersections appear because of the trigonal warping (see also the left panel of Fig. 4.2). The effective field texture around the K point is the one of the Dresselhaus field, as shall be discussed below. The case with $\alpha_2 \neq 0$ is shown on the Figs. 4.1(b),(f). We have chosen to use $\alpha_2 = -0.2\alpha_1$ for all calculations, although the exact value depends on the configuration (in particular, on the detuning). In general, α_2 is usually negative [182] and small with respect to α_1. The scattering rates leading to the creation of a bogolon with polarisations parallel and perpendicular to the one of the condensate are therefore different, which affects the sound velocities of the dispersions at $k = 0$. The eigenstates close to the Γ point correspond to these two polarisations, with their slope given by $c_\parallel = \sqrt{(\alpha_1 + \alpha_2)n/m^*}$ and $c_\perp = \sqrt{(\alpha_1 - \alpha_2)n/2m^*}$ respectively (where m^* is the polariton effective mass (2.43)). The polarization texture is hence strongly modified in the center of the Brillouin zone, which is the consequence of the symmetry breaking by an in-plane field, see Fig. 4.1(f).

Due to this symmetry breaking, the form of the bands changes: the trigonal warping initially present around the K point, as in the linear case, can disappear (Fig. 4.1(b)). In this case two Dirac cones remain instead of four around each K point. The evolution of the fine energy structure near K point when α_2 is switched on is shown in figure 4.2. One can see that with the increase of α_2 the central Dirac cone and the additional one oriented in the k_y direction merge with each other and disappear. This transition from four to two Dirac cones can be described in term of their respective associated Berry phases ($\pm\pi$) as $(+, +, +, -) \longrightarrow (+, +)$ and is analogous to the one discussed in ref. [222] (Figs. 1 and 7 of that paper) for bilayer graphene. In our case however, this effect is induced by the mean field spin anisotropic interaction rather than lattice distortion. It is important to note that whereas the number of Dirac cones change, the total Berry flux (2π) is conserved.

Moreover, the branches of the same band cross each other, which modifies the
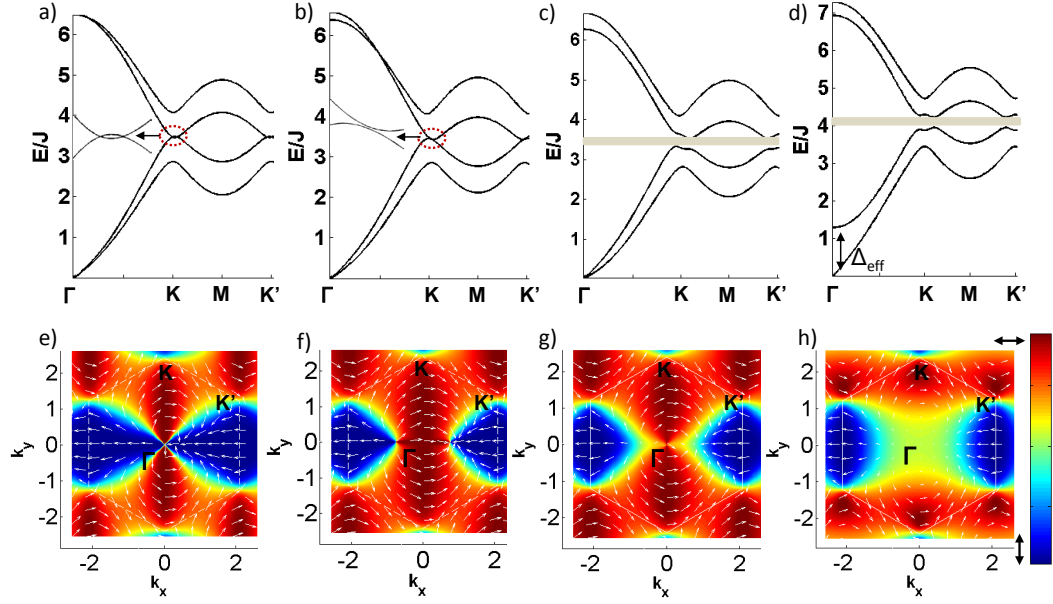
Figure 4.1: **Thermal equilibrium bogolon dispersions.** Band structures and polarization textures of Bogoliubov excitations without and with applied magnetic field. (a)-(b) Energy dispersions without applied magnetic field: $\alpha_2 = 0, -0.2\alpha_1$ respectively. (c) Dispersions with applied magnetic field $B < B_C$, (d) with $B > B_C$. (e)-(f)-(g)-(h) Corresponding polarization and pseudospin textures. The colors represent the linear polarization degree while the white arrows show the corresponding pseudospin orientation of the lowest energy state. (Set of parameters: $\delta J = 0.2J$, $\alpha_1 n = J$)
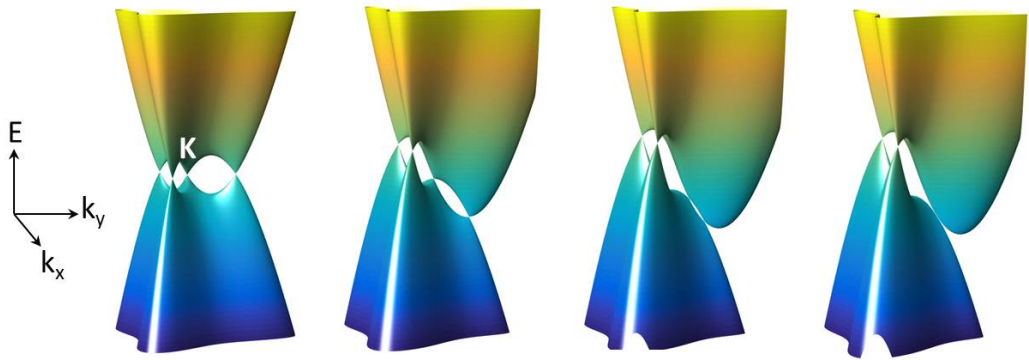
Figure 4.2: **Dirac cones merging.** 3D zoom of the dispersion near K point when α_2 is switched on. From left to right: $\alpha_2 = 0$ to $\alpha_2 = -0.2\alpha_1$, other parameters are fixed: $\delta J = 0.2J$, $\alpha_1 n = J$, no Zeeman field $B = 0$)

polarization texture of each branch. We point here that this effective field does not open a gap, moreover, because the contribution of α_2 changes the energy of the condensate, it can even lead to the closing of a gap, destroying the effect of the applied magnetic field. This will be discussed in details in further sections.

Indeed, in the following, we study the polariton graphene under an applied magnetic field, which overcomes the anisotropy induced by nonzero α_2, and the effective in-plane field in $K - K'$ valleys come back in its Dresselhaus-like form.

4.1.2   Nonzero magnetic field

As in the linear case discussed in Chapter 3, we apply an external magnetic field in order to open a gap and compute the Chern numbers characterizing the band structure of bologons. For this we have to remind the spin-Meissner effect, predicted for polariton condensates in planar cavities [See 2.2.2.3] which is linked to different condensate polarization configurations. An applied magnetic field B oriented in the growth direction leads to the polariton Zeeman splitting characterized by $-\Delta\sigma_z$ term in the Hamiltonian. (Note: in this section based on a self-consistent work performed at the beginning of this thesis [276] we use this convention of sign to be consistent with the definition of the spin-Meissner effect 2.2.2.3 [194], this results in opposite Chern numbers in the non-interacting limit with respect to the one discussed in section 3.1 but does not change the general meaning of the topological transition induced by the interactions.). $\Delta = |X|^2 g_X \mu_B B/2$, where X is the exciton Hopfield coefficient, g_X is the exciton g-factor, μ_B is the Bohr magneton.

Another aspect, which will play a key role in the following, is that the energy renormalization induced by the interactions is larger for the bogolon states than for the condensate itself. Indeed, if one neglects α_2, in the absence of the magnetic field the condensate is shifted by $\alpha_1 n/2$ with respect to the non-interacting case at $k = 0$, whereas for large wavevectors the bogolon energy is shifted by $2\alpha_1 n/2$ with respect to the corresponding non-interacting dispersion, as one can directly see from the Bogoliubov formula for the excitations $\hbar\omega = \sqrt{(\hbar^2 k^2/2m)^2 + 2\alpha_1 n/2(\hbar^2 k^2/2m)}$, where the energy $\hbar\omega$ is measured from the chemical potential, itself being $\alpha_1 n/2$. The consequence is that the self-induced Zeeman field is larger for the excited states than for the ground state, while the Zeeman splitting induced by an applied field remains the same (unless the excitonic fraction changes significantly). Hence, in the magnetic field range $2B_C > B > B_C$, the bogolon dispersions with opposite circular polarizations should cross each other. The total Zeeman field (applied and self-induced) at large wave vectors is in that case opposite to the one in the ground state.

4.1.2.1   Weak magnetic field $B < B_C$

We now turn back to the polariton graphene case considering an applied magnetic field weaker than the critical field B_C. In such case, the condensate at equilibrium

is elliptically polarized, with the polarization spinor being:

$$\boldsymbol{\Psi}_0 = \sqrt{n/2} \begin{pmatrix} \cos\theta \\ \sin\theta \\ \cos\theta \\ \sin\theta \end{pmatrix} \quad , \quad \theta = \frac{1}{2}\arcsin\sqrt{1 - \left(\frac{B}{B_C}\right)^2} \tag{4.15}$$

By using this spinor in the expression of the condensate wavefunction $\boldsymbol{\Psi}$, we find the chemical potential:

$$\mu = \frac{\alpha_1 + \alpha_2}{2}n - 3J \tag{4.16}$$

Then, we can compute the matrix for the Bogoliubov coefficients, that we can diagonalize in order to get the energy dispersions and polarization texture (Fig. 4.1(c),(g)). In this section and the following one we restrict the consideration to the case of $\delta J < J/2$, typical for polariton graphene etched out of a planar cavity.

Figure 4.1(c) demonstrates a gap opening at K and K', similar to the linear case. Here, the self-induced Zeeman field completely compensates the external magnetic field around the Γ point. The spin-Meissner effect is present, like in a planar microcavity without a periodic potential. The lower branches remain linear near the center of Brillouin zone.

The presence of the gap allows us to compute the band Chern numbers $(C_{C(V)})$ by using the gauge-invariant approach described above (4.12). In the weak field regime ($\Delta \ll B_C < \alpha_1 n/2$), the calculated Chern numbers $C_C = -2$, $C_V = +2$ are inverted with respect to the non-interacting case, where they have the values $C_C = +2$, $C_V = -2$, because the non-interacting case by definition corresponds to the opposite limit of large magnetic fields $\alpha_1 n = 0 \ll \Delta$. This topological inversion occurs because of the self-induced Zeeman splitting at high wavevectors, which is opposite to the applied magnetic field and strongly exceeds it. The system is in a different topological phase with inverted propagation direction of the chiral edge states, as compared with the linear case.

We stress here that if α_2 becomes large (for example, in the regime of polariton Feshbach resonance [180, 181]), the strength of the external field has to be large enough ($\Delta > |\alpha_2| n$) to overcome the anisotropy effect described in the previous section, in order to open a gap and obtain this topological insulating phase.

4.1.2.2 Large magnetic field $B > B_C$

In this subsection, we consider the case of magnetic field above the critical value $B > B_C$. Hence, a Zeeman splitting appears between the two lower branches in the Γ point, where interactions do not compensate the magnetic field anymore. The condensate polarization becomes circular in Γ: $\boldsymbol{\Psi}_0 = \sqrt{n/2}(1,0,1,0)^T$ and the chemical potential becomes $\mu = \alpha_1 n - \Delta - 3J$. We can observe that the chemical potential now depends of the applied magnetic field. Using the Bogoliubov approach as above, we find the eigenenergies and the eigenstates for this configuration. One of the two lower branches (polarized opposite to the condensate) becomes parabolic

in Γ and the degeneracy is lifted (see Fig. 4.1(d),(h)). The Zeeman splitting in the Γ point is proportional to the difference between B and B_C, exactly as in the spin-Meissner effect in planar cavities:

$$\Delta_{eff} = \Delta - \Delta_C = |X|^2 g_X \mu_B B_{eff}/2 \tag{4.17}$$

As we can see on Fig. 4.1(d), a gap opens between the valence and conduction bands. For B just over B_C, the topology of the bands ($C_C = -2$, $C_V = +2$) is still inverted with respect to the non-interacting case. Since the gap does not close at B_C, the band topology cannot change, and this result is expected. However, when increasing the magnetic field again, the real Zeeman energy continues to rise whereas the self-induced Zeeman field, created by the interactions, is saturated. Consequently, there exists a threshold field $B = B_S$, where the net Zeeman field at K and K' cancels and the gap closes and immediately re-opens when $B > B_S$ with an inverted topology of the bands, associated with a change of the signs of the Chern numbers ($C_C = +2$, $C_V = -2$). This topology now corresponds to the non-interacting case. The phenomenon of the topology inversion is entirely due to the fact that interaction energy with the condensate is larger for large wavevector bogolons than in the center of Brillouin zone.

By writing the matrix M in the upper B_C case at K point, we can find the analytical expression for the threshold magnetic field, at which the gap closes:

$$\Delta_S = \frac{1}{2} \left(\alpha_1 n - \alpha_2 n - 3J \pm \sqrt{6J\alpha_1 n + 9J^2} \right) \tag{4.18}$$

$$B_S = 2 \frac{\Delta_S}{|x|^2 g_X \mu_B} \tag{4.19}$$

4.1.3 Discussion

In the previous subsections, we have demonstrated that a topological inversion occurs at a threshold magnetic field B_S. The inversion of the topology at $B = B_S$ can be observed either varying the magnetic field or the polariton density. Whatever the density, if it is fixed, one can always increase the magnetic field to achieve the threshold value giving the inversion. If one fixes the magnetic field at some value, it is possible to observe the transition in the opposite direction: from the normal topology of the non-interacting system to inverted topology of the strongly-interacting system. Indeed, in polaritonic systems, the main experimentally adjustable parameter is the optical pumping, which controls the creation of polaritons, while their lifetime is generally fixed by the properties of the cavity. The evolution of the gap as a function of the condensate density is shown on the Fig. 4.3, where we can observe that the gap closes at a critical density n_S. The black solid line corresponds to the realistic value of $\alpha_2 = -0.2\alpha_1$ (the same as in previous sections), while the red dashed line has been plotted with $\alpha_2 = -0.5\alpha_1$, in order to clearly demonstrate
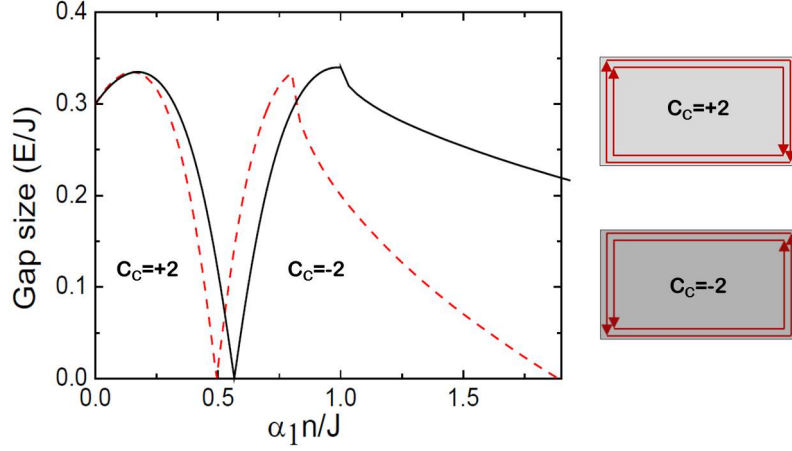
Figure 4.3: **Interaction induced topological inversion.** Left panel: plot of the gap value under a constant magnetic field as a function of the density. The gap closes at the critical density $n = n_S$. (Parameters $\delta J = 0.2J$, $\Delta = 0.6J$, black solid line: $\alpha_2 = -0.2\alpha_1$, red dashed line: $\alpha_2 = -0.5\alpha_1$). Right: Illustration of the edge states at the boundary of the sample.

the suppression of the topological insulator behaviour by the anisotropy induced by the spin-anisotropic interactions of the condensate and its fixed linear polarization. Indeed, for any value of the applied magnetic field, one can always increase the density and close the gap via $\alpha_2 n$. Thus, the effect of this constant, which is usually relatively weak, can appear critical in certain configurations.

In the simplest configuration of relatively weak interactions, where $\alpha_1 n << J$, we can derive a simpler expression for the threshold magnetic field at which the inversion occurs, using the Taylor series expansion:

$$\Delta_S = \frac{2\alpha_1 - \alpha_2}{2} n \qquad (4.20)$$

This result can be rewritten to give the threshold density as a function of an applied magnetic field:

$$n_S = \frac{2\Delta}{2\alpha_1 - \alpha_2} \quad , \quad \Delta = |x|^2 g_x \mu_B \frac{B}{2} \qquad (4.21)$$

For $n < n_S$, the topology of Bogoliubov excitations is the same as in the linear case. The topology of the bare dispersion is transferred to the bogolon dispersion, as it has been already shown for atomic systems [272]. Nevertheless, in the case of polaritons with their spin-anisotropic interaction and the resulting self-induced Larmor precession, the topology of the bogolon dispersion is inverted at the threshold density $n = n_S$ (Fig. 4.3). This result implies the inversion of the propagation direction of the topologically protected edge states.

The potential of polariton graphene is therefore confirmed by the coexistence of two dissipation-less phenomena, which are the superfluidity of the condensate and

the existence of the topologically protected edge states. It will be especially useful to study the case of resonant pumping, which is the easiest feasible experiment to study the macro-occupied states in polaritonic systems.

4.2   Bogoliubov excitations in the resonant pump regime

In what follows, we concentrate on the experimentally realistic configuration of a resonantly driven photonic (polaritonic) lattice [200, 203], including finite particle lifetime, without any applied magnetic field and demonstrate the all-optical control of the band topology. We show that the topologically trivial band structure becomes non-trivial under resonant circularly polarized pumping at the Γ point of the dispersion. A self-induced topological gap opens in the dispersion of the elementary excitations. The tuning of the pump intensity allows to go through several topological transitions demonstrating the chirality inversion.

A coherent macro-occupied state of exciton-polaritons is usually created by resonant optical excitation. This regime is well described in the mean-field approximation [171, 197] [2.2.2]. We can derive the driven tight-binding Gross-Pitaevskii equation in this honeycomb lattice for a homogeneous laser pump F ($\hbar = 1$).

$$i\frac{\partial}{\partial t}\Psi_i = \int \sum_j H_{ij}(\mathbf{k}')\widetilde{\Psi}_j(\mathbf{k}')e^{i\mathbf{k}'\cdot\mathbf{r}}d\mathbf{k}' + F_i e^{i(\mathbf{k}_p\cdot\mathbf{r}-\omega_p t)}$$
$$+ \left(\alpha_1|\Psi_i|^2 + \alpha_2|\Psi_{i+(-1)^{(i+1)\mathrm{mod}2}}|^2 - i\gamma_p\right)\Psi_i \qquad (4.22)$$

where i, j indices runs from 1 to 4 corresponding to the four wavefunction components $(\Psi_A^+, \Psi_A^-, \Psi_B^+, \Psi_B^-)$. H_{ij} are the matrix elements of the tight-binding Hamiltonian *without the Zeeman term* on the diagonal ($\Delta = 0$). Ψ_i are the components of the coherent macro-occupied state wave function. α_1 and α_2 are the interaction constants between particles with the same and opposite spins respectively. γ_p is the linewidth related to (spin-independent) polariton lifetime (τ_p), which allows to take the dissipation into account. F_i is the pump amplitude. ω_p and $\mathbf{k}_p$ are the frequency and wavevector of the pump mode. In the following, we consider a homogeneous pump at $k = 0$ (pumping beam perpendicular to the cavity plane) , which implies that its amplitude on A and B pillars is the same. However, the spin projections F_s^+ and F_s^- (where s refers to the sublattice index), determining the spin polarization of the pump, can be different. Using the sublattice and the spin indices (s and σ), the quasi-stationary driven solution has the same frequency and wavevector as the pump ($\Psi_s^\sigma = e^{i(\mathbf{k}_p\cdot\mathbf{r}-\omega_p t)}\Psi_{p,s}^\sigma$) and satisfies the equations:

$$\left(\omega_p + i\gamma_p - \alpha_1|\Psi_{p,s}^\sigma|^2 - \alpha_2|\Psi_{p,s}^{-\sigma}|^2\right)\Psi_{p,s}^\sigma + f_{k_p}J\Psi_{p,-s}^\sigma + f_{k_p}^\sigma\lambda_p\Psi_{p,-s}^{-\sigma} = F_s^\sigma \quad (4.23)$$

The tight-binding terms ($f_{k_p}, f_{k_p}^\sigma$) of the polariton graphene induce a coupling between the sublattices and polarizations. We compute the dispersion of the elementary excitations using the standard wave function of a weak perturbation

$(|\mathbf{u}|, |\mathbf{v}| \ll |\boldsymbol{\Psi}_p|)$:

$$\boldsymbol{\Psi} = e^{i(\mathbf{k}_p.r - \omega_p t)}(\boldsymbol{\Psi}_p + \mathbf{u}e^{i(\mathbf{k}.r - \omega t)} + \mathbf{v}^* e^{-i(\mathbf{k}.r - \omega^* t)}) \tag{4.24}$$

where $\boldsymbol{\Psi}_p = (\Psi_{p,A}^+, \Psi_{p,A}^-, \Psi_{p,B}^+, \Psi_{p,B}^-)^T$, $\mathbf{u}$ and $\mathbf{v}$ are vectors of the form $(u_A^+, u_A^-, u_B^+, u_B^-)^T$. Using the same method as in the thermal equilibrium case, we arrive to the following matrix to diagonalize:

$$M = \begin{pmatrix} H_{\mathbf{k_p}+\mathbf{k}} + D_p - \omega_p \mathbb{1}_4 & A_p \\ -A_p^\dagger & -(H_{\mathbf{k_p}-\mathbf{k}}^T + D_p - \omega_p \mathbb{1}_4) \end{pmatrix} \tag{4.25}$$

where D_p and A_p are defined as in Eqs. (4.8), (4.9) with $\Psi_{p,i}$ replacing $\Psi_{0,i}$.

Note that Eqs. (4.23) and (4.25) are written for an arbitrary pump wave vector k_p. In the following, we consider a pump resonant with the energy of the bare lower polariton dispersion branch in the Γ point ($\omega_p = -f_\Gamma J = -3J$ and $k_p = 0$), which implies the stability of the elementary excitations ($\Im[\omega] < 0$) and does not modify the Brillouin zone with respect to the linear case.

4.2.1 Topological phase diagram

A circularly polarized pump induces circularly polarized macro-occupied state ($n^- = 0$), and $n = n^+ = n_A^+ + n_B^+ = |\Psi_{p,A}^+|^2 + |\Psi_{p,B}^+|^2$. Combined with spin anisotropic interactions, it leads to a Self-Induced Zeeman (SIZ) splitting which breaks time reversal symmetry. A simple analytical formula of the k-dependent SIZ splitting between the two lower dispersion branches is obtained by neglecting the SOC ($\lambda_p = 0$):

$$\Omega_{SI} = \omega_p + |f_k| + \sqrt{(\omega_p + |f_k|J - 2\alpha_1 n_{A/B}^+)^2 - (\alpha_1 n_{A/B}^+)^2}$$

(In the expression for the self-induced field at the Γ point $\Omega_{SI}(\Gamma) = \sqrt{3}\alpha_1 n/2$ the factor $1/2$ comes from the presence of two sublattices and the $\sqrt{3}$ appears from resonant pumping, as compared with a blue shift of an equilibrium condensate $\mu = \alpha n$.) One of the key differences with respect to the magnetic field induced Zeeman field is the SIZ dependence on the wavevectors and energies of the bare modes. This dependence has already been shown to lead to the inversion of the effective field sign at the K point (and thus the inversion of the topology) when both applied and SIZ fields are present in a Bose-Einstein condensate in the previous subsection.

The figure 4.4(a) shows the diagram of topological phases under resonant pumping (versus the SIZ) which is quite similar to the one under magnetic field [See Fig. 3.4(a)] (the 2D dispersions are also pretty similar to the ones in the linear regime [See Figs. 3.5] and are not shown here).

The only difference with respect to the linear case concerns the opening of the two additional gaps which does not take place at the same pumping values, because of the difference between the SIZ fields in the upper and lower bands. The figure 4.4(b) shows the magnitude of the different gaps multiplied by the sign of the C_n
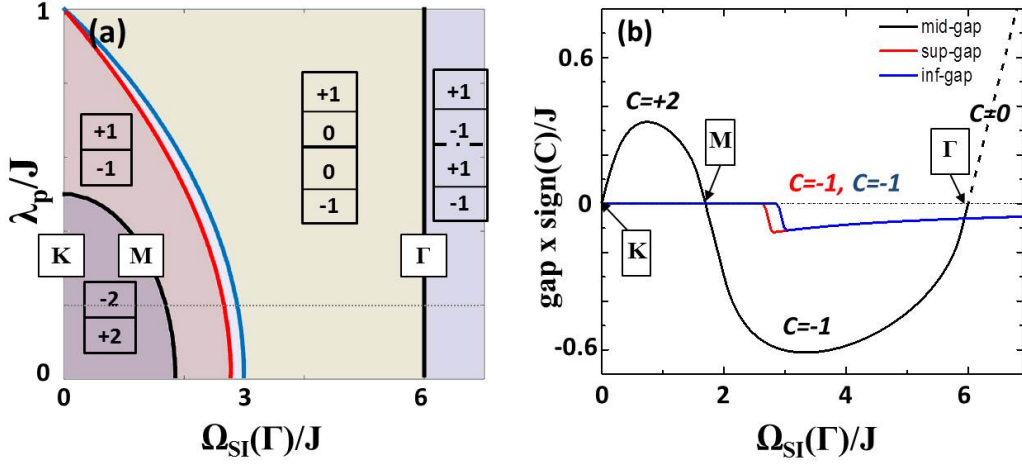
Figure 4.4: **All-optical topological phase transitions.** (a) Topological phase diagram in the resonant pump regime versus the TE-TM SOC and SIZ. (b) Gap sizes and sign evolution along a path of constant SOC $\lambda_p = 0.2J$ (dashed line in panel (a)). The red and blue curves correspond to the opening of additional gaps.

of the valence band ($C = \sum_{i=1}^{n} C_n$) [33] for a given value of the SOC, a quantity highly relevant experimentally. In [200, 203] J is of the order or 0.3 meV, whereas the mode linewidth is of the order of 0.05 meV. Band gaps of the order of 0.2 J should be observable. Also the SIZ magnitude shown on the x-axis (below 1.5 meV) is compatible with the experimentally accessible values. So in practice the topological transition is observable together with the specific dispersion of the edge states in the different phases which are presented in Figs 4.5.

We would like to note that the emergence of topological effects driven by inter-actions in bosonic systems has already been theoretically proposed, such as non zero Berry curvature in a Lieb lattice filled by atomic condensates [290] and topological Bogoliubov edge modes in two different driven schemes based on Kagome lattices [275, 273] with scalar particles.

4.2.2   Bogoliubov edge states

To demonstrate one-way edge states in the tight-binding approach, we derive a $8N \times 8N$ Bogoliubov matrix for a polariton graphene stripe, consisting of N coupled infinite zig-zag chains following the procedure of subsection 3.2.2. For this, we set a basis of Bogoliubov Bloch waves ($u_{A/B,n}^{\pm}, v_{A/B,n}^{\pm}$) where n index numerates stripes, and k_y is the quasi-wavevector in the zigzag direction. The diagonal blocks describe coupling within one chain and are derived in the same fashion as the M matrix in the previous section, coupling between stripes is accounted for in subdiagonal blocks.

Figures 4.5(a,b) show the results of the band structure calculation for two differ-
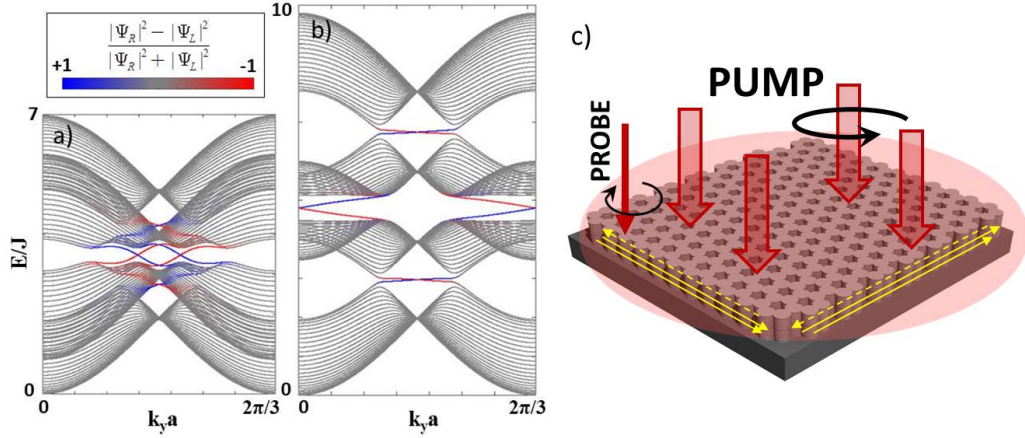
Figure 4.5: **Bogoliubov edge states.** (a,b) Band structures of a graphene ribbon in two different phases. Blue and red colors refer to the states localized on the right and left edges. Parameters: $\lambda_p = 0.2J$ and (a) $\alpha_1 n = 1J$, (b) $\alpha_1 n = 4J$. (c) Real space sketch of the experimental setup. The yellow arrows represent the edge states when $C = +2$ (dashed ones when $C = -1$).

ent values of $\alpha_1 n$. The degree of localization on edges is calculated from the wave function densities on the edge chains $|\Psi_R|^2$ and $|\Psi_L|^2$ (left/right, see inset), and is shown with colour, so that the edge states are blue and red.

In Fig. 4.5(a) there is only one topological gap characterized by a Chern number $+2$ and hence there are two edge modes on each side of the ribbon. In Fig. 4.5(b), we can observe three topological gaps with the Chern number of the top and bottom bands being ± 1 respectively. Each of them is characterized by the presence of only one edge mode on a given edge of the ribbon, and the group velocities of the modes are opposite to the previous phase: the chirality is controlled by the intensity of the pump. This inversion, associated with the change of the topological phase ($|C| = 2 \rightarrow 1$), is fundamentally different from the one discussed in the previous section, observed for the same phase ($|C| = 2$).

This optically-controlled transition allows to observe the inversion of chirality for weak modulations of a TR-symmetry breaking pump around a non-zero constant value, which can also possibly be used for amplification. The inversion of chirality of center gap edge states (Figs. 4.5(a,b)) should be observable in a pump-probe experiment as shown by the numerical simulation presented below. A sketch of the experiment using a σ^+ and a σ^- polarized lasers (the homogeneous pump and the localized probe) is presented on Fig. 4.5(c). One should notice that we can also obtain the inverted phases more conventionally by inverting the direction of the self-induced Zeeman field which is controlled by the circularity of the homogeneous pump.
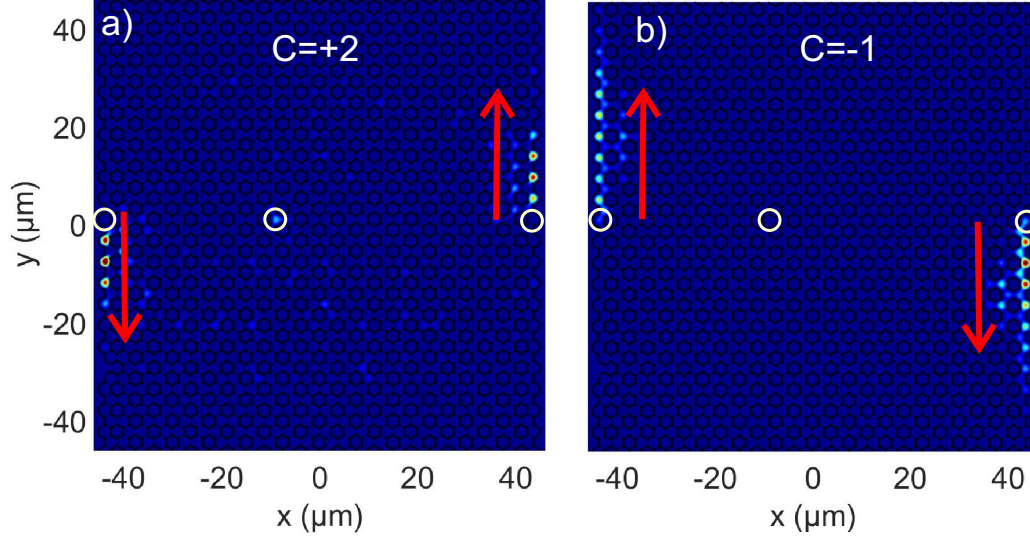
Figure 4.6: Calculated images of emission from the surface states (a) $\Omega_{SI} = 0.3$ meV, $C = 2$ (b) $\Omega_{SI} = 0.6$ meV, C=-1. Arrows mark the propagation direction.

4.2.3   Numerical experiment

To confirm our analytical predictions and support the observability in a realistic pump-probe experiment (sketch shown in Fig 4.5(c)), we perform a full numerical simulation beyond the tight-binding or Bogoliubov approximations. We solve the spinor Gross-Pitaevskii equation for polaritons with quasi-resonant pumping with a honeycomb lattice potential U:

$$i\hbar \frac{\partial}{\partial t}\psi_\pm = -\frac{\hbar^2}{2m}\Delta\psi_\pm + \alpha_1 |\psi_\pm|^2 \psi_\pm + U\psi_\pm - \frac{i\hbar}{2\tau}\psi_\pm + \beta\left(\frac{\partial}{\partial x} \mp i\frac{\partial}{\partial y}\right)^2 \psi_\mp \quad (4.26)$$

$$+ P_{0+}e^{-i\omega t} + \sum_j P_{j-}e^{-\frac{(t-t_0)^2}{\tau_0^2}} e^{-\frac{\left(\mathbf{r}-\mathbf{r}_j\right)^2}{\sigma^2}} e^{-i\omega t}$$

where $\psi_+(\mathbf{r}, t), \psi_-(\mathbf{r}, t)$ are the two circular components of the wave function, $m = 5 \times 10^{-5} m_{el}$ is the polariton mass, $\tau = 30$ ps the lifetime. The main pumping term P_{0+} is circular polarized (σ^+) and spatially homogeneous, while the 3 pulsed probes are σ^- and localized on 3 pillars: 2 on the edges and 1 in the bulk. The results (filtered at the edge states energy) are shown in Fig. 4.6. As compared with the $C = 2$ case (a), a larger gap of the $C = -1$ phase (b) demonstrates a better protection against bulk excitation, a longer propagation distance, and an inverted direction, all achieved by modulating the pump intensity.

Effect of gain and losses. It has to be noticed that contrary to the thermal equilibrium regime discussed in the previous section, pump and losses are inherently present in the quasi-resonant regime considered here. In the specific case we consider, the homogeneous pump is necessary for the formation of the macro-occupied stationary state at the Γ point. The losses encoded by the polariton lifetime lead to a damping of the Bogoliubov excitations. In the numerical simulation discussed above this implies that the propagating edge states will disappear after some time. Note that the same type of dissipation occurs in the linear regime. In both cases, it is possible to detect the chiral propagation of a wavepacket on the edge if the cavity quality factor is sufficiently high. For example, if one assume the edge state group velocity to be $v_g = 0.7 \mu m/\text{ps}$ and the polariton lifetime $\tau = 30\text{ps}$ (typical for state of the art GaAs-based cavities), the propagation length can be estimated to be of $21\mu\text{m}$ (about 10 cavity pillars).

One can also speculate about the effect of a local gain on the edge of the sample on the Bogoliubov edge states. In a polariton system, this situation can be organized by adding an off-resonant pump located on the edge of the lattice which will create an excitonic reservoir. If the gain is not too strong one can expect that it will increase the sustain of the Bogoliubov edge modes and hence their propagation length. However, if the gain is too strong it can lead to a high increase of population in these modes. In this case, instabilities can develop and the Bogoliubov approximation (available for weak density perturbation) will not be valid anymore.

4.3 Quantum spin Hall effect analog for BEC vortices

Topological defects are a distinctive feature of quantum fluids [268]. Such real space excitations are stable and cannot be removed by a continuous transformation, which is called topological protection. They are known for more than fifty years and determine the fluid properties, for example, in the Berezinskii-Kosterlitz-Thouless phase transition in Bose-Einstein condensates [137].

As we have seen in the first chapter, the concept of topology has been applied in a different context to reciprocal space since the eighties. This field expanded further recently with the discovery of the quantum spin Hall effect and of the associated class of $\mathbb{Z}_2$ topological insulators [73] that we introduced in 1.3.3. In that case the bulk-boundary correspondence applies and guarantees on the interface with a trivial insulator the presence of a pair of counter-propagating spin-polarized states, which because of the preserved time-reversal symmetry (TRS) do not couple with each other.

This important discovery was followed by the attempts to extend the concept of topologically protected spin transport to other type of two-level systems which can be mapped to a pseudospin representing either an internal degree of freedom (photon polarization) or an external one (angular momentum, valley [209], etc.). However, for photons, TRS acts differently from fermions [7] and rigorously, there is no symmetry-protected photonic quantum spin Hall effect. This can be clearly

visualized by explicitly considering the photonic spin-orbit coupling due to the energy splitting between TE and TM modes [160, 213] [See Fig. (2.6)]. It respects TRS, but it has a double winding which couples counter-propagating spin-polarized photonic modes. The realization of topological spin transport for light therefore requires to fabricate a structure where the TE-TM splitting is suppressed, which is possible but very demanding [292, 293]. Other degrees of freedom, like the angular momentum of photons in lattices of ring cavities have been considered [92, 93, 95], with the formal problem that no specific symmetry protects this pseudospin from disorder.

Finally, the quantum valley Hall effect in staggered honeycomb lattices uses the valley pseudospin [37, 294, 209] to which one can associate valley Chern numbers [235]. QVH has been evidenced experimentally in electronic systems [245] and recently considered in a large series of works in photonics [295, 251, 252, 296, 250, 254] including our work [260] presented in section 3.3 showing the interest of this system beyond condensed matter physics [256]. In these systems the dissipation mechanism is the inter-valley scattering. Even if it is argued to be weak, any defect localized on the interface induces a backscattering of the edge modes as demonstrated in section 3.3 [Figs. 3.13(a) and 3.14] and can lead to the Anderson localization of the 1D edge states.

In this section, we propose an original combination of real and reciprocal space topologies, creating a truly protected pseudospin current in a bosonic system. Here, the pseudospin current is not protected by a symmetry of the Hamiltonian, but by the winding number of the quantized vortices (real space topological invariant). We consider a BEC at the Γ point of the Brillouin zone of a QVH system based on two staggered honeycomb lattices. We demonstrate the existence of a coupling between the vortex winding and the valley of the bulk Bloch band. This coupling leads to chiral vortex propagation on each side of an interface between two regions with inverted staggering, with a true topological protection against backscattering, contrary to the interface states of the non-interacting Hamiltonian. This configuration can be seen as a quantum spin Hall effect analog, but where the role of spin is played by the winding of the vortices. Our results apply to polariton condensates in recently fabricated polariton honeycomb lattices [200] and to atomic BECs in optical lattices [297].

Note: Interestingly, motivated as us by the possibility to build artificial lattices in cold atom and nonlinear photonic systems several theoretical works have recently appeared dedicated to the study of 2D nonlinear Dirac equation. The authors find novel non-linear solutions such as solitons, vortices, and ring solitons and study their stability in various configurations [298, 299, 300, 301]. We stress that the vortex excitations that we present below cannot be described by a non-linear Dirac equation because the unperturbed condensate is in its ground state at Γ point and needs to be described by a Gross-Pitaevskii equation including the lattice potential.

4.3.1 Winding-valley coupling

First, we shall demonstrate that the core of a vortex with a given winding corresponds to a certain valley (K or K') of the single-particle dispersion of staggered graphene, that is, the existence of winding-valley coupling for vortices.

Let us consider the core of a sufficiently large vortex ($\xi \gg a$, where a is the distance between nearest neighbors), where the density is necessarily small and the interactions can be neglected. To minimize the on-site energy given by $E = E_A|\psi_A|^2 + E_B|\psi_B|^2$, the WF is mostly localized on the sites of the A type, which have lower energy (assuming $E_A < E_B$). In the limit of a large gap, $\Delta \gg J$, only the A-sites are populated and therefore the Bloch function in the vicinity of the vortex center is $(1,0)^T$. Therefore, in the TB approach the vortex core can be defined as a combination of three on-site orbitals:

$$|\psi_c\rangle = |\omega_{A,R_1}\rangle + e^{i\frac{2\pi}{3}p}|\omega_{A,R_2}\rangle + e^{i\frac{4\pi}{3}p}|\omega_{A,R_3}\rangle \tag{4.27}$$

where p encodes the winding of the vortex [See subsection 2.1.4]. Using the definition of the Bloch state $|\psi_{A,\mathbf{k}}\rangle$ on A sublattice (1.56), one can obtain the amplitude in momentum space:

$$\tilde{\psi}_p(\mathbf{k}) = \langle\psi_{A,\mathbf{k}}|\psi_c\rangle = \left(e^{i\mathbf{k}.\mathbf{R}_1} + e^{i\mathbf{k}.\mathbf{R}_2}e^{i\frac{2\pi}{3}p} + e^{i\mathbf{k}.\mathbf{R}_3}e^{i\frac{4\pi}{3}p}\right) \tag{4.28}$$

Taking the first atoms as the origin, the three on-site vectors are defined by: $\mathbf{R}_1 = (0,0)$, $\mathbf{R}_2 = (\frac{3a}{2}, \frac{\sqrt{3}a}{2})$, $\mathbf{R}_3 = (0, \sqrt{3}a)$. One can introduce two new variables:

$$\eta_p = \frac{2\pi}{3}p + \frac{3}{2}ak_x + \frac{\sqrt{3}}{2}ak_y \tag{4.29}$$

$$\zeta_p = \frac{4\pi}{3}p + \sqrt{3}ak_y \tag{4.30}$$

We can then find the position of the maximal probability density in the reciprocal space $|\psi(\mathbf{k})|^2$, which is given by:

$$|\tilde{\psi}_p(\mathbf{k})|^2 = 3 + 2\left(\cos\eta_p + \cos\zeta_p + \cos(\eta_p - \zeta_p)\right) \tag{4.31}$$

The maximal value of this expression is achieved when both $\eta_p = 2\pi\nu$ and $\zeta_p = 2\pi\mu$, where ν and μ are integer numbers. From the latter, taking for example $\nu = 0$, it is easy to obtain, for $p = 1$, $k_y = -K$ (where $K = 4\pi/3\sqrt{3}a$), and $k_x = 0$, and for $p = -1$, $k_y = K$ and $k_x = 0$.

Therefore, we find that the maximum value of the WF is achieved for $\mathbf{k} = K$ and $\mathbf{k} = K'$, depending on the vortex winding p. Thus, both the Bloch wave and the plane wave part of the WF in the core of a vortex of a given winding define a state corresponding to a certain well-defined valley of the single-particle dispersion. One can define a winding-valley coupling law as:

$$\tau = ps \tag{4.32}$$
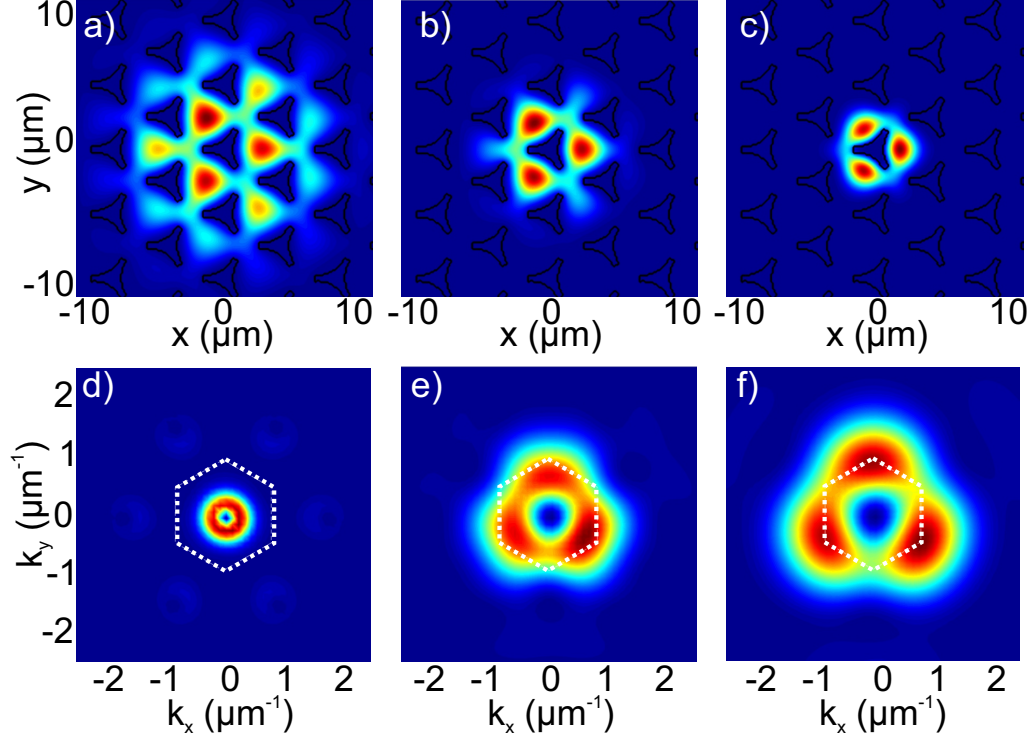
Figure 4.7:   Numerical density profile of the vortex stationary solution in real (a,b,c) and reciprocal (d,e,f) space for different filtering scales ($w = 7, 3, 1$ μm, respectively). Black lines in (a,b,c) represent the lattice potential contour, and dashed white lines in (d,e,f) highlight the first Brillouin zone.

where $\tau = \pm 1$ is the valley number and $s = \text{sgn}(\Delta) = \text{sgn}(E_A - E_B)$ is the lattice staggering. This result is linked with the well-known optical selection rules in Transitional Metal Dichalcogenides [228] where the phase pattern at the K point exhibits an angular momentum for *each* unit cell, determining the angular momentum of photons for a given valley.

To confirm this analytical result, we have performed numerical simulations by solving the GPE beyond the TB approximation, with an explicit honeycomb lattice potential $U(r)$. Without losing generality, we consider all parameters as in section 3.2 (typical for exciton-polaritons [200]), but considering a quasi-conservative case. The neighbour distance is $d = 2.5$ μm, pillar radius $r = 1.5$ μm, $m = 5 \times 10^{-5} m_0$ (m_0 is the free electron mass), corresponding to $J \approx 0.25$ meV, and $\alpha n = 0.3$ meV. To find the stationary vortex wavefunction in presence of a honeycomb lattice potential,

we solve the damped Gross-Pitaevskii equation [302]:

$$i\hbar\frac{\partial\psi}{\partial t} = (1 - i\Lambda)\left(-\frac{\hbar^2}{2m}\Delta\psi + \alpha|\psi|^2\psi + U\psi - \mu\psi\right) \tag{4.33}$$

where $\Lambda = 0.03$ is the dimensionless damping coefficient. This equation guarantees that a stationary solution with an energy μ persists, whereas any perturbations to this solution with higher energies decay, with the characteristic decay rate proportional to the energy deviation $\Gamma = \langle H \rangle - \mu$. We start with a wavefunction $\psi \sim \tanh(r/r_0)\exp(ip\varphi)$, where φ is the polar angle, $p = \pm 1$ and r_0 is of the order of expected healing length ξ (several microns). The damped equation conserves the zeroes of the wavefunction, because in the point $r = 0$ where $\psi = 0$ the right part of the equation vanishes and thus $\partial\psi/\partial t = 0$. The wavefunction cannot therefore evolve towards the ground state, so it stabilizes at a stationary solution with winding $p = \pm 1$.

The results of these calculations are shown in Fig. 4.7. To get the information on the vortex core, we apply spatial filtering using a Gaussian of size w (panels (a)-(c)). For large w, the image in the reciprocal space (Fig. 4.7(d)) is dominated by the condensate centered at the ground state (Γ point). The ground state itself is empty, because the vortex imposes $v \neq 0$ everywhere. For smaller w (Fig. 4.7(e,f)), the core of the vortex is centered at the K points of the reciprocal space, while the K' valleys are empty. Opposite results are obtained for opposite winding, confirming the valley-winding coupling for vortices.

4.3.2 Vortex at the interface

We have shown that the vortex WF in the reciprocal space has two contributions. Most of the condensed particles, far from the vortex core, are concentrated around the Γ point (small k). These particles are practically unaffected neither by the presence of the lattice, nor by any possible interfaces because at this scale the particles are lying in the parabolic part of the dispersion in reciprocal space. On the other hand, the core of the vortex is at the K point, and we can expect interesting effects linked with the interfaces, where in the linear regime the states from the bulk K points give rise to chiral propagative interface states (QVH states).

In what follows, we estimate analytically the energy of the vortex as a function of both the wavevector of the core (dispersion) and of its position in real space. For this task one can start from the grand canonical expression [137]:

$$E_v = \int \left(\frac{\hbar^2}{2m}|\nabla\psi|^2 + \psi^* U\psi + \frac{\alpha}{2}\left(|\psi|^2 - n\right)^2\right)\mathbf{dR} \tag{4.34}$$

Qualitatively, this expression is the difference between the energy of a system with a vortex and the energy of a system without a vortex (but with a condensate in the ground state with the unperturbed density n). The first step is to split the integral into 2 regions: the core ($|\mathbf{R}| \leq \xi$) and the outside zone ($|\mathbf{R}| > \xi$). In the second region, $|\psi|^2 \approx n$, and the only contribution to the vortex energy comes from
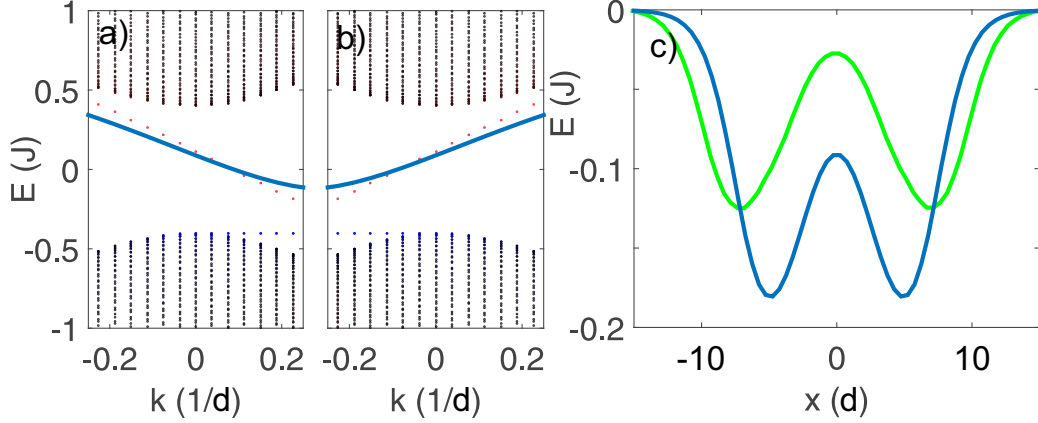
Figure 4.8:   a,b) Energy of the vortex core at the interface as a function of its central wavevector, exhibiting valley chirality (a - K, b - K') (Blue solid lines). The dotted curves represent the linear TB ribbon dispersions, the different colors corresponding to the localization on the interface (red) and on the edges (blue) as in Fig. 3.7(a). c) Energy of the vortex as a function of position. (Blue and green curves correspond to a direct interface or a larger one constituted of 4 unstaggered zigzag chains centered at $x = 0$ respectively.)

the kinetic energy term, which can be estimated by the well-known logarithmic expression $E_v^{r>\xi} = \pi n \hbar^2 \ln\left(1.46 R_0/\xi\right)/m$ (R_0 is the system size) neglecting the lattice potential.

In the vortex core, the presence of the lattice has to be taken into account. As we have shown above both analytically and numerically, the core of the vortex is a wavepacket centered at k_0 close to either K or K' (we take a Gaussian wavepacket ψ_G). We calculate its energy versus k_0 using the TB approximation. The X spatial direction, perpendicular to the interface, has to be treated in the real space (x_0 is the vortex center). The contribution to the kinetic energy is calculated as:

$$E_v^{kin,r<\xi}(x_0, k_0) = \int_{x_0-\xi}^{x_0+\xi} dx \int dk \psi_G^* \psi_0^* H_k \psi_0 \psi_G \tag{4.35}$$

where H_k is the Bloch Hamiltonian of a ribbon of coupled infinite zigzag chain (3.12) ($k = k_y$) and $\psi_0(x, k)$ are the single-particle eigenstates of the lattice. These eigenstates are quantized in the X direction. Their spatial overlap with the vortex core plays an important role. For the delocalized bulk states the overlap tends to zero with increase of the stripe width. On the other hand, the state localized at the interface (width κ [See Fig. 3.7(b)]) has a non-vanishing overlap and the contribution of this state dominates the dispersion of the vortex core. An example of such dispersion in the vicinity of the K and K' points is shown in Fig. 4.8(a,b): the dispersion of the core (blue line) inherits the dispersion of the linear eigenstates

at the interface (red dots), and therefore their valley-dependent propagation direction (chirality), as compared with the non-propagating bulk states with zero group velocity exactly at K or K' (black points).

The kinetic energy of the core also depends on the position of its center x_0: if the core is perfectly centered at the interface, the energy at $k_0 = K$ is exactly the same as that of the interface state. On the other hand, if the core is located in the bulk, its energy is that of the top of the valence band, determined by the energy splitting $E^{kin}(x_0, k_0) = -\Delta$. The interface therefore represents a *barrier* of a height of the order of the gap Δ, if only the kinetic energy is taken into account.

The contribution of the interactions to the vortex energy comes from the sensitivity of the vortex to the local changes of the density in the condensate. In the vortex core, the density $|\psi|^2$ is small as compared with the background density $n(\mathbf{r})$, and the integral reads:

$$E_v^{int, r < \xi} = \int_0^\xi \alpha n^2 \pi r \, dr \tag{4.36}$$

Thus, the vortices are attracted to lower-density regions minimizing the total energy of the system. The density of the condensate without a vortex depends on the local potential, which affects the density of the condensate at the scale given by the healing length ξ. Considering the interface as a Delta barrier $V_0 \delta(x)$ and neglecting the lattice, the density profile of the condensate can be found analytically [286]:

$$n(x) = n_0 \left(1 - \frac{1}{\cosh^2((x_c + |x|)/\xi')} \right) \tag{4.37}$$

where x_c and ξ' depend on V_0. The interaction energy of the vortex core as a function of x_0 therefore exhibits a *minimum* of width $\xi' \approx \xi$.

The sum of kinetic (4.35) and interaction (4.36) energies depends on the parameters of the system. Two examples of such dependence as a function of x_0 are shown in Fig. 4.8(c) for $\xi > \kappa$. The vortex can be localized on either side of the interface, the latter acting as a barrier preventing the vortex from changing domain.

The vortex core is therefore located in a given domain where the winding-valley coupling defined by Eq. (4.32) is well defined. It will move along the interface in the direction given by its winding (which gives its valley localization). The resonant intervalley scattering present for a linear wavepacket is completely forbidden here because it would require to invert the vortex winding and therefore to change the velocity of all the particles in the condensate which has a huge energy cost. Actually, the only way for a vortex to move backward is by tunnelling through the interface barrier. Indeed, on the other side the vortex keeping its winding will change valley because of the staggering potential inversion (Eq. (4.32)). The different possible mechanisms for this tunnelling are discussed in subsection 4.3.4 but it is typically negligible.

Our analytical results are again fully confirmed by numerical simulations of vortex propagation along the interface using Eq. (4.33) (with $\Lambda = 0$). The snapshots of one of such simulations are shown in Fig. 4.9 (the full movie is available at [303]).
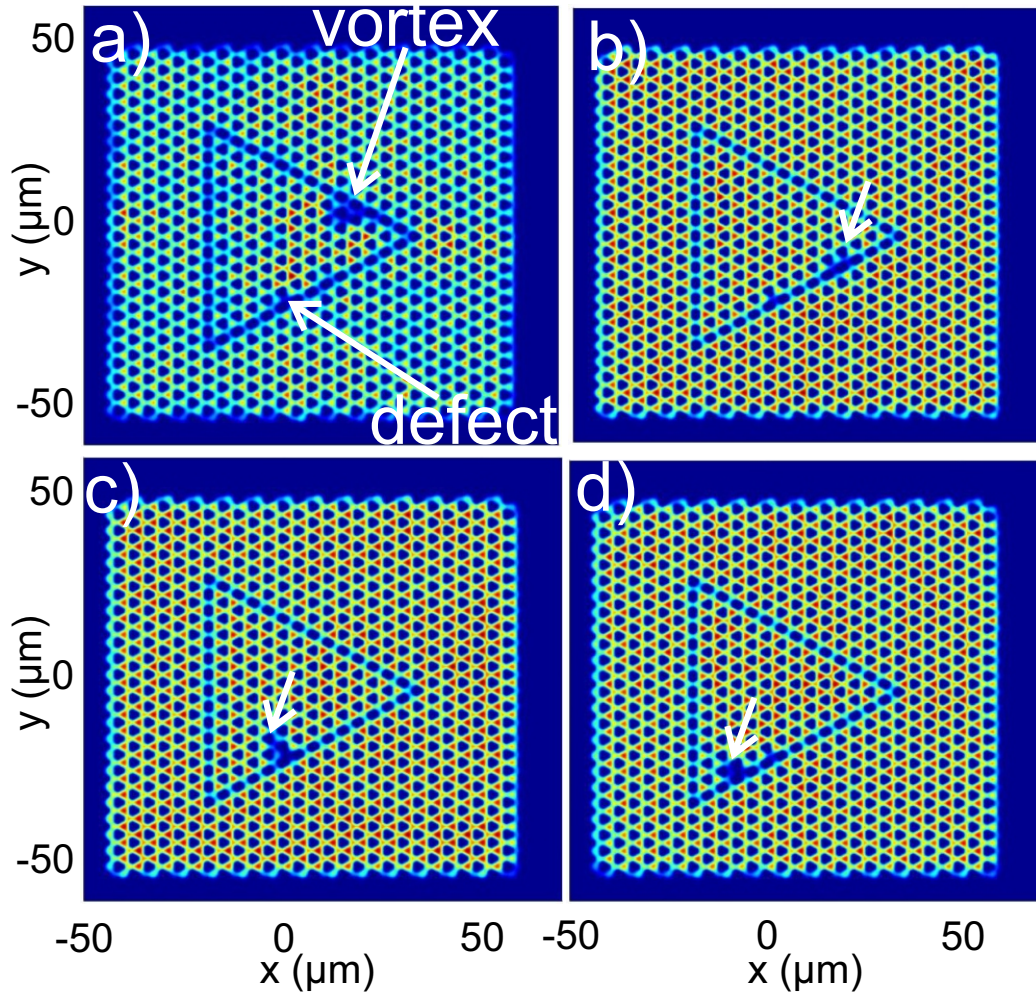
Figure 4.9:   Snapshots of the vortex propagation along the interface, showing the spatial density distribution $|\psi(x,y)|^2$.
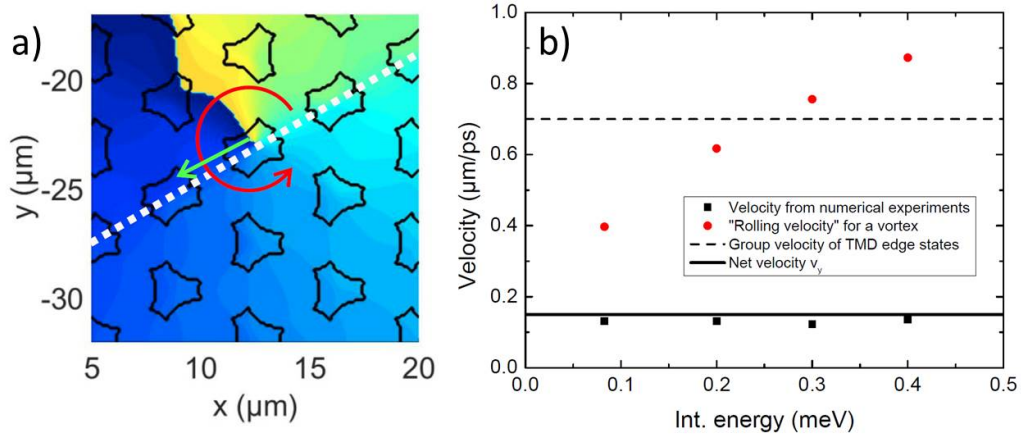
Figure 4.10: a) Contour plot of the potential (black line) and the phase of the vortex (in color). Red arrow shows the rotation direction, green arrow shows the propagation direction of the vortex. b) Vortex velocity from numerical calculations and its estimation by different models.

We see that the vortex remains attached to the interface and propagates along, without being scattered backwards on the corners. An additional defect of 1 meV ($\sim 4J \gg \Delta$) and 1 μm width has been added on an interface pillar for comparison with the linear case, where it leads to strong backscattering [Figs. 3.13(a) and 3.14]. This allows us to check that the vortex is indeed immune to backscattering thanks to the additional topological protection provided by its winding via the winding-valley coupling. We stress, however, that in contrast with electronic quantum spin Hall insulators, where the particle number is conserved, counter-propagating vortices can annihilate.

4.3.3 Vortex velocity estimation

Here, we study how the vortex velocity depends on the parameters of the system in order to check that the propagation along the interface is not linked with the well-known vortex rolling effect. First, let us see that the vortex really follows the interface, and its core is located exactly within the unit cell, which separates the two inverted materials. Figure 4.10 shows a snapshot of the phase of the wavefunction with a vortex. A 2π phase jump line is clearly visible, and the core of the vortex is located at the end of this line. The rotation direction of the vortex is shown with a red arrow, and the green arrow indicates the propagation direction of the vortex along the interface (white dashed line). We see that the edge of the phase jump line is within the unit cell located at the interface.

One might think that the vortex is simply rolling along the interface, like a wheel, converting rotation into propagation. The characteristic distance at which
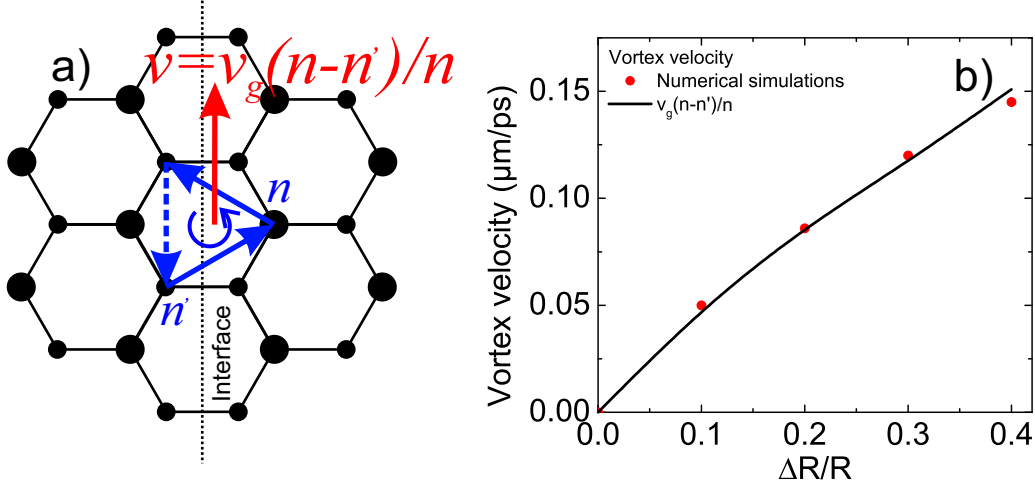
Figure 4.11:   a) A vortex at an interface and its net velocity. b) Vortex velocity as a function of the gap size. Red points - numerical results, black - analytical solution.

the density can vary in the condensate is given by the healing length ξ and therefore the center of the vortex in this "rolling wheel" image has to be located at a distance ξ from the wall, which allows to find the speed of rotation of the particles where they meet with the wall (and therefore the vortex propagation speed) using the expression

$$v_{rol} = \frac{\hbar}{m} \frac{1}{r} \tag{4.38}$$

where one takes $r = \xi$, which gives simply that the vortex propagates with a velocity roughly equal to the speed of sound in the condensate $v_{rol} = \sqrt{\alpha n/m}$. In this model, one could therefore expect a pronounced dependence of the vortex propagation velocity on the particle density.

Another alternative could be that the vortex simply propagates with the group velocity of linear states at the interface, which can be calculated from the numerical dispersion [Fig 3.11]. This gives $v_g = \hbar^{-1}\partial E/\partial k = 0.7 \times 10^6$ m/s or 0.7 μm/ps. This is the velocity with which the WPs at the interface can be expected to propagate in this particular lattice. Interestingly, the vortex velocity is different from v_g.

Figure 4.10(b) compares the predictions of these models as a function of interaction energy αn with numerical results (black squares). Clearly, the simple predictions of the two naive models (red circles for rolling effect and black dashed line for the linear group velocity) strongly deviate from numerics. The model of the rolling wheel (red dots) predicts a dependence on the density which is not observed at all (the interaction energy changes by a factor 5, and there is no significant change of the vortex velocity). The group velocity of the interface states strongly overestimates the real vortex propagation speed (also by a factor 5). Qualitatively, one can understand this by the fact that the vortex core being located on one side

of the interface, its overlap with the linear interface state is slightly reduced.

To calculate the vortex velocity, we analyze the currents that take place within its core (concentrated in a given valley because of winding-valley coupling). In the bulk, the valley states are not propagating, but rotating, because the 3 quantum-mechanical current terms between the 3 pillars of the same type which have different phases $(0, 2\pi/3, 4\pi/3)$ exactly compensate each other, as these are three identical vectors rotated at 120 degrees. Indeed,

$$j = \frac{n\hbar}{m}\nabla\varphi$$

where n is the particle density, and therefore, to calculate current in the tight-binding approach we need to consider only pillars with nonzero density (the A sites) n and take into account the phase difference between each pair.

At the interface the situation changes, as can be seen in Fig. 4.11(a). The A pillars on the left of the interface are not large pillars (with lower energy) but small pillars (with higher energy), and therefore, the 3 current terms (blue arrows) do not have the same prefactor. The phase differences are the same, but the density on the pillars on the left of the interface is smaller (it is not zero as it would be in the bulk, because the presence of the interface mixes the Bloch states), and therefore the current term marked as a dashed line has a smaller magnitude than the other two. This results in a net current pointing upwards, and this is what leads to the propagative nature of the interface states. The total current reads

$$\mathbf{j} = \mathbf{j}_1 + \mathbf{j}_2 + \mathbf{j}_3.$$

Assuming that the density on the A pillars on the right of the interface is n and the density on the A pillars on the left of the interface is n', we can write the magnitude of the current terms as:

$$j_{1,2} = \frac{n + n'}{2}\frac{\hbar}{m}\frac{2\pi}{3\sqrt{3}a}$$

and

$$j_3 = \frac{n'\hbar}{m}\frac{2\pi}{3\sqrt{3}a}$$

The orientation of the vectors makes that the X projection of j_3 is 0, while the X projections of j_1 and j_2 are opposite, and so they compensate each other. The Y projections give:

$$j_Y = \frac{1}{2}\left(j_1 + j_2\right) - j_3$$

which gives

$$j_Y = \frac{n - n'}{2}\frac{\hbar}{m}\frac{2\pi}{3\sqrt{3}a}$$

Without the interface, $n_A = n'_A$ and $\mathbf{j} = 0$, as expected. The presence of the interface makes $n' < n$. If we consider an isolated problem of two pillars with coupling J

and energy splitting Δ (which determines the gap in the bulk TMD analog), we can estimate n' as

$$n' = \frac{2n}{1 + \left(\Delta + \sqrt{\Delta^2 + 4J^2}\right)^2/4J^2} \tag{4.39}$$

One can then estimate the vortex velocity by j_Y/n which yields:

$$v = v_g \left(n - n'\right)/n \tag{4.40}$$

because $2\pi\hbar/m 3\sqrt{3}a$ is simply an estimate of the group velocity v_g in terms of the parameters.

We plot the dependence of v on the pillar size ratio $\Delta R/R$ (determining the gap size Δ) in Fig. 4.11(b). Red dots show the results of numerical simulations. Black line is the analytical solution given by Eq. (4.40), where v_g and Δ are taken from numerical simulations in linear regime. We see that it corresponds almost perfectly to the points (exact numerical solution) while there are no fitting parameters. This confirms the validity of our interpretation.

4.3.4   Interface properties and disorder effects

As discussed in the subsection 4.3.2, vortices stay attached to the interface thanks to the interplay of kinetic and interaction energy. The interface itself represents a barrier of kinetic energy for vortices. On the other hand, the presence of the interface modifies the density of the condensate which creates a potential trap for the vortices. The sum of the two forms a double-trap structure at both sides of the interface. Resonant intervalley scattering is completely forbidden and the only way for them to move backward is to tunnel through the interface barrier in real space. Here, we discuss the possible mechanism leading to such tunneling.

Vortex tunneling has been studied in the past since the discovery of magnetic vortices in superconductors. Two main mechanisms can be responsible for this tunneling: quantum-mechanical [304, 305] and thermal [306].

The quantum-mechanical tunneling rate is proportional to the amplitude of the pinning potential and exponentially decays with the square of the distance and with the density [304]: $t_{QM} = V_{pin}\exp(-\pi n l^2/2)$. For polaritons, the interaction constant [307] is $\alpha \approx 9$ μeV/μm^2 meaning that for the interaction energy of 0.3 meV the polariton density is of the order of 30 μm^{-2} and the corresponding tunneling rate for a tunneling distance of 1 μm is less than 10^{-11} s^{-1} (three thousand years), supposing a pinning potential V_{pin} of the order of 1 meV. This rate can therefore be made negligible if the width of the barrier (l) is sufficiently large.

The thermal tunneling, responsible for the well-known vortex creep [306], is governed by the thermal activation mechanism involving an exponent of the barrier height $\sim \exp(-\Delta/k_B T)$. If one considers the specific example of polaritons, they are strongly decoupled from the thermal reservoir thanks to their photonic fraction and the steepness of their dispersion. Thermal broadening in polariton systems like polariton graphene is comparable with the broadening induced by the lifetime [200]:

the total broadening σ is of the order of 30 μeV, Hence, vortex tunneling is thus restricted by the same condition as the observation of the edge states: $\sigma < \Delta$ – the broadening of all sources should be smaller than the gap. In our simulations, stable vortex propagation on one side of the interface is observed despite the residual bogolons (density waves) in the condensate that can be seen in the movies [303].

Even though the quantum and thermal tunneling are suppressed, a localized defect can perturb the interface barrier. While positive potential barriers repel vortices and do not lead to the crossing of the interface, negative potential traps can partially destroy the protective effect of the interface and make a vortex cross it. Our simulations show that this is indeed possible, if the size of the defect is comparable with the size of a single pillar (or larger), while its amplitude is comparable with the total size of the conduction band ($6J \propto 1$ meV), much higher than the size of the gap (0.1 meV).

However, the interface width can actually be increased by inserting several regular (not staggered) zigzag chains without affecting the behavior of the chiral interface states [See subsection 3.2.3]. The thickness of the barrier leads to an exponential decrease of the vortex tunneling probability and also enhances protection against potential defects, ensuring that the vortices always remain at the same side of the interface. In this sense, the interface is similar to the bulk of the sample: there is an exponentially small overlap of the edge states, which decreases with the increase of the sample size (for the bulk) or of the interface thickness (for the interface), and which provides protection against scattering on relatively large defects, which for the bulk would lead to scattering to the opposite side of the sample, and for the interface would lead to scattering to the opposite side of the interface.

We have checked that the vortex propagation is robust against defects up to ± 1.5 meV ($\sim 6J$, the size of the whole band) in amplitude and up to 2.5 μm ($\sim$lattice constant) in size. Defects with the amplitude of the order of the gap do not perturb the vortex propagation even with larger sizes (checked up to 5 μm).

4.3.5   Conclusions

The above section highlights a new combination of topological quantities: real space topological charge characterized by the vortex winding number and momentum space topology characterized by the valley Chern number. We see that the properties of the single-particle dispersion of the interface states are inherited by the vortex solution of the non-linear equation via the core, the vortex providing protection against backscattering by localized disorder on the interface. We demonstrate that this combination allows to achieve topologically robust QVH effect which can be interpreted as an analog of quantum spin Hall effect. These results are promising for the development of a new field of vortextronics, where the information will be carried by vortices. The possibility to create chiral pathways for vortices and to automatically sort them according to their winding could be crucial for such information treatment.

Band geometry measurement and anomalous Hall effect

Contents

In section 5.1, we present a protocol to measure the components of the quantum geometric tensor in photonic systems. Several images presented correspond to reciprocal space maps of the Berry curvature in spinor or scalar honeycomb lattices directly related to the effects discussed in the previous chapters. In section 5.2, considering a two-band system we highlight the link between local non-adiabaticity and the quantum metric. We propose a way to take the non-adiabatic fraction into account in the semi-classical equations describing the anomalous Hall effect.

5.1 Measuring the quantum geometric tensor in 2D photonic and exciton-polariton systems

Analog systems such as cold atoms or photonic systems bring new experimental perspectives to probe the band geometry/topology. Recently, several protocols have been proposed to measure the Berry curvature or Chern numbers in such systems [41, 308, 309, 310] and some of them have been implemented experimentally [103, 311]. However, the real part of the QGT –– the quantum metric –– has never been measured experimentally, to our knowledge. In a recent paper, T. Ozawa proposes an experimental protocol to reconstruct the QGT components in a photonic flat band [312]. This reconstruction is based on the anomalous Hall drift measurement of the driven-dissipative stationary solution in different configurations, similar to previous works on the Berry curvature extraction [249, 308].

In this section, we propose a different method to extract the components of the quantum geometric tensor by *direct* measurements using polarization-resolved and spatially resolved interference techniques. This proposal is based on the experimental ability to perform direct measurement of photon wave-function in radiative photonic systems such as planar cavities and cavity lattices [200, 201], but can be extended to other systems where **k**-dependent pseudospin orientations can be measured. Our method is designed to extract QGT components of systems with one or two coupled pseudospins (two-band or four-band models), independently of the band curvature.

We emphasize that our proposal concerns the measurement of geometrical quantities linked to the Hermitian part of the system. However, the dissipation (finite lifetime of the radiative states) is the key ingredient which enables the measurement. As highlighted in recent works, dissipation can also be linked to new topological numbers related to the non-hermiticity and the complex eigenenergies [313, 314], but this is not the subject of the present section.

Subsection 5.1.1 is dedicated to two-band systems keeping in mind two particular implementations. The first case we consider is a planar microcavity taking into account the light polarization degree of freedom. The second case is a staggered honeycomb lattice for scalar photons, where the pseudospin of interest is associated with the lattice degree of freedom. We generalize the measurement protocol to generic four-band systems described with two coupled pseudospins in subsection 5.1.2. This situation is realized in the s-band of a lattice with two atoms per

unit cell (e.g. honeycomb lattice) taking into account the polarization of light. It is also realized for scalar particles in the p-band of a honeycomb lattice. For all examples, in addition to the analytical and tight-binding results, we perform numerical simulations which aim to reproduce the experimental measurement. We solve numerically the Schrödinger equation including pumping and finite lifetime of the photonic states, we then extract the experimentally accessible parameters and use them to reconstruct the QGT components.

5.1.1 Two-band systems

The Hamiltonian of any two-level (two-band) system can be mapped to a pseudospin coupled to an effective magnetic field, because the two-by-two Hamiltonian matrix can be decomposed into a linear combination of Pauli matrices and of the identity matrix. As shown below, the knowledge of the pseudospin is sufficient to reconstruct all the geometrical quantities linked with the eigenstates. A general spinor wavefunction can be mapped on the Bloch sphere using two angles (θ - polar, ϕ - azimuthal) and written in circular polarization (spin-up, spin-down) basis:

$$|u_{n,\mathbf{k}}\rangle = \begin{pmatrix} \psi^+ \\ \psi^- \end{pmatrix} = \begin{pmatrix} \cos\frac{\theta(\mathbf{k})}{2}e^{i\phi(\mathbf{k})} \\ \sin\frac{\theta(\mathbf{k})}{2} \end{pmatrix} \tag{5.1}$$

θ and ϕ are defined for each band as:

$$\theta(\mathbf{k}) = \arccos S_z(\mathbf{k}), \quad \phi = \arctan\frac{S_y(\mathbf{k})}{S_x(\mathbf{k})} \tag{5.2}$$

where the pseudospin components are linked with the intensity of each polarization of light, if the particular pseudospin is the Stokes vector of light:

$$S_z = \frac{|\psi^+|^2 - |\psi^-|^2}{|\psi^+|^2 + |\psi^-|^2}, \quad S_x = \frac{|\psi^H|^2 - |\psi^V|^2}{|\psi^H|^2 + |\psi^V|^2}, \quad S_y = \frac{|\psi^D|^2 - |\psi^A|^2}{|\psi^D|^2 + |\psi^A|^2} \tag{5.3}$$

where the ψ^i correspond to horizontal, vertical, diagonal, anti-diagonal and circular polarization amplitudes. We stress here that pseudospin is arbitrary and can correspond to polarization pseudospin or to sublattice pseudospin if the system is a lattice with two atoms per unit cell. While for light the physical meaning of the vertical and diagonal polarizations is quite natural, for an arbitrary pseudospin they have to be reconstructed from the "circular" (ψ^+, ψ^-) basis as follows:

$$\psi^H = \frac{1}{\sqrt{2}}\left(\psi^+ + \psi^-\right)$$
$$\psi^V = \frac{i}{\sqrt{2}}\left(\psi^+ - \psi^-\right)$$
$$\psi^D = \frac{1}{\sqrt{2}}\left(e^{i\pi/4}\psi^+ + e^{-i\pi/4}\psi^-\right)$$
$$\psi^A = \frac{i}{\sqrt{2}}\left(e^{i\pi/4}\psi^+ - e^{-i\pi/4}\psi^-\right)$$

Applying Eq. (1.37) to the eigenstates (5.1) leads to the formula:

$$g_{ij} = \frac{1}{4}(\partial_i\theta\partial_j\theta + \sin^2\theta\partial_i\phi\partial_j\phi) \tag{5.4}$$

$$\mathcal{B}_z = \frac{1}{2}\sin\theta(\partial_x\theta\partial_y\phi - \partial_y\theta\partial_x\phi) \tag{5.5}$$

where i,j indices stand for k_x,k_y components. Therefore, extracting $\theta(\mathbf{k})$ and $\phi(\mathbf{k})$ for a given energy band at each wavevector $\mathbf{k}$ allows to fully reconstruct the components of the QGT in momentum space. This protocol can be implemented using polarization-resolved photoluminescence or interferometry techniques available for light in the state-of-the-art experiments [200, 211, 201]. For two-band systems, the metric tensor is the same for each band ($g_{ij}^+ = g_{ij}^- = g_{ij}$), whereas the Berry curvatures are opposite ($\mathcal{B}_z^+ = -\mathcal{B}_z^-$) [115].

5.1.1.1 Planar cavity

A planar microcavity has two main features important for our study. First, it has a two-dimensional parabolic dispersion of photons close to zero in-plane wavevector, because of the quantization in the growth direction. This allows to use the Schrödinger formalism to deal with massive photons. Second, the energy splitting between TE and TM polarized eigenmodes is analogous to a spin-orbit coupling for photons, which is a necessary ingredient to obtain a non-zero Berry curvature. The other necessary ingredient to get non-zero Berry curvature is an effective Zeeman splitting, which in practice can be implemented by using strong coupling of cavity photons and quantum well excitons, achieved in modern microcavities [148]. The excitons are sensitive to applied magnetic fields: they exhibit a Zeeman splitting between the components coupled to σ^+ and σ^--polarized photons, inducing a Zeeman splitting for the resulting quasiparticles - exciton-polaritons [315].

Here, we consider an additional splitting between linear polarizations which acts as a static in-plane field [316]. Such field, usually linked with the crystallographic axes, can appear because of the anisotropy of the quantum well, and it can be controlled by an electric field applied in the growth direction [317]. The resulting Hamiltonian in momentum space can be written as a two-by-two matrix in circular basis $(\psi^+, \psi^-)^T$.

$$H_k = \begin{pmatrix} \frac{\hbar^2 k^2}{2m^*} + \Delta_z & \alpha e^{-i\varphi_0} + \beta k^2 e^{2i\varphi} \\ \alpha e^{i\varphi_0} + \beta k^2 e^{-2i\varphi} & \frac{\hbar^2 k^2}{2m^*} - \Delta_z \end{pmatrix} \tag{5.6}$$

where α, β, and Δ_z define the strength of the effective fields corresponding to the constant X-Y splitting, TE-TM SOC, and the Zeeman splitting, respectively. $m^* = m_l m_t/(m_l + m_t)$, with m_l and m_t corresponding to the longitudinal and transverse effective masses. $k = \sqrt{k_x^2 + k_y^2}$ is the in-plane wavevector with $k_x = k\cos\varphi$, $k_y = k\sin\varphi$. φ_0 is the in-plane angle of the constant field. The eigenvalues of this Hamiltonian for realistic parameters are shown in Fig. 5.1 as the cross-sections of the 2D dispersion in the k_x and k_y directions.
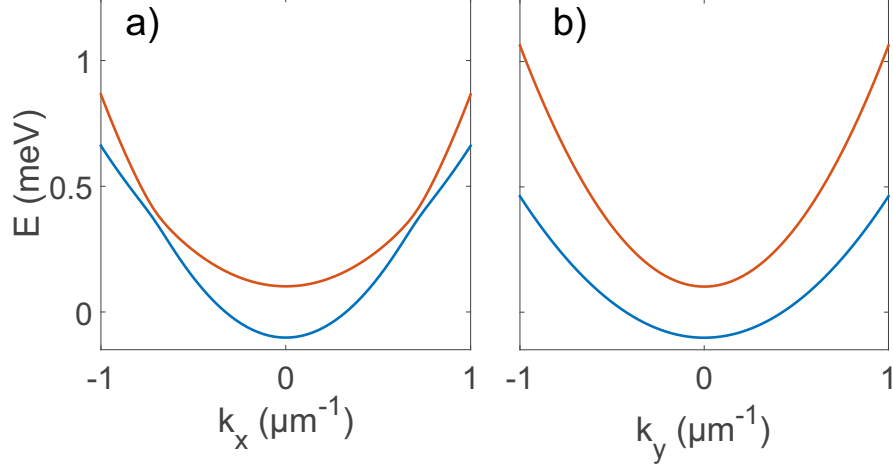
Figure 5.1: Dispersion of the planar microcavity with crossed effective magnetic fields (XY, Zeeman and TE-TM splittings. a) k_x cross-section, b) k_y cross-section.
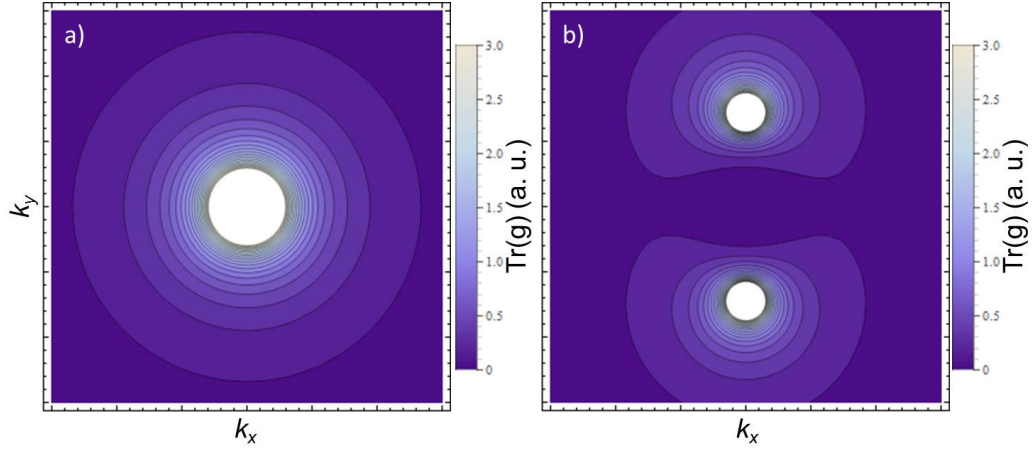

Figure 5.2: Trace of the metric tensor $g_{xx} + g_{yy}$ of the LPB in a cavity system *without Zeeman splitting*: without (a) and with XY splitting (b) from the analytical formula (5.7).
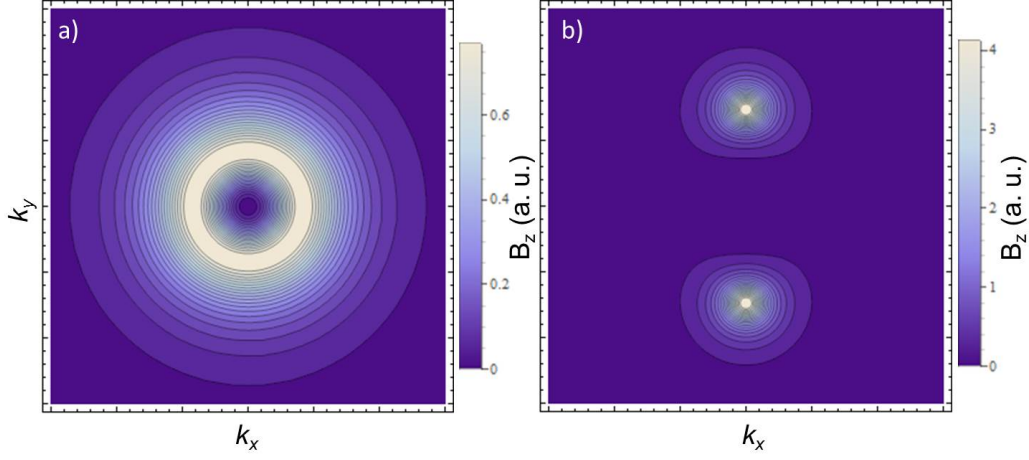
Figure 5.3: Berry curvature of the LPB in a cavity system with Zeeman splitting: without (a) and with XY splitting (b) from the analytical formula (5.7).

Choosing $\varphi_0 = 0$, which means that the constant field is in the x direction, the QGT components are found analytically:

$$g_{xx} = \frac{\beta^2 \left(k_y^2 \left(\alpha - k^2 \beta \right)^2 + k^2 \Delta_z^2 \right)}{\left(\alpha^2 + 2 \left(k_x^2 - k_y^2 \right) \alpha\beta + k^4 \beta^2 + \Delta_z^2 \right)^2}$$

$$g_{yy} = \frac{\beta^2 \left(k_x^2 \left(\alpha + k^2 \beta \right)^2 + k^2 \Delta_z^2 \right)}{\left(\alpha^2 + 2 \left(k_x^2 - k_y^2 \right) \alpha\beta + k^4 \beta^2 + \Delta_z^2 \right)^2}$$

$$g_{xy} = \frac{\beta^2 k_x k_y \left(\alpha^2 - k^4 \beta^2 \right)}{\left(\alpha^2 + 2 \left(k_x^2 - k_y^2 \right) \alpha\beta + k^4 \beta^2 + \Delta_z^2 \right)^2}$$

$$\mathcal{B}_z^{\pm} = \frac{\pm 2\beta^2 k^2 \Delta_z}{\left(\alpha^2 + 2 \left(k_x^2 - k_y^2 \right) \alpha\beta + k^4 \beta^2 + \Delta_z^2 \right)^{3/2}} \tag{5.7}$$

We see that while the Berry curvature requires a non-vanishing Zeeman splitting, the metric tensor can be nonzero even without any applied magnetic field: the TE-TM spin-orbit coupling is sufficient. Such possibility for the metric to subsist when the Berry curvature is null has also been noticed in [115] for two-band TB models. We plot the calculated trace of the metric tensor as a function of wavevector for $\beta = 0.1$ in the absence of Zeeman splitting ($\Delta_z = 0$) in Fig. 5.2. Panel (a) exhibits cylindrical symmetry due to $\alpha = 0$, while panel (b) demonstrates the transformation of the metric in the reciprocal space in presence of non-zero in-plane effective field $\alpha = 0.2$. We stress that the metric diverges where the states become degenerate (an emergent non-Abelian gauge field forms around these points [318] when $\alpha \neq 0$), but it can nevertheless be measured sufficiently far from the points of degeneracy.

Next, we plot the Berry curvature for a non-zero Zeeman splitting $\Delta_z = 0.1$ in Fig. 5.3. Note that a $\alpha \neq 0$ implying anisotropic eigenenergies leads to an important change in the Berry curvature distribution in momentum space from a ring-like maximum to two point-like maxima in the k_y direction, similar to what happened to the metric tensor. Actually, Berry curvature is highest at the anticrossing of the branches, where the metric tensor was divergent for zero Zeeman splitting. In the isotropic case, this anticrossing does not depend on the direction of the wavevector, while the in-plane field breaks this isotropy and gives two preferential directions for the anticrossing, where the TE-TM splitting and the in-plane field compensate each other (see Fig. 5.1).

These results can be directly compared with numerical simulations, from which the QGT components are extracted using Eq. (5.5). Here, and in the following, we are solving the 2D Schrödinger equation numerically over time:

$$i\hbar\frac{\partial\psi_\pm}{\partial t} = -\frac{\hbar^2}{2m}\Delta\psi_\pm - \frac{i\hbar}{2\tau}\psi_\pm \pm \Delta_z\psi_\pm + \beta\left(\frac{\partial}{\partial x} \mp i\frac{\partial}{\partial y}\right)^2\psi_\mp + \alpha e^{\mp i\varphi_0}\psi_\mp + U\psi_\pm + \hat{P}$$
(5.8)

where $\psi_+(\mathbf{r},t), \psi_-(\mathbf{r},t)$ are the two circular components, $m = 5 \times 10^{-5}m_{el}$ is the polariton mass, $\tau = 30$ ps the lifetime, β is the TE-TM coupling constant (corresponding to a 5% difference in the longitudinal and transverse masses). $\Delta_z = 0.06$ meV is the magnetic field in the Z direction (Zeeman splitting), α is the in-plane effective magnetic field (splitting between linear polarizations) with its orientation given by $\varphi_0 = 0$, $\hat{P}$ is the pump operator (Gaussian noise or Gaussian pulse exciting all states at $t = 0$). U is an external potential used in the following subsections to encode the lattice potential (here, $U = 0$). The solution of this equation is then Fourier-transformed $\psi(\mathbf{r},t) \to \psi(\mathbf{k},\omega)$ and analyzed as follows. For each wavevector $\mathbf{k}$, we find the corresponding eigenenergy as a maximum of $|\psi(\mathbf{k},\omega)|^2$ over ω. Then, the pseudospin $\mathbf{S}$ and its polar and azimuthal angles θ, ϕ are calculated from the wavefunction $\psi(\mathbf{k},\omega)$ using Eqs. (5.2)-(5.3). This corresponds to optical measurements of all 6 polarization projections at a given wavevector and energy. Finally, the Berry curvature is extracted from $\theta(\mathbf{k}), \phi(\mathbf{k})$ using Eq. (5.5). The results are shown in Fig. 5.4. Panel (a) shows the Berry curvature in a planar cavity without the in-plane splitting ($\alpha = 0$). Panel (b) demonstrates the modification of the Berry curvature under the effect of a non-zero in-plane field $\alpha = 0.1$ meV. As in the analytical solution, the ring is continuously transformed into two maxima.

5.1.1.2 Staggered honeycomb lattice for scalar particles

The Hamiltonian of a staggered honeycomb lattice for scalar particles, in the tight-binding approximation with two atoms per unit cell, is also a two-by-two matrix which can be mapped to an effective magnetic field acting on the *sublattice* pseudospin. The Bloch Hamiltonian in $(\psi_A, \psi_B)^T$ basis reads:

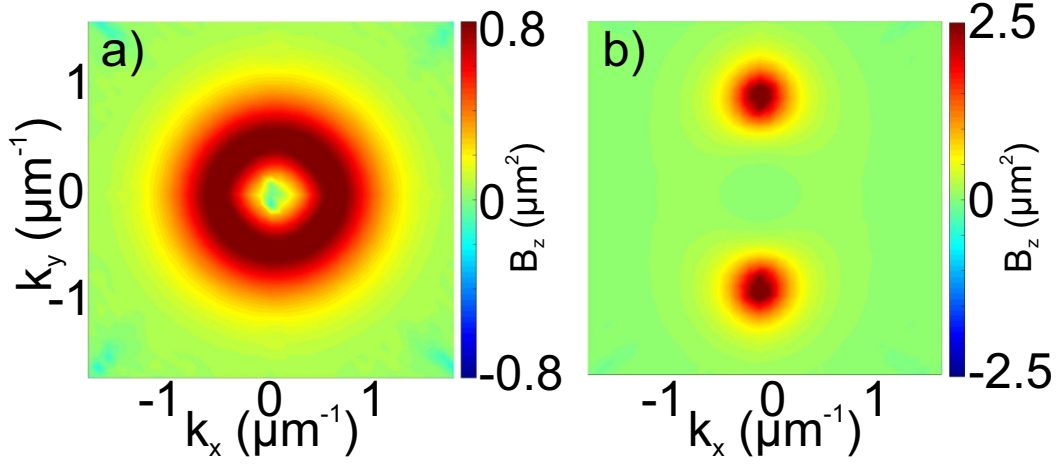$$H_k = \begin{pmatrix} \Delta_{AB} & -Jf_k \\ -Jf_k^* & -\Delta_{AB} \end{pmatrix}$$
(5.9)

Figure 5.4: Berry curvature extracted from numerical simulations using Schrödinger equation and Eq. (5.5).

where $f_k = \sum_{j=1}^{3} \exp\left(-i\mathbf{k}\mathbf{d}_{\phi_j}\right)$ and Δ_{AB} is energy difference between A and B sublattice states. The corresponding tight-binding dispersion is plotted in Fig. 5.5. The gap, opened by the staggering potential, leads to opposite Berry curvatures at K and K' points [37][see Sec. 3.2]. While simple analytical formula can be achieved by linearization of the Hamiltonian around these points, here, we compute the geometrical quantities numerically using eqs. (1.27), (1.28) which, thanks to a better precision, allows to recover the signature of the underlying lattice in the QGT components (Fig. 5.6). Indeed, the presence of two valleys in the hexagonal Brillouin zone implies a triangular shape of QGT components around K and K' points, which is neglected in the first-order approximation. Similar images can also be achieved analytically [39].

We have also performed numerical simulations with the QGT extraction for the staggered honeycomb lattice. In this section, to consider scalar particles, **only one spin component** was taken into account in the Schrödinger equation (5.8) (ψ_+) and all coupling between the components was removed ($\alpha = 0$, $\beta = 0$). Thus, the only remaining pseudospin is the sublattice pseudospin linked with the honeycomb potential encoded in $U(\mathbf{r}) \neq 0$. We use a lattice potential $U(\mathbf{r})$ of 26×26 unit cells with radius of the pillars $r = 1.5\mu m$, pillar radius modulation of 30%, and lattice parameter $a = 2.5\mu m$.

Once the wavefunction $\psi(\mathbf{r}, t)$ and its image $\psi(\mathbf{k}, \omega)$ are found, we extract the angles θ and ϕ defining the spinor. The physical meaning of the spinor here is different from that of the previous section, and the meaning of these angles differs as well. For S_z and θ the measurement is straightforward, because $|\psi_+|^2$ and $|\psi_-|^2$ are simply the intensities of emission from the two pillars A and B in the unit cell.
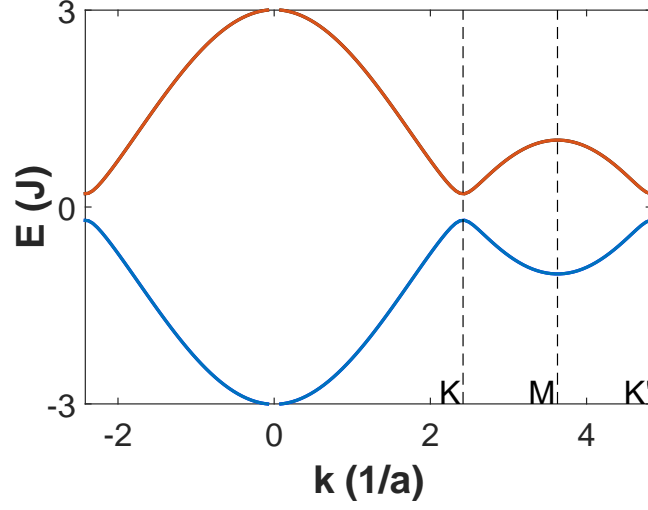
Figure 5.5: Staggered honeycomb lattice tight-binding dispersion ($\Delta_{AB}/J = 0.2$). Dashed vertical lines mark high symmetry points in the first Brillouin zone.

To determine ϕ, the phase difference between the two pillars, one has to consider the real space Fourier image of the corresponding wavevector state (the Bloch wave in real space) and determine this phase by interference measurements with a reference beam. This technique is analogous to the one used recently to measure the phase difference between pillars in a honeycomb photonic molecule [211]. Figure 5.7 shows two interference patterns for two opposite wavevectors q close to a particular Dirac point K. The reference beam propagates along the x direction, and the deviation of the interference fringes from the vertical direction is an evidence for the phase difference between the pillars.

Figure 5.8 shows the results of the extraction of the QGT components as discussed above. Panel (a) shows the Berry curvature $\mathcal{B}_z$, and panel (c) shows the XX component of the quantum metric (g_{xx}), with corresponding tight-binding results shown in panels (b) and (d), respectively. All panels are shown in the vicinity of one of the Dirac points (chosen as the reference for the wavevector $\mathbf{q}$), where these components differ from zero. This allows to demonstrate that the resolution of the method is sufficient for the extraction in spite of the broadening due to the finite lifetime, numerical disorder, and the finite size of the structure. We see that the g_{xx} component is compressed along the vertical direction, as in the tight-binding calculation (Fig. 5.6(a), and zoom in Fig. 5.8(d)), and that the Berry curvature shows a slight triangular distortion due to the symmetry of the valley, which would be simply cylindrical in the first order.
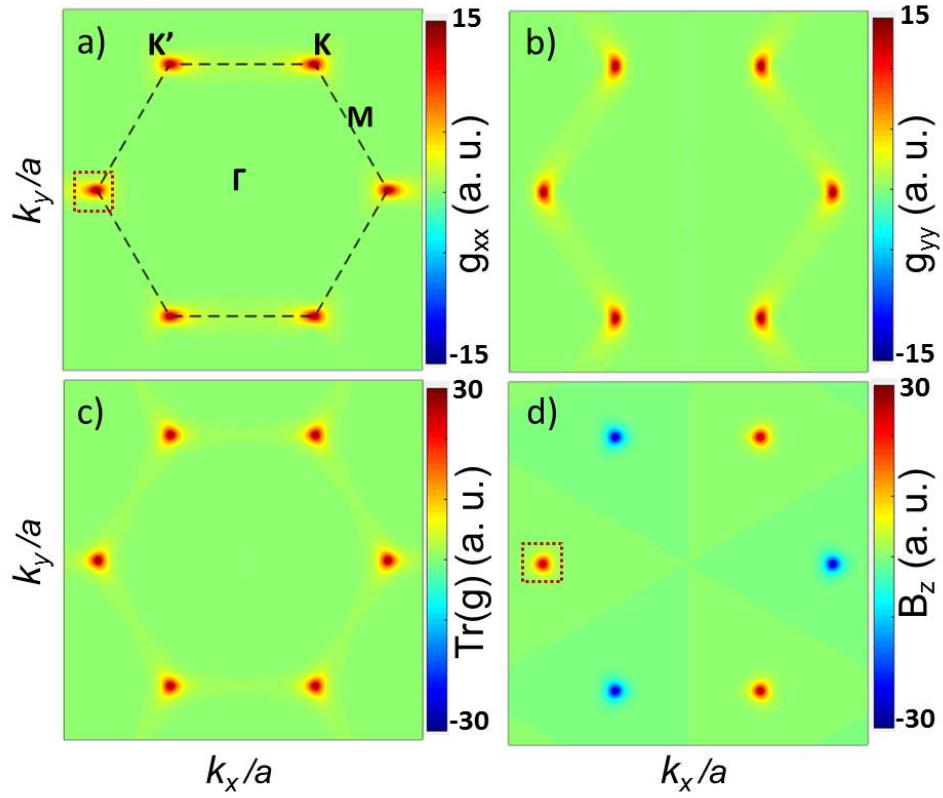
Figure 5.6: Quantum geometric tensor components in staggered honeycomb lattice (tight-binding results). (a) g_{xx}, (b) g_{yy}, (c) $g_{xx} + g_{yy}$, (d) Berry curvature $\mathcal{B}_z$. (lower band, $\Delta_{AB}/J = 0.2$). Dashed red squares around K point show the zoomed region for the numeric QGT extraction.
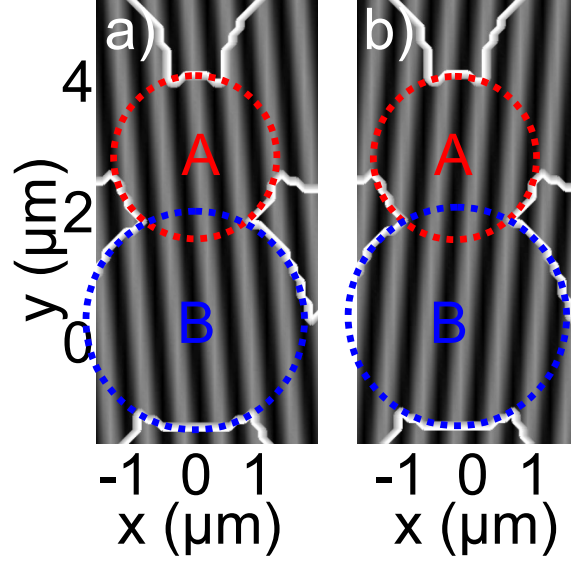
Figure 5.7: Examples of interference pattern in real space used in order to recon-
struct phase difference between A and B pillars for two opposite values of q. The
thick white lines are the contour of the numerical staggered honeycomb potential
used in the simulations. Red (blue) dashed circles highlight the A (B) pillars.

5.1.2 Four-band systems

Several systems are well described by four-band Hamiltonians. Some examples are
bilayer honeycomb lattices [223], spinor s-bands or p-bands in lattices with two
atoms per unit cell [319]. When it comes to accounting for an additional degree of
freedom like polarization pseudospin in a two-band lattice system, where there is
already a sublattice pseudospin, one may think that measuring the two pseudospins
should be sufficient to deduce the QGT in the first Brillouin zone.

It is indeed the case when the Hamiltonian can be decomposed in two uncoupled
two-by-two blocks, which means that the two pseudospins are independent. This
situation is realized for fermions in lattices in presence of time reversal symmetry
for instance [44, 80] [see Sec. 1.3.3]. Here, we consider a more generic situation,
where we account for the possible coupling of the two pseudospins: an eigenstate
of the full system cannot be decomposed as a product of the two pseudospins. The
wavefunction has to take into account the entanglement of the two subsystems. A
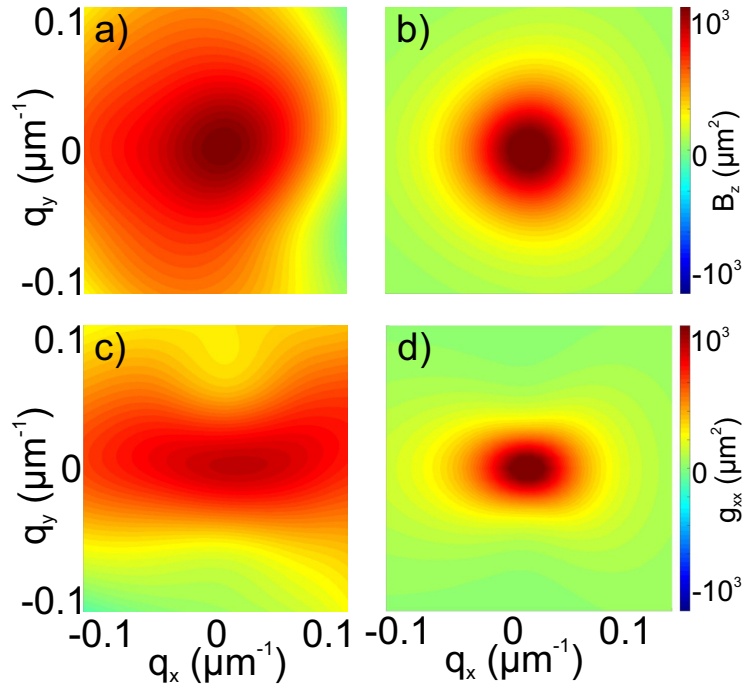
Figure 5.8: Berry curvature (a) and metric tensor component g_{xx} (c), extracted from numerical simulations based on the Schrödinger equation (5.8), compared with corresponding tight-binding results (b,d). Zoom around K point (dashed red square in Fig. 5.6).

general 4-component wavefunction can be written as:

$$
\begin{aligned}
|u_{n,\mathbf{k}}\rangle &= \left(c_A^+ e^{i\phi_A^+}, c_A^- e^{i\phi_A^-}, c_B^+ e^{i\phi_B^+}, c_B^- e^{i\phi_B^-} \right)^T \\
&= e^{i\phi_B^-}
\begin{pmatrix}
\cos\frac{\theta^A}{2}\cos\frac{\theta^{AB}}{2}e^{i\phi_A}e^{i\phi_{AB}} \\
\sin\frac{\theta^A}{2}\cos\frac{\theta^{AB}}{2}e^{i\phi_{AB}} \\
\cos\frac{\theta^B}{2}\sin\frac{\theta^{AB}}{2}e^{i\phi_B} \\
\sin\frac{\theta^B}{2}\sin\frac{\theta^{AB}}{2}
\end{pmatrix}
\end{aligned}
\tag{5.10}
$$

Hence, six angles are necessary to parametrize the general wavefunction. As in the previous section, they are related to pseudospin components:

$$
\begin{aligned}
\phi_A &= \phi_A^+ - \phi_A^- = \arctan\frac{S_y^A}{S_x^A} \\
\phi_B &= \phi_B^+ - \phi_B^- = \arctan\frac{S_y^B}{S_x^B} \\
\phi_{AB} &= \phi_A^- - \phi_B^- = \arctan\frac{S_y^{AB-}}{S_x^{AB-}}
\end{aligned}
\tag{5.11}
$$

and

$$
\begin{aligned}
\theta_A &= \arccos S_z^A \\
\theta_B &= \arccos S_z^B \\
\theta_{AB} &= \arccos S_z^{AB}
\end{aligned}
\tag{5.12}
$$

where ϕ_A, ϕ_B, θ_A, θ_B are defined by the internal pseudospin (eg. polarization) on each component of the external pseudospin (A/B sublattices), ϕ_{AB} is the phase difference between the sublattice components for a given component (σ^-) of the internal pseudospin. θ_{AB} is defined by the *total* intensity difference between the two sublattices. The measurement of these six angles in a band allows a full reconstruction of the corresponding eigenstate. Using the eigenstate formulation (5.10), one can derive the QGT component formulas in terms of these angles:

$$
\begin{aligned}
g_{ij} = \quad & \frac{1}{4}(\partial_i\theta^{AB}\partial_j\theta^{AB} + \partial_i\theta^A\partial_j\theta^A\cos^2\frac{\theta^{AB}}{2} \\
& + \partial_i\theta^B\partial_j\theta^B\sin^2\frac{\theta^{AB}}{2} + \partial_i\phi^{AB}\partial_j\phi^{AB}\sin^2\theta^{AB} \\
& + \cos^2\frac{\theta^A}{2}\cos^2\frac{\theta^{AB}}{2}(3 - \cos\theta^{AB} - \cos\theta^A(1 + \cos\theta^{AB}))\partial_i\phi^A\partial_j\phi^A \\
& + \cos^2\frac{\theta^B}{2}\sin^2\frac{\theta^{AB}}{2}(3 + \cos\theta^{AB} + \cos\theta^B(\cos\theta^{AB} - 1))\partial_i\phi^B\partial_j\phi^B \\
& + \cos^2\frac{\theta^A}{2}\sin^2\theta^{AB}(\partial_i\phi^{AB}\partial_j\phi^A + \partial_j\phi^{AB}\partial_i\phi^A) \\
& - \cos^2\frac{\theta^B}{2}\sin^2\theta^{AB}(\partial_i\phi^{AB}\partial_j\phi^B + \partial_j\phi^{AB}\partial_i\phi^B) \\
& - \cos^2\frac{\theta^A}{2}\cos^2\frac{\theta^B}{2}\sin^2\theta^{AB}(\partial_i\phi^A\partial_j\phi^B + \partial_j\phi^A\partial_i\phi^B))
\end{aligned}
\tag{5.13}
$$
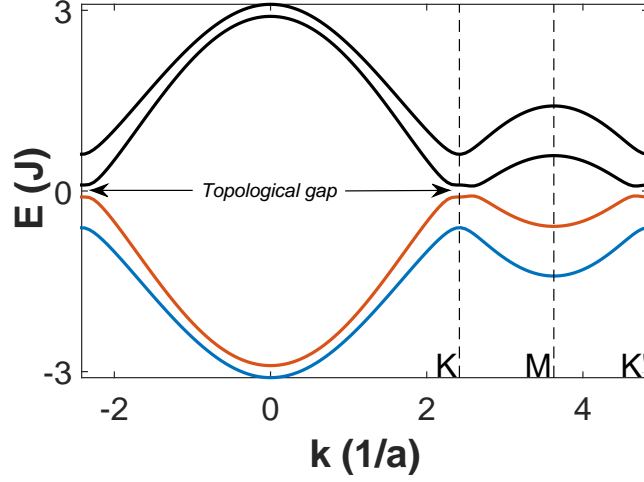
Figure 5.9: Tight-binding dispersion of regular honeycomb lattice with TE-TM SOC and Zeeman field ($\Delta_z/J = 0.1$, $\delta J/J = 0.2$). Dashed vertical lines mark high symmetry points in the first Brillouin zone.

$$
\begin{aligned}
\mathcal{B}_z = \quad & \frac{1}{4}(\sin\theta^A \cos^2\frac{\theta^{AB}}{2}(\partial_x\theta^A\partial_y\phi^A - \partial_y\theta^A\partial_x\phi^A) \\
& + \sin\theta^B \sin^2\frac{\theta^{AB}}{2}(\partial_x\theta^B\partial_y\phi^B - \partial_y\theta^B\partial_x\phi^B) \\
& + \sin\theta^{AB}\cos^2\frac{\theta^A}{2}(\partial_x\theta^{AB}\partial_y\phi^A - \partial_y\theta^{AB}\partial_x\phi^A) \\
& - \sin\theta^{AB}\cos^2\frac{\theta^B}{2}(\partial_x\theta^{AB}\partial_y\phi^B - \partial_y\theta^{AB}\partial_x\phi^B) \\
& + \sin\theta^{AB}(\partial_x\theta^{AB}\partial_y\phi^{AB} - \partial_y\theta^{AB}\partial_x\phi^{AB}))
\end{aligned}
\tag{5.14}
$$

One can observe that the formula complexity has clearly increased compared to the two-state system. However, we stress that if the energy spectrum is accessible experimentally with sufficient resolution, the extraction protocol difficulty does not increase despite the higher number of angles. In the following, we use a specific case in order to demonstrate the feasibility of the measurement.

Honeycomb lattice for spinor particles

In this section, we consider the s-band of a regular honeycomb lattice containing vectorial (polarized) photons with TE-TM splitting and an external Zeeman field as an example of a four-state system. In such system, the quantum anomalous Hall effect for polaritons has been predicted recently [see Sec. 3.1][212]. The minimal tight-binding Bloch Hamiltonian written in circular basis $(\psi_A^+, \psi_A^-, \psi_B^+, \psi_B^-)^T$ is the following:

$$
H_k = \begin{pmatrix} \Delta_z\sigma_z & F_k \\ F_k^+ & \Delta_z\sigma_z \end{pmatrix}, \quad F_k = -\begin{pmatrix} f_kJ & f_k^+\delta J \\ f_k^-\delta J & f_kJ \end{pmatrix}
\tag{5.15}
$$
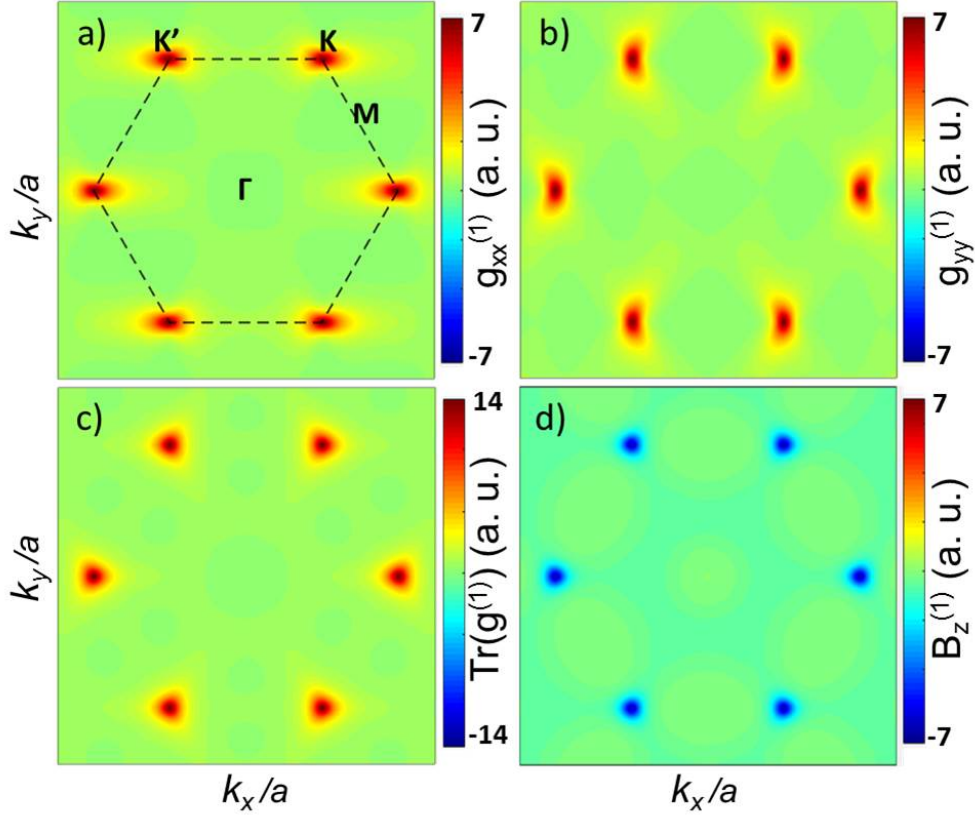
Figure 5.10: Quantum geometric tensor components in regular honeycomb lattice (1st band, tight-binding results). (a) $g_{xx}^{(1)}$, (b) $g_{yy}^{(1)}$, (c) $g_{xx}^{(1)} + g_{yy}^{(1)}$, (d) Berry curvature $\mathcal{B}_z^{(1)}$. (1st band, $\Delta_z/J = 0.1$, $\delta J/J = 0.2$)

where δJ is the TE-TM SOC strength and $f_k^\pm = \sum_{j=1}^3 \exp\left(-i[\mathbf{k}\mathbf{d}_{\phi_j} \mp 2\phi_j]\right)$. Δ_z is the Zeeman field and σ_z the third Pauli matrix.

The Hamiltonian becomes four-by-four matrix due to the additional polarization degree of freedom. The typical dispersion in the first Brillouin zone is plotted in Figure 5.9. This time the full bandgap between the two lower and two upper bands is opened thanks to the combination of the Zeeman field (which breaks time-reversal symmetry) and the TE-TM SOC. In this configuration, the Berry curvatures around K and K' point have the same sign and the gap Chern number (or Hall number) $C = \sum_n^2 C_n$ is non-zero. In figures 5.10 and 5.11, we plot the QGT components in reciprocal space of the two bands below the bandgap (blue and red lines in Fig. 5.9) computed using eqs. (1.27), (1.28). One can see that the map of these quantities is slightly more complicated than before due to the coupling between the two pseudospins (sublattice and polarization). Indeed one can observe clear reminiscences of the trigonal warping around the corner of the Brillouin zone. One further remark, for the first band each Brillouin zone corner is linked with one
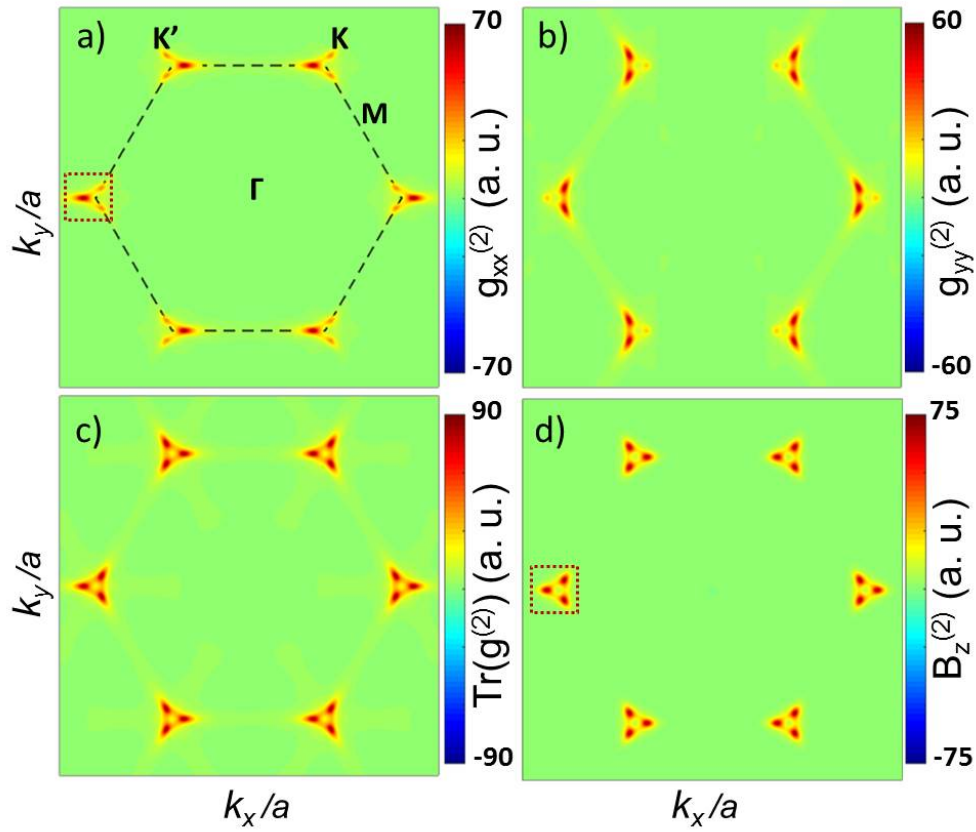
Figure 5.11: Quantum geometric tensor components in regular honeycomb lattice (tight-binding results). (a) $g_{xx}^{(2)}$, (b) $g_{yy}^{(2)}$, (c) $g_{xx}^{(2)} + g_{yy}^{(2)}$, (d) Berry curvature $\mathcal{B}_z^{(2)}$. (2nd band, $\Delta_z/J = 0.1$, $\delta J/J = 0.2$)
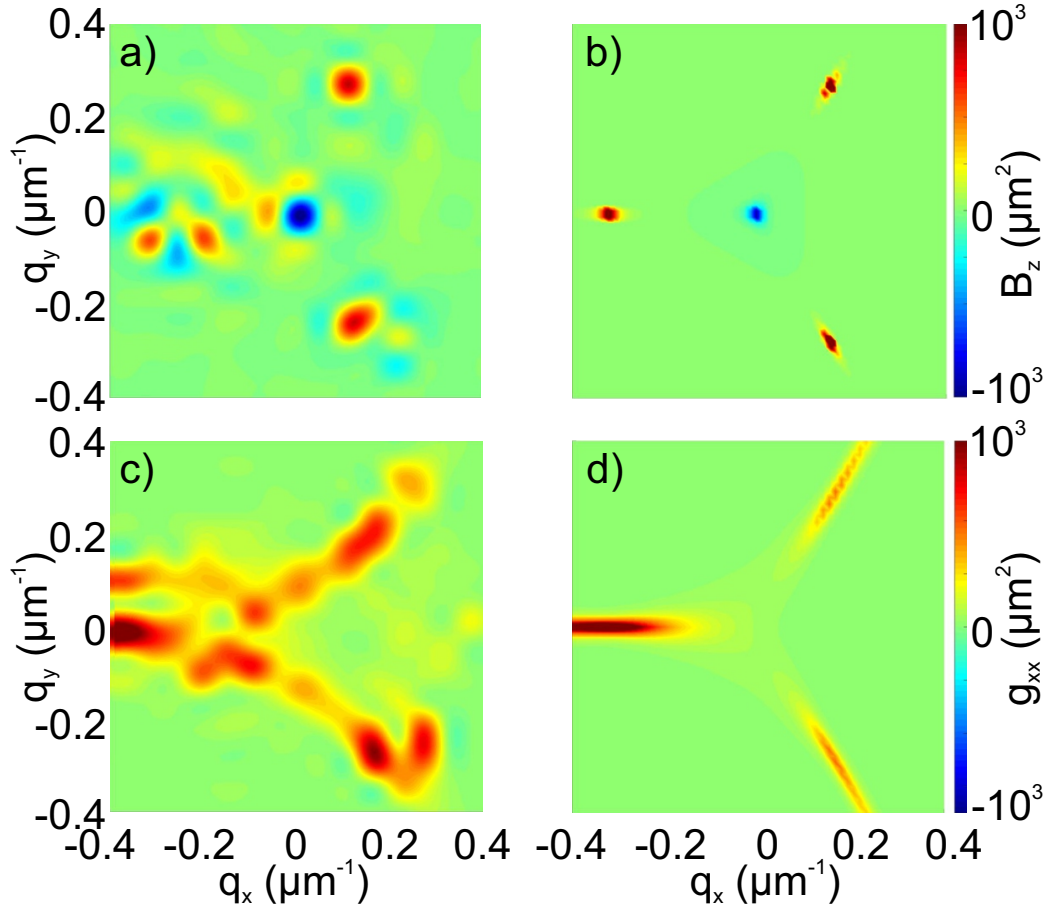
Figure 5.12: Berry curvature $\Omega_z^{(2)}$ (a) and metric component $g_{xx}^{(2)}$ (c) extracted from numerical simulations based on (5.8) using (5.13),(5.14). (b)-(d) Tight binding results. Zoom around K point.

negative contribution to the Berry curvature whereas for the second band each of them is associated with three positive contributions. This allows to visualize why the gap Chern number will be $C = \sum_n^2 C_n = C_1 + C_2 = +2$. However, while the total Chern number remains unchanged as long as the gap does not close, the local Berry curvature can be redistributed between the two bands below the bandgap as a function of the parameters: geometry can be smoothly deformed without changing the overall topology.

In numerical simulations, the main difference with respect to the staggered (but spinless) honeycomb lattice is the necessity to extract the phase difference between the pillars for a single spin component (σ^-), which can be experimentally realized by making interfere the light emitted by different pillars [211] using an additional polarizer. After solving the Schrödinger equation Eq. (5.8) for a lattice of 26×26 unit cells, taking into account the TE-TM coupling and Zeeman splitting, we have extracted the Berry curvature close to one of the K points of the 2nd band (the one on the left of Fig. 5.11). The results of the extraction are shown in Fig. 5.12 (a,c). Zoomed tight-binding results are plotted in Fig. 5.12 (b,d) for clarity. The parameters are inherently different from the ones of figures 5.10 and 5.11: $\delta J = 0.44$, $\Delta_z = 0.1$: the TE-TM splitting has been enhanced to allow clear observation of the trigonal warping. As a consequence of the latter, we observe 3 points with positive Berry curvature and 1 point with negative Berry curvature in the middle (QGT components have been redistributed with respect to figures 5.10 and 5.11). The positive point on the left is less visible because it is not on the edge of the first Brillouin zone.

5.1.3 Conclusions

We have presented a method of direct extraction of the quantum geometric tensor components in reciprocal space from the results of the optical measurements in photonic systems. We demonstrate the successful application of this method to two different two-band systems: a planar cavity and a staggered honeycomb lattice. The protocol for a two band system is similar in spirit with the one performed in a cold atom experiment recently [103] (also based on the measurement of the angles $\theta(\mathbf{k})$ and $\phi(\mathbf{k})$ parametrizing the spinor). The advantage of the photonic platform is the possibility to perform this extraction by direct measurements (no manipulation of the lattice potential is required). In the second part, we generalize the method to a four-band system, considering a regular honeycomb lattice with TE-TM splitting and Zeeman splitting as an example. The numerical experiment accuracy enables to observe the interesting patterns of the quantum metric and the Berry curvature, as the signature of the trigonal warping in the case of a four-component spinor, which allows to be optimistic for future experiments. The access to these geometrical quantities can allow to increase our understanding of each of the systems presented in the different examples, where the QGT could affect the transport phenomena (e.g. via the anomalous Hall effect as discussed in the next section).

5.2 Effective theory of non-adiabatic evolution based on the quantum geometric tensor

Non-adiabaticity (NA) in quantum systems has been studied extensively since the pioneering works of Landau [320, 321], Zener [322], and others [323, 324, 325, 326], concerning the regime where the NA is exponentially small, whereas configurations with power-law NA were generally considered as somewhat less interesting [327, 328]. The Landau quasi-classical formalism allows to calculate the final non-adiabatic fraction (transition probability) when the perturbation smoothly vanish at infinities. However, this approach cannot be applied to a simple yet important situation of a magnetic field rotating with a constant angular velocity, because the perturbation does not vanish. Moreover, the NA changes during the evolution, and its final value is different from the maximal one. The Landau-Zener formalism allows to find only the former, while the latter is not exponentially small even if the evolution is perfectly smooth. In all these cases, the real part of the QGT allows to quantify the NA and brings a correction to the Berry phase.

In this section, we calculate the non-adiabatic corrections (NAC) for the phases and trajectories of wavepacket for a finite-time quantum evolution beyond the Landau-Zener approximation, considering the important family of geodesic trajectories, corresponding to acceleration from zero initial velocity. We show that these NACs are quantitatively described by the real part of the QGT, whereas the adiabatic limit is described by the imaginary part (Berry phase). In subsection 5.2.1, we compute the first order non-adiabatic correction to the geometric phase acquired by a spin in a rotating magnetic field. Then, in subsection 5.2.2, we introduce a new term in the semiclassical equations of motion describing the anomalous Hall effect (AHE) to take into account this non-adiabaticity and show that other corrections are null for geodesic trajectories. Finally in 5.2.3, we propose a specific example of application: a planar microcavity in the strong coupling regime as a a practical experimental situation showing how the real and imaginary part of the QGT control the AHE.

5.2.1 Two-level system in a magnetic field

A spin, which follows a slowly rotating magnetic field, is never perfectly aligned with it, and thus it exhibits fast precession (frequency Ω) about the magnetic field together with the slow rotation (ω) of both of them in the azimuthal plane (Fig. 5.13(a)). This behavior is similar to the rotation of a small wheel attached to a long shaft (Fig. 5.13(b)): the wheel, rotating around its axis with the angular frequency Ω, at the same time rotates with the frequency ω around the shaft fixation point. For both the spin and the wheel, there is an important rotational energy associated with the large frequency Ω, but another part of the energy is associated with the circular motion ω.

Nobody could think of neglecting the kinetic energy of the wheel's motion. However, the energy of the spin's slow rotation encoded in the Berry phase has been less
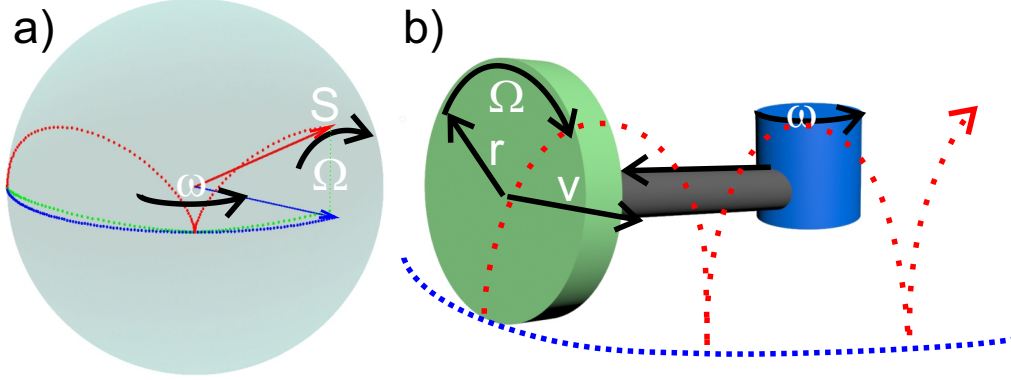
Figure 5.13: (a) Bloch sphere with the spin (red arrow) and the magnetic field Ω (blue arrow), adiabatic trajectory (blue) and real trajectory (red dashed line); (b) Mechanical analog: "adiabatic" trajectory of an infinitely small wheel (blue), cycloid trajectory of a point on a wheel (red). Ω - wheel rotation frequency, v - wheel velocity, ω - shaft center rotation.

evident to see. It can be obtained by applying the energy operator $\hat{E} = i\hbar\partial/\partial t$ to the rotating spinor $\psi(t) = 1/\sqrt{2}(e^{-i\omega t}, 1)^T e^{i\Omega t/2}$ (valid in the adiabatic limit when $\omega \to 0$), which gives $\langle \hat{E} \rangle = -\hbar\Omega/2 + \hbar\omega/2$. The first term in this expression is the usual energy of the spin in the magnetic field ("dynamical phase"), and the second is the energy associated with the Berry phase which appears because of the time dependence of the spinor. For the time $T = 2\pi/\omega$ of one full rotation of the field it gives the well known result $\gamma_B = \hbar\omega T/\hbar = \pi$.

However, because of the finite experiment duration, the spin does not perfectly follow the field and gets out of the azimuthal plane, tracing a cycloidal trajectory. The corresponding WF reads

$$\psi\left(t\right) = \begin{pmatrix} \cos\frac{\theta(t)}{2}e^{-i\omega t} \\ \sin\frac{\theta(t)}{2} \end{pmatrix} e^{i\frac{\Omega\cos\xi(t)}{2}t} \tag{5.16}$$

where θ is the polar angle and ξ is the angle between the field and the spin. Averaging this expression over precession time allows obtaining the correction to the energy.

5.2.1.1 Spin dynamics in a slowly rotating field

To estimate the correction close to the adiabatic limit, we use precession equation for the spin dynamics, which reads:

$$\frac{d\mathbf{S}}{dt} = \mathbf{S} \times \mathbf{\Omega} \tag{5.17}$$
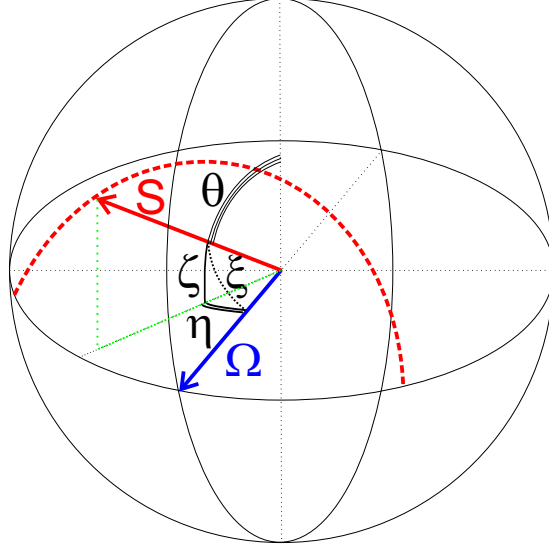
Figure 5.14: The spin vector **S** (red), its projection on the equatorial plane (green), and the magnetic field **Ω** (blue) on the Bloch sphere, with the angles used in the text: θ (polar angle of **S**), ζ (latitude of **S**), η (difference between the longitudes of **S** and **Ω**), and ξ (angle between **S** and **Ω**). Red dashed line shows the cycloidal spin trajectory.

Here, $\mathbf{\Omega}(t)$ is the magnetic field vector, which can change both in direction and magnitude in the general case. **S** is the spin vector whose components correspond to the mean value of the Pauli spin operators $\mathbf{S} = \frac{1}{2}(\langle\psi|\,\hat{\sigma}_x\,|\psi\rangle\,,\langle\psi|\,\hat{\sigma}_y\,|\psi\rangle\,,\langle\psi|\,\hat{\sigma}_z\,|\psi\rangle)^T$.

To be specific, we consider the rotation of the magnetic field in the equatorial plane $\mathbf{\Omega}(t) = \Omega(\cos(\omega t), \sin(\omega t), 0)$. The scheme of the Bloch sphere with the spin and the magnetic field and their relative angles is shown in Fig. 5.14. Since we are going to study small deviations from the adiabatic regime, the motion of the spin vector is limited to small angles close to the equator of the sphere. We can rewrite the equations using two new variables: the angle between the spin and the equatorial plane ζ (latitude), and the azimuthal angle between the spin projection on this plane and the magnetic field η (measured in the same direction as usual azimuthal angle). These equations read:

$$\begin{aligned} \frac{d\zeta}{dt} &= -\Omega\eta \\ \frac{d\eta}{dt} &= \Omega\left(\zeta - \frac{\omega}{\Omega}\right) \end{aligned} \tag{5.18}$$

Here, Ω is the magnitude of the magnetic field, while ω is its angular velocity: $\omega = d\phi/dt$ (ϕ is the azimuthal angle of the magnetic field). We see that these equations are similar to the Hamilton's equations for a harmonic oscillator in rescaled coordinates (η plays the role of coordinate q and ζ - the role of momentum p), but with an extra term $d\eta/dt = -\omega$, corresponding to a constant velocity of the harmonic oscillator, meaning that we consider it in a moving reference frame, or

that the oscillator itself is moving in our fixed reference frame. First of all, we can find a stationary solution:

$$\zeta_{eq} = \frac{\omega}{\Omega} \tag{5.19}$$

It means that if the magnetic field rotates with a constant angular velocity ω, the spin is able to follow it with the same angular velocity if it is deviated from the equatorial plane towards the pole by ω/Ω. In this case, $\eta = 0$.

Non-adiabatic fraction   This solution is very important, because it allows us to estimate the non-adiabaticity in a general case considered below. The fraction of the excited state in the wavefunction is given by:

$$f_{NA,eq} = \left| \left\langle \begin{array}{c} \cos\frac{\pi/2-\zeta_{eq}}{2} \\ \sin\frac{\pi/2-\zeta_{eq}}{2} \end{array} \middle| \begin{array}{c} 1/\sqrt{2} \\ -1/\sqrt{2} \end{array} \right\rangle \right|^2 \approx \frac{\zeta_{eq}^2}{4} = \frac{\omega^2}{4\Omega^2} \tag{5.20}$$

As it could be intuitively understood, it increases when the angular velocity of the rotating magnetic field increases. This fraction is complementary to fidelity $F = |\langle\psi|\psi_0\rangle|$, where ψ_0 is the ground state in which the system is expected to remain:

$$f_{NA} + F^2 = 1 \tag{5.21}$$

If at $t = 0$ the spin is not in the position corresponding to the stationary solution (the equilibrium point $\zeta = \zeta_{eq}$, $\eta = 0$), it will precess about the equilibrium position, exactly as the harmonic oscillator with some initial displacement oscillates around the equilibrium point. The solutions for a spin aligned with the magnetic field as initial condition read:

$$\zeta(t) = \frac{\omega}{\Omega}(1 - \cos\Omega t), \quad \eta(t) = -\frac{\omega}{\Omega}\sin\Omega t \tag{5.22}$$

Hence, if at $t = 0$ the spin is in equatorial plane, it will oscillate around the equilibrium position $\zeta_{eq} = \omega/\Omega$, that is, between $\zeta = 0$ and $\zeta = 2\zeta_{eq}$. The non-adiabatic fraction associated with the average spin position will also be will be given (5.20).

Interestingly, this NA fraction (fraction of the excited state in the WF) for a spin on the Bloch sphere (5.20) can be expressed for an arbitrary parameter space using the quantum metric tensor (1.6) of a two level system. Indeed, using the relation $\omega(\lambda) = \frac{d\phi}{dt} = 2\frac{ds}{dt}$ and the definition of ds^2

$$ds^2 = g_{ij}d\lambda_i d\lambda_j \tag{5.23}$$

one can rewrite as:

$$f_{NA,eq}(\lambda) = \frac{g_{\lambda_i\lambda_j}}{\Omega^2}\frac{d\lambda_i}{dt}\frac{d\lambda_j}{dt} \tag{5.24}$$

with $\Omega = \Omega(\lambda)$. This will be particularly useful to express it in momentum space.

5.2.1.2 Geometric phase correction.

One can estimate the average correction to the energy due to the deviation of $\mathbf{S}$ from $\boldsymbol{\Omega}$ by applying the energy operator $\hat{E}$ to the general spinor 5.16.

$$
\begin{aligned}
\langle \hat{E} \rangle &= \frac{\Omega}{2\pi} \int_0^{2\pi/\Omega} \psi^\dagger (i\hbar \frac{\partial}{\partial t} \psi) dt \\
&= \frac{\Omega}{2\pi} \int_0^{2\pi/\Omega} \left(\hbar\omega \cos^2(\theta/2) - \frac{\hbar\Omega}{2}\cos\xi + \frac{\hbar\Omega t}{2}\sin\xi \frac{\partial\xi}{\partial t} \right) dt
\end{aligned}
\tag{5.25}
$$

The time dependence of $\theta(t)$ and $\xi(t)$ are found from the equations for the spin dynamics (5.22) using:

$$
\theta(t) = \frac{\pi}{2} - \zeta(t), \quad \xi = \sqrt{\zeta^2 + \eta^2}
\tag{5.26}
$$

For small angles, one can Taylor expand the integrand up to the second order in ζ, η and ξ and find an analytical solution for the average energy:

$$
\langle \hat{E} \rangle = \frac{\Omega}{2\pi} \int_0^{2\pi/\Omega} \psi^\dagger (i\hbar \frac{\partial}{\partial t} \psi) dt = -\frac{\hbar\Omega}{2} + \frac{\hbar\omega}{2}\left(1 + \frac{\omega}{\Omega}\right)
\tag{5.27}
$$

where the last term allows to find the corrected geometrical phase after a full rotation time T:

$$
\gamma = \pi(1 + 2\omega/\Omega)
\tag{5.28}
$$

or a correction of the form:

$$
\frac{\gamma - \gamma_B}{\gamma_B} = \frac{2\pi}{\Omega T}
\tag{5.29}
$$

The adiabatic limit is recovered when $\omega/\Omega \to 0$, one can observe that the correction decreases as $1/T$ and not exponentially.

To illustrate it better, the total extra phase after one full rotation of the magnetic field from the numerical solution of the Schrödinger equation is plotted in Fig. 5.15(a) as a function of the rotation duration T measured in units of precession periods $2\pi/\Omega$ (equivalent to the frequency ratio Ω/ω). Larger T means slower rotation and the adiabatic limit corresponds to $T \to \infty$ or $\omega/\Omega \to 0$. We see that the extra phase indeed converges to the value π, but the correction is not negligible: $\Delta\gamma/\gamma_B > 30\%$ for $\omega > \Omega/10$. The difference between the exact extra phase and the adiabatic value of π is shown in a Log-Log plot on Fig. 5.15(b), again as a function of T (black curve). We see that instead of being exponentially small, this correction decreases only as $1/T$. The analytical non adiabatic correction (5.29) (red curve), fits the exact result. The small oscillations which can be seen in the numerical result (black curves) of the Schrödinger equation are due to the fact that the spin does not stop its cycloidal trajectory at the same position on the Bloch sphere at the end of
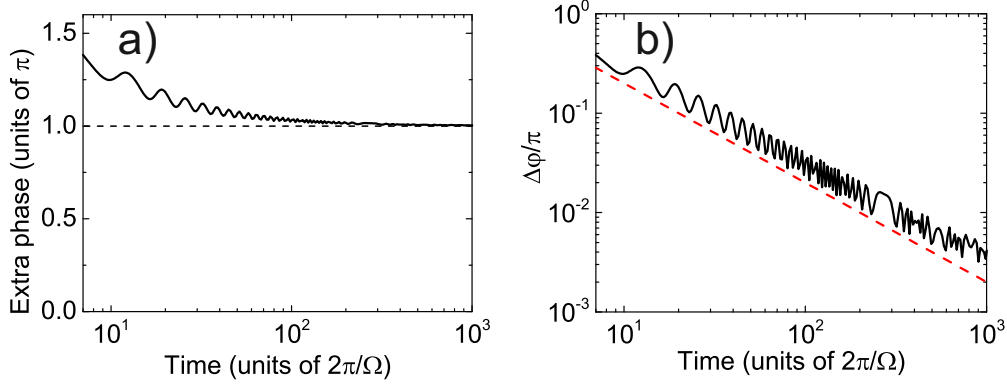
Figure 5.15: (a) Total extra phase for one full spinor rotation as a function of the rotation time; (b) Deviation from the adiabatic Berry phase: numerical calculation (black) and analytical correction exhibiting $1/T$ decay (red dashed).

each periods T. Indeed, after one period the spin is not aligned with the magnetic field and their relative position, different at the end of each cycle, leads to these small oscillations in the numerically extracted geometric phase.

This type of non-adiabatic correction for the geometrical phase acquired by a spin in a rotating magnetic field has been considered in several works based on different approaches which give similar results [329, 330, 331]. Note that this correction is a part of the general Aharonov-Anandan phase [17].

5.2.2 Semiclassical equations of a wavepacket

Berry curvature has been shown to affect the trajectory of accelerated wavepackets, creating an anomalous velocity contribution in the anomalous Hall effect [332, 333]. The semiclassical equations of motion for the center of mass of a wavepacket in presence of Berry curvature can be derived using an effective Lagrangian formalism [333, 3] [Appendix B.1]and read:

$$\hbar\frac{\partial \mathbf{k}}{\partial t} = \mathbf{F}, \quad \hbar\frac{\partial \mathbf{r}}{\partial t} = \frac{\partial \varepsilon_n}{\partial \mathbf{k}} - \hbar\frac{\partial \mathbf{k}}{\partial t} \times \mathbf{B} \tag{5.30}$$

where ε_n is the energy dispersion, $\mathbf{B} = (\Omega_{yz}, \Omega_{zx}, \Omega_{xy})^T$ is the Berry curvature vector and $\mathbf{F}$ is an external conservative force, accelerating the WP. For charged particles, $\mathbf{F} = q\mathbf{E}$. Magnetic forces, known to affect the magnetic susceptibility [114, 115], are not the subject of the present work. The velocity of the wavepacket center of mass has two contributions: the normal group velocity $v_n = \partial \varepsilon_n/\partial \mathbf{k}$, and the *anomalous* term proportional to the Berry curvature of the band which appears in the transversal direction with respect to the applied force. These equations are valid in the adiabatic limit assuming that the wavepacket remains in a given band and

that its momentum space center of mass remains in the corresponding instantaneous eigenstate $|u_{n,\mathbf{k}}\rangle$.

5.2.2.1 Effective non-adiabatic correction

The simplest systems which can exhibit non-zero Berry curvature in momentum space are two band systems. The corresponding Hamiltonian can be decomposed as $H_{\mathbf{k}} = h_0 + \mathbf{h}(\mathbf{k}).\hat{\boldsymbol{\sigma}}$. The acceleration of a wavepacket in these systems, meaning $\mathbf{k} \rightarrow \mathbf{F}t$ is similar to the problem of a spin in a time-dependent magnetic field considered in the previous section, where the role of the magnetic field is played by $\mathbf{h}(\mathbf{k})$.

We have highlighted 5.2.1 that non-adiabaticity is unavoidable in finite time experiments and we have derived the first order non-adiabatic correction to the geometrical phase in the configuration where the magnetic field is rotating along a geodesic of the Bloch sphere (great circle). The non-adiabatic fraction should play a role in the wavepacket dynamic.

NACs account for the fact that the WF is a superposition of two eigenstates $|u\rangle = f_0 |u_0\rangle + f_1 |u_1\rangle$ (where $|f_1|^2 = f_{NA}$ found above). Their respective energies contribute both to the first term on the right hand side of Eq. (5.30): $\tilde{\varepsilon}(k) = |f_0|^2 \varepsilon_0(k) + |f_1|^2 \varepsilon_1(k)$, ultimately providing a second-order correction to the group velocity. Other NACs concern the second term on the right hand side.

We consider the specific case where the effective magnetic field is rotating on geodesics as considered above (even if of course NAC should play a role for any trajectory in the Bloch sphere). In this case, the corrections derived from the standard effective Lagrangian formalism [333] applied to higher order in the external force vanish as discussed below. To take into account the NAC to the Berry curvature term in the semiclassical equations, we need to keep track of the real trajectory of the spin on the Bloch sphere. A good estimation is given by its equilibrium trajectory $\theta = \theta_{eq}$, $\eta = 0$. This is done by replacing the ∂_ϕ derivation by $1/\sin\theta_{eq}\partial_\phi$ to define the corrected Berry curvature:

$$\Omega_{\theta\phi} = i\left(\langle\partial_\theta u_0|\partial_\phi u_0\rangle - \langle\partial_\phi u_0|\partial_\theta u_0\rangle\right) \tag{5.31}$$

becomes:

$$\Omega_{NA,\theta\phi} = \frac{i}{\sin\theta_{eq}}\left(\langle\partial_\theta u_0|\partial_\phi u_n\rangle - \langle\partial_\phi u_0|\partial_\theta u_0\rangle\right) \approx (1 + \frac{\zeta_{eq}^2}{2})\Omega_{\theta\phi} \tag{5.32}$$

The correcting factor appears to be proportional to the equilibrium non-adiabatic fraction $f_{NA,eq}$ introduced above. Moreover, we have seen previously that this fraction can be expressed in term of the quantum metric for an arbitrary parameter space (5.24). Rewriting the expression in $\mathbf{k}$ space gives:

$$\Omega_{NA,ij} = \left(1 + \sum_{l,m}\frac{g_{lm}}{(\varepsilon_0 - \varepsilon_1)^2}\frac{\partial k_l}{\partial t}\frac{\partial k_m}{\partial t}\right)\Omega_{ij} \tag{5.33}$$

which finally leads the following corrected semiclassical equation:

$$\hbar\frac{\partial \mathbf{r}}{\partial t} = \frac{\partial \tilde{\varepsilon}}{\partial \mathbf{k}} - \hbar\frac{\partial \mathbf{k}}{\partial t} \times \mathbf{B}_{NA} \tag{5.34}$$

where $\mathbf{B}_{NA} = (\Omega_{NA,yz}, \Omega_{NA,zx}, \Omega_{NA,xy})^T$. Since $\mathbf{k} = \mathbf{F}t$, the correction of the Berry curvature appears to the second order in the external force leading to a third order correction for the center of mass velocity. This means that correction to the energy should be taken up to this order.

This equation shows that the anomalous velocity is a sum of the adiabatic value (as in Eq. (5.30)) and a NAC (the second term in the parenthesis in (5.33)). We stress that this equation is only valid when the field follows a geodesic trajectory in the parameter space. In such a case, while the renormalized energy $\tilde{\varepsilon}$ brings second-order corrections to the acceleration in the direction of the force, the anomalous velocity only includes this ad hoc correction, because the other first and second-order corrections to this term cancel out. Since the transverse conductivity arising from the anomalous velocity is known to be determined by the integral of the Berry curvature, its NAC could be linked with the integral of the quantum metric.

5.2.2.2 Corrections from the effective Lagrangian approach

Corrections to semiclassical equation up to the second order in the applied field have been considered using the effective Lagrangian formalism in previous works by Gao and Niu [116, 114]. Applying the technique up to the third order in the applied force gives the following semi-classical equations [Appendix B.2]:

$$\hbar\frac{\partial \mathbf{k}}{\partial t} = \mathbf{F} \tag{5.35}$$

$$\hbar\frac{\partial \mathbf{r}}{\partial t} = \frac{\partial \tilde{\varepsilon}}{\partial \mathbf{k}} - \hbar\frac{\partial \mathbf{k}}{\partial t} \times \tilde{\mathbf{B}} \tag{5.36}$$

with the corrected energy:

$$\tilde{\varepsilon} = |f_0|^2\varepsilon_0 + |f_1|^2\varepsilon_1 \tag{5.37}$$

and $\tilde{\mathbf{B}}$ the corrected Berry curvature up to the third order in the external electric force:

$$\tilde{\mathbf{B}} = \mathbf{B} + \mathbf{B}^{(c1)} + \mathbf{B}^{(c3)} \tag{5.38}$$

where the correction to the Berry curvature vector can be expressed in terms of the quantum metric tensor:

$$\mathbf{B}^{(c1)} = \nabla_{\mathbf{k}} \times \left(\frac{2\overleftrightarrow{g}\mathbf{F}}{(\varepsilon_0 - \varepsilon_1)}\right) \tag{5.39}$$

$$\mathbf{B}^{(c3)} = -\frac{1}{2}\nabla_{\mathbf{k}} \times \left(\left(\sum_{i,j} g_{ij}F_iF_j\right)\frac{2\overleftrightarrow{g}\mathbf{F}}{(\varepsilon_0 - \varepsilon_1)^3}\right) \tag{5.40}$$

where $\overleftrightarrow{g}$ is the metric in the matrix form. $\mathbf{B}^{(c1)}$ corresponds to the first order correction found by Gao and Niu in [116, 114] recently written for a two-band

system. Its contribution to the anomalous velocity being of second order in the applied force, this correction should dominate the one we have introduced above.

However, in the case where energy bands have a rotational symmetry, one can show that both $\mathbf{B}^{(c1)}$ and $\mathbf{B}^{(c3)}$ vanish on geodesics. Hence, if the wavepacket follows geodesics in momentum space, the only correction will be given by (5.34).

Zero contribution along geodesics To demonstrate this we analyze the first-order contribution of the real part of the quantum geometric tensor to the trajectory along the geodesic lines in the parameter space. This contribution to the dynamical equation reads:

$$\dot{\mathbf{r}} = \dot{\mathbf{k}} \times \mathbf{B}^{(c1)} \tag{5.41}$$

where the first order correction of the Berry curvature is given by Eq. (B.26) Let us consider a particle accelerated from $k = 0$ in the X direction by a field along the X axis $\mathbf{F} = F_x \mathbf{e}_x$. The contribution to the trajectory in the transverse direction is given by

$$\dot{y} = B_z^{(1)} \dot{k}_x \tag{5.42}$$

where

$$B_z^{(1)} = 2 \left[\frac{\partial}{\partial k_x} \left(\frac{g_{yx} F_x}{\varepsilon_0 - \varepsilon_1} \right) - \frac{\partial}{\partial k_y} \left(\frac{g_{xx} F_x}{\varepsilon_0 - \varepsilon_1} \right) \right] \tag{5.43}$$

Other terms proportional to F_y disappear because $F_y = 0$. Note that the indices of the tensor correspond to the coordinates in the reciprocal space, but are written as x, y to save space. The real space component of the force actually represents the time derivative of the wave vector as well: $F_x = \hbar dk_x/dt$. We need to analyze each of these two terms. First, we show that the off-diagonal components of the metric tensor are zero when the basis vectors are chosen tangential and perpendicular to the geodesic curve, along which the system propagates. The first term is therefore zero. Then we show that the terms $\frac{\partial}{\partial k_j} g_{ii}$ are zero as well. Finally, we show that rotational symmetry of the energy bands on the top of that implies the vanishing of first and third order contributions to the Berry curvature defined by eqs. (B.26)-(B.27).

Metric tensor along geodesic lines The length of a parametric curve in a space with a metric tensor g_{ij} is given by:

$$L = \int \sqrt{\sum_{i,j} g_{ij} \frac{dx_i}{dt} \frac{dx_j}{dt}} dt \tag{5.44}$$

The length of a small part of this curve is simply

$$dL = \sqrt{\sum_{i,j} g_{ij} \frac{dx_i}{dt} \frac{dx_j}{dt}} dt \tag{5.45}$$

We choose the basis vector x_i to be tangential to the trajectory and x_j to be normal to the trajectory. The latter means that $dx_j/dt = 0$. In this basis, we have therefore

a simplified expression for the length of the curve:

$$dL = \sqrt{g_{ii}}dx_i \tag{5.46}$$

which is quite natural. We suppose that this parametric curve is a geodesic one, which means that it has the smallest possible length. Now, let us consider a curve which deviates slightly from the geodesic curve: dx_j/dt is not zero, but much smaller than dx_i/dt. The fact that the geodesic curve has the smallest possible length means that dL is minimized with respect to dx_j , and therefore its derivative should be zero:

$$\frac{\partial L}{\partial x_j} = 0 \tag{5.47}$$

The length of this curve now reads

$$dL = \sqrt{g_{ii}\left(\frac{dx_i}{dt}\right)^2 + g_{jj}\left(\frac{dx_j}{dt}\right)^2 + 2g_{ij}\frac{dx_i}{dt}\frac{dx_j}{dt}}dt \tag{5.48}$$

Neglecting the second order term and expanding the square root in series of dx_j/dt, we obtain

$$dL \approx \sqrt{g_{ii}}dx_i + \frac{g_{ij}}{\sqrt{g_{ii}}}dx_j \tag{5.49}$$

We now see that the geodesic nature of the curve

$$\frac{\partial L}{\partial x_j} = \frac{g_{ij}}{\sqrt{g_{ii}}} = 0 \tag{5.50}$$

is equivalent to the diagonality of the metric tensor in tangential/normal basis:

$$g_{ij} = 0 \tag{5.51}$$

and therefore the first contribution of Eq. (5.43) is zero.

Transverse derivative of the metric tensor   We need to analyze the second term given by

$$\frac{\partial}{\partial k_y}g_{xx}F_x \tag{5.52}$$

While in general, the diagonal term g_{xx} can, of course, depend on k_y, the first order derivative is zero on the geodesic line, as we show below. Indeed, on the one hand we have

$$dL = \sqrt{g_{xx}}dk_x \tag{5.53}$$

And on the other hand, the minimal length of the geodesic requires that

$$\frac{\partial L}{\partial k_y} = 0 \tag{5.54}$$

Thus,

$$\frac{1}{2\sqrt{g_{xx}}}\frac{\partial g_{xx}}{\partial k_y} = 0 \tag{5.55}$$

And finally

$$\frac{\partial g_{xx}}{\partial k_y} = 0 \tag{5.56}$$

This contribution to Eq. (5.43) is also zero along a geodesic line.

Rotational symmetry Rotational symmetry of the energy bands means that $\varepsilon_i(\mathbf{k}) = \varepsilon_i(k)$ (with $k = |\mathbf{k}| = \sqrt{k_x^2 + k_y^2}$). Therefore, one has:

$$\frac{\partial}{\partial k_i}(\varepsilon_0 - \varepsilon_1) = \frac{\partial(\varepsilon_0 - \varepsilon_1)}{\partial k}\frac{\partial k}{\partial k_i} = \frac{\partial(\varepsilon_0 - \varepsilon_1)}{\partial k}\frac{k_i}{k} \tag{5.57}$$

Combining the results of the above paragraphs with this one in Eq. (5.43) with $k_x = F_x t/\hbar$ and $k_y = 0$ finally gives $B_z^{(1)} = 0$. The same arguments applied to Eq. (B.27) can be used to show that $B_z^{(3)}$ vanishes too.

Comment on the absence of non-adiabatic correction. We have shown above that higher order corrections found in the effective Lagrangian formalism vanish on geodesics. One can wonder why our effective correction is not described by this approach. This can be qualitatively understood as follows: the average deviation of the spin due to the cycloidal trajectory that we take into account is not a perturbation. It is an estimation of the exact solution of the dynamical Schrödinger equation. The cycloidal trajectory is due to real interband oscillations and such effect cannot be described by a semiclassical theory even if one use perturbation theory to higher orders. Our effective correction allows to estimate at which order in the applied force it can become important. Even if the corrected semiclassical equations written in the form of eqs. (5.34) are valid only on geodesics, the non-adiabatic behaviour will be present for any trajectories. The comparison with the work of Gao and Niu allows to stress that some care is needed if one want to use their semiclassical theory to higher order in the external force because non-adiabatic effects can become non-negligible compared to the perturbative corrections.

5.2.3 Polariton anomalous Hall effect

We begin with the parabolic spinor Hamiltonian of the lower polariton branch (LPB) of a planar cavity:

$$H_0 = \begin{pmatrix} \frac{\hbar^2 k^2}{2m^*} + \Delta & \beta k^2 e^{2i\phi} \\ \beta k^2 e^{-2i\phi} & \frac{\hbar^2 k^2}{2m^*} - \Delta \end{pmatrix} \tag{5.58}$$

with the following eigenvalues (Fig. 5.16(a)):

$$\varepsilon_\pm(k) = \frac{\hbar^2 k^2}{2m^*} \pm \sqrt{(\Delta^2 + \beta^2 k^4)} \tag{5.59}$$

with $\Delta = 60\ \mu$eV, $\beta = 0.14$ meV/μm^{-2}. While the system shows no gap because of the positive mass of both branches, and therefore is not a topological insulator, it
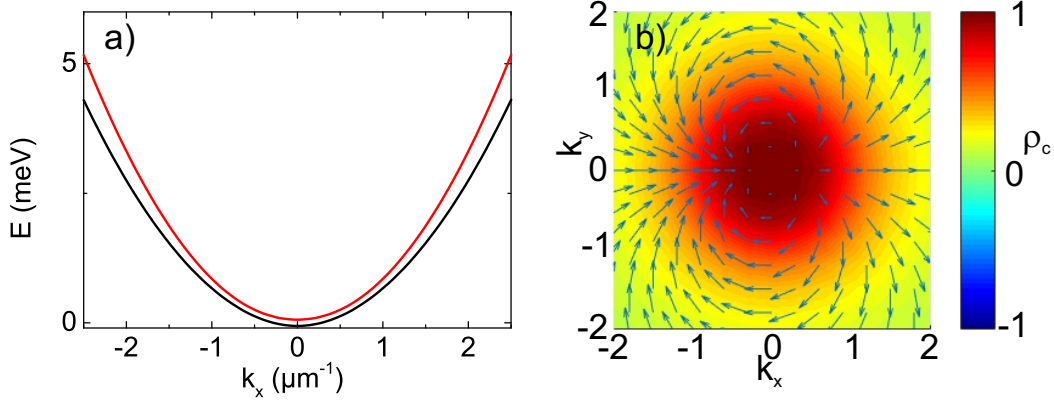
Figure 5.16: (a) LPB split by Zeeman field and TE-TM SOC; (b) Pseudospin texture of the lower eigenstate: in-plane pseudospin projection (arrows) and S_Z (color).

nevertheless exhibits a non-zero Berry curvature, reflected by the pseudospin texture (Fig. 5.16(b)), similar to bilayer graphene under bias voltage [334, 221, 242]. We compute analytically the QGT for the lower eigenstate in polar coordinates (k,ϕ):

$$g_{kk} = \frac{\Delta^2 k^2 \beta^2}{(\Delta^2 + \beta^2 k^4)^2}, \quad g_{\phi\phi} = \frac{k^2 \beta^2}{\Delta^2 + \beta^2 k^4} \tag{5.60}$$

$$g_{k\phi} = g_{\phi k} = 0, \quad \mathbf{B} = \frac{2\Delta k^2 \beta^2}{(\Delta^2 + k^4 \beta^2)^{3/2}} \mathbf{e_z}$$

These are plotted as solid curves in Fig. 5.18(a). Because of the k^2 dependence of the TE-TM SOC, the form of the Berry curvature is different from the one of Rashba SOC [3, 205] (with maximum at $k = 0$) and similar to the one of bilayer graphene [294].

   This particular system allows to directly compare the result of the corrected semiclassical equations (5.34) with the exact numerical solution of the time dependent spinor Schrödinger equation with a gradient potential (5.8). In the simulation, a gaussian wavepacket is created at $t = 0$ with σ^+ polarization, we then extract its center of mass position over time. A video of such numerical experiment is available in the supplemental material of ref. [117].

   Figure 5.17(a) shows the trajectories of polariton WP accelerated in a microcavity by a realistic wedge $U(x) = -Fx$, where $F = 1$ meV/128 μm for 3 values of β. The red-dashed curves calculated using equation (5.34) (accounting for both $\Re[T]$ and $\Im[T]$) are in excellent agreement with direct numerical solution of the Schrödinger equation (5.8) (black curves). The blue dotted curve shows the trajectory without the correction (5.30). The difference becomes more important for higher gradients. Fig. 5.17(b) shows the final lateral shift ΔY as a function of β: adiabatic ($\Delta Y = \sqrt{\beta}\Gamma^2(3/4)/\sqrt{\Delta\pi}$ - blue dotted [Appendix C]) and corrected (red) curves, as well as results of simulations (black dots). Numerical results are much
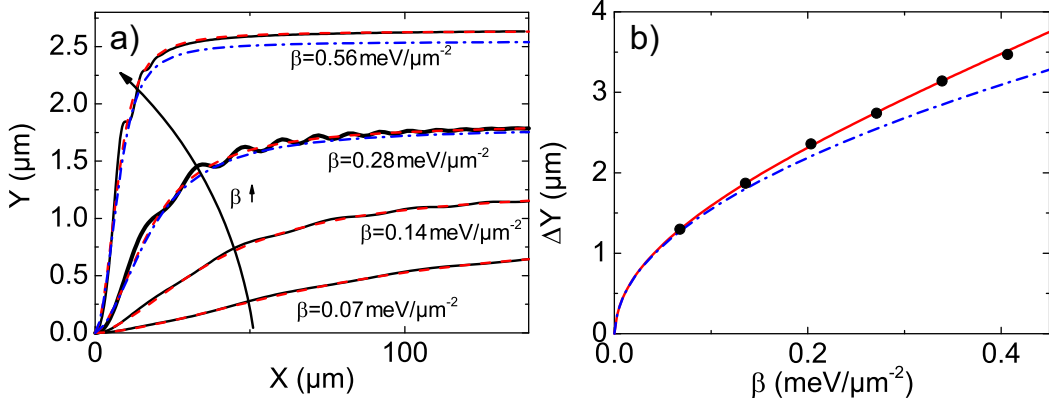
Figure 5.17: **Polariton anomalous Hall drift.** (a) WP trajectories in real space: numerical (black) and analytical (red dashed, uncorrected - blue dash-dotted) for 3 values of TE-TM SOC β ($\Delta = 0.06$ meV); (b) Final lateral shift as a function of β: adiabatic (blue dash-dotted line), corrected (red solid line), and numerical (black dots). Here, $\Delta = 0.03$ meV.

better fitted by the theory including the NAC. Both the *relative* lateral shift and the NAC are comparable to the values reported for metamaterials [335]. Such effects could be important for applications in integrated polaritonics.

By looking carefully on the numerically extracted curve in Fig. 5.17(a) one can distinguish some small oscillations. These oscillations are reminiscence of the cycloidal trajectory of the spin in the Bloch sphere which do not appear in the corrected semiclassical equations because it accounts only the average position of the spin. Interestingly, similar oscillations of the center of mass position appear in the *Zitterbewegung* effect due to spin oscillations. In the conventional effect, this behaviour occurs when the wavepacket is moving at a constant longitudinal velocity ($\mathbf{k} = \mathbf{cte}$) and if its center in $\mathbf{k}$ space is not in an eigenstate of the two-band system. In this sense, Zitterbewegung oscillations can be seen as a purely non-adiabatic behaviour. The configuration of an accelerated wavepacket considered here is more subtle (both the spin dynamics and the transverse motion of the wavepacket are more complicated). The study of the interplay between an "accelerated Zitterbewegung" (non-adiabatic origin) and the anomalous Hall effect (valid in the adiabatic limit) in two band systems is of interest for future works.

5.2.3.1 QGT and non-adiabaticity measurement

A very interesting opportunity to measure the QGT directly is offered by the radiative states of photonic systems which allow to access all pseudospin components $\mathbf{S}$ via polarization as discussed in the previous section [5.1.1.1]. The results of the extraction are presented in Fig. 5.18(a) as dashed curves, whose agreement with the
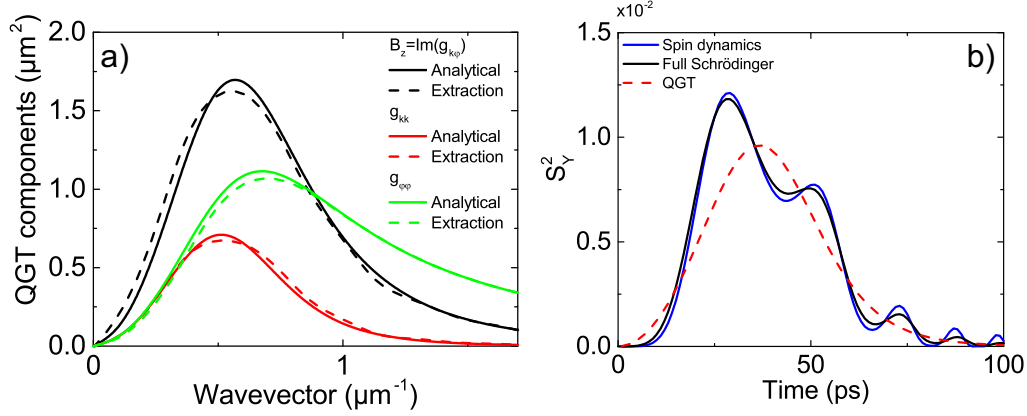
Figure 5.18: (a) QGT components: B_Z (black); g_{kk} (red) and $g_{\phi\phi}$ (green) calculated analytically (solid lines) and extracted from numerical experiment (dashed lines). (b) The non-adiabaticity (S_Y^2), calculated using the full Schrodinger equation (black), the spin dynamics equation (blue), and the QGT (red dashed).

solid lines obtained from Eq. (5.60) confirms the validity of this method.

We can use Eq. (5.24) to estimate the non-adiabaticity of a polariton wavepacket, accelerated in combined TE-TM and Zeeman fields. In this case the total magnetic field energy reads:

$$\hbar\Omega = \sqrt{\Delta^2 + \left(\beta k^2\right)^2} \tag{5.61}$$

The non-adiabaticity can therefore be written as:

$$f_{NA}\left(k\right) = \frac{F^2 g_{kk}}{\hbar^2 \Omega^2} \tag{5.62}$$

We stress that the non-adiabatic fraction and the corresponding correction are calculated from the adiabatic metric. In the experimental configuration we consider, where the polaritons propagate in a constant gradient, the non-adiabaticity of the wavepacket can be measured via the diagonal polarization degree. For this, one should orient the cavity in such a way that the wedge points in the X direction. Then, the "horizontal" polarization should be chosen parallel to this X axis. In this case, the adiabatic evolution means that the spin rotates from the Z axis (circular eigenstate at $k = 0$) to the X pseudospin axis (horizonal polarization), while the deviation from this rotation is necessarily towards the Y pseudospin axis (diagonal polarization). The three pseudospin components can be extracted from the spatially-integrated intensities measured in 3 pairs of orthogonal polarizations (5.3).

Figure 5.18(b) shows the agreement between the non-adiabaticity, given by the S_Y^2 pseudospin component, calculated by solving full Schrodinger equations (black), the simple spin dynamics equation, Eq. (5.18) (blue), and given by the component of the QGT, Eq. (5.62) (red dashed). We see that the latter captures very well the

behavior of the full system, and that the spin dynamics equation for small angles is sufficiently precise. The figure is plotted for $\beta = 0.14$ meV/μm^{-2}.

5.2.4 Conclusions

We introduce a new type of correction to the semiclassical equations of motion of an accelerated WP on geodesic trajectories in two-band systems appearing in any realistic finite-duration experiment. While the adiabatic limit is determined by the Berry curvature, the NAC is determined by the quantum metric. This correction is not present in semiclassical equation derived from the wavepacket effective Lagrangian. Moreover, all the corrections found in this approach vanish on geodesic trajectories.

Whereas, we have studied the specific case of geodesic trajectories, such non-adiabatic contribution should play a role for any trajectory (exactly as a spin will exhibit cycloidal trajectory on the Bloch sphere even if the magnetic field is not evolving on a great circle). Therefore, in general, some care will be needed when studying the wavepacket response to higher order in the external force.

The particular case of a planar microcavity in the strong coupling regime allows to extract the QGT components by direct measurements and to check their effects on the wavepacket evolution.

Recently, we became aware of a work by A. Gutierrez-Rubio et al. [336] devoted to a microscopic study of the (adiabatic) polariton anomalous Hall effect in a system based on a Transition-Metal Dichalcogenides monolayer embedded in perfect metallic cavity. They give an interesting discussion on the different contributions to the Berry curvature of polaritons in this system and derive an effective two-by-two Hamiltonian equivalent to Eq. (5.58). In the system they consider, the TE-TM splitting arises from the exciton-photon coupling, the bare photonic one being zero in metallic cavities.

Conclusions and perspectives

In this thesis we studied different transport phenomena related to the presence of non-zero Berry curvature. In chapter 3, we considered single particle effects. We have computed the topological phase diagrams for two models leading to the quantum anomalous Hall effect for electrons or photons in honeycomb lattices. We have also discussed the quantum valley Hall effect. In this case, if the existence of interface states can be understood in term of valley Berry curvatures, they are not topologically robust against backscattering.

In chapter 4, to look at the effect of interactions we considered macroscopic Bose-Einstein condensates loaded in honeycomb potentials. We showed that spin-anisotropic interactions of polaritons can lead to density driven topological phase transitions for the Bogoliubov density waves both at thermal equilibrium and under quasi-resonant excitation. We also considered vortex excitations in a staggered honeycomb potential and showed that their intrinsic robustness combined with the vortex-valley coupling leads to a topologically protected vortex propagation.

In the last chapter 5, we proposed a protocol to measure the quantum geometric tensor components in reciprocal space for different photonic or polaritonic systems. Then, considering a two band system we highlighted the unavoidable non-adiabaticity during a wavepacket acceleration in an anomalous Hall experiment. We proposed a way to take this effect into account in the semiclassical equations of motion. As an illustration, we considered the original polariton anomalous Hall effect which allowed us to compare our result with numerical simulations.

These results appeal for further studies. Concerning the non-adiabatic correction, different directions are opened. In electronic systems, the anomalous Hall effect being linked with a quantized transverse conductivity when integrated over the occupied states, we can wonder if the non-adiabaticity could bring additional corrections to this quantity. Different two-band models can be studied such as the 1988 Haldane model in two dimensions and Weyl semimetals in three dimensions. For the cavity polariton system, it could be useful to think about specific experimental conditions to increase the anomalous Hall drift and its observability. Another interesting question concerns the effect of interactions during the wavepacket acceleration.

Keeping the interacting regime in mind, the study of vortex excitations in honeycomb lattices taking into account TE-TM SOC and a Zeeman field appears quite naturally. Whereas we do not expect a vortex-valley coupling in this situation as in a staggered potential, the understanding of their core structure and stability in the bulk is still of interest. The possibility to make them move thanks to the underlying band topology remains an interesting question.

Another long-term topic concerns vortex mutual interactions. For instance, the presence of a large number of vortices can lead to vortex clustering, a scaling be-

haviour related to 2D quantum turbulence. The interplay of this universal scaling phenomena with the presence of Berry curvature (both with and without lattices) appears as a very attractive direction of research.

Effective 2 by 2 Hamiltonian with trigonal warping

Between the two limits considered in section 3.3.1 of the manuscript to compute analytically valley topological charges, it is still possible to write an effective 2 by 2 Hamiltonian which reads:

$$
\begin{aligned}
H_{K,eff} \quad = \quad & \begin{pmatrix} \Delta_{AB} & \frac{3a\delta J}{2}(q_y - iq_x) \\ \frac{3a\delta J}{2}(q_y + iq_x) & -\Delta_{AB} \end{pmatrix} \\
+ \quad & \frac{1}{\Delta_{AB}^2 + 9\delta J^2} \begin{pmatrix} \frac{9a^2 J^2 \Delta_{AB}}{4}q^2 & \frac{27a^2 J^2 \delta J}{4}(q_y + iq_x)^2 \\ \frac{27a^2 J^2 \delta J}{4}(q_y - iq_x)^2 & -\frac{9a^2 J^2 \Delta_{AB}}{4}q^2 \end{pmatrix}
\end{aligned} \tag{A.1}
$$

This effective Hamiltonian allows to compute the energy dispersion taking into account the trigonal warping. Moreover, one can also compute the Berry curvature of the low energy bands which can be written as follow in polar coordinates (q, ϕ).

$$
\mathcal{B}_z = -\frac{\tau_z 18a^2 \Delta_{AB}\delta J^4 (4\delta J^4 - a^2 J^2(\delta J^2 + 4J^2))q^2 + a^3 J^4 q^3 \sin(3\phi)}{(\Delta_{AB}^2(4\delta J^2 + a^2 J^2 q^2)^2 + 9a^2\delta J^2 q^2(4\delta J^4 + a^2 J^4 q^2) + 36a^3\delta J^4 J^2 q^3 \sin(3\phi))^{3/2}} \tag{A.2}
$$
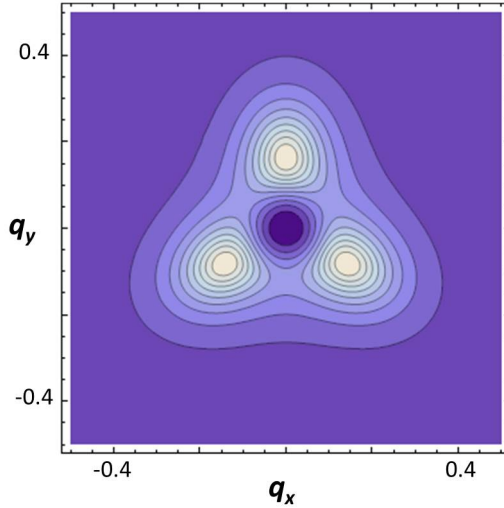
Figure A.1: Berry curvature around K point with trigonal warping contribution (Eq. (A.2)). (Parameters: $\Delta_{AB}(r) = 0.1J$, $\delta J = 0.2J$)

The form of the the resulting Berry curvature describes well the additional bands extrema contributions (see Fig. A.1). This quantity is not integrable analytically but converge numerically to 2π when $\delta J \gg \Delta_{AB}$. Each additional Dirac points, located at $t_1 = \left(0, \frac{2\delta J^2}{aJ^2}\right)$, $t_2 = \left(\frac{\sqrt{3}\delta J^2}{aJ^2}, -\frac{\delta J^2}{aJ^2}\right)$, $t_3 = \left(-\frac{\delta J^2}{aJ^2}, -\frac{\sqrt{3}\delta J^2}{aJ^2}\right)$, carrying π whereas the central one carries $-\pi$.

However, this low energy effective theory doesn't carry information about the second valley. When δJ increases, the additional Dirac points of the K and K' carrying opposite topological charges move in opposite directions on the same line KK' and cancel each others for some critical parameters due to the finite size of the Brillouin zone. Then, the second limit with $C_{K,K'}^{(2)} = -\tau_z \frac{1}{2} \text{sign}(\Delta_{AB})$, discussed in the section 3.3.1 is achieved when the concept of valley is again well defined: that is when δJ becomes sufficiently large.

Effective Lagrangian formalism

In 1999, Niu and Sundaram derived the semiclassical equations of motion of an electron wavepacket in Bloch bands [333] using a time-dependent variational method. Their approach allowed to confirm the anomalous Hall effect predicted by Karplus and Luttinger [332] and to express this effect in terms of Berry curvature. The goal of this appendix is to introduce their derivation for the case where only a constant electric field is applied. We first introduce this approach to the first order in electric field, and then its extension to higher order corrections as introduced by Gao and Niu for the two-band case.

B.1 Semiclassical equations derivation

One consider a wavepacket restricted to move in one band. The evolution of its amplitude shape over time is neglected. The wavepacket state is written as a superposition of the eigenstates of the given band in reciprocal space.

$$|W\rangle = \int a(\mathbf{k}, t) \, |\psi_{n,\mathbf{k}}\rangle \, d\mathbf{k} \tag{B.1}$$

$a(\mathbf{k}, t) = |a(\mathbf{k})|e^{-i\gamma(\mathbf{k},t)}$ is the distribution of the wavepacket in momentum space centred at $\mathbf{k} = \mathbf{k_c}$ and $\int |a(\mathbf{k})|^2 d\mathbf{k} = 1$. This distribution is assumed to be sharp in momentum space such that $|a(\mathbf{k})|^2 \approx \delta(\mathbf{k} - \mathbf{k}_c)$ which implies the following relation:

$$f(\mathbf{k_c}) = \int f(\mathbf{k})|a(\mathbf{k})|^2 d\mathbf{k} \tag{B.2}$$

One also assume that the wavepacket has a well defined center of mass position in real space, which leads the following relation.

$$\mathbf{r_c} = \langle W| \, \hat{\mathbf{r}} \, |W\rangle = \int |a(\mathbf{k})|^2 \left(\frac{\partial \gamma(\mathbf{k})}{\partial \mathbf{k}} d\mathbf{k} - \boldsymbol{\mathcal{A}}_n(\mathbf{k}) \right) = \frac{\partial \gamma(\mathbf{k}_c)}{\partial \mathbf{k}_c} - \boldsymbol{\mathcal{A}}_n(\mathbf{k}_c) \tag{B.3}$$

The effective Lagrangian of the wave packet can then be written as [3, 333]: $\mathcal{L} = \langle W| \, (i\frac{d}{dt} - H) \, |W\rangle$. The Hamiltonian can be expanded around $\mathbf{r_c}$ using gradient correction in external electric potential V (the second order gradient correction is zero since we consider a constant external force):

$$H \quad = H_c - e(\mathbf{r} - \mathbf{r_c}).\nabla V(\mathbf{r}) \tag{B.4}$$

$$= H_c + e(\mathbf{r} - \mathbf{r_c}).\mathbf{E} \tag{B.5}$$

H_c is the exact quantum Hamiltonian evaluated at $\mathbf{r_c}$

$$H_c = H_0 - eV(\mathbf{r_c}) \tag{B.6}$$

where H_0 is the unperturbed Hamiltonian $(H_0 \ket{\psi_n} = \varepsilon_n \ket{\psi_n})$. The second contribution to the effective Lagrangian is then given by:

$$\bra{W} H \ket{W} = \varepsilon_n(\mathbf{k}_c) - eV(\mathbf{r}_c) \tag{B.7}$$

The first term gives:

$$\bra{W} i\hbar \frac{d}{dt} \ket{W} = \frac{\partial \gamma(\mathbf{k}_c, t)}{\partial t} \tag{B.8}$$

Using the relation

$$\frac{d\gamma(\mathbf{k}_c, t)}{dt} = \frac{\partial \gamma(\mathbf{k}_c, t)}{\partial t} + \frac{\partial \gamma(\mathbf{k}_c, t)}{\partial \mathbf{k}_c} \cdot \dot{\mathbf{k}}_c \tag{B.9}$$

one can rewrite this term as:

$$\bra{W} i\hbar \frac{d}{dt} \ket{W} = \frac{d\gamma(\mathbf{k}_c, t)}{dt} - (\mathbf{r}_c + \boldsymbol{\mathcal{A}}_n(\mathbf{k}_c)) \cdot \dot{\mathbf{k}}_c \tag{B.10}$$

Omitting the total time derivative which does not contribute to the equation of motions leads to the following effective Lagrangian:

$$\mathcal{L} = -(\mathbf{r}_c + \boldsymbol{\mathcal{A}}_n(\mathbf{k}_c)) \cdot \dot{\mathbf{k}}_c - \varepsilon_n(\mathbf{k}_c) + eV(\mathbf{r}_c) \tag{B.11}$$

Then, apply Euler-Lagrange equations for the wavepacket center of mass coordinates $\mathbf{r_c}$ and $\mathbf{k}_c$ gives the semiclassical equations (5.30).

B.2   Higher-order corrections

In the ref. [116], Gao and Niu extend this formalism to derive the semiclassical equation up to higher order in the external fields. This is done by assuming that the wavepacket is moving in a perturbed band. Therefore the wavepacket state is now written as a superposition of the unperturbed states.

$$\ket{W} = \int a(\mathbf{k}, t)(f_0 \ket{\psi_{0\mathbf{k}}} + \sum_n f_n \ket{\psi_{n\mathbf{k}}}) d\mathbf{k} \tag{B.12}$$

where the coefficients f_0 and f_n are obtained from perturbation theory up to the wanted order and respect the normalization condition $|f_0|^2 + \sum_n |f_n|^2 = 1$. For a two band system one has:

$$\ket{W} = \int a(\mathbf{k}, t)(f_0 \ket{\psi_{0\mathbf{k}}} + f_1 \ket{\psi_{1\mathbf{k}}}) d\mathbf{k} \tag{B.13}$$

Again, $a(\mathbf{k})$ is the distribution of the wavepacket in momentum space centred at $\mathbf{k} = \mathbf{k_c}$ and $\int |a(\mathbf{k})|^2 d\mathbf{k} = 1$. One can generalize the wavepacket center of mass position:

$$\mathbf{r_c} = \bra{W} \hat{\mathbf{r}} \ket{W} = \frac{\partial \gamma(\mathbf{k}_c)}{\partial \mathbf{k}_c} - \left(|f_0|^2 \mathbf{A}_{00} + |f_1|^2 \mathbf{A}_{11} + f_0^* f_1 \mathbf{A}_{01} + f_1^* f_0 \mathbf{A}_{10} \right) \tag{B.14}$$

with $f_{i,j} = f_{i,j}(\mathbf{k_c})$, and $\mathbf{A}_{ij}(\mathbf{k}_c) = \langle u_i | \, i\frac{\partial}{\partial \mathbf{k}_c} \, | u_j \rangle$ are the intraband and interband Berry connection in the momentum space. (To obtain this result equivalent to the one given by Gao and Niu, the relative phase between f_0 and f_1 coefficients has to be constant or zero.) The average energy of the wavepacket is given by:

$$\langle W | \, H \, | W \rangle = |f_0|^2 \varepsilon_0 \left(\mathbf{k_c}\right) + |f_1|^2 \varepsilon_1 \left(\mathbf{k_c}\right) - eV\left(\mathbf{r_c}\right) \tag{B.15}$$

where ε_i are the energies of the two unperturbed bands. The complete effective Lagrangian $\mathcal{L}(\mathbf{r}_c, \dot{\mathbf{r}}_c, \mathbf{k}_c, \dot{\mathbf{k}}_c)$ has the following form:

$$\mathcal{L} = - \left(\mathbf{r}_c + \tilde{\mathbf{A}}(\mathbf{k}_c)\right) \cdot \dot{\mathbf{k}}_c - \tilde{\varepsilon} + eV\left(\mathbf{r_c}\right) \tag{B.16}$$

where we have introduced $\tilde{\mathbf{A}}$

$$\tilde{\mathbf{A}} = \left(|f_0|^2 \mathbf{A}_{00} + |f_1|^2 \mathbf{A}_{11} + f_0^* f_1 \mathbf{A}_{01} + f_1^* f_0 \mathbf{A}_{10}\right) \tag{B.17}$$

and the corrected energy defined by:

$$\tilde{\varepsilon} = |f_0|^2 \varepsilon_0 + |f_1|^2 \varepsilon_1 \tag{B.18}$$

If we keep only the terms up to the first order in the electric field (see below) this Lagrangian is exactly the one used by Gao and Niu in [116]. (In the following, we drop the index c to simplify the notations.)

In order to prove that higher-order corrections do not contribute neither to the wavepacket trajectory in the configuration we consider (on geodesics), we use perturbation theory up to the third order in the external electric force to write f_0 and f_1:

$$f_0 = 1 - \frac{e^2}{2}\frac{\mathbf{E}.\mathbf{A}_{01} * \mathbf{E}.\mathbf{A}_{10}}{(\varepsilon_0 - \varepsilon_1)^2} + 2e^3 \frac{\mathbf{E}.\mathbf{A}_{01} * \mathbf{E}.\mathbf{A}_{11} * \mathbf{E}.\mathbf{A}_{10}}{(\varepsilon_0 - \varepsilon_1)^3} - e^3 \frac{|\mathbf{E}.\mathbf{A}_{01}|^2 * \mathbf{E}.\mathbf{A}_{00}}{(\varepsilon_0 - \varepsilon_1)^3} \tag{B.19}$$

$$\begin{aligned} f_1 = \quad - \quad & e\frac{\mathbf{E}.\mathbf{A}_{10}}{(\varepsilon_0 - \varepsilon_1)} - e^2 \frac{\mathbf{E}.\mathbf{A}_{10} * \mathbf{E}.\mathbf{A}_{00}}{(\varepsilon_0 - \varepsilon_1)^2} + e^2 \frac{\mathbf{E}.\mathbf{A}_{11} * \mathbf{E}.\mathbf{A}_{10}}{(\varepsilon_0 - \varepsilon_1)^2} \\ + \quad & e^3 \frac{\mathbf{E}.\mathbf{A}_{11} * \mathbf{E}.\mathbf{A}_{11} * \mathbf{E}.\mathbf{A}_{10}}{(\varepsilon_0 - \varepsilon_1)^2(\varepsilon_1 - \varepsilon_0)} - e^3 \frac{|\mathbf{E}.\mathbf{A}_{00}|^2 * \mathbf{E}.\mathbf{A}_{10}}{(\varepsilon_0 - \varepsilon_1)^2(\varepsilon_1 - \varepsilon_0)} \end{aligned} \tag{B.20}$$

$\mathbf{E}$ is the constant electric field ($\mathbf{E} = -\frac{\partial V}{\partial \mathbf{r_c}}$). Moreover, on geodesics on has $\mathbf{A}_{00} = \mathbf{A}_{11}$. Using this property and the above formulas, we can develop the second term in the Lagrangian:

$$\begin{aligned} \tilde{\mathbf{A}}.\dot{\mathbf{k}} = \quad & \mathbf{A}_{00}.\dot{\mathbf{k}} - e\frac{\mathbf{A}_{10}.\mathbf{E} * \mathbf{A}_{01}.\dot{\mathbf{k}} + \mathbf{A}_{01}.\mathbf{E} * \mathbf{A}_{10}.\dot{\mathbf{k}}}{(\varepsilon_0 - \varepsilon_1)} \\ + \quad & e^3 \frac{(\mathbf{E}.\mathbf{A}_{10} * \mathbf{E}.\mathbf{A}_{01})(\mathbf{E}.\mathbf{A}_{10} * \mathbf{A}_{01}.\dot{\mathbf{k}} + \mathbf{E}.\mathbf{A}_{01} * \mathbf{A}_{10}.\dot{\mathbf{k}})}{2(\varepsilon_0 - \varepsilon_1)^3} \end{aligned} \tag{B.21}$$

Then, inserting the remaining expression in (B.16) and applying Euler-Lagrange equations allows to find the equations of motion:

$$\hbar \frac{\partial \mathbf{k}}{\partial t} = -e\mathbf{E} \tag{B.22}$$

$$\hbar \frac{\partial \mathbf{r}}{\partial t} = \frac{\partial \tilde{\varepsilon}}{\partial \mathbf{k}} - \hbar \frac{\partial \mathbf{k}}{\partial t} \times \tilde{\mathbf{B}} \tag{B.23}$$

with $\tilde{\mathbf{B}}$ the corrected Berry curvature up to the third order:

$$\tilde{\mathbf{B}} = \nabla_{\mathbf{k}} \times \tilde{\mathbf{A}} = \mathbf{B} + \mathbf{B}^{(c1)} + \mathbf{B}^{(c3)} \tag{B.24}$$

These equations have the same form as the one derived keeping only first order term in electric field. It is not surprising since the Lagrangian (B.16) have already the same form as (B.11). Using the identity [114, 115]:

$$g_{\alpha\beta} = \frac{1}{2}(\langle u_0 | i\frac{\partial}{\partial k_\alpha} | u_1 \rangle \langle u_1 | i\frac{\partial}{\partial k_\beta} | u_0 \rangle + h.c.) \tag{B.25}$$

we can express the corrections in terms of the quantum metric tensor $\overleftrightarrow{g}$ as presented in section 5.2.2.2 where $F_i = -eE_i$:

$$\mathbf{B}^{(c1)} = -e\nabla_{\mathbf{k}} \times \left(\frac{2\overleftrightarrow{g}\mathbf{E}}{(\varepsilon_0 - \varepsilon_1)} \right) \tag{B.26}$$

$$\mathbf{B}^{(c3)} = \frac{e^3}{2}\nabla_{\mathbf{k}} \times \left((\sum_{i,j} g_{ij}E_iE_j)\frac{2\overleftrightarrow{g}\mathbf{E}}{(\varepsilon_0 - \varepsilon_1)^3} \right) \tag{B.27}$$

Polariton anomalous Hall effect wavepacket trajectory

In this section, we present the detailed results concerning the trajectory of an accelerated wavepacket (under the effect of a force F applied in the X direction) in presence of the TE-TM SOC and a constant magnetic field providing Zeeman splitting, solving equations (5.30) and (5.34) of section 5.2.

The analytical solution of Eq. (5.30) which does not include the non-adiabatic correction reads:

$$x\left(t\right) = \frac{Ft^2}{2m} - \frac{\sqrt{\Delta^2 + \frac{\beta^2 F^4 t^4}{\hbar^4}}}{F} + \frac{\Delta}{F} \tag{C.1}$$

and

$$y\left(t\right) = \frac{F^3\hbar t^3\beta^2\sqrt{\Delta^2 + F^4t^4\beta^2/\hbar^4}\left(3 - \left(1 + \frac{F^4t^4\beta^2}{\Delta^2\hbar^4}\right)\,_2F_1\left(1,\frac{5}{4},\frac{7}{4},-\frac{F^4t^4\beta^2}{\Delta^2\hbar^4}\right)\right)}{3\left(\Delta^3\hbar^4 + \Delta F^4t^4\beta^2\right)} \tag{C.2}$$

The maximal shift of the wavepacket in the Y direction at $t \to \infty$ is given by:

$$y_\infty = \frac{\sqrt{\beta}}{\sqrt{\Delta}}\frac{\Gamma^2\left(\frac{3}{4}\right)}{\sqrt{\pi}} \tag{C.3}$$

We see that increasing the lateral shift requires increasing the TE-TM splitting β or decreasing the magnetic field Δ.

The importance non-adiabatic correction can be estimated by the maximal value of the non-adiabatic fraction f_{NA} behaves as:

$$f_{NA,max} \propto \frac{\beta}{\Delta^3} \tag{C.4}$$

To reduce the maximal non-adiabaticity, it is therefore important to have a sufficiently large Zeeman splitting Δ. To have a maximal displacement and a good adiabaticity at the same time, it is better to increase the TE-TM SOC β instead of reducing the magnetic field Δ, because the non-adiabaticity behaves as $1/\Delta^3$.

The analytical solution for the equation (5.34) of the main text including the non-adiabatic correction can also be found:

$$y\left(t\right) = \frac{F^3\beta^3\left(\Delta t\left(15 + 2\Delta^2\left(70t^2 + \frac{-15\Delta^4\hbar^{12} + 8\Delta^2 F^4\hbar^8 t^4\beta^2 + 3F^8\hbar^4 t^8\beta^4}{(\Delta^2\hbar^4 + F^4t^4\beta^2)^3}\right)\right) + \frac{5(-1)^{3/4}\Delta\hbar\sqrt{\frac{\Delta}{\beta} + \frac{F^4t^4\beta}{\Delta\hbar^4}}\nu}{F^3\beta}\right)}{140\Delta^4\hbar^3\sqrt{\Delta^2 + F^4t^4\beta^2/\hbar^4}} \tag{C.5}$$

where

$$\nu = 28\Delta^3\hbar^2 \mathrm{E}\left(i\mathrm{arcsinh}\left(\frac{Ft\sqrt{\frac{i\beta}{\Delta}}}{\hbar}\right), -1\right) + \left(-28\Delta^3\hbar^2 + 3iF^2\beta\right) \mathrm{F}\left(i\mathrm{arcsinh}\left(\frac{Ft\sqrt{\frac{i\beta}{\Delta}}}{\hbar}\right), -1\right)$$

$$(\mathrm{C.6})$$

where E and F are the elliptic integrals of the second kind. Unfortunately, we did not manage to find the limit of this expression for $t \to \infty$.

From the practical point of view, the above analytical expressions for $y(t)$ appear quite cumbersome, and we advise the direct numerical solution of equations (5.30) and (5.34), because the calculation time of the hypergeometric function and the elliptic integrals is quite comparable or even longer than the direct solution of the equations, while the results are identical.

Bibliography

[1] C. Kittel, *Introduction to Solid State Physics*. New York: John Wiley & Sons, Inc., 6th ed., 1986. (Cited on page 4.)

[2] N. Ashcroft and N. Mermin, *Solid State Physics*. Philadelphia: Saunders College, 1976. (Cited on page 4.)

[3] D. Xiao, M.-C. Chang, and Q. Niu, "Berry phase effects on electronic properties," *Rev. Mod. Phys.*, vol. 82, pp. 1959–2007, Jul 2010. (Cited on pages 4, 7, 144, 150 and 159.)

[4] M. Z. Hasan and C. L. Kane, "Colloquium: Topological insulators," *Rev. Mod. Phys.*, vol. 82, pp. 3045–3067, Nov 2010. (Cited on pages 4, 25, 26, 62 and 92.)

[5] X.-L. Qi and S.-C. Zhang, "Topological insulators and superconductors," *Rev. Mod. Phys.*, vol. 83, pp. 1057–1110, Oct 2011. (Cited on pages 4, 26 and 62.)

[6] B. A. Bernevig and T. L. Hughes, *Topological insulators and topological superconductors*. Princeton university press, 2013. (Cited on page 4.)

[7] L. Lu, J. D. Joannopoulos, and M. Soljačić, "Topological photonics," *Nature Photonics*, vol. 8, no. 11, pp. 821–829, 2014. (Cited on pages 4, 28, 30 and 107.)

[8] T. Ozawa, H. M. Price, A. Amo, N. Goldman, M. Hafezi, L. Lu, M. Rechtsman, D. Schuster, J. Simon, O. Zilberberg, *et al.*, "Topological photonics," *arXiv preprint arXiv:1802.04173*, 2018. (Cited on pages 4, 28 and 32.)

[9] N. Cooper, J. Dalibard, and I. Spielman, "Topological bands for ultracold atoms," *arXiv preprint arXiv:1803.00249*, 2018. (Cited on pages 4 and 33.)

[10] J. Provost and G. Vallee, "Riemannian structure on manifolds of quantum states," *Communications in Mathematical Physics*, vol. 76, no. 3, pp. 289–301, 1980. (Cited on page 5.)

[11] J. Anandan and Y. Aharonov, "Geometry of quantum evolution," *Phys. Rev. Lett.*, vol. 65, pp. 1697–1700, Oct 1990. (Cited on page 5.)

[12] W. K. Wootters, "Statistical distance and Hilbert space," *Phys. Rev. D*, vol. 23, pp. 357–362, Jan 1981. (Cited on page 5.)

[13] S. L. Braunstein and C. M. Caves, "Statistical distance and the geometry of quantum states," *Phys. Rev. Lett.*, vol. 72, pp. 3439–3443, May 1994. (Cited on page 5.)

[14] M. V. Berry, "Quantal phase factors accompanying adiabatic changes," in *Proceedings of the Royal Society of London A: Mathematical, Physical and Engineering Sciences*, vol. 392, pp. 45–57, The Royal Society, 1984. (Cited on page 5.)

[15] F. Wilczek and A. Zee, "Appearance of gauge structure in simple dynamical systems," *Phys. Rev. Lett.*, vol. 52, pp. 2111–2114, Jun 1984. (Cited on page 7.)

[16] M. Berry, "The quantum phase, five years after," in *Geometric phases in physics*, p. 7, World Scientific, Singapore, 1989. (Cited on page 8.)

[17] Y. Aharonov and J. Anandan, "Phase change during a cyclic quantum evolution," *Phys. Rev. Lett.*, vol. 58, pp. 1593–1596, Apr 1987. (Cited on pages 8 and 144.)

[18] J. Samuel and R. Bhandari, "General setting for Berry's phase," *Phys. Rev. Lett.*, vol. 60, pp. 2339–2342, Jun 1988. (Cited on page 8.)

[19] S. Pancharatnam, "Generalized theory of interference and its applications," in *Proceedings of the Indian Academy of Sciences-Section A*, vol. 44, pp. 398–417, Springer, 1956. (Cited on page 9.)

[20] M. V. Berry, "The adiabatic phase and Pancharatnam's phase for polarized light," *Journal of Modern Optics*, vol. 34, no. 11, pp. 1401–1407, 1987. (Cited on page 9.)

[21] A. Tomita and R. Y. Chiao, "Observation of Berry's topological phase by use of an optical fiber," *Phys. Rev. Lett.*, vol. 57, pp. 937–940, Aug 1986. (Cited on page 9.)

[22] R. Tycko, "Adiabatic rotational splittings and Berry's phase in nuclear quadrupole resonance," *Phys. Rev. Lett.*, vol. 58, pp. 2281–2284, Jun 1987. (Cited on page 9.)

[23] D. Suter, G. C. Chingas, R. A. Harris, and A. Pines, "Berry's phase in magnetic resonance," *Molecular Physics*, vol. 61, no. 6, pp. 1327–1340, 1987. (Cited on page 9.)

[24] P. Zanardi, P. Giorda, and M. Cozzini, "Information-theoretic differential geometry of quantum phase transitions," *Phys. Rev. Lett.*, vol. 99, p. 100603, Sep 2007. (Cited on page 9.)

[25] M. Kolodrubetz, V. Gritsev, and A. Polkovnikov, "Classifying and measuring geometry of a quantum ground state manifold," *Phys. Rev. B*, vol. 88, p. 064304, Aug 2013. (Cited on page 9.)

[26] J. D. Joannopoulos, S. G. Johnson, J. N. Winn, and R. D. Meade, *Photonic crystals: molding the flow of light*. Princeton university press, 2011. (Cited on pages 10 and 28.)

[27] E. Yablonovitch, "Inhibited spontaneous emission in solid-state physics and electronics," *Phys. Rev. Lett.*, vol. 58, pp. 2059–2062, May 1987. (Cited on page 11.)

[28] S. John, "Strong localization of photons in certain disordered dielectric superlattices," *Phys. Rev. Lett.*, vol. 58, pp. 2486–2489, Jun 1987. (Cited on page 11.)

[29] D. J. Thouless, M. Kohmoto, M. P. Nightingale, and M. den Nijs, "Quantized Hall conductance in a two-dimensional periodic potential," *Phys. Rev. Lett.*, vol. 49, pp. 405–408, Aug 1982. (Cited on pages 13 and 62.)

[30] K. v. Klitzing, G. Dorda, and M. Pepper, "New method for high-accuracy determination of the fine-structure constant based on quantized Hall resistance," *Phys. Rev. Lett.*, vol. 45, pp. 494–497, Aug 1980. (Cited on pages 13 and 62.)

[31] J. E. Avron, R. Seiler, and B. Simon, "Homotopy and quantization in condensed matter physics," *Phys. Rev. Lett.*, vol. 51, pp. 51–53, Jul 1983. (Cited on page 13.)

[32] B. Simon, "Holonomy, the quantum adiabatic theorem, and Berry's phase," *Phys. Rev. Lett.*, vol. 51, pp. 2167–2170, Dec 1983. (Cited on pages 13 and 62.)

[33] Y. Hatsugai, "Chern number and edge states in the integer quantum Hall effect," *Phys. Rev. Lett.*, vol. 71, pp. 3697–3700, Nov 1993. (Cited on pages 13 and 104.)

[34] G. M. Graf and M. Porta, "Bulk-edge correspondence for two-dimensional topological insulators," *Communications in mathematical physics*, vol. 324, no. 3, pp. 851–895, 2013. (Cited on page 13.)

[35] C. Bena and G. Montambaux, "Remarks on the tight-binding model of graphene," *New Journal of Physics*, vol. 11, no. 9, p. 095003, 2009. (Cited on page 15.)

[36] P. R. Wallace, "The band theory of graphite," *Phys. Rev.*, vol. 71, pp. 622–634, May 1947. (Cited on page 16.)

[37] D. Xiao, W. Yao, and Q. Niu, "Valley-contrasting physics in graphene: Magnetic moment and topological transport," *Phys. Rev. Lett.*, vol. 99, p. 236809, Dec 2007. (Cited on pages 16, 69, 71, 108 and 128.)

[38] A. H. Castro Neto, F. Guinea, N. M. R. Peres, K. S. Novoselov, and A. K. Geim, "The electronic properties of graphene," *Rev. Mod. Phys.*, vol. 81, pp. 109–162, Jan 2009. (Cited on page 16.)

[39] J. Fuchs, F. Piéchon, M. Goerbig, and G. Montambaux, "Topological Berry phase and semiclassical quantization of cyclotron orbits for two dimensional

electrons in coupled band models," *The European Physical Journal B*, vol. 77, no. 3, pp. 351–362, 2010. (Cited on pages 16, 71 and 128.)

[40] M. Fruchart, D. Carpentier, and K. Gawędzki, "Parallel transport and band theory in crystals," *EPL (Europhysics Letters)*, vol. 106, no. 6, p. 60002, 2014. (Cited on page 16.)

[41] L.-K. Lim, J.-N. Fuchs, and G. Montambaux, "Geometry of Bloch states probed by Stückelberg interferometry," *Phys. Rev. A*, vol. 92, p. 063627, Dec 2015. (Cited on pages 17 and 122.)

[42] W. P. Su, J. R. Schrieffer, and A. J. Heeger, "Soliton excitations in polyacety-lene," *Phys. Rev. B*, vol. 22, pp. 2099–2111, Aug 1980. (Cited on pages 18 and 88.)

[43] F. D. M. Haldane, "Model for a quantum Hall effect without Landau lev-els: Condensed-matter realization of the "parity anomaly"," *Phys. Rev. Lett.*, vol. 61, pp. 2015–2018, Oct 1988. (Cited on pages 18 and 62.)

[44] C. L. Kane and E. J. Mele, "Quantum spin Hall effect in graphene," *Phys. Rev. Lett.*, vol. 95, p. 226801, Nov 2005. (Cited on pages 18, 24, 62 and 131.)

[45] W. P. Su, J. R. Schrieffer, and A. J. Heeger, "Solitons in polyacetylene," *Phys. Rev. Lett.*, vol. 42, pp. 1698–1701, Jun 1979. (Cited on page 18.)

[46] J. Zak, "Berry's phase for energy bands in solids," *Phys. Rev. Lett.*, vol. 62, pp. 2747–2750, Jun 1989. (Cited on page 18.)

[47] P. Delplace, D. Ullmo, and G. Montambaux, "Zak phase and the existence of edge states in graphene," *Phys. Rev. B*, vol. 84, p. 195452, Nov 2011. (Cited on page 18.)

[48] R. Jackiw and C. Rebbi, "Solitons with fermion number," *Phys. Rev. D*, vol. 13, pp. 3398–3409, Jun 1976. (Cited on pages 20 and 21.)

[49] R. Jackiw and J. R. Schrieffer, "Solitons with fermion number 12 in con-densed matter and relativistic field theories," *Nuclear Physics B*, vol. 190, no. 2, pp. 253–265, 1981. (Cited on page 20.)

[50] A. J. Heeger, S. Kivelson, J. R. Schrieffer, and W. P. Su, "Solitons in con-ducting polymers," *Rev. Mod. Phys.*, vol. 60, pp. 781–850, Jul 1988. (Cited on page 21.)

[51] C.-Y. Hou, C. Chamon, and C. Mudry, "Electron fractionalization in two-dimensional graphenelike structures," *Phys. Rev. Lett.*, vol. 98, p. 186809, May 2007. (Cited on page 21.)

[52] R. Jackiw and S.-Y. Pi, "Chiral gauge theory for graphene," *Phys. Rev. Lett.*, vol. 98, p. 266402, Jun 2007. (Cited on page 21.)

[53] C. Chamon, C.-Y. Hou, R. Jackiw, C. Mudry, S.-Y. Pi, and G. Semenoff, "Electron fractionalization for two-dimensional Dirac fermions," *Phys. Rev. B*, vol. 77, p. 235431, Jun 2008. (Cited on page 21.)

[54] C. Poli, M. Bellec, U. Kuhl, F. Mortessagne, and H. Schomerus, "Selective enhancement of topologically induced interface states in a dielectric resonator chain," *Nature communications*, vol. 6, p. 6710, 2015. (Cited on page 21.)

[55] D. D. Solnyshkov, A. V. Nalitov, and G. Malpuech, "Kibble-Zurek mechanism in topologically nontrivial zigzag chains of polariton micropillars," *Phys. Rev. Lett.*, vol. 116, p. 046402, Jan 2016. (Cited on pages 21 and 92.)

[56] P. St-Jean, V. Goblot, E. Galopin, A. Lemaître, T. Ozawa, L. Le Gratiet, I. Sagnes, J. Bloch, and A. Amo, "Lasing in topological edge states of a one-dimensional lattice," *Nature Photonics*, vol. 11, no. 10, p. 651, 2017. (Cited on page 21.)

[57] M. Parto, S. Wittek, H. Hodaei, G. Harari, M. A. Bandres, J. Ren, M. C. Rechtsman, M. Segev, D. N. Christodoulides, and M. Khajavikhan, "Edge-mode lasing in 1D topological active arrays," *Phys. Rev. Lett.*, vol. 120, p. 113901, Mar 2018. (Cited on page 21.)

[58] H. Zhao, P. Miao, M. H. Teimourpour, S. Malzard, R. El-Ganainy, H. Schomerus, and L. Feng, "Topological hybrid silicon microlasers," *Nature communications*, vol. 9, no. 1, p. 981, 2018. (Cited on page 21.)

[59] D. D. Solnyshkov, O. Bleu, B. Teklu, and G. Malpuech, "Chirality of topological gap solitons in bosonic dimer chains," *Phys. Rev. Lett.*, vol. 118, p. 023901, Jan 2017. (Cited on pages 21 and 92.)

[60] A. Kanshu, C. Rüter, D. Kip, V. Shandarov, P. Beličev, I. Ilić, and M. Stepić, "Observation of discrete gap solitons in one-dimensional waveguide arrays with alternating spacings and saturable defocusing nonlinearity," *Optics letters*, vol. 37, no. 7, pp. 1253–1255, 2012. (Cited on page 21.)

[61] D. J. Thouless, "Theory of the quantized Hall effect," *Surface Science*, vol. 142, no. 1-3, pp. 147–154, 1984. (Cited on page 21.)

[62] P. G. Harper, "Single band motion of conduction electrons in a uniform magnetic field," *Proceedings of the Physical Society. Section A*, vol. 68, no. 10, p. 874, 1955. (Cited on page 21.)

[63] D. R. Hofstadter, "Energy levels and wave functions of Bloch electrons in rational and irrational magnetic fields," *Phys. Rev. B*, vol. 14, pp. 2239–2249, Sep 1976. (Cited on page 21.)

[64] G. W. Semenoff, "Condensed-matter simulation of a three-dimensional anomaly," *Phys. Rev. Lett.*, vol. 53, pp. 2449–2452, Dec 1984. (Cited on pages 21 and 69.)

[65] C. Mudry, "Two-dimensional materials: Heavy going," *Nature Physics*, vol. 12, no. 10, p. 895, 2016. (Cited on page 24.)

[66] G. Jotzu, M. Messer, R. Desbuquois, M. Lebrat, T. Uehlinger, D. Greif, and T. Esslinger, "Experimental realization of the topological Haldane model with ultracold fermions," *Nature*, vol. 515, no. 7526, p. 237, 2014. (Cited on pages 24 and 33.)

[67] C.-X. Liu, X.-L. Qi, X. Dai, Z. Fang, and S.-C. Zhang, "Quantum anomalous Hall effect in $Hg_{1-y}Mn_yTe$ quantum wells," *Phys. Rev. Lett.*, vol. 101, p. 146802, Oct 2008. (Cited on pages 24 and 62.)

[68] Z. Qiao, S. A. Yang, W. Feng, W.-K. Tse, J. Ding, Y. Yao, J. Wang, and Q. Niu, "Quantum anomalous Hall effect in graphene from Rashba and exchange effects," *Phys. Rev. B*, vol. 82, p. 161414, Oct 2010. (Cited on pages 24, 62 and 65.)

[69] R. Yu, W. Zhang, H.-J. Zhang, S.-C. Zhang, X. Dai, and Z. Fang, "Quantized anomalous hall effect in magnetic topological insulators," *Science*, vol. 329, no. 5987, pp. 61–64, 2010. (Cited on page 24.)

[70] C.-Z. Chang, J. Zhang, X. Feng, J. Shen, Z. Zhang, M. Guo, K. Li, Y. Ou, P. Wei, L.-L. Wang, *et al.*, "Experimental observation of the quantum anomalous hall effect in a magnetic topological insulator," *Science*, vol. 340, no. 6129, pp. 167–170, 2013. (Cited on page 24.)

[71] J. Checkelsky, R. Yoshimi, A. Tsukazaki, K. Takahashi, Y. Kozuka, J. Falson, M. Kawasaki, and Y. Tokura, "Trajectory of the anomalous hall effect towards the quantized state in a ferromagnetic topological insulator," *Nature Physics*, vol. 10, no. 10, p. 731, 2014. (Cited on page 24.)

[72] A. J. Bestwick, E. J. Fox, X. Kou, L. Pan, K. L. Wang, and D. Goldhaber-Gordon, "Precise quantization of the anomalous hall effect near zero magnetic field," *Phys. Rev. Lett.*, vol. 114, p. 187201, May 2015. (Cited on page 24.)

[73] C. L. Kane and E. J. Mele, "Z_2 topological order and the quantum spin Hall effect," *Phys. Rev. Lett.*, vol. 95, p. 146802, Sep 2005. (Cited on pages 24, 25, 71 and 107.)

[74] A. Kitaev, "Periodic table for topological insulators and superconductors," in *AIP Conference Proceedings*, vol. 1134, pp. 22–30, AIP, 2009. (Cited on page 26.)

[75] S. Ryu, A. P. Schnyder, A. Furusaki, and A. W. Ludwig, "Topological insulators and superconductors: tenfold way and dimensional hierarchy," *New Journal of Physics*, vol. 12, no. 6, p. 065010, 2010. (Cited on page 26.)

[76] C.-K. Chiu, J. C. Y. Teo, A. P. Schnyder, and S. Ryu, "Classification of topological quantum matter with symmetries," *Rev. Mod. Phys.*, vol. 88, p. 035005, Aug 2016. (Cited on pages 26 and 31.)

[77] H. Min, J. E. Hill, N. A. Sinitsyn, B. R. Sahu, L. Kleinman, and A. H. MacDonald, "Intrinsic and Rashba spin-orbit interactions in graphene sheets," *Phys. Rev. B*, vol. 74, p. 165310, Oct 2006. (Cited on pages 26 and 62.)

[78] D. Huertas-Hernando, F. Guinea, and A. Brataas, "Spin-orbit coupling in curved graphene, fullerenes, nanotubes, and nanotube caps," *Phys. Rev. B*, vol. 74, p. 155426, Oct 2006. (Cited on pages 26 and 62.)

[79] Y. Yao, F. Ye, X.-L. Qi, S.-C. Zhang, and Z. Fang, "Spin-orbit gap of graphene: First-principles calculations," *Phys. Rev. B*, vol. 75, p. 041401, Jan 2007. (Cited on page 26.)

[80] B. A. Bernevig, T. L. Hughes, and S.-C. Zhang, "Quantum spin Hall effect and topological phase transition in HgTe quantum wells," *Science*, vol. 314, no. 5806, pp. 1757–1761, 2006. (Cited on pages 26, 62 and 131.)

[81] M. König, S. Wiedmann, C. Brüne, A. Roth, H. Buhmann, L. W. Molenkamp, X.-L. Qi, and S.-C. Zhang, "Quantum spin Hall insulator state in HgTe quantum wells," *Science*, vol. 318, no. 5851, pp. 766–770, 2007. (Cited on pages 27 and 62.)

[82] A. Roth, C. Brüne, H. Buhmann, L. W. Molenkamp, J. Maciejko, X.-L. Qi, and S.-C. Zhang, "Nonlocal transport in the quantum spin Hall state," *Science*, vol. 325, no. 5938, pp. 294–297, 2009. (Cited on page 27.)

[83] F. D. M. Haldane and S. Raghu, "Possible realization of directional optical waveguides in photonic crystals with broken time-reversal symmetry," *Phys. Rev. Lett.*, vol. 100, p. 013904, Jan 2008. (Cited on pages 27, 28, 29 and 62.)

[84] S. Raghu and F. D. M. Haldane, "Analogs of quantum-Hall-effect edge states in photonic crystals," *Phys. Rev. A*, vol. 78, p. 033834, Sep 2008. (Cited on page 28.)

[85] Z. Wang, Y. D. Chong, J. D. Joannopoulos, and M. Soljačić, "Reflection-free one-way edge modes in a gyromagnetic photonic crystal," *Phys. Rev. Lett.*, vol. 100, p. 013905, Jan 2008. (Cited on pages 28 and 29.)

[86] Z. Wang, Y. Chong, J. D. Joannopoulos, and M. Soljačić, "Observation of unidirectional backscattering-immune topological electromagnetic states," *Nature*, vol. 461, no. 7265, p. 772, 2009. (Cited on pages 28, 29, 30 and 31.)

[87] B. Bahari, R. Tellez-Limon, and B. Kanté, "Topological terahertz circuits using semiconductors," *Applied Physics Letters*, vol. 109, no. 14, p. 143501, 2016. (Cited on page 31.)

[88] B. Bahari, A. Ndao, F. Vallini, A. El Amili, Y. Fainman, and B. Kanté, "Nonreciprocal lasing in topological cavities of arbitrary geometries," *Science*, vol. 358, no. 6363, pp. 636–640, 2017. (Cited on page 31.)

[89] G. De Nittis and M. Lein, "On the role of symmetries in the theory of photonic crystals," *Annals of Physics*, vol. 350, pp. 568–587, 2014. (Cited on page 31.)

[90] G. De Nittis and M. Lein, "Symmetry classification of topological photonic crystals," *arXiv preprint arXiv:1710.08104*, 2017. (Cited on pages 31 and 32.)

[91] M. C. Rechtsman, J. M. Zeuner, Y. Plotnik, Y. Lumer, D. Podolsky, F. Dreisow, S. Nolte, M. Segev, and A. Szameit, "Photonic Floquet topological insulators," *Nature*, vol. 496, no. 7444, p. 196, 2013. (Cited on pages 32 and 92.)

[92] M. Hafezi, E. A. Demler, M. D. Lukin, and J. M. Taylor, "Robust optical delay lines with topological protection," *Nature Physics*, vol. 7, no. 11, p. 907, 2011. (Cited on pages 32 and 108.)

[93] M. Hafezi, S. Mittal, J. Fan, A. Migdall, and J. Taylor, "Imaging topological edge states in silicon photonics," *Nature Photonics*, vol. 7, no. 12, p. 1001, 2013. (Cited on pages 32 and 108.)

[94] G. Harari, M. A. Bandres, Y. Lumer, M. C. Rechtsman, Y. Chong, M. Khajavikhan, D. N. Christodoulides, and M. Segev, "Topological insulator laser: Theory," *Science*, vol. 359, no. 6381, p. eaar4003, 2018. (Cited on page 32.)

[95] M. A. Bandres, S. Wittek, G. Harari, M. Parto, J. Ren, M. Segev, D. N. Christodoulides, and M. Khajavikhan, "Topological insulator laser: Experiments," *Science*, vol. 359, no. 6381, p. eaar4005, 2018. (Cited on pages 32 and 108.)

[96] I. Bloch, "Ultracold quantum gases in optical lattices," *Nature Physics*, vol. 1, no. 1, p. 23, 2005. (Cited on page 32.)

[97] M. Greiner, O. Mandel, T. Esslinger, T. W. Hänsch, and I. Bloch, "Quantum phase transition from a superfluid to a Mott insulator in a gas of ultracold atoms," *nature*, vol. 415, no. 6867, p. 39, 2002. (Cited on page 33.)

[98] I. Bloch, J. Dalibard, and W. Zwerger, "Many-body physics with ultracold gases," *Rev. Mod. Phys.*, vol. 80, pp. 885–964, Jul 2008. (Cited on page 33.)

[99] M. Aidelsburger, M. Atala, M. Lohse, J. T. Barreiro, B. Paredes, and I. Bloch, "Realization of the Hofstadter hamiltonian with ultracold atoms in optical lattices," *Phys. Rev. Lett.*, vol. 111, p. 185301, Oct 2013. (Cited on page 33.)

[100] M. Atala, M. Aidelsburger, J. T. Barreiro, D. Abanin, T. Kitagawa, E. Demler, and I. Bloch, "Direct measurement of the Zak phase in topological Bloch bands," *Nature Physics*, vol. 9, no. 12, p. 795, 2013. (Cited on page 33.)

[101] M. Aidelsburger, M. Lohse, C. Schweizer, M. Atala, J. T. Barreiro, S. Nascim-bene, N. Cooper, I. Bloch, and N. Goldman, "Measuring the Chern number of Hofstadter bands with ultracold bosonic atoms," *Nature Physics*, vol. 11, no. 2, p. 162, 2015. (Cited on page 33.)

[102] P. Hauke, M. Lewenstein, and A. Eckardt, "Tomography of band insulators from quench dynamics," *Phys. Rev. Lett.*, vol. 113, p. 045303, Jul 2014. (Cited on page 33.)

[103] N. Fläschner, B. Rem, M. Tarnowski, D. Vogel, D.-S. Lühmann, K. Sengstock, and C. Weitenberg, "Experimental reconstruction of the Berry curvature in a Floquet Bloch band," *Science*, vol. 352, no. 6289, pp. 1091–1094, 2016. (Cited on pages 33, 122 and 138.)

[104] E. Prodan and C. Prodan, "Topological phonon modes and their role in dy-namic instability of microtubules," *Phys. Rev. Lett.*, vol. 103, p. 248101, Dec 2009. (Cited on page 33.)

[105] V. Peano, C. Brendel, M. Schmidt, and F. Marquardt, "Topological phases of sound and light," *Phys. Rev. X*, vol. 5, p. 031011, Jul 2015. (Cited on page 33.)

[106] Z. Yang, F. Gao, X. Shi, X. Lin, Z. Gao, Y. Chong, and B. Zhang, "Topological acoustics," *Phys. Rev. Lett.*, vol. 114, p. 114301, Mar 2015. (Cited on page 33.)

[107] C. Kane and T. Lubensky, "Topological boundary modes in isostatic lattices," *Nature Physics*, vol. 10, no. 1, p. 39, 2014. (Cited on page 33.)

[108] S. D. Huber, "Topological mechanics," *Nature Physics*, vol. 12, no. 7, p. 621, 2016. (Cited on page 33.)

[109] R. Süsstrunk and S. D. Huber, "Classification of topological phonons in linear mechanical metamaterials," *Proceedings of the National Academy of Sciences*, vol. 113, no. 33, pp. E4767–E4775, 2016. (Cited on page 33.)

[110] M. Wheeler and G. N. Kiladis, "Convectively coupled equatorial waves: Analy-sis of clouds and temperature in the wavenumber–frequency domain," *Journal of the Atmospheric Sciences*, vol. 56, no. 3, pp. 374–399, 1999. (Cited on pages 34 and 35.)

[111] P. Delplace, J. Marston, and A. Venaille, "Topological origin of equatorial waves," *Science*, vol. 358, no. 6366, pp. 1075–1077, 2017. (Cited on pages 33, 34 and 35.)

[112] G. K. Vallis, *Atmospheric and oceanic fluid dynamics*. Cambridge University Press, 2017. (Cited on page 35.)

[113] T. Matsuno, "Quasi-geostrophic motions in the equatorial area," *Journal of the Meteorological Society of Japan. Ser. II*, vol. 44, no. 1, pp. 25–43, 1966. (Cited on page 35.)

[114] Y. Gao, S. A. Yang, and Q. Niu, "Geometrical effects in orbital magnetic susceptibility," *Phys. Rev. B*, vol. 91, p. 214405, Jun 2015. (Cited on pages 36, 144, 146 and 162.)

[115] F. Piéchon, A. Raoux, J.-N. Fuchs, and G. Montambaux, "Geometric orbital susceptibility: Quantum metric without Berry curvature," *Phys. Rev. B*, vol. 94, p. 134423, Oct 2016. (Cited on pages 36, 124, 126, 144 and 162.)

[116] Y. Gao, S. A. Yang, and Q. Niu, "Field induced positional shift of Bloch electrons and its dynamical implications," *Phys. Rev. Lett.*, vol. 112, p. 166601, Apr 2014. (Cited on pages 36, 146, 160 and 161.)

[117] O. Bleu, G. Malpuech, Y. Gao, and D. D. Solnyshkov, "Effective theory of nonadiabatic quantum evolution based on the quantum geometric tensor," *Phys. Rev. Lett.*, vol. 121, p. 020401, Jul 2018. (Cited on pages 36 and 150.)

[118] A. Srivastava and A. Imamoglu, "Signatures of Bloch-band geometry on excitons: Nonhydrogenic spectra in transition-metal dichalcogenides," *Phys. Rev. Lett.*, vol. 115, p. 166802, Oct 2015. (Cited on page 36.)

[119] S. Peotta and P. Törmä, "Superfluidity in topologically nontrivial flat bands," *Nature communications*, vol. 6, p. 8944, 2015. (Cited on page 36.)

[120] A. Julku, S. Peotta, T. I. Vanhala, D.-H. Kim, and P. Törmä, "Geometric origin of superfluidity in the Lieb-lattice flat band," *Phys. Rev. Lett.*, vol. 117, p. 045303, Jul 2016. (Cited on page 36.)

[121] D. C. Tsui, H. L. Stormer, and A. C. Gossard, "Two-dimensional magneto-transport in the extreme quantum limit," *Phys. Rev. Lett.*, vol. 48, pp. 1559–1562, May 1982. (Cited on page 36.)

[122] R. B. Laughlin, "Anomalous quantum Hall effect: An incompressible quantum fluid with fractionally charged excitations," *Phys. Rev. Lett.*, vol. 50, pp. 1395–1398, May 1983. (Cited on pages 36 and 92.)

[123] D. Arovas, J. R. Schrieffer, and F. Wilczek, "Fractional statistics and the quantum Hall effect," *Phys. Rev. Lett.*, vol. 53, pp. 722–723, Aug 1984. (Cited on page 36.)

[124] B. I. Halperin, "Statistics of quasiparticles and the hierarchy of fractional quantized Hall states," *Phys. Rev. Lett.*, vol. 52, pp. 1583–1586, Apr 1984. (Cited on page 36.)

[125] A. Einstein, *Quantentheorie des einatomigen idealen Gases*. Akademie der Wissenshaften, in Kommission bei W. de Gruyter, 1924. (Cited on pages 38 and 92.)

[126] S. N. Bose, "Plancks gesetz und lichtquantenhypothese," 1924. (Cited on page 38.)

[127] M. H. Anderson, J. R. Ensher, M. R. Matthews, C. E. Wieman, and E. A. Cornell, "Observation of Bose-Einstein condensation in a dilute atomic vapor," *science*, vol. 269, no. 5221, pp. 198–201, 1995. (Cited on pages 39 and 40.)

[128] F. London, "The λ-phenomenon of liquid helium and the Bose-Einstein degeneracy," *Nature*, vol. 141, no. 3571, p. 643, 1938. (Cited on page 40.)

[129] C. C. Bradley, C. A. Sackett, J. J. Tollett, and R. G. Hulet, "Evidence of Bose-Einstein condensation in an atomic gas with attractive interactions," *Phys. Rev. Lett.*, vol. 75, pp. 1687–1690, Aug 1995. (Cited on page 40.)

[130] K. B. Davis, M. O. Mewes, M. R. Andrews, N. J. van Druten, D. S. Durfee, D. M. Kurn, and W. Ketterle, "Bose-Einstein condensation in a gas of sodium atoms," *Phys. Rev. Lett.*, vol. 75, pp. 3969–3973, Nov 1995. (Cited on page 40.)

[131] F. Dalfovo, S. Giorgini, L. P. Pitaevskii, and S. Stringari, "Theory of Bose-Einstein condensation in trapped gases," *Rev. Mod. Phys.*, vol. 71, pp. 463–512, Apr 1999. (Cited on page 40.)

[132] J. Kasprzak, M. Richard, S. Kundermann, A. Baas, P. Jeambrun, J. Keeling, F. Marchetti, M. Szymańska, R. Andre, J. Staehli, *et al.*, "Bose-Einstein condensation of exciton polaritons," *Nature*, vol. 443, no. 7110, p. 409, 2006. (Cited on pages 40, 41 and 93.)

[133] S. Demokritov, V. Demidov, O. Dzyapko, G. Melkov, A. Serga, B. Hillebrands, and A. Slavin, "Bose-Einstein condensation of quasi-equilibrium magnons at room temperature under pumping," *Nature*, vol. 443, no. 7110, p. 430, 2006. (Cited on page 40.)

[134] R. Balili, V. Hartwell, D. Snoke, L. Pfeiffer, and K. West, "Bose-Einstein condensation of microcavity polaritons in a trap," *Science*, vol. 316, no. 5827, pp. 1007–1010, 2007. (Cited on page 40.)

[135] J. Kasprzak, D. D. Solnyshkov, R. André, L. S. Dang, and G. Malpuech, "Formation of an exciton polariton condensate: Thermodynamic versus kinetic regimes," *Phys. Rev. Lett.*, vol. 101, p. 146404, Oct 2008. (Cited on page 40.)

[136] N. Bogoliubov, "On the theory of superfluidity," *J. Phys*, vol. 11, no. 1, p. 23. (Cited on pages 42 and 43.)

[137] L. Pitaevskii and S. Stringari, *Bose-Einstein condensation and superfluidity*, vol. 164. Oxford University Press, 2016. (Cited on pages 42, 45, 92, 95, 107 and 111.)

[138] E. P. Gross, "Structure of a quantized vortex in boson systems," *Il Nuovo Cimento (1955-1965)*, vol. 20, no. 3, pp. 454–477, 1961. (Cited on page 42.)

[139] E. P. Gross, "Hydrodynamics of a superfluid condensate," *Journal of Mathematical Physics*, vol. 4, no. 2, pp. 195–207, 1963. (Cited on page 42.)

[140] L. Pitaevskii, "Vortex lines in an imperfect Bose gas," *Sov. Phys. JETP*, vol. 13, no. 2, pp. 451–454, 1961. (Cited on pages 42 and 46.)

[141] L. Onsager, "Statistical hydrodynamics," *Il Nuovo Cimento (1943-1954)*, vol. 6, no. 2, p. 249, 1949. (Cited on page 45.)

[142] R. P. Feynman, "Chapter II application of quantum mechanics to liquid helium," in *Progress in low temperature physics*, vol. 1, pp. 17–53, Elsevier, 1955. (Cited on page 45.)

[143] D. Thouless, *Topological quantum numbers in nonrelativistic physics*. World Scientific, 1998. (Cited on page 45.)

[144] V. Ginzburg and L. Pitaevskii, "On the theory of superfluidity," *Sov. Phys. JETP*, vol. 7, no. 5, pp. 858–861, 1958. (Cited on pages 45 and 46.)

[145] J. T. Mendonça and H. Terças, *Physics of Ultra-Cold Matter: Atomic Clouds, Bose-Einstein Condensates and Rydberg Plasmas*, vol. 70. Springer Science & Business Media, 2012. (Cited on page 45.)

[146] J. J. Hopfield, "Theory of the contribution of excitons to the complex dielectric constant of crystals," *Phys. Rev.*, vol. 112, pp. 1555–1567, Dec 1958. (Cited on page 47.)

[147] V. Agranovich, "Dispersion of electromagnetic waves in crystals," *SOVIET PHYSICS JETP-USSR*, vol. 10, no. 2, pp. 307–313, 1960. (Cited on page 47.)

[148] C. Weisbuch, M. Nishioka, A. Ishikawa, and Y. Arakawa, "Observation of the coupled exciton-photon mode splitting in a semiconductor quantum microcavity," *Phys. Rev. Lett.*, vol. 69, pp. 3314–3317, Dec 1992. (Cited on pages 47 and 124.)

[149] A. Kavokin and G. Malpuech, *Cavity polaritons*, vol. 32. Elsevier, 2003. (Cited on page 47.)

[150] H. Deng, H. Haug, and Y. Yamamoto, "Exciton-polariton Bose-Einstein condensation," *Reviews of Modern Physics*, vol. 82, no. 2, p. 1489, 2010. (Cited on page 47.)

[151] I. Shelykh, A. Kavokin, Y. G. Rubo, T. Liew, and G. Malpuech, "Polariton polarization-sensitive phenomena in planar semiconductor microcavities," *Semiconductor Science and Technology*, vol. 25, no. 1, p. 013001, 2009. (Cited on pages 47 and 54.)

[152] I. Carusotto and C. Ciuti, "Quantum fluids of light," *Rev. Mod. Phys.*, vol. 85, pp. 299–366, Feb 2013. (Cited on pages 47 and 92.)

[153] A. V. Kavokin and F. P. Laussy, *Microcavities*. No. 21, Oxford University Press, 2017. (Cited on page 47.)

[154] M. Z. Maialle, E. A. de Andrada e Silva, and L. J. Sham, "Exciton spin dynamics in quantum wells," *Phys. Rev. B*, vol. 47, pp. 15776–15788, Jun 1993. (Cited on page 49.)

[155] M. Glazov, E. Ivchenko, G. Wang, T. Amand, X. Marie, B. Urbaszek, and B. Liu, "Spin and valley dynamics of excitons in transition metal dichalcogenide monolayers," *physica status solidi (b)*, vol. 252, no. 11, pp. 2349–2362, 2015. (Cited on page 49.)

[156] G. Panzarini, L. C. Andreani, A. Armitage, D. Baxter, M. S. Skolnick, V. N. Astratov, J. S. Roberts, A. V. Kavokin, M. R. Vladimirova, and M. A. Kaliteevski, "Exciton-light coupling in single and coupled semiconductor microcavities: Polariton dispersion and polarization splitting," *Phys. Rev. B*, vol. 59, pp. 5082–5089, Feb 1999. (Cited on page 49.)

[157] G. Dresselhaus, "Spin-orbit coupling effects in zinc blende structures," *Phys. Rev.*, vol. 100, pp. 580–586, Oct 1955. (Cited on page 50.)

[158] Y. A. Bychkov and E. Rashba, "Properties of a 2D electron gas with lifted spectral degeneracy," *JETP lett*, vol. 39, no. 2, p. 78, 1984. (Cited on page 50.)

[159] A. Manchon, H. C. Koo, J. Nitta, S. Frolov, and R. Duine, "New perspectives for Rashba spin–orbit coupling," *Nature materials*, vol. 14, no. 9, p. 871, 2015. (Cited on page 50.)

[160] A. Kavokin, G. Malpuech, and M. Glazov, "Optical spin Hall effect," *Phys. Rev. Lett.*, vol. 95, p. 136601, Sep 2005. (Cited on pages 52, 62 and 108.)

[161] C. Leyder, M. Romanelli, J. P. Karr, E. Giacobino, T. C. Liew, M. M. Glazov, A. V. Kavokin, G. Malpuech, and A. Bramati, "Observation of the optical spin Hall effect," *Nature Physics*, vol. 3, no. 9, p. 628, 2007. (Cited on pages 52 and 62.)

[162] M. Dyakonov and V. Perel, "Current-induced spin orientation of electrons in semiconductors," *Physics Letters A*, vol. 35, no. 6, pp. 459–460, 1971. (Cited on page 52.)

[163] T. A. Fisher, A. M. Afshar, M. S. Skolnick, D. M. Whittaker, and J. S. Roberts, "Vacuum Rabi coupling enhancement and Zeeman splitting in semiconductor quantum microcavity structures in a high magnetic field," *Phys. Rev. B*, vol. 53, pp. R10469–R10472, Apr 1996. (Cited on page 52.)

[164] A. Armitage, T. A. Fisher, M. S. Skolnick, D. M. Whittaker, P. Kinsler, and J. S. Roberts, "Exciton polaritons in semiconductor quantum microcavities in a high magnetic field," *Phys. Rev. B*, vol. 55, pp. 16395–16403, Jun 1997. (Cited on page 52.)

[165] Y. D. Chong, X.-G. Wen, and M. Soljačić, "Effective theory of quadratic degeneracies," *Phys. Rev. B*, vol. 77, p. 235125, Jun 2008. (Cited on page 52.)

[166] K. Sun, H. Yao, E. Fradkin, and S. A. Kivelson, "Topological insulators and nematic phases from spontaneous symmetry breaking in 2d Fermi systems with a quadratic band crossing," *Phys. Rev. Lett.*, vol. 103, p. 046811, Jul 2009. (Cited on page 52.)

[167] P. G. Savvidis, J. J. Baumberg, R. M. Stevenson, M. S. Skolnick, D. M. Whittaker, and J. S. Roberts, "Angle-resonant stimulated polariton amplifier," *Phys. Rev. Lett.*, vol. 84, pp. 1547–1550, Feb 2000. (Cited on page 52.)

[168] A. Baas, J. P. Karr, H. Eleuch, and E. Giacobino, "Optical bistability in semiconductor microcavities," *Phys. Rev. A*, vol. 69, p. 023809, Feb 2004. (Cited on pages 52 and 57.)

[169] A. Baas, J.-P. Karr, M. Romanelli, A. Bramati, and E. Giacobino, "Optical bistability in semiconductor microcavities in the nondegenerate parametric oscillation regime: Analogy with the optical parametric oscillator," *Phys. Rev. B*, vol. 70, p. 161307, Oct 2004. (Cited on page 52.)

[170] A. Kavokin, G. Malpuech, and F. P. Laussy, "Polariton laser and polariton superfluidity in microcavities," *Physics Letters A*, vol. 306, no. 4, pp. 187–199, 2003. (Cited on page 53.)

[171] I. Carusotto and C. Ciuti, "Probing microcavity polariton superfluidity through resonant rayleigh scattering," *Phys. Rev. Lett.*, vol. 93, p. 166401, Oct 2004. (Cited on pages 53, 57 and 102.)

[172] A. Amo, J. Lefrère, S. Pigeon, C. Adrados, C. Ciuti, I. Carusotto, R. Houdré, E. Giacobino, and A. Bramati, "Superfluidity of polaritons in semiconductor microcavities," *Nature Physics*, vol. 5, no. 11, p. 805, 2009. (Cited on page 53.)

[173] K. G. Lagoudakis, M. Wouters, M. Richard, A. Baas, I. Carusotto, R. André, L. S. Dang, and B. Deveaud-Plédran, "Quantized vortices in an exciton–polariton condensate," *Nature Physics*, vol. 4, no. 9, pp. 706–710, 2008. (Cited on page 53.)

[174] C. Ciuti, V. Savona, C. Piermarocchi, A. Quattropani, and P. Schwendimann, "Role of the exchange of carriers in elastic exciton-exciton scattering in quantum wells," *Phys. Rev. B*, vol. 58, pp. 7926–7933, Sep 1998. (Cited on pages 53 and 54.)

[175] F. Tassone and Y. Yamamoto, "Exciton-exciton scattering dynamics in a semiconductor microcavity and stimulated scattering into polaritons," *Phys. Rev. B*, vol. 59, pp. 10830–10842, Apr 1999. (Cited on page 53.)

[176] C. Ciuti, P. Schwendimann, and A. Quattropani, "Parametric luminescence of microcavity polaritons," *Phys. Rev. B*, vol. 63, p. 041303, Jan 2001. (Cited on page 53.)

[177] M. M. Glazov, H. Ouerdane, L. Pilozzi, G. Malpuech, A. V. Kavokin, and A. D'Andrea, "Polariton-polariton scattering in microcavities: A microscopic theory," *Phys. Rev. B*, vol. 80, p. 155306, Oct 2009. (Cited on page 53.)

[178] M. Wouters, "Resonant polariton-polariton scattering in semiconductor microcavities," *Phys. Rev. B*, vol. 76, p. 045319, Jul 2007. (Cited on page 53.)

[179] M. Vladimirova, S. Cronenberger, D. Scalbert, K. V. Kavokin, A. Miard, A. Lemaître, J. Bloch, D. Solnyshkov, G. Malpuech, and A. V. Kavokin, "Polariton-polariton interaction constants in microcavities," *Phys. Rev. B*, vol. 82, p. 075301, Aug 2010. (Cited on pages 54 and 93.)

[180] N. Takemura, S. Trebaol, M. Wouters, M. T. Portella-Oberli, and B. Deveaud, "Polaritonic Feshbach resonance," *Nature Physics*, vol. 10, no. 7, p. 500, 2014. (Cited on pages 54 and 99.)

[181] N. Takemura, M. D. Anderson, M. Navadeh-Toupchi, D. Y. Oberli, M. T. Portella-Oberli, and B. Deveaud, "Spin anisotropic interactions of lower polaritons in the vicinity of polaritonic Feshbach resonance," *Phys. Rev. B*, vol. 95, p. 205303, May 2017. (Cited on pages 54 and 99.)

[182] P. Renucci, T. Amand, X. Marie, P. Senellart, J. Bloch, B. Sermage, and K. V. Kavokin, "Microcavity polariton spin quantum beats without a magnetic field: A manifestation of Coulomb exchange in dense and polarized polariton systems," *Phys. Rev. B*, vol. 72, p. 075317, Aug 2005. (Cited on pages 54 and 96.)

[183] I. A. Shelykh, Y. G. Rubo, G. Malpuech, D. D. Solnyshkov, and A. Kavokin, "Polarization and propagation of polariton condensates," *Phys. Rev. Lett.*, vol. 97, p. 066402, Aug 2006. (Cited on pages 54 and 95.)

[184] H. Flayac, I. A. Shelykh, D. D. Solnyshkov, and G. Malpuech, "Topological stability of the half-vortices in spinor exciton-polariton condensates," *Phys. Rev. B*, vol. 81, p. 045318, Jan 2010. (Cited on page 54.)

[185] T.-L. Ho and V. Shenoy, "Binary mixtures of Bose condensates of alkali atoms," *Physical review letters*, vol. 77, no. 16, p. 3276, 1996. (Cited on page 54.)

[186] D. S. Hall, M. R. Matthews, J. R. Ensher, C. E. Wieman, and E. A. Cornell, "Dynamics of component separation in a binary mixture of Bose-Einstein condensates," *Phys. Rev. Lett.*, vol. 81, pp. 1539–1542, Aug 1998. (Cited on page 54.)

[187] H. Pu and N. P. Bigelow, "Properties of two-species Bose condensates," *Phys. Rev. Lett.*, vol. 80, pp. 1130–1133, Feb 1998. (Cited on page 54.)

[188] Y. G. Rubo, "Half vortices in exciton polariton condensates," *Phys. Rev. Lett.*, vol. 99, p. 106401, Sep 2007. (Cited on page 54.)

[189] H. Flayac, D. D. Solnyshkov, and G. Malpuech, "Oblique half-solitons and their generation in exciton-polariton condensates," *Phys. Rev. B*, vol. 83, p. 193305, May 2011. (Cited on page 54.)

[190] D. D. Solnyshkov, H. Flayac, and G. Malpuech, "Stable magnetic monopoles in spinor polariton condensates," *Phys. Rev. B*, vol. 85, p. 073105, Feb 2012. (Cited on page 54.)

[191] K. Lagoudakis, T. Ostatnický, A. Kavokin, Y. G. Rubo, R. André, and B. Deveaud-Plédran, "Observation of half-quantum vortices in an exciton-polariton condensate," *Science*, vol. 326, no. 5955, pp. 974–976, 2009. (Cited on page 54.)

[192] R. Hivet, H. Flayac, D. Solnyshkov, D. Tanese, T. Boulier, D. Andreoli, E. Giacobino, J. Bloch, A. Bramati, G. Malpuech, and A. Amo, "Half-solitons in a polariton quantum fluid behave like magnetic monopoles," *Nature Physics*, vol. 8, no. 10, pp. 724–728, 2012. (Cited on page 54.)

[193] L. Dominici, G. Dagvadorj, J. M. Fellows, D. Ballarini, M. De Giorgi, F. M. Marchetti, B. Piccirillo, L. Marrucci, A. Bramati, G. Gigli, M. H. Szymańska, and D. Sanvitto, "Vortex and half-vortex dynamics in a nonlinear spinor quantum fluid," *Science advances*, vol. 1, no. 11, p. e1500807, 2015. (Cited on page 54.)

[194] Y. G. Rubo, A. Kavokin, and I. Shelykh, "Suppression of superfluidity of exciton-polaritons by magnetic field," *Physics Letters A*, vol. 358, no. 3, pp. 227–230, 2006. (Cited on pages 55, 56 and 98.)

[195] D. M. Whittaker, "Effects of polariton-energy renormalization in the microcavity optical parametric oscillator," *Phys. Rev. B*, vol. 71, p. 115301, Mar 2005. (Cited on page 57.)

[196] N. A. Gippius, I. A. Shelykh, D. D. Solnyshkov, S. S. Gavrilov, Y. G. Rubo, A. V. Kavokin, S. G. Tikhodeev, and G. Malpuech, "Polarization multistability of cavity polaritons," *Phys. Rev. Lett.*, vol. 98, p. 236401, Jun 2007. (Cited on page 58.)

[197] D. D. Solnyshkov, I. A. Shelykh, N. A. Gippius, A. V. Kavokin, and G. Malpuech, "Dispersion of interacting spinor cavity polaritons out of thermal equilibrium," *Phys. Rev. B*, vol. 77, p. 045314, Jan 2008. (Cited on pages 58 and 102.)

[198] M. Milićević, T. Ozawa, G. Montambaux, I. Carusotto, E. Galopin, A. Lemaître, L. Le Gratiet, I. Sagnes, J. Bloch, and A. Amo, "Orbital edge states in a photonic honeycomb lattice," *Phys. Rev. Lett.*, vol. 118, p. 107403, Mar 2017. (Cited on pages 58 and 60.)

[199] M. Galbiati, L. Ferrier, D. D. Solnyshkov, D. Tanese, E. Wertz, A. Amo, M. Abbarchi, P. Senellart, I. Sagnes, A. Lemaître, E. Galopin, G. Malpuech, and J. Bloch, "Polariton condensation in photonic molecules," *Phys. Rev. Lett.*, vol. 108, p. 126403, Mar 2012. (Cited on page 58.)

[200] T. Jacqmin, I. Carusotto, I. Sagnes, M. Abbarchi, D. D. Solnyshkov, G. Malpuech, E. Galopin, A. Lemaître, J. Bloch, and A. Amo, "Direct observation of Dirac cones and a flatband in a honeycomb lattice for polaritons," *Phys. Rev. Lett.*, vol. 112, p. 116402, Mar 2014. (Cited on pages 59, 60, 70, 85, 93, 102, 104, 108, 110, 118, 122 and 124.)

[201] C. E. Whittaker, E. Cancellieri, P. M. Walker, D. R. Gulevich, H. Schomerus, D. Vaitiekus, B. Royall, D. M. Whittaker, E. Clarke, I. V. Iorsh, I. A. Shelykh, M. S. Skolnick, and D. N. Krizhanovskii, "Exciton polaritons in a two-dimensional Lieb lattice with spin-orbit coupling," *Phys. Rev. Lett.*, vol. 120, p. 097401, Mar 2018. (Cited on pages 59, 60, 122 and 124.)

[202] C. Schneider, K. Winkler, M. Fraser, M. Kamp, Y. Yamamoto, E. Ostrovskaya, and S. Höfling, "Exciton-polariton trapping and potential landscape engineering," *Reports on Progress in Physics*, vol. 80, no. 1, p. 016503, 2016. (Cited on page 59.)

[203] M. Milićević, T. Ozawa, P. Andreakou, I. Carusotto, T. Jacqmin, E. Galopin, A. Lemaître, L. Le Gratiet, I. Sagnes, J. Bloch, and A. Amo, "Edge states in polariton honeycomb lattices," *2D Materials*, vol. 2, no. 3, p. 034012, 2015. (Cited on pages 60, 102 and 104.)

[204] O. Morsch and M. Oberthaler, "Dynamics of Bose-Einstein condensates in optical lattices," *Rev. Mod. Phys.*, vol. 78, pp. 179–215, Feb 2006. (Cited on page 60.)

[205] N. Nagaosa, J. Sinova, S. Onoda, A. H. MacDonald, and N. P. Ong, "Anomalous Hall effect," *Rev. Mod. Phys.*, vol. 82, pp. 1539–1592, May 2010. (Cited on pages 62 and 150.)

[206] W.-K. Tse, Z. Qiao, Y. Yao, A. H. MacDonald, and Q. Niu, "Quantum anomalous Hall effect in single-layer and bilayer graphene," *Phys. Rev. B*, vol. 83, p. 155447, Apr 2011. (Cited on page 62.)

[207] Z. Qiao, H. Jiang, X. Li, Y. Yao, and Q. Niu, "Microscopic theory of quantum anomalous Hall effect in graphene," *Phys. Rev. B*, vol. 85, p. 115439, Mar 2012. (Cited on pages 62 and 65.)

[208] Z.-Y. Zhang, "The quantum anomalous Hall effect in kagomé lattices," *Journal of Physics: Condensed Matter*, vol. 23, no. 36, p. 365801, 2011. (Cited on pages 62 and 69.)

[209] Y. Ren, Z. Qiao, and Q. Niu, "Topological phases in two-dimensional materials: a review," *Reports on Progress in Physics*, vol. 79, no. 6, p. 066501, 2016. (Cited on pages 62, 75, 107 and 108.)

[210] I. A. Shelykh, G. Pavlovic, D. D. Solnyshkov, and G. Malpuech, "Proposal for a mesoscopic optical Berry-phase interferometer," *Phys. Rev. Lett.*, vol. 102, p. 046407, Jan 2009. (Cited on page 62.)

[211] V. G. Sala, D. D. Solnyshkov, I. Carusotto, T. Jacqmin, A. Lemaître, H. Terças, A. Nalitov, M. Abbarchi, E. Galopin, I. Sagnes, J. Bloch, G. Malpuech, and A. Amo, "Spin-orbit coupling for photons and polaritons in microstructures," *Phys. Rev. X*, vol. 5, p. 011034, Mar 2015. (Cited on pages 62, 124, 129 and 138.)

[212] A. V. Nalitov, D. D. Solnyshkov, and G. Malpuech, "Polariton $\mathbb{Z}$ topological insulator," *Phys. Rev. Lett.*, vol. 114, p. 116401, Mar 2015. (Cited on pages 62, 65, 80, 86 and 134.)

[213] D. Solnyshkov and G. Malpuech, "Chirality in photonic systems," *Comptes Rendus Physique*, vol. 17, p. 920, 2016. (Cited on pages 62, 65, 76 and 108.)

[214] T. Karzig, C.-E. Bardyn, N. H. Lindner, and G. Refael, "Topological polaritons," *Phys. Rev. X*, vol. 5, p. 031001, Jul 2015. (Cited on page 62.)

[215] C.-E. Bardyn, T. Karzig, G. Refael, and T. C. H. Liew, "Topological polaritons and excitons in garden-variety systems," *Phys. Rev. B*, vol. 91, p. 161413, Apr 2015. (Cited on page 62.)

[216] K. Yi and T. Karzig, "Topological polaritons from photonic Dirac cones coupled to excitons in a magnetic field," *Phys. Rev. B*, vol. 93, p. 104303, Mar 2016. (Cited on page 62.)

[217] D. R. Gulevich, D. Yudin, I. V. Iorsh, and I. A. Shelykh, "Kagome lattice from an exciton-polariton perspective," *Phys. Rev. B*, vol. 94, p. 115437, Sep 2016. (Cited on pages 62 and 69.)

[218] M. Zarea and N. Sandler, "Rashba spin-orbit interaction in graphene and zigzag nanoribbons," *Phys. Rev. B*, vol. 79, p. 165442, Apr 2009. (Cited on page 63.)

[219] A. V. Nalitov, G. Malpuech, H. Terças, and D. D. Solnyshkov, "Spin-orbit coupling and the optical spin Hall effect in photonic graphene," *Phys. Rev. Lett.*, vol. 114, p. 026803, Jan 2015. (Cited on pages 63, 64, 76 and 77.)

[220] P. Rakyta, A. Kormányos, and J. Cserti, "Trigonal warping and anisotropic band splitting in monolayer graphene due to rashba spin-orbit coupling," *Phys. Rev. B*, vol. 82, p. 113405, Sep 2010. (Cited on page 64.)

[221] E. McCann, "Asymmetry gap in the electronic band structure of bilayer graphene," *Phys. Rev. B*, vol. 74, p. 161403, Oct 2006. (Cited on pages 64, 75 and 150.)

[222] R. De Gail, J.-N. Fuchs, M. Goerbig, F. Piéchon, and G. Montambaux, "Manipulation of dirac points in graphene-like crystals," *Physica B: Condensed Matter*, vol. 407, no. 11, pp. 1948–1952, 2012. (Cited on pages 64 and 96.)

[223] E. McCann and M. Koshino, "The electronic properties of bilayer graphene," *Reports on Progress in Physics*, vol. 76, no. 5, p. 056503, 2013. (Cited on pages 64 and 131.)

[224] T. Fukui, Y. Hatsugai, and H. Suzuki, "Chern numbers in discretized Brillouin zone: Efficient method of computing (spin) Hall conductances," *Journal of the Physical Society of Japan*, vol. 74, no. 6, pp. 1674–1677, 2005. (Cited on pages 65 and 95.)

[225] R. Wang, Q. Qiao, B. Wang, X.-H. Ding, and Y.-F. Zhang, "The topological quantum phase transitions in Lieb lattice driven by the Rashba soc and exchange field," *The European Physical Journal B*, vol. 89, no. 9, p. 192, 2016. (Cited on page 69.)

[226] C. Li, F. Ye, X. Chen, Y. V. Kartashov, A. Ferrando, L. Torner, and D. V. Skryabin, "Lieb polariton topological insulators," *Phys. Rev. B*, vol. 97, p. 081103, Feb 2018. (Cited on page 69.)

[227] S. Klembt, T. Harder, O. Egorov, K. Winkler, R. Ge, M. Bandres, M. Emmerling, L. Worschech, T. Liew, M. Segev, *et al.*, "Exciton-polariton topological insulator," *Nature*, vol. 562, no. 7728, p. 552, 2018. (Cited on page 69.)

[228] D. Xiao, G.-B. Liu, W. Feng, X. Xu, and W. Yao, "Coupled spin and valley physics in monolayers of mos_2 and other group-vi dichalcogenides," *Phys. Rev. Lett.*, vol. 108, p. 196802, May 2012. (Cited on pages 69 and 110.)

[229] M. Trushin, M. O. Goerbig, and W. Belzig, "Optical absorption by Dirac excitons in single-layer transition-metal dichalcogenides," *Phys. Rev. B*, vol. 94, p. 041301, Jul 2016. (Cited on page 69.)

[230] H. Zeng, J. Dai, W. Yao, D. Xiao, and X. Cui, "Valley polarization in MoS2 monolayers by optical pumping," *Nature nanotechnology*, vol. 7, no. 8, pp. 490–493, 2012. (Cited on page 69.)

[231] K. F. Mak, K. He, J. Shan, and T. F. Heinz, "Control of valley polarization in monolayer MoS2 by optical helicity," *Nature nanotechnology*, vol. 7, no. 8, pp. 494–498, 2012. (Cited on page 69.)

[232] W. Yao, D. Xiao, and Q. Niu, "Valley-dependent optoelectronics from inversion symmetry breaking," *Phys. Rev. B*, vol. 77, p. 235406, Jun 2008. (Cited on page 69.)

[233] T. Cao, G. Wang, W. Han, H. Ye, C. Zhu, J. Shi, Q. Niu, P. Tan, E. Wang, B. Liu, *et al.*, "Valley-selective circular dichroism of monolayer molybdenum disulphide," *Nature communications*, vol. 3, p. 887, 2012. (Cited on page 69.)

[234] K. F. Mak, K. L. McGill, J. Park, and P. L. McEuen, "The valley Hall effect in MoS2 transistors," *Science*, vol. 344, no. 6191, pp. 1489–1492, 2014. (Cited on page 69.)

[235] F. Zhang, A. H. MacDonald, and E. J. Mele, "Valley Chern numbers and boundary modes in gapped bilayer graphene," *Proceedings of the National Academy of Sciences*, vol. 110, no. 26, pp. 10546–10551, 2013. (Cited on pages 71, 75 and 108.)

[236] G. W. Semenoff, V. Semenoff, and F. Zhou, "Domain walls in gapped graphene," *Phys. Rev. Lett.*, vol. 101, p. 087204, Aug 2008. (Cited on pages 71 and 73.)

[237] I. Martin, Y. M. Blanter, and A. F. Morpurgo, "Topological confinement in bilayer graphene," *Phys. Rev. Lett.*, vol. 100, p. 036804, Jan 2008. (Cited on pages 71, 73 and 75.)

[238] J. Li, A. F. Morpurgo, M. Büttiker, and I. Martin, "Marginality of bulk-edge correspondence for single-valley hamiltonians," *Phys. Rev. B*, vol. 82, p. 245404, Dec 2010. (Cited on page 71.)

[239] G. E. Volovik, *The universe in a helium droplet*, vol. 117. Oxford University Press on Demand, 2003. (Cited on pages 71 and 92.)

[240] Y.-T. Zhang, Z. Qiao, and Q.-F. Sun, "Detecting zero-line mode in bilayer graphene via the quantum Hall effect," *Phys. Rev. B*, vol. 87, p. 235405, Jun 2013. (Cited on page 73.)

[241] V. M. Pereira, F. Guinea, J. L. Dos Santos, N. Peres, and A. C. Neto, "Disorder induced localized states in graphene," *Physical review letters*, vol. 96, no. 3, p. 036801, 2006. (Cited on page 73.)

[242] E. V. Castro, K. S. Novoselov, S. V. Morozov, N. M. R. Peres, J. M. B. L. dos Santos, J. Nilsson, F. Guinea, A. K. Geim, and A. H. C. Neto, "Biased bilayer graphene: Semiconductor with a gap tunable by the electric field effect," *Phys. Rev. Lett.*, vol. 99, p. 216802, Nov 2007. (Cited on pages 75 and 150.)

[243] J. Li, I. Martin, M. Büttiker, and A. F. Morpurgo, "Topological origin of subgap conductance in insulating bilayer graphene," *Nature Physics*, vol. 7, no. 1, pp. 38–42, 2011. (Cited on page 75.)

[244] E. V. Castro, N. M. R. Peres, J. M. B. Lopes dos Santos, A. H. C. Neto, and F. Guinea, "Localized states at zigzag edges of bilayer graphene," *Phys. Rev. Lett.*, vol. 100, p. 026802, Jan 2008. (Cited on page 75.)

[245] L. Ju, Z. Shi, N. Nair, Y. Lv, C. Jin, J. Velasco Jr, C. Ojeda-Aristizabal, H. A. Bechtel, M. C. Martin, A. Zettl, J. Analytis, and F. Wang, "Topological valley transport at bilayer graphene domain walls," *Nature*, vol. 520, no. 7549, pp. 650–655, 2015. (Cited on pages 75 and 108.)

[246] A. Vaezi, Y. Liang, D. H. Ngai, L. Yang, and E.-A. Kim, "Topological edge states at a tilt boundary in gated multilayer graphene," *Phys. Rev. X*, vol. 3, p. 021018, Jun 2013. (Cited on page 75.)

[247] E. C. Marino, L. O. Nascimento, V. S. Alves, and C. M. Smith, "Interaction induced quantum valley Hall effect in graphene," *Phys. Rev. X*, vol. 5, p. 011040, Mar 2015. (Cited on page 75.)

[248] H. Pan, Z. Li, C.-C. Liu, G. Zhu, Z. Qiao, and Y. Yao, "Valley-polarized quantum anomalous Hall effect in silicene," *Phys. Rev. Lett.*, vol. 112, p. 106802, Mar 2014. (Cited on page 75.)

[249] T. Ozawa and I. Carusotto, "Anomalous and quantum Hall effects in lossy photonic lattices," *Phys. Rev. Lett.*, vol. 112, p. 133902, Apr 2014. (Cited on pages 75 and 122.)

[250] S. Barik, H. Miyake, W. DeGottardi, E. Waks, and M. Hafezi, "Two-dimensionally confined topological edge states in photonic crystals," *New Journal of Physics*, vol. 18, no. 11, p. 113013, 2016. (Cited on pages 75 and 108.)

[251] T. Ma, A. B. Khanikaev, S. H. Mousavi, and G. Shvets, "Guiding electromagnetic waves around sharp corners: Topologically protected photonic transport in metawaveguides," *Phys. Rev. Lett.*, vol. 114, p. 127401, Mar 2015. (Cited on pages 75 and 108.)

[252] T. Ma and G. Shvets, "All-Si valley-Hall photonic topological insulator," *New Journal of Physics*, vol. 18, no. 2, p. 025012, 2016. (Cited on pages 75 and 108.)

[253] X.-D. Chen and J.-W. Dong, "Valley-protected backscattering suppression in silicon photonic graphene," *arXiv preprint arXiv:1602.03352*, 2016. (Cited on page 75.)

[254] F. Gao, H. Xue, Z. Yang, K. Lai, Y. Yu, X. Lin, Y. Chong, G. Shvets, and B. Zhang, "Topologically protected refraction of robust kink states in valley photonic crystals," *Nature Physics*, vol. 14, no. 2, p. 140, 2018. (Cited on pages 75 and 108.)

[255] X. Wu, Y. Meng, J. Tian, Y. Huang, H. Xiang, D. Han, and W. Wen, "Direct observation of valley-polarized topological edge states in designer surface plasmon crystals," *Nature communications*, vol. 8, no. 1, p. 1304, 2017. (Cited on page 75.)

[256] F. Zhang, "Topological valleytronics: Brought to light," *Nature Physics*, vol. 14, no. 2, p. 111, 2018. (Cited on pages 75 and 108.)

[257] J. Noh, S. Huang, K. P. Chen, and M. C. Rechtsman, "Observation of photonic topological valley hall edge states," *Phys. Rev. Lett.*, vol. 120, p. 063902, Feb 2018. (Cited on page 75.)

[258] O. Bleu, D. D. Solnyshkov, and G. Malpuech, "Photonic versus electronic quantum anomalous Hall effect," *Phys. Rev. B*, vol. 95, p. 115415, Mar 2017. (Cited on pages 80 and 87.)

[259] H. Pan, X. Li, F. Zhang, and S. A. Yang, "Perfect valley filter in a topological domain wall," *Phys. Rev. B*, vol. 92, p. 041404, Jul 2015. (Cited on page 80.)

[260] O. Bleu, D. D. Solnyshkov, and G. Malpuech, "Quantum valley Hall effect and perfect valley filter based on photonic analogs of transitional metal dichalcogenides," *Phys. Rev. B*, vol. 95, p. 235431, Jun 2017. (Cited on pages 85, 86, 87, 88, 89 and 108.)

[261] Y. Sun, P. Wen, Y. Yoon, G. Liu, M. Steger, L. N. Pfeiffer, K. West, D. W. Snoke, and K. A. Nelson, "Bose-Einstein condensation of long-lifetime polaritons in thermal equilibrium," *Phys. Rev. Lett.*, vol. 118, p. 016602, Jan 2017. (Cited on page 86.)

[262] G. Volovik, "Fermion zero modes on vortices in chiral superconductors," *Journal of Experimental and Theoretical Physics Letters*, vol. 70, no. 9, pp. 609–614, 1999. (Cited on page 92.)

[263] L. Fu and C. L. Kane, "Superconducting proximity effect and Majorana fermions at the surface of a topological insulator," *Phys. Rev. Lett.*, vol. 100, p. 096407, Mar 2008. (Cited on page 92.)

[264] M. Sato and Y. Ando, "Topological superconductors: a review," *Reports on Progress in Physics*, vol. 80, no. 7, p. 076501, 2017. (Cited on page 92.)

[265] S. R. Elliott and M. Franz, "Colloquium," *Rev. Mod. Phys.*, vol. 87, pp. 137–163, Feb 2015. (Cited on page 92.)

[266] C. Nayak, S. H. Simon, A. Stern, M. Freedman, and S. Das Sarma, "Non-abelian anyons and topological quantum computation," *Rev. Mod. Phys.*, vol. 80, pp. 1083–1159, Sep 2008. (Cited on page 92.)

[267] A. J. Leggett, "Superfluidity," *Rev. Mod. Phys.*, vol. 71, pp. S318–S323, Mar 1999. (Cited on page 92.)

[268] A. Leggett, *Quantum Liquids.* Oxford Graduate Texts, 2006. (Cited on pages 92 and 107.)

[269] M. Machholm, C. J. Pethick, and H. Smith, "Band structure, elementary excitations, and stability of a bose-einstein condensate in a periodic potential," *Phys. Rev. A*, vol. 67, p. 053613, May 2003. (Cited on page 92.)

[270] Z. Chen and B. Wu, "Bose-Einstein condensate in a honeycomb optical lattice: Fingerprint of superfluidity at the Dirac point," *Phys. Rev. Lett.*, vol. 107, p. 065301, Aug 2011. (Cited on page 92.)

[271] R. Shindou, R. Matsumoto, S. Murakami, and J.-i. Ohe, "Topological chiral magnonic edge mode in a magnonic crystal," *Phys. Rev. B*, vol. 87, p. 174427, May 2013. (Cited on pages 92 and 95.)

[272] S. Furukawa and M. Ueda, "Excitation band topology and edge matter waves in Bose-Einstein condensates in optical lattices," *New Journal of Physics*, vol. 17, no. 11, p. 115014, 2015. (Cited on pages 92, 95 and 101.)

[273] V. Peano, M. Houde, C. Brendel, F. Marquardt, and A. A. Clerk, "Topological phase transitions and chiral inelastic transport induced by the squeezing of light," *Nature communications*, vol. 7, p. 10779, 2016. (Cited on pages 92, 95 and 104.)

[274] G. Engelhardt and T. Brandes, "Topological Bogoliubov excitations in inversion-symmetric systems of interacting bosons," *Phys. Rev. A*, vol. 91, p. 053621, May 2015. (Cited on pages 92 and 95.)

[275] C.-E. Bardyn, T. Karzig, G. Refael, and T. C. H. Liew, "Chiral Bogoliubov excitations in nonlinear bosonic systems," *Phys. Rev. B*, vol. 93, p. 020502, Jan 2016. (Cited on pages 92 and 104.)

[276] O. Bleu, D. D. Solnyshkov, and G. Malpuech, "Interacting quantum fluid in a polariton Chern insulator," *Phys. Rev. B*, vol. 93, p. 085438, Feb 2016. (Cited on pages 92 and 98.)

[277] G. Engelhardt, M. Benito, G. Platero, and T. Brandes, "Topological instabilities in ac-driven bosonic systems," *Phys. Rev. Lett.*, vol. 117, p. 045302, Jul 2016. (Cited on page 92.)

[278] H. Sigurdsson, G. Li, and T. C. H. Liew, "Spontaneous and superfluid chiral edge states in exciton-polariton condensates," *Phys. Rev. B*, vol. 96, p. 115453, Sep 2017. (Cited on page 92.)

[279] Y. V. Kartashov and D. V. Skryabin, "Modulational instability and solitary waves in polariton topological insulators," *Optica*, vol. 3, no. 11, pp. 1228–1236, 2016. (Cited on page 92.)

[280] D. R. Gulevich, D. Yudin, D. V. Skryabin, I. V. Iorsh, and I. A. Shelykh, "Exploring nonlinear topological states of matter with exciton-polaritons: Edge solitons in kagome lattice," *Scientific Reports*, vol. 7, no. 1, p. 1780, 2017. (Cited on page 92.)

[281] Y. V. Kartashov and D. V. Skryabin, "Bistable topological insulator with exciton-polaritons," *Phys. Rev. Lett.*, vol. 119, p. 253904, Dec 2017. (Cited on page 92.)

[282] Y. Lumer, Y. Plotnik, M. C. Rechtsman, and M. Segev, "Self-localized states in photonic topological insulators," *Phys. Rev. Lett.*, vol. 111, p. 243905, Dec 2013. (Cited on page 92.)

[283] J. J. Baumberg, A. V. Kavokin, S. Christopoulos, A. J. D. Grundy, R. Butté, G. Christmann, D. D. Solnyshkov, G. Malpuech, G. Baldassarri Höger von Högersthal, E. Feltin, J.-F. Carlin, and N. Grandjean, "Spontaneous polarization buildup in a room-temperature polariton laser," *Phys. Rev. Lett.*, vol. 101, p. 136409, Sep 2008. (Cited on page 93.)

[284] E. Wertz, L. Ferrier, D. D. Solnyshkov, P. Senellart, D. Bajoni, A. Miard, A. Lemaître, G. Malpuech, and J. Bloch, "Spontaneous formation of a polariton condensate in a planar GaAs microcavity," *Applied Physics Letters*, vol. 95, no. 5, p. 051108, 2009. (Cited on page 93.)

[285] J. Levrat, R. Butté, E. Feltin, J.-F. m. c. Carlin, N. Grandjean, D. Solnyshkov, and G. Malpuech, "Condensation phase diagram of cavity polaritons in GaN-based microcavities: Experiment and theory," *Phys. Rev. B*, vol. 81, p. 125305, Mar 2010. (Cited on page 93.)

[286] D. Tanese, H. Flayac, D. Solnyshkov, A. Amo, A. Lemaitre, E. Galopin, R. Braive, P. Senellart, I. Sagnes, G. Malpuech, and J. Bloch, "Polariton condensation in solitonic gap states in a one-dimensional periodic potential," *Nature communications*, vol. 4, p. 1749, 2013. (Cited on pages 93 and 113.)

[287] L. Zhang, W. Xie, J. Wang, A. Poddubny, J. Lu, Y. Wang, J. Gu, W. Liu, D. Xu, X. Shen, *et al.*, "Weak lasing in one-dimensional polariton superlattices," *Proceedings of the National Academy of Sciences*, vol. 112, no. 13, pp. E1516–E1519, 2015. (Cited on page 93.)

[288] C. Sturm, D. Solnyshkov, O. Krebs, A. Lemaître, I. Sagnes, E. Galopin, A. Amo, G. Malpuech, and J. Bloch, "Nonequilibrium polariton condensate in a magnetic field," *Phys. Rev. B*, vol. 91, p. 155130, Apr 2015. (Cited on page 93.)

[289] E. Lifshitz and L. Pitaevskii, *Statistical Mechanics, Part 2*. Pergamon Press, New York, 1980. (Cited on page 95.)

[290] M. Di Liberto, A. Hemmerich, and C. Morais Smith, "Topological Varma superfluid in optical lattices," *Phys. Rev. Lett.*, vol. 117, p. 163001, Oct 2016. (Cited on pages 95 and 104.)

[291] V. Peano and H. Schulz-Baldes, "Topological edge states for disordered bosonic systems," *Journal of Mathematical Physics*, vol. 59, no. 3, p. 031901, 2018. (Cited on page 95.)

[292] A. B. Khanikaev, S. H. Mousavi, W.-K. Tse, M. Kargarian, A. H. MacDonald, and G. Shvets, "Photonic topological insulators," *Nature materials*, vol. 12, no. 3, p. 233, 2013. (Cited on page 108.)

[293] A. Slobozhanyuk, S. H. Mousavi, X. Ni, D. Smirnova, Y. S. Kivshar, and A. B. Khanikaev, "Three-dimensional all-dielectric photonic topological insulator," *Nature Photonics*, vol. 11, no. 2, p. 130, 2017. (Cited on page 108.)

[294] F. Zhang, J. Jung, G. A. Fiete, Q. Niu, and A. H. MacDonald, "Spontaneous quantum Hall states in chirally stacked few-layer graphene systems," *Phys. Rev. Lett.*, vol. 106, p. 156801, Apr 2011. (Cited on pages 108 and 150.)

[295] L.-H. Wu and X. Hu, "Scheme for achieving a topological photonic crystal by using dielectric material," *Phys. Rev. Lett.*, vol. 114, p. 223901, Jun 2015. (Cited on page 108.)

[296] L. Xu, H.-X. Wang, Y.-D. Xu, H.-Y. Chen, and J.-H. Jiang, "Accidental degeneracy in photonic bands and topological phase transitions in two-dimensional core-shell dielectric photonic crystals," *Opt. Express*, vol. 24, pp. 18059–18071, Aug 2016. (Cited on page 108.)

[297] P. Soltan-Panahi, J. Struck, P. Hauke, A. Bick, W. Plenkers, G. Meineke, C. Becker, P. Windpassinger, M. Lewenstein, and K. Sengstock, "Multicomponent quantum gases in spin-dependent hexagonal lattices," *Nature Physics*, vol. 7, no. 5, p. 434, 2011. (Cited on page 108.)

[298] L. Haddad, C. Weaver, and L. D. Carr, "The nonlinear Dirac equation in Bose-Einstein condensates: I. relativistic solitons in armchair nanoribbon optical lattices," *New Journal of Physics*, vol. 17, no. 6, p. 063033, 2015. (Cited on page 108.)

[299] L. Haddad and L. D. Carr, "The nonlinear Dirac equation in Bose-Einstein condensates: Vortex solutions and spectra in a weak harmonic trap," *New Journal of Physics*, vol. 17, no. 11, p. 113011, 2015. (Cited on page 108.)

[300] J. Cuevas-Maraver, P. G. Kevrekidis, A. Saxena, A. Comech, and R. Lan, "Stability of solitary waves and vortices in a 2D nonlinear Dirac model," *Phys. Rev. Lett.*, vol. 116, p. 214101, May 2016. (Cited on page 108.)

[301] A. N. Poddubny and D. A. Smirnova, "Ring Dirac solitons in nonlinear topological systems," *Phys. Rev. A*, vol. 98, p. 013827, Jul 2018. (Cited on page 108.)

[302] L. P. Pitaevskii *Sov. Phys. JETP*, vol. 35, p. 282, 1959. (Cited on page 111.)

[303] D. D. Solnyshkov, "Quantized vortex chiral propagation." https://www.youtube.com/watch?v=PNsDF5xUvH4. (Cited on pages 113 and 119.)

[304] A. Auerbach, D. P. Arovas, and S. Ghosh, "Quantum tunneling of vortices in two-dimensional condensates," *Phys. Rev. B*, vol. 74, p. 064511, Aug 2006. (Cited on page 118.)

[305] O. Fialko, A. S. Bradley, and J. Brand, "Quantum tunneling of a vortex between two pinning potentials," *Phys. Rev. Lett.*, vol. 108, p. 015301, Jan 2012. (Cited on page 118.)

[306] P. W. Anderson, "Theory of flux creep in hard superconductors," *Phys. Rev. Lett.*, vol. 9, pp. 309–311, Oct 1962. (Cited on page 118.)

[307] L. Ferrier, E. Wertz, R. Johne, D. D. Solnyshkov, P. Senellart, I. Sagnes, A. Lemaître, G. Malpuech, and J. Bloch, "Interactions in confined polariton condensates," *Phys. Rev. Lett.*, vol. 106, p. 126401, Mar 2011. (Cited on page 118.)

[308] H. M. Price, O. Zilberberg, T. Ozawa, I. Carusotto, and N. Goldman, "Measurement of Chern numbers through center-of-mass responses," *Phys. Rev. B*, vol. 93, p. 245113, Jun 2016. (Cited on page 122.)

[309] M. Hafezi, "Measuring topological invariants in photonic systems," *Phys. Rev. Lett.*, vol. 112, p. 210405, May 2014. (Cited on page 122.)

[310] A. V. Poshakinskiy, A. N. Poddubny, and M. Hafezi, "Phase spectroscopy of topological invariants in photonic crystals," *Phys. Rev. A*, vol. 91, p. 043830, Apr 2015. (Cited on page 122.)

[311] M. Wimmer, H. M. Price, I. Carusotto, and U. Peschel, "Experimental measurement of the Berry curvature from anomalous transport," *Nature Physics*, vol. 13, no. 6, p. 545, 2017. (Cited on page 122.)

[312] T. Ozawa, "Steady-state Hall response and quantum geometry of driven-dissipative lattices," *Phys. Rev. B*, vol. 97, p. 041108, Jan 2018. (Cited on page 122.)

[313] D. Leykam, K. Y. Bliokh, C. Huang, Y. D. Chong, and F. Nori, "Edge modes, degeneracies, and topological numbers in non-hermitian systems," *Phys. Rev. Lett.*, vol. 118, p. 040401, Jan 2017. (Cited on page 122.)

[314] H. Shen, B. Zhen, and L. Fu, "Topological band theory for non-hermitian hamiltonians," *Phys. Rev. Lett.*, vol. 120, p. 146402, Apr 2018. (Cited on page 122.)

[315] D. D. Solnyshkov, M. M. Glazov, I. A. Shelykh, A. V. Kavokin, E. L. Ivchenko, and G. Malpuech, "Magnetic field effect on polarization and dispersion of exciton-polaritons in planar microcavities," *Phys. Rev. B*, vol. 78, p. 165323, Oct 2008. (Cited on page 124.)

[316] M. Martín, A. Amo, L. Viña, I. Shelykh, M. Glazov, G. Malpuech, A. Kavokin, R. André, *et al.*, "Optical anisotropy and pinning of the linear polarization of light in semiconductor microcavities," *Solid state communications*, vol. 139, no. 10, pp. 511–515, 2006. (Cited on page 124.)

[317] G. Malpuech, M. M. Glazov, I. A. Shelykh, P. Bigenwald, and K. V. Kavokin, "Electronic control of the polarization of light emitted by polariton lasers," *Applied Physics Letters*, vol. 88, no. 11, p. 111118, 2006. (Cited on page 124.)

[318] H. Terças, H. Flayac, D. D. Solnyshkov, and G. Malpuech, "Non-abelian gauge fields in photonic cavities and photonic superfluids," *Phys. Rev. Lett.*, vol. 112, p. 066402, Feb 2014. (Cited on page 126.)

[319] C. Wu and S. Das Sarma, "$p_{x,y}$-orbital counterpart of graphene: Cold atoms in the honeycomb optical lattice," *Phys. Rev. B*, vol. 77, p. 235107, Jun 2008. (Cited on page 131.)

[320] L. D. Landau *Phys. Z. Sovjetunion*, vol. 1, p. 88, 1932. (Cited on page 139.)

[321] L. D. Landau *Phys. Z. Sovjetunion*, vol. 2, p. 46, 1932. (Cited on page 139.)

[322] C. Zener, "Non-adiabatic crossing of energy levels," *Proc. R. Soc. Lond. A*, vol. 137, no. 833, pp. 696–702, 1932. (Cited on page 139.)

[323] L. D. Landau and E. Teller *Phys. Z. Sowjetunion*, vol. 10, p. 34, 1936. (Cited on page 139.)

[324] E. Stückelberg, "Theory of inelastic collisions between atoms(theory of inelastic collisions between atoms, using two simultaneous differential equations)," *Helv. Phys. Acta,(Basel)*, vol. 5, pp. 369–422, 1932. (Cited on page 139.)

[325] J. P. Davis and P. Pechukas *J. Chem. Phys.*, vol. 64, p. 3129, 1976. (Cited on page 139.)

[326] S. Shevchenko, S. Ashhab, and F. Nori, "Landau–Zener–Stückelberg interferometry," *Physics Reports*, vol. 492, no. 1, pp. 1 – 30, 2010. (Cited on page 139.)

[327] A. M. Dykhne *Sov. Phys. JETP*, vol. 11, p. 411, 1960. (Cited on page 139.)

[328] L. D. Landau and E. M. Lifshitz, *Quantum Mechanics: Non-relativistic theory*. Pergamon Press, 1991. (Cited on page 139.)

[329] K. Y. Bliokh, "On spin evolution in a time-dependent magnetic field: Post-adiabatic corrections and geometric phases," *Physics Letters A*, vol. 372, no. 3, pp. 204–209, 2008. (Cited on page 144.)

[330] P. Gosselin and H. Mohrbach, "Appearance of gauge fields and forces beyond the adiabatic approximation," *Journal of Physics A: Mathematical and Theoretical*, vol. 43, no. 35, p. 354025, 2010. (Cited on page 144.)

[331] S. Oh, X. Hu, F. Nori, and S. Kais, "Singularity of the time-energy uncertainty in adiabatic perturbation and cycloids on a Bloch sphere," *Scientific reports*, vol. 6, p. 20824, 2016. (Cited on page 144.)

[332] R. Karplus and J. M. Luttinger, "Hall effect in ferromagnetics," *Phys. Rev.*, vol. 95, pp. 1154–1160, Sep 1954. (Cited on pages 144 and 159.)

[333] G. Sundaram and Q. Niu, "Wave-packet dynamics in slowly perturbed crystals: Gradient corrections and Berry-phase effects," *Phys. Rev. B*, vol. 59, pp. 14915–14925, Jun 1999. (Cited on pages 144, 145 and 159.)

[334] A. H. MacDonald, J. Jung, and F. Zhang, "Pseudospin order in monolayer, bilayer and double-layer graphene," *Physica Scripta*, vol. 2012, no. T146, p. 014012, 2012. (Cited on page 150.)

[335] X. Ling, X. Zhou, X. Yi, W. Shu, Y. Liu, S. Chen, H. Luo, S. Wen, and D. Fan, "Giant photonic spin Hall effect in momentum space in a structured metamaterial with spatially varying birefringence," *Light: Science & Applications*, vol. 4, no. 5, p. e290, 2015. (Cited on page 151.)

[336] A. Gutiérrez-Rubio, L. Chirolli, L. Martín-Moreno, F. J. García-Vidal, and F. Guinea, "Polariton anomalous Hall effect in transition-metal dichalcogenides," *Phys. Rev. Lett.*, vol. 121, p. 137402, Sep 2018. (Cited on page 153.)

Publications

1. D. D. Solnyshkov, <u>O. Bleu</u>, and G. Malpuech, "All-optical Controlled-NOT gate based on exciton-polariton circuit", *Superlattices and Microstructures 83 466475 (2015)*

2. <u>O. Bleu</u>, D. D. Solnyshkov, and G. Malpuech, "Interacting quantum fluid in a polariton Chern insulator", *Phys. Rev. B 93, 085438 (2016)*

3. D. D. Solnyshkov, <u>O. Bleu</u>, B. Teklu and G. Malpuech, "Chirality of Topological Gap Solitons in Bosonic Dimer Chains", *Phys. Rev. Lett. 118, 023901 (2017)*

4. <u>O. Bleu</u>, D. D. Solnyshkov, and G. Malpuech, "Photonic versus electronic quantum anomalous Hall effect", *Phys. Rev. B 95, 115415 (2017)*

5. <u>O. Bleu</u>, D. D. Solnyshkov, and G. Malpuech, "Quantum valley Hall effect and perfect valley filter based on photonic analogs of transitional metal dichalcogenides", *Phys. Rev. B 95, 235431 (2017)*

6. <u>O. Bleu</u>, D. D. Solnyshkov, and G. Malpuech, "Optical valley Hall effect based on transitional metal dichalcogenide cavity polaritons", *Phys. Rev. B 96, 165432 (2017)*

7. <u>O. Bleu</u>, D. D. Solnyshkov, and G. Malpuech, "Measuring the quantum geometric tensor in two-dimensional photonic and exciton-polariton systems", *Phys. Rev. B 97, 195422 (2018)*

8. <u>O. Bleu</u>, G. Malpuech, Y. Gao and D. D. Solnyshkov, "Effective theory of nonadiabatic quantum evolution based on the quantum geometric tensor", *Phys. Rev. Lett. 121, 020401 (2018)*

9. <u>O. Bleu</u>, G. Malpuech and D. D. Solnyshkov, "Robust quantum valley Hall effect for vortices in an interacting bosonic quantum fluid", *Nat. Comm. 9, 3991 (2018)*

10. M. Milićević, <u>O. Bleu</u>, D. D. Solnyshkov, I. Sagnes, A. Lemaître, L. Le Gratiet, A. Harouri, J. Bloch, G. Malpuech, A. Amo, "Lasing in optically induced gap states in photonic graphene", *SciPost Phys. 5, 064 (2018)*

11. N. C. Zambon, P. St-Jean, M. Milićević, A. Lemaître, A. Harouri, L. LeGratiet, <u>O. Bleu</u>, D. D. Solnyshkov, G. Malpuech, I. Sagnes, S. Ravets, A. Amo, J. Bloch, "Optically controlling the emission chirality of microlasers", *arXiv:1806.04590 (2018) (accepted to Nature Photonics)*

12. Z. Zhang, F. Li, G. Malpuech, Y. Zhang, <u>O. Bleu</u>, S. Koniakhin, C. Li, Y. Zhang, M. Xiao, D. D. Solnyshkov, "Particle-like behavior of topological defects in linear wave packets in photonic graphene", *arXiv:1806.05540 (2018) (submitted to PRL)*

Conferences

Oral contributions

1. 17th International Conference on Physics of Light-Matter Coupling in Nanostructures (2016) – Nara, Japan

2. 33rd International Conference on the Physics of Semiconductors (2016) – Beijing, China

3. Séminaire «théorie de la matière condensée sur le plateau» (2017) –Laboratoire de Physique des Solides, Orsay, France

4. International Conference on Optics of Excitons in Confined Structures (2017) – Bath, UK

5. Topical research meeting on topological states in strongly interacting light-matter systems (2018) – Milton Keynes, UK

6. 19th International Conference on Physics of Light-Matter Coupling in Nanostructures (2018) – Chengdu, China

Poster contributions

1. Quantum Fluids of Light and Matter (2017) – Cargese, Corsica

2. 18th International Conference on Physics of Light-Matter Coupling in Nanostructures (2017) – Würzburg, Germany

3. International Conference on Optics of Excitons in Confined Structures (2017) – Bath, UK

Physics of quantum fluids in two-dimensional topological systems

Abstract: This thesis is dedicated to the description of both single-particle and bosonic quantum fluid Physics in topological systems.

After introductory chapters on these subjects, I first discuss single-particle topological phenomena in honeycomb lattices. This allows to compare two theoretical models leading to quantum anomalous Hall effect for electrons and photons and to discuss the photonic quantum valley Hall effect at the interface between opposite staggered cavity lattices.

In a second part, I present some phenomena which emerge due to the interplay of the linear topological effects with the presence of interacting bosonic quantum fluid described by mean-field Gross-Pitaevskii equation. First, I show that the spin-anisotropic interactions lead to density-driven topological transitions for elementary excitations of a condensate loaded in the polariton quantum anomalous Hall model (thermal equilibrium and out-of-equilibrium quasi-resonant excitation configurations).

Then, I show that the vortex excitations of a scalar condensate in a quantum valley Hall system, contrary to linear wavepackets, can exhibit a robust chiral propagation along the interface, with direction given by their winding in real space, leading to an analog of quantum spin Hall effect for these non-linear excitations.

Finally, coming back to linear geometrical effects, I will focus on the anomalous Hall effect exhibited by an accelerated wavepacket in a two-band system. In this context, I present a non-adiabatic correction to the known semiclassical equations of motion which can be expressed in terms of the quantum geometric tensor elements. We also propose a protocol to directly measure the tensor components in radiative photonic systems.

Keywords: Topological insulators, band geometry, Berry curvature, anomalous Hall effect, Chern insulators, spin-orbit coupling, topological photonics, exciton-polaritons, Bose-Einstein condensates, Bogoliubov excitations, quantized vortices.